



**TECHNISCHE UNIVERSITÄT
MÜNCHEN**



Fakultät für Chemie

**Structural Design and Modification of Surface
Anchored Metal-Organic Frameworks:
from Fundamental Study towards Applications**

Suttipong Wannapaiboon

Vollständiger Abdruck der von der Fakultät für Chemie der Technischen Universität München zur Erlangung des akademischen Grades eines Doktors der Naturwissenschaften genehmigten Dissertation.

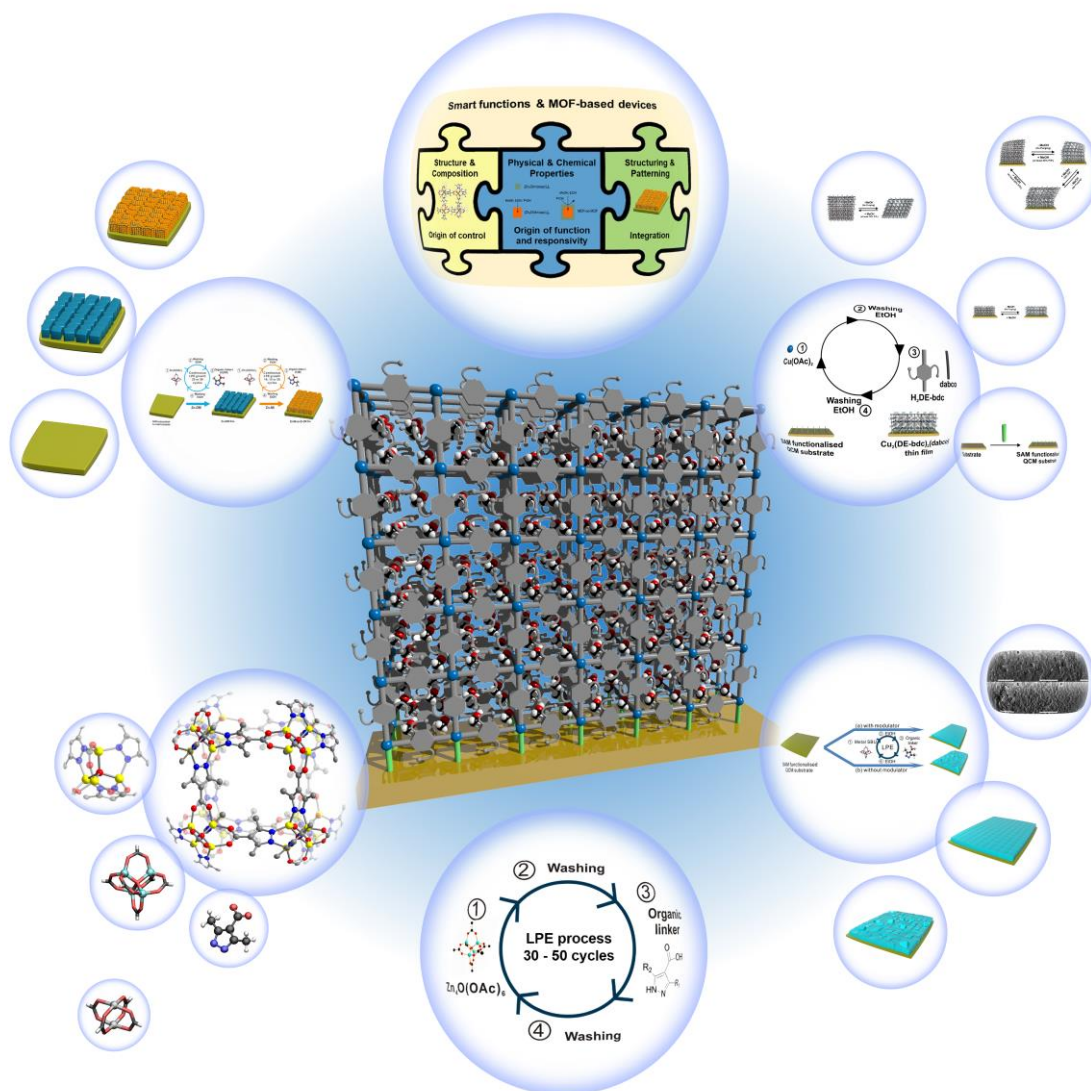
Vorsitzender: Prof. Dr. Dr. h.c. Bernhard Rieger

Prüfende der Dissertation:

1. Prof. Dr. Roland A. Fischer
2. Assoc. Prof. Dr. Shuhei Furukawa
3. Prof. Dr. Christof Wöll

Die Dissertation wurde am 09.11.2017 bei der Technischen Universität München eingereicht und durch die Fakultät für Chemie am 11.12.2017 angenommen.

Structural Design and Modification of Surface Anchored Metal-Organic Frameworks: from Fundamental Study towards Applications



DISSERTATION

Submitted by

Suttipong Wannapaiboon

November 2017

Anhang I

Eidesstattliche Erklärung

Ich erkläre an Eides statt, dass ich die bei der Fakultät für Chemie der TUM zur Promotionsprüfung vorgelegte Arbeit mit dem Titel:

Structural Design and Modification of Surface Anchored Metal-Organic Frameworks: from Fundamental Study towards Applications

in der Fakultät für Chemie, Lehrstuhl für Anorganische und Metallorganische Chemie unter der Anleitung und Betreuung durch Prof. Dr. Roland A. Fischer ohne sonstige Hilfe erstellt und bei der Abfassung nur die gemäß § 6 Ab. 6 und 7 Satz 2 angebotenen Hilfsmittel benutzt habe.

⊗ Ich habe keine Organisation eingeschaltet, die gegen Entgelt Betreuerinnen und Betreuer für die Anfertigung von Dissertationen sucht, oder die mir obliegenden Pflichten hinsichtlich der Prüfungsleistungen für mich ganz oder teilweise erledigt.

⊗ Ich habe die Dissertation in dieser oder ähnlicher Form in keinem anderen Prüfungsverfahren als Prüfungsleistung vorgelegt.

⊗ Ich habe den angestrebten Doktorgrad noch nicht erworben und bin nicht in einem früheren Promotionsverfahren für den angestrebten Doktorgrad endgültig gescheitert.

Die öffentlich zugängliche Promotionsordnung der TUM ist mir bekannt, insbesondere habe ich die Bedeutung von § 28 (Nichtigkeit der Promotion) und § 29 (Entzug des Doktorgrades) zur Kenntnis genommen. Ich bin mir der Konsequenzen einer falschen Eidesstattlichen Erklärung bewusst.

Mit der Aufnahme meiner personenbezogenen Daten in die Alumni-Datei bei der TUM bin ich einverstanden,

Suttipong Wannapaiboon

Garching, 03.11.2017

Acknowledgement

First of all, I would like to express my special thanks and appreciation to my supervisor, **Prof. Dr. Roland A. Fischer**, for his welcome, valuable guidance, support and inspiration throughout the study. His suggestions help me to broaden my knowledge and improve my scientific skills a lot. I acknowledge his trust and various wonderful opportunities that have been given to me.

I acknowledge to the Royal Thai Government Scholarship under the Office of the Civil Service Commission (OCSC), Thailand for the full scholarship through my study. I would like to reveal my acknowledgements to the Chair of Inorganic chemistry II, Ruhr University Bochum and the Chair of Inorganic and Metal-Organic Chemistry, Technical University of Munich for the accessibility to their laboratory facilities for the experiments within my PhD thesis. I acknowledge the Research School Plus, Ruhr University Bochum for the international travel grant from the International Realization Budget (IRB).

I would like to address my special thanks to **Prof. Dr. Dr. h.c. Bernhard Rieger** for accepting to be the chairperson for my disputation. I would like to express my special thanks and appreciation to **Prof. Dr. Roland A. Fischer**, **Assoc. Prof. Dr. Shuhei Furukawa** and **Prof. Dr. Christof Wöll** for accepting to be the examiners for my disputation.

Special thanks to **Prof. Dr. Susumu Kitagawa** and **Assoc. Prof. Dr. Shuhei Furukawa** for their warmly welcome and fruitful discussions during my research stays at Kyoto University.

Sincere thanks to **Dr. Angélique Bétard** for introducing me to MOFs and SURMOFs during the first in-depth practical project in 2011, which has inspired me to continue my work on this area since then. I am sincerely grateful to **Dr. Kenji Sumida**, **Dr. Min Tu** and **Dr. Sareeya Bureekaew** for a lot of valuable discussions and supports during the whole time of my thesis. Thank you for being always available for me when I have some problems concerning to my work. Many thanks to **Dr. Gregor Kieslich** (my PhD mentor), **Dr. Raghavender Medishetty** and **Dr. Andreas Schneemann** for lots of helpful supports. I am also grateful to **Dr. Christian Sternemann** and **Dr. Michael Paulus** for a valuable support at the GIXRD at BL9 DELTA synchrotron.

Moreover, I acknowledge to all of my teachers for their kindness and valuable suggestions.

I am grateful to **all members of the Chair of inorganic chemistry II, Ruhr University Bochum** and **all members of the Chair of Inorganic and Metal-Organic Chemistry, Technical University of Munich** for such a nice working atmosphere, very sincere guidance, kind help and also for everything not only the work that we have done together. I am really appreciated to be one of the group members. You have made my life in Germany to be such a very memorable experience. Particularly, special thanks to **Dr. Hung Banh, Dr. Kerstin Freitag, Christian Schneider, Anna Lisa Semrau, Jana Weßing, Dr. Daniel Peeters, Dr. Inke Hante, Dr. Jiyeon Kim and Zheng Wang** for lots of suggestions, supports and helps. I also thank my students, **Katharina Dilchert, Konstantin Epp and Anna Lisa Semrau** for spending their time performing some experiments together with me. Thanks for such great performances too. Moreover, thanks to **all the MOF members** for such a great working team and very nice time at the MOF2014 and MOF2016 Conferences.

I could not have done anything without encouragements and helps from my mom, my aunt, my families and my best friends. You always stand by my side and show me unconditional love and supports, which always help me to get through any difficult situations. Special thanks to **Dr. Worawat Wattanathana** for all of his support, encouragement and concern. Many thanks to **Dr. Jesada Temaismithi, Apisara Soontron, Attakorn Putwattana and Sorawat Siangpipop** for their supports.

Suttipong Wannapaiboon

For my mom (Pattana Muangjaima)
and my aunt (Phathanee Muangjaima)

“Every great and deep difficulty bears in itself its own solution.
It forces us to change our thinking in order to find it.”

Niels Bohr

Table of content

Acknowledgement	I
List of Abbreviations	IX
Chapter 1 General introduction and motivations	1
1.1 Metal–organic framework (MOFs), an emerging class of porous materials	2
1.2 Smart functions and integration of MOFs into real-world technology	5
1.2.1 Structure and composition: origin of control	6
1.2.2 Physical and chemical properties: origin of function and responsivity	10
1.2.3 Structuring and patterning for integration of MOFs into devices	11
1.3 Challenges and perspective in preparation of MOF-based devices	16
1.4 Motivation and scopes	17
1.5 References	19
Chapter 2 Continuous liquid phase epitaxial growth of moisture-tolerant carboxypyrazolate-based MOF-5 isotype thin films	24
2.1 Introduction and state of the art	25
2.1.1 Rational design of MOF materials towards real-world utilisation	25
2.1.2 Carboxypyrazolate-based MOF-5 isotype MOFs	26
2.1.3 Fabrication of Zn-L MOF thin-films by static stepwise deposition	28
2.2 Continuous liquid phase epitaxial growth of Zn-L thin films	31
2.2.1 Growth of homostructured Zn-L films	32
2.2.2 Adsorption properties of homostructured Zn-L films	44
2.2.3 Fabrication of heterostructured Zn-L films	48
2.2.4 Adsorption properties of heterostructured Zn-L films	51
2.2.5 Moisture Tolerance of Zn-L films	55
2.3 Summary	58
2.4 References	59
Chapter 3 Enhanced properties of MOF thin-films fabricated via a coordination modulation-controlled layer-by-layer process	62
3.1 Introduction and state of the art	63
3.1.1 Integration of MOFs with devices by stepwise LPE method and its limitation	63

3.1.2 Improvement of MOF features at the molecular self-assembly level by coordination modulation method	64
3.2 Preparation of bulk Zn-L powders via coordination modulation	66
3.3 Integration of coordination modulation in the LPE-based fabrication of Zn-L films	74
3.3.1 Coordination modulation in LPE-based growth of Zn-DM films	74
3.3.2 Coordination modulation in LPE-based growth of Zn-ME films	83
3.3.3 Coordination modulation in LPE-based growth of Zn-DE films	86
3.4 Probing the role of coordination modulation in optimizing LPE Fabrication	90
3.4.1 Film nucleation and growth	90
3.4.2 Film crystallinity and preferred orientation	92
3.5 Summary	98
3.6 References	100
Chapter 4 Hierarchical structuring of MOF thin-films on quartz crystal microbalance substrates for selective adsorption applications	104
4.1 Introduction and state of the art	105
4.1.1 Functionalisation of bulk MOFs	105
4.1.2 Stepwise LPE process as a tool for functionalisation of MOF films	107
4.1.3 Growth and Functions of paddlewheel-based heterostructured MOF films	110
4.2 Hierarchical structuring of heterostructured Zn-L thin-films	115
4.2.1 Stepwise LPE growth of Zn-L heterostructured films	117
4.2.2 Characterisations of LPE-fabricated Zn-L heterostructured films	119
4.3 Sorption properties of heterostructured Zn-L thin-films	125
4.3.1 Single-component alcohol adsorption	125
4.3.2 Size-selective adsorption of alcohols	129
4.3.3 Molecular recognition of methanol over water	131
4.4 Summary	132
4.5 Appendix: multi-component adsorptions	133
4.6 References	140

Chapter 5 Systematic control of structural flexibility of MOF crystallites anchored at surfaces	143
5.1 Introduction and state of the art	144
5.1.1 Stimuli-responsive materials and the attempt to combine flexibility in crystalline solid materials	144
5.1.2 Flexible MOFs and how to fine tune structural flexibility	146
5.1.3 Nanoscale MOFs and size-dependent flexibility	149
5.1.4 Transfer of flexibility into MOF-based devices	150
5.2 Structural flexibility of Cu-based layered-pillared bulk MOF powders upon methanol sorption	152
5.3 Structural flexibility of Cu-based layered-pillared MOF crystallites anchored at surfaces	157
5.4 Summary	172
5.5 References	173
Chapter 6 Experimental	178
6.1 Precursor syntheses	179
6.1.1 Synthesis of basic zinc acetate cluster	179
6.1.2 Synthesis of 3-alkyl-5-alkyl-4-carboxypyrazole (H ₂ L) linkers	180
6.1.3 Synthesis of alkoxy-functionalised linkers	183
6.2 Syntheses of bulk MOF powders	185
6.2.1 Syntheses of Zn-L MOFs by ligand replacement approach	185
6.2.2 Syntheses of Zn-L MOFs by integration of coordination modulation with the ligand replacement approach	186
6.2.3 Syntheses of Cu ₂ (fu-bdc) ₂ (dabco) MOFs	186
6.3 Characterisations of MOF powders	187
6.4 Fabrication of MOF thin-films	188
6.4.1 Preparation of functionalised QCM substrates	188
6.4.2 Fabrication of Zn-L thin-films by stepwise LPE process	188
6.4.3 Fabrication of Zn-L thin-films by integration of coordination modulation with stepwise LPE process	189

6.4.4 Fabrication of heterostructured, core-shell Zn-L thin-films by stepwise LPE process	189
6.4.5 Fabrication of alkoxy-functionalised layered-pillared MOF films by stepwise LPE process	190
6.5 Characterisations of MOF thin-films	192
6.6 Organic vapour sorption measurements	192
6.6.1 Single-component sorption isotherms measured by QCM	192
6.6.2 Multiple-component sorption isotherms measured by QCM	193
6.6.3 In-situ synchrotron X-ray diffraction during methanol adsorption	195
6.7 References	197
Chapter 7 Conclusions and outlook	198
Appendix	202

List of Abbreviations

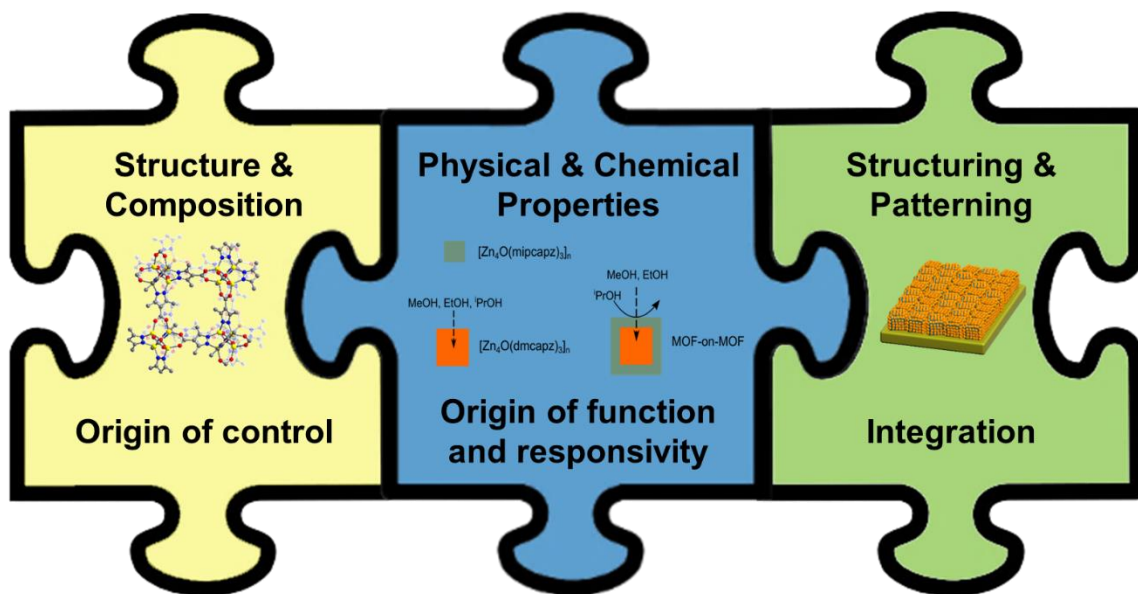
2,6-ndc	2,6-naphthalenedicarboxylate
AES	Auger electron spectroscopy
AFM	atomic force microscopy
ALD	atomic layer deposition
azo-bpdc	3-azobenzene-4,4'-biphenyldicarboxylate
bdc	1,4-benzenedicarboxylate
bdpb	1,4-bis[(3,5-dimethylpyrazol-4-yl)]benzene
bipy	4,4'-bipyridine
bpdc	4,4'-biphenyldicarboxylate
bzac	1-benzoylacetone
BME-bdc	2,5-bis(2-methoxyethoxy)-1,4-benzene dicarboxylate
bpz	3,3',5,5'-tetramethyl-4,4'-bipyrazolate
btc	1,3,5-benzenetricarboxylate
CID	coordination polymer with an interdigitated structure
CSA	controlled secondary building units (SBU) approach
CVD	chemical vapour deposition
dabco	1,4-diazabicyclo[2.2.2]octane
DUT-8(M)	$M_2(2,6\text{-ndc})_2(\text{dabco})$, $M = \text{Cu}^{2+}$, Zn^{2+} , Co^{2+} and Ni^{2+}
F ₄ bdc	tetrafluorobenzene-1,4-dicarboxylate
fu-bdc	2,5-alkoxy-1,4-benzenedicarboxylate
GIXRD	grazing incidence X-ray diffraction
H ₂ BME-bdc	2,5-bis(2-methoxyethoxy)-1,4-benzenedicarboxylic acid
H ₂ DE-bdc	2,5-diethoxy-1,4-benzenedicarboxylic acid
H ₂ DE	3,5-diethyl-4-carboxypyrazole
H ₂ DM	3,5-dimethyl-4-carboxypyrazole
H ₂ DP	3,5-dipropyl-4-carboxypyrazole

H ₂ MB	3-methyl-5-butyl-4-carboxypyrazole
H ₂ ME	3-methyl-5-ethyl-4-carboxypyrazole
H ₂ MI	3-methyl-5-isopropyl-4-carboxypyrazole
H ₂ MP	3-methyl-5-propyl-4-carboxypyrazole,
HKUST-1	Cu ₃ (btc) ₂ or Cu ₃ (1,3,5-benzenetricarboxylate) ₂
ip	isophthalate
IRMOF	isorecticular metal-organic framework
IRRAS	infrared reflection absorption spectroscopy
IUPAC	International Union of Pure and Applied Chemistry
LB	Langmuir-Blodgett method
lp	large-pore phase
LPE	(stepwise) liquid phase epitaxy
MeIm ⁻	2-methyl imidazolate
MFU-1	Co ^{II} ₄ O(bdpb) ₃ or Co ^{II} ₄ O(1,4-bis[(3,5-dimethylpyrazol-4-yl]benzene) ₃
MHDA	16-mercaptohexadecanoic acid
MOFs	metal-organic framework
MOF-5	Zn ₄ O(bdc) ₃ or Zn ₄ O(1,4-benzenedicarboxylate) ₃
MTV-MOFs	multivariate MOFs
N ₃ -bdc	2-azido-benzene-1,4-dicarboxylate
ndc	naphthalene-1,4-dicarboxylate
NH ₂ -bdc	2-amino-benzene-1,4-dicarboxylate
NMR	nuclear magnetic resonance spectroscopy
np	narrow-pore form
OAc ⁻	acetate
PBMT	4-(4-pyridyl)phenylmethylthiol
PCN-250	(Fe ₃ O ₄ H) ₂ (C ₁₆ H ₆ N ₂ O ₈) ₃ (C ₁₆ H ₆ N ₂ O ₈ ⁴⁻ = azobenzenetetracarboxylate)
PCPs	porous coordination polymers
PSM	post-synthetic modification

PXRD	powder X-ray diffraction
py	pyridine
pz	pyrazine
QCM	quartz crystal microbalance
RIU	refractive index unit
SAM	self-assembly monolayer
SBU	secondary building unit
SDAs	structure directing agents
SEM	scanning electron microscopy
SPR	surface plasmon resonance spectroscopy
SURMOFs	surface-mounted metal-organic frameworks
tBITC	<i>tert</i> -butyl isothiocyanate
TCNQ	7,7,8,8-tetracyanoquinodimethane
TGA	thermogravimetric analysis
UHV-FTIR	ultrahigh-vacuum Fourier transformed infrared spectroscopy
UiO-66	Zr ₆ O ₄ (OH) ₄ (1,4-benzenedicarboxylate) ₆
VOCs	volatile organic compounds
XAS	X-ray absorption spectroscopy
XPS	X-ray photoelectron spectroscopy
XRD	X-ray diffraction
ZIF-8	Zn(MeIm) ₂ or Zn(2-methyl imidazolate) ₂
Zn-DE	Zn ₄ O(DE) ₃ or Zn ₄ O(3,5-diethyl-4-carboxypyrazolate) ₃
Zn-DM	Zn ₄ O(DM) ₃ or Zn ₄ O(3,5-dimethyl-4-carboxypyrazolate) ₃
Zn-ME	Zn ₄ O(ME) ₃ or Zn ₄ O(3-methyl-5-ethyl-4-carboxypyrazolate) ₃
Zn-MI	Zn ₄ O(MI) ₃ or Zn ₄ O(3-methyl-5-isopropyl-4-carboxypyrazolate) ₃
Zn-MP	Zn ₄ O(MP) ₃ or Zn ₄ O(3-methyl-5-propyl-4-carboxypyrazolate) ₃
Zn-L	Zn ₄ O(3-alkyl-5-alkyl-4-carboxypyrazolate) ₃

Chapter 1

General introduction and motivations



1.1. Metal–organic framework (MOFs), an emerging class of porous materials

Porous materials, defined as solids containing empty voids, are one of the important classes of materials which attract various attentions ranging from fundamental research study (e.g. material science, chemistry and biology) to large-scale industrial process. Due to a variety of their pore sizes, shapes, functionalities and their structural uniformity, porous materials provide a broader range of applications such as storage and separation, heterogeneous catalysis, energy storage and biomedicine. One of the most well-known examples is activated carbon, which provides the utilities in purification of water or gas, filter materials, capturing of volatile organic compounds (VOCs) and medicine.^{1,2} However, the pore sizes and shapes within the activated carbon are non-uniform and disordered, which are limited for specific uses for size-selective applications.

Another remarkable class of porous materials is zeolites, which are economically attractive and have been commercially established with the largest contribution in industry among various porous materials. Zeolites are rigid, well-defined crystalline inorganic frameworks, of which the network structures are constructed from coordination bonds between silicon or aluminium tetrahedra and the bridging oxygens. Due to their uniform porosity and rigidity, zeolites have been widely used as a size and shape sorting agent (molecular sieving of guest species), heterogeneous catalysis and storage applications.³⁻⁵ However, the elements using for constructing zeolites are limited (Si, O and Al), leading to a difficulty to modify and functionalise the networks for such specific features. In order to design a specific zeolitic topology, the structure directing agents (SDAs) are required as the controlling template.⁵

Even though the abovementioned classes of porous materials are efficient for scale-up manufacturing due to inexpensive raw materials, there are limitations for the target applications which demand such specific functionalities. Hence, the design of new functional porous materials, which combine the characteristics of the rigid, well-defined structures of the crystalline inorganic networks and the flexibility and versatility of the organic-based moieties, is necessary; resulting in the development of a new potential class of porous materials so-called metal–organic framework (MOFs).

MOFs, also referred to as porous coordination polymers (PCPs), are constructed from metal-based nodes and multitopic organic bridging linkers to form infinite networks containing potential voids.⁶ Note that, according to the defined terminology from International Union of Pure and Applied Chemistry (IUPAC) in 2013, it is recommended to apply the following definition for a MOF:⁷

“A metal–organic framework, abbreviated to MOF, is a coordination network with organic ligands containing potential voids.”

Herein, MOF is a subset of a coordination network, which is defined by IUPAC in 2013 as follow:⁷

“A coordination compound extending, through repeating coordination entities, in 1 dimension, but with cross-links between two or more individual chains, loops, or spiro-links, or a coordination compound extending through repeating coordination entities in 2 or 3 dimensions.”

And again, a coordination network is a subset of a coordination polymer defined by IUPAC in 2013 as follow:⁷

“A coordination compound with repeating coordination entities extending in 1, 2, or 3 dimensions.”

The tremendous diversity of the precursor components that can be used to construct MOFs reveals broad perspectives for systematic, bottom-up designs and fine tunings of the framework structures, characteristic features and chemical properties of the pore surfaces.⁸⁻¹² In the early 2017, there are more than 70000 existing MOFs, which have been synthesised by various combinations of approximately 100 different metal-based nodes with approximately 1000 different linkers.¹³ MOFs exhibit such inorganic-organic hybrid characters, combining rigidity and regularity of inorganic materials with flexibility and responsivity of the organic materials (Figure 1.1).¹⁴ Based on the properties of the constructed networks, MOFs can be classified into three categories: the 1st, 2nd and 3rd generations (Figure 1.1).¹⁴ The 1st generation MOF materials remain their porous frameworks only in the presence of guest molecules within the pores. Removal of guest molecules leads to an irreversible collapse of the frameworks. The improvement in

stability and robustness of MOF frameworks can be observed in the 2nd generation of MOFs, of which the original porous structure remains regardless on guest sorption. $Zn_4O(bdc)_3$ (MOF-5, $bdc = 1,4\text{-benzenedicarboxylate}$)⁶ is one of the firstly-reported rigid networks which is classified to be the 2nd generation of MOFs. MOFs of the 3rd generation as-called “soft porous crystals” reveal dynamic framework flexibility which is reversibly responsive to (physically and/or chemically) external stimuli (e.g. light, heat, electric field or the presence of particular guest species) only at the suitable conditions.¹⁴

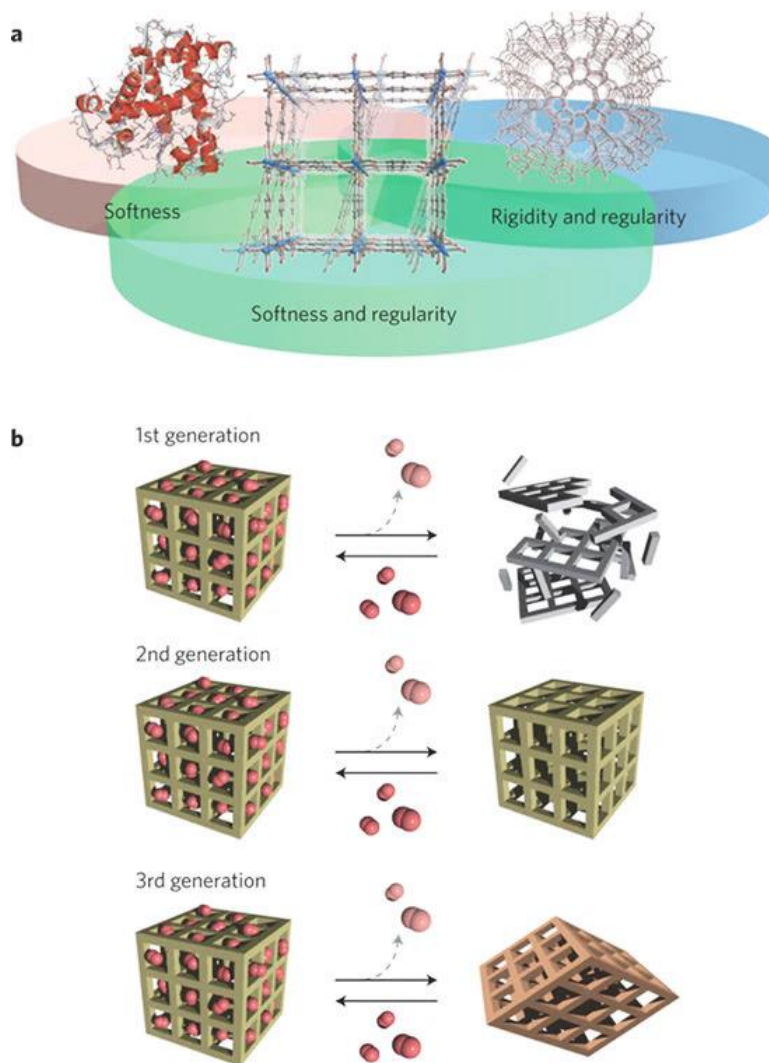


Figure 1.1 (A) MOFs as a class of porous (host) materials possess both softness (flexibility and responsivity) and hardness (rigidity and regularity) as a hybrid character. (B) Classification of MOFs into three categories depending on properties of the networks e.g. upon guest sorption process. Reprint with permission. Copyright © 2009 Macmillan Publishers Limited.¹⁴

1.2 Smart functions and integration of MOFs into real-world technology

To achieve target performances and desired functions of MOFs especially aiming for integration into real-world technology, combined controls and synergistic designs in various perspectives *i.e.* a) structure and composition, b) physical and chemical properties, and c) structuring and patterning are of concern (Figure 1.2). Since the beginning of MOF discovery, potential applications in gas storage and capture,¹⁵⁻²⁰ molecular separation²¹⁻²⁷ and heterogenous catalysis^{28,29} have indicated a success in systematic design of smart functions at the framework components as well as the pore cavities. Moreover, the potential to incorporate MOFs into functional devices has resulted in their emerging applications, including electronics,³⁰⁻³³ sensing,³⁴⁻³⁶ optics,³⁷⁻³⁹ proton conduction,⁴⁰ photosynthesis and photocatalysis,⁴¹ and biomedicines.^{42,43} According to potential reviews and original research articles available in the literatures, we herein summarise the fruitful achievements and knowledge to design smart functions of MOF-based devices in three categories as follows.

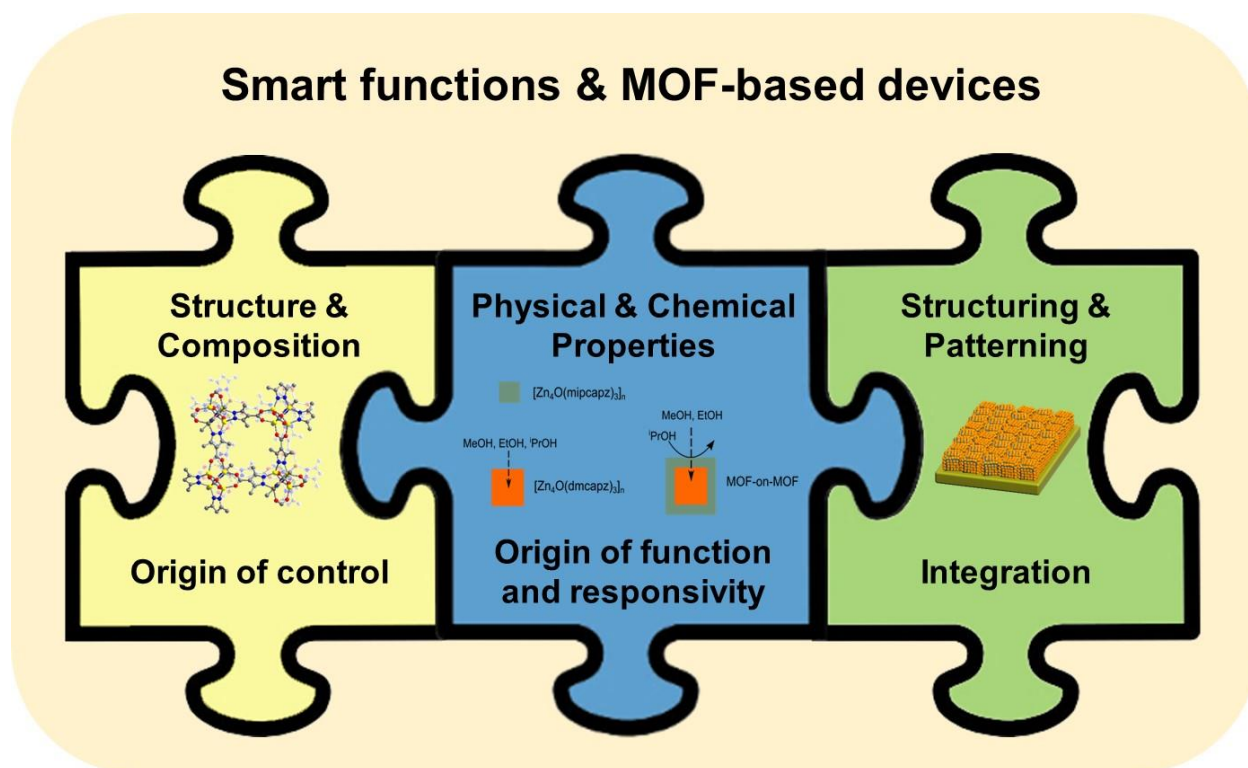


Figure 1.2 Mission concept to achieve smart functions in MOF-based devices

1.2.1 Structure and composition: origin of control

Due to the fact that MOFs are flexible for structural modification, in which a variety of precursor components can be used for MOF assembly. In addition to straightforward bottom-up solvothermal synthesis between metal ions and organic linkers, the alternative concept for MOF syntheses so-called “reticular synthesis” has been emerged, which employs a use of pre-designed, MOF-structural-related components. According to reticular synthesis, choosing of the right building blocks (also called secondary building unit (SBU) as shown the examples in Figure 1.3) based on the knowledge in coordination chemistry together with optimising of the right conditions leads to the self-assembly of these units and then forms the MOF crystals with the desired topology and porosity.¹¹ This method is able to control the pore structure, size and shape without changing their underlying topology, which offers a targeted function for selective inclusion of such specific guest molecules into MOF pores (selective storage and/or capture). The expansion of MOFs with the same topology and the alteration of the pore functionality without a change of pore capacity so-called “isoreticular MOFs” have been achieved. Analysis of the network topologies by deconstructing the crystal structures is noteworthy for reaching the controlled level in MOF syntheses.⁴⁴

Properties and functions of MOFs depend not only on the characteristic features of pores but also on their chemical functionalities.¹⁵ In order to achieve the target performances of MOFs, optimisation of the force fields and coordination spaces as well as the reactive centres incorporated within the framework is required. The attempt to functionalise MOFs for supplying in such specific applications has become mature. Pre-functionalisation of organic linkers (structures, conformations, and incorporating of reactive pendent groups) prior to the MOF syntheses has been employed in order to modify the size, shape and chemical functionality of the MOF pore surfaces. However, the direct introduction of organic linkers consisting of more sophisticated chemical functionalities under solvothermal conditions is still limited, and certain substituents at the linkers may prevent the formation of the desired MOFs as a result of interference with the desired coordination chemistry of the metal-based nodes. Post-synthetic modification (PSM) circumvents this problem by interchanging the reactive organic functional groups

at the linkers into the desired functional groups (normally with more sophisticated one) after the construction of the parent MOF.⁴⁵⁻⁴⁷ Specifically, the organic linkers containing reactive functional groups (e.g. amino groups) are firstly used to construct the parent MOF, which is isoreticular to the target MOF. Then, the specific organic reaction is performed in order to exchange the reactive functional groups into the desired ones, resulting in the conversion of pore-surface properties.

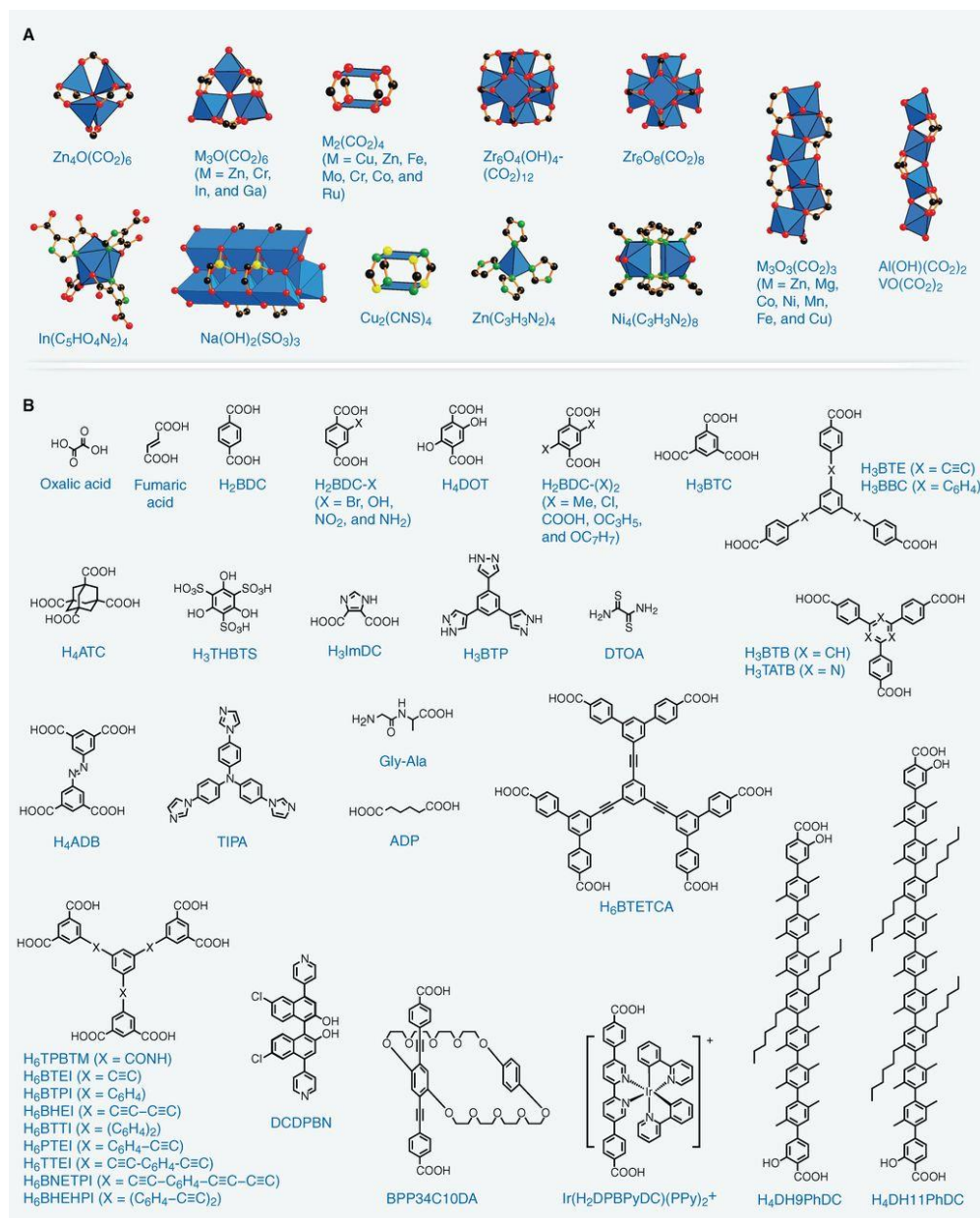


Figure 1.3 (A) Selected inorganic secondary building units and (B) organic linkers of particular relevance for isoreticular syntheses of MOFs. Reprint with permission. Copyright © 2013 American Association for the Advancement of Science.¹¹

Extending from a single function to achieve such integrated smart functions in MOFs, the concept of solid-solution MOFs or multivariate MOFs (MTV-MOFs) is emerged, in which more than one types of isostructural metal nodes and/or organic linkers are combined as a synergistic unit within a single-phase MOF (Figure 1.4).^{11,48} In this way, (non-linear) combined functional-controlled features can be achieved. It is expected to actuate the novel realms of material science and chemistry. Highlighting the advantages, the material consisting different compartments linked together could be able to carry out parallel operations as a synergistic functional unit, which could be better than the operation of each compartments separately.

In addition, the mesoscopic-controlled arrangement of individual MOFs with unique features to the desired spatial positions within the hybrid MOF materials (so-called heterostructure) can also provide further opportunities to manipulate the characteristics of the system, particularly when a single MOF does not offer all required functions for a specific application.⁴⁹⁻⁵¹ The integrated functions in the multifunctional MOF materials are displayed by both the choice of microscopic-scale derivatives (linker functionalization) and mesoscopic-scale arrangement of the different sub-unit crystals (as depicted in Figure 1.5).⁵⁰ For example, the smart function for using as the extractor is obtained by combining two analogous MOFs consisting of different-size organic linkers in the core-shell architecture, which leads to the size selective separation at the shell crystal (smaller pore window) and the high-capacity storage container at the core crystal (larger pore opening and volume).⁵⁰ Moreover, the modification of the pore structures and functionalities can be achieved by performing selective PSM at only specific component.⁵¹

Heterogeneity, structural disorders, and defects are known as key attributes which strongly affect properties of solid-state materials. Wise control over the defect creation, known as “defect engineering”, in MOF crystals can manipulate the crystal quality and features. Within the past decade, research in control and generation of defects in MOFs e.g. ligand fragments and metal-node vacancies with a defined portion within the MOF matrix has attracted significant attention, opening a way to initiate and/or enhance the smart functions of MOFs especially for the applications in catalysis, storage and separation and extending towards other physical properties such as luminescence.⁵²

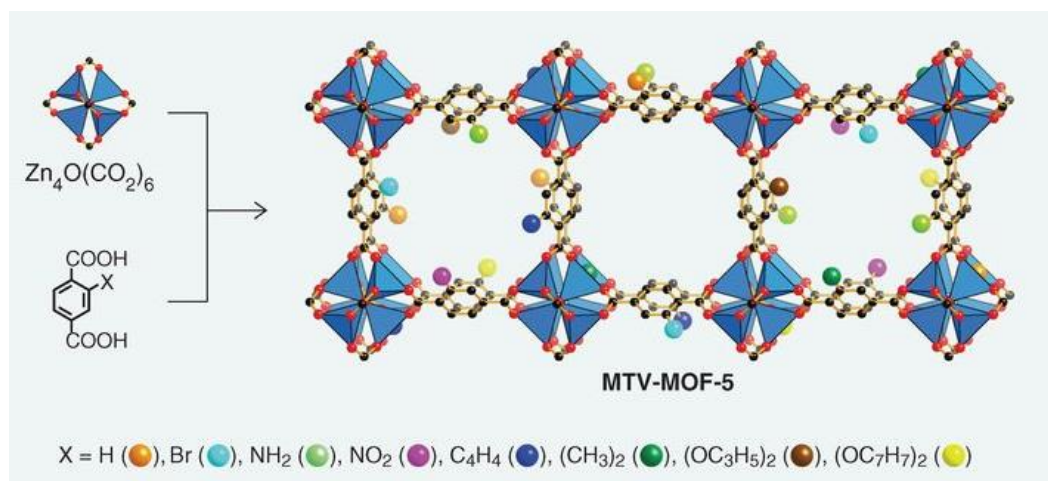


Figure 1.4 An example of multivariate MOFs (MTV-MOF-5) indicating an incorporation of several organic linkers consisting of different functionalised pendent sidechains in a single-phase MOF in a solid solution fashion. Adapted with permission. Copyright © 2013 American Association for the Advancement of Science.¹¹

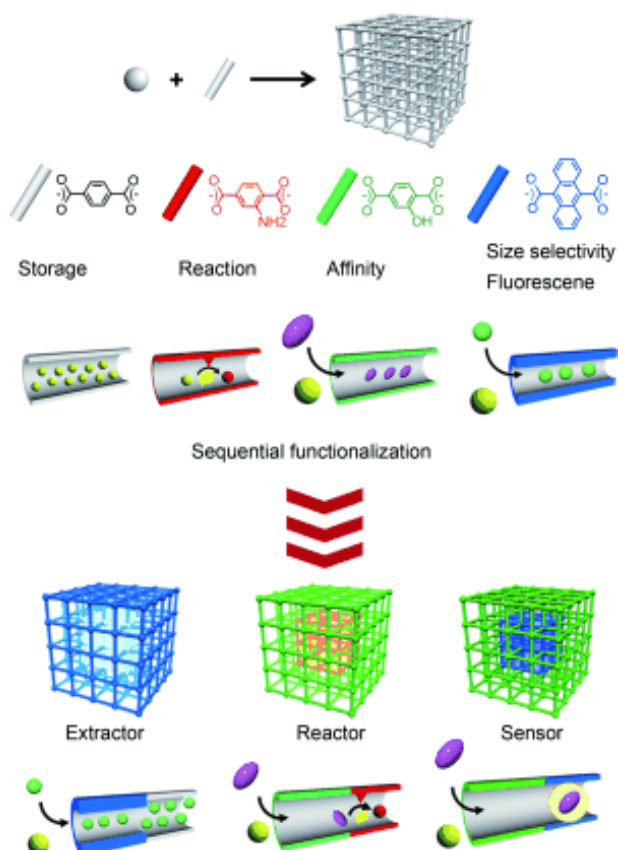


Figure 1.5 Schematic illustrations of the sequential functionalization systems of the epitaxial core-shell hybrid MOFs. The desired features are achieved by spatial-controlled arrangement of individual MOF components. Reprint with permission. Copyright © 2011 WILEY-VCH Verlag GmbH & Co. KGaA.⁵⁰

1.2.2 Physical and chemical properties: origin of function and responsivity

Physical and chemical properties of MOFs are the origin of functions and responsivities which provide promising possibilities for applying MOFs in various applications. Properties of MOFs are directly influenced and controlled by their structures, functionalities and compositions.^{9,11} Moreover, the process for integration of MOFs into the nanotechnological devices also plays a role in controlling and transferring of MOF properties into real-world utilities.^{53,54} Considering of various interesting properties emerging in MOF research, they can be classified into two main categories according to the origin of the properties; namely the intrinsic (direct) and the extrinsic (indirect) properties of MOFs.

The intrinsic properties of MOFs are achieved by such discerning selection of the reactive MOF components, which generally exhibit the desired functions even as the discrete moieties themselves, and/or generating of reactive sites by selected chemical reactions and specific synthetic procedures (referring back to section 1.2.1). For example, incorporation of the metal nodes providing reactive open metal sites and/or of the organic linkers with reactive pendent functionalities into the framework can enhance the catalytic properties of the materials.^{28,29} Moreover, chirality, luminescent and optical properties of MOFs can be achieved by incorporation of the chiral organic linkers²⁸ and the fluorophore moieties³⁷⁻³⁹ into the framework, respectively. Alternatingly, the assembly of MOF components which do not directly display the desired properties as a discrete compound in the defined positions within the MOF structures, can also create such desired functions. For example, incorporation of alkoxy-functionalised linkers into layered-pillared MOFs initiates the framework flexibility (stimuli-responsive properties) by means of the weak interactions between the functionalised sidechains and the sidechains with the guest molecules and the metal nodes.^{55,56} Control and manipulation of the weak forces within the MOF structures provide possibilities to design smart materials with selective adsorption and release properties upon external stimuli as well as a promising candidate for development of selective, gate-lock catalysts.

The extrinsic (indirect) properties of MOFs are achieved by using MOFs as hosts for insertion of reactive species (such as metal nanoparticles, fluorophores, catalytic

active compounds) into their pores, hence, generating the desired functions of the materials. One of the interesting examples is the incorporation of 7,7,8,8-tetracyanoquinodimethane (TCNQ) into the MOF and MOF thin-film of a type $\text{Cu}_3(\text{btc})_2$ (HKUST-1, $\text{btc} = 1,3,5\text{-benzenetricarboxylate}$) to enhance the electronic conductivity of the MOF materials.³² Moreover, combining of MOFs with other materials in the composite or solid-solution forms (such as polymer-MOF composites, MOF-graphene oxide composites) can also provide such desired properties. In all, the control of physical and chemical properties of MOFs leads to a goal for such smart functions, which are suitable for further uses in MOF-based nanotechnology and devices.

1.2.3 Structuring and patterning for integration of MOFs into devices

One of primary challenges facing the integration of MOFs with real-world technologies is the development of enhanced and optimized fabrication processes, that allow MOFs to be compatibly structuralised into mesoscopic and macroscopic forms on the specific device configurations, while maintaining or even improving the performance profile of the materials in the bulk stage. The key steps for integration of MOFs into nanotechnological and microelectronic devices involve in the ability to engineer the MOF characteristic features (desired functions, controlled geometry, defined size, shape and crystallographic orientation) and the ability to spatially control the crystallisation process leading to the integration into a useful platform.^{53,54}

During the past decade, various methods have been emerged for structuring and patterning of MOF on a variety of substrate types which have been continuously reviewed in the literatures.^{30-31,53-54,57-63} Note for terminology, structuring is a construction of more complex MOF architectures by creating higher-order mesoscopic superstructures composed of nanocrystals as building blocks, resulting in 0-dimensional (0D) (microspheres and hollow capsules), 1D (nanorods and nanofibers), 2D (thin-films and membranes) and 3D architectures.⁵³ Patterning is extended from the 1D spatial-controlled structuring (also known as fabrication) to the 2D (planes) or 3D (spaces) control.⁵⁴ The promising fabrication methods, especially used for fabrication of MOF thin-films, are briefly summarised hereafter and categorised by means of the synthetic strategies and the roles of substrate and the reaction system according to the literatures.^{53,54,63}

(1) Solution-based fabrication and using of macrostructural (hard) template

In this approach, pre-shaped solid-state macrostructure, of which the surface is generally functionalised prior to the reaction by self-assembly monolayer or surface activation and modification, is used as a template. Immersing the functionalised substrate into the mother solution (a mixture metal-based and organic linker reactants) and performing the solvothermal reaction, so-called “direct synthesis”, is the simplest strategy to obtain MOF crystallites attached on the substrate. However, this method is rather limited for spatial-controlled structuring since the crystallisation process can occur both in the solution and at the surface of the template, leading to a lack of homogeneity of the obtained MOF thin-films. For MOFs, of which the crystallisation process is relatively fast, the repeated immersion of the template into the freshly-prepared mother solution could be an effective procedure to obtain MOF thin-films. In addition, modification of the substrate surface by coating with the pre-formed MOF nanocrystals (acting as nucleation seed), so-called “the secondary growth”, can enhance nucleation and growth process of the MOF thin-films. However, the stability of the anchored MOF films is still a main drawback due to a lack of strong chemical binding of the MOF crystallites to the substrate.

The strategy of this approach has been advanced by employing an alternate immersion of the substrate into the solutions containing individual MOF precursor components, coined the term as “stepwise liquid phase epitaxy, LPE” or “layer-by-layer approach”. After optimisation of the synthetic conditions, this method results in the formation of homogeneous, highly-oriented MOF thin-films with controllable thickness via the ability to explicitly program the step and the number of fabrication cycles. Building up upon this synthetic concept, design and building various automatic set-ups for more efficiency in the large-scale processing have been developed (see Figure 1.6). Although the utility of this technique has been fruitfully demonstrated, a well-controlled film growth is still limited to the paddlewheel-based MOF systems.⁶³

(2) Solution-based fabrication and using of molecular (soft) template

Instead of using the hard template as in the previous section, this approach uses the in-situ assembly of surfactants to form molecular superstructures and act as a template in the similar manner for nucleation of MOF on their surface.

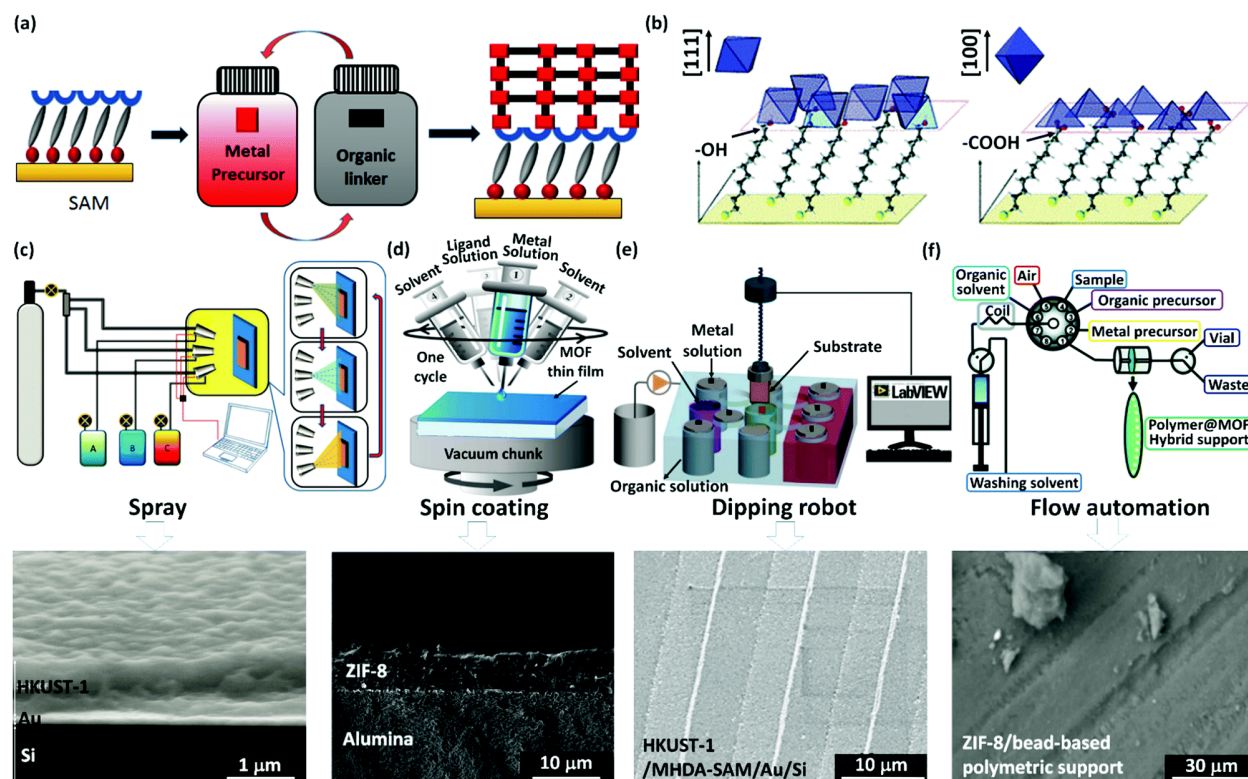


Figure 1.6 Schematic representations of the stepwise LPE method for fabrication of MOF thin-films, highlighting the well-controlled thin-film growth and the control of crystallite orientation by surface functionalisation with SAM; and of the corresponding designs of various automatic set-ups for more efficiency in the large-scale processing. Reprint with permission. Copyright © The Royal Society of Chemistry 2017.⁶³

(3) Liquid-solid interfacial reaction and sacrificial template

In this method, the solid template is directly used as a metal source through its partial or total dissolution by the contact with the organic linker solution under solvothermal condition. Here, the metal source is in the solid phase (metal oxides and metal hydroxides) while the organic linker is dissolved in the liquid phase. The MOF formation occurs at the liquid-solid interface, at which the concentrations of both precursor components are higher than the other place. Studying in details of the mechanism of MOF formation (optimised conditions, growth direction, and lattice matching between the sacrificial substrate and the generated MOF), it is possible to achieve highly-oriented polycrystalline MOF film on the centimetre scale in both the perpendicular and parallel directions with respect to the substrate surface.⁶⁴

(4) Liquid-liquid interfacial reaction

This method relies on the immiscibility of a liquid-liquid biphasic mixture, in which each phase contains either metal precursor (e.g. the metal salt dissolved in water-based solution) or the organic linker (dissolved in organic-solvent-based solution). Again, the formation of the desired MOF occurs at the immiscible liquid-liquid interface, of which the defined shape and superstructure can be controlled. Note that, free-standing MOF membranes can be prepared by employing this procedure.

(5) Air-liquid interfacial reaction

There are two main strategic methods leading to the formation of MOF superstructures at the air-liquid interface. Firstly, the method so-called “reaction confinement” relies on the evaporation-induced MOF crystallisation. Here the solvent must dissolve and stabilise the MOF precursors in the solution at the initial concentration and then impose the crystallisation process of MOF when concentrating the solution by the evaporation of the solvent (induced by the contact with air). Secondly, the method so-called “Langmuir-Blodgett (LB)” depends on the pre-orientation of one of the MOF building block at the surface of the solvent (liquid) phase (induced by the contact with air). Then, the desired MOF is formed by the reaction of the pre-oriented building block with the other MOF building block dissolved in the underlying phase of the pre-oriented one, leading to the formation of the 2D-sheet MOF at the surface (which is in contact with air). Repeating the transfer of this 2D sheets onto the solid substrate several times yields stacked MOF nanofilms anchored on the substrate.

(6) Vacuum-based fabrication

The vacuum-based fabrication methods have recently been reported for structuring and patterning of MOFs on the substrates. Taking the concept of sacrificial template, chemical vapour deposition (CVD) has been employed for the structuring of MOF thin-films. Firstly, the metal oxides (known as the sacrificial template) is deposited as films on the substrate surface. Then, the conversion of this oxide into MOFs is performed by a reaction with the organic linker in the vapour phase using CVD technique (instead of the liquid phase as mentioned above).⁶⁵ Thanks to the advantages of CVD

method, the MOF structuring and patterning on such a high-aspect-ratio substrate can be achieved. Moreover, the pre-deposited oxide layers can also be prepared by the atomic layer deposition (ALD). Secondly, ALD technique has been directly used for fabrication of MOF thin-films by relying on sequential, self-limiting gas-in-surface reactions. Here, sequential dosing of volatile metal precursor and volatile organic linker on the surface leads to the self-saturating growth of MOF thin-film with well-defined thickness.⁶⁶

(7) Top-down approach

Instead of bottom-up assembly MOF from the precursor components, this approach uses the pre-formed MOF crystals as the building blocks for arranging on the substrate by using various coating procedures such as drop casting, dip coating, spin coating and electrospray deposition. Moreover, photolithography and imprinting methods have been also applied for patterning of the pre-fabricated MOF thin-film into a desired pattern on the substrate.

(8) Electrochemical reaction

There are three different approaches have been reported so far for the use of electrochemical reactions for fabrication of MOF thin-films, namely anodic, cathodic and electrophoretic deposition. In the anodic deposition process, the metallic electrode is used as the targeted substrate by connected at the anode within the electrolytic cell and the organic linker is dissolved in the electrolyte. When applying the voltage, the anodic metallic electrode acts as a sacrificial template for generating the metal ions and further react with the organic linker to form a desired MOF anchoring at the anodic electrode. In the cathodic deposition process, the electrodes are used as a source of electrons without participating as the MOF precursors. Both of the MOF precursors are dissolved in the electrolyte. The key step is to generate a high-concentrated alkali region near the cathode in order to deprotonate the organic linker there. When applying the voltage, the deprotonated organic linkers are reacted with the metal ions accumulating in the solution close to the cathode and consequently form the MOF films anchoring at the cathode. In electrophoretic deposition, the applying voltage creates an electric field between the two electrodes and drives the surface-charged MOF particles dispersed within the electrolyte to accumulate on the opposite-charged electrode and form a MOF film.

1.3 Challenges and perspective in preparation of MOF-based devices

The rapidly increasing attention on integration of MOFs into nanotechnological devices has made this research field more attractive for further development in various aspects in order to facilitate the commercialisation of highly-efficient MOF-based devices. Regarding to the fabrication, the ability to entirely control MOF crystallisation process at the surface of the target devices in the aspects of controlled location and enhanced quality is of concern. Fabrication processes that provide good thin-film qualities (homogeneity, uniformity, high crystallinity, preferred crystallite orientation, and high-resolution patterns) are interesting to focus on further improvements in the level of detailed techniques. To date, the LPE and ALD method have been illustrated to be the most suitable procedure with respect to the thin-film quality. However, the versatility of these techniques is still limited to small amounts of desired MOF systems. Advanced enhancement of the prototypical methodology and understanding of the formation mechanism would open the possibilities to apply the method for various MOFs by paying more attentions to control and adjust the critical parameters influencing the MOF formation process.

Not only the fabrication process, focussing on advanced characterisation techniques is also a crucial step to advance the MOF-based technology. The techniques should be suitable for surface-sensitive resolution and localised analysis in order to obtain the detailed characteristics of the thin-film qualities. Ultrahigh-vacuum infrared spectroscopy (UHV-FTIR), Raman spectroscopy, X-ray photoelectron spectroscopy (XPS), Auger electron spectroscopy (AES), X-ray absorption spectroscopy (XAS), grazing incidence X-ray diffraction (GIXRD) with the confocal micro- or even nano- X-ray beam could be appropriate characterisation techniques concerning these purposes. Optimisation of the detailed analytical steps is still required for achieving specific, useful information, which further could correlate for controlling the performance of MOF thin-film devices.

In addition, investigations about the compatibility, robustness, interfacial stability and aging of the fabricated MOF-based devices are also the challenges that need to be clarified. Not only the optimisation of the MOF structures which can be stable under the operation conditions of the devices, maintaining of the integrity of MOFs at the device

surface is also the main concern in order to avoid the degradation of the device performances, the contamination of the decomposed MOF components and the loss of functionalities. Aging and degradation from the standard operating performance of the devices need to be tested. Moreover, investigation on the mechanical stability, biocompatibility and environmental compatibility for the MOF-based devices is necessary to be examined prior to the beginning of commercialisation.

The further concern is related to the enhancement of the MOF properties which could be helpful for transferring of the signals with the commercially available nanotechnological devices, namely electrical conductivity and other charge carrier mobility, while still maintaining the desired functions of MOFs as the active unit within the devices.

1.4 Motivation and scopes

As having been discussed previously, primary challenges facing in real-world technologies are the discovery of novel materials with specific functions and the development of enhanced and optimized fabrication processes which are effective for integration of these smart materials into the nanotechnological devices. Stepwise LPE process is among several methods that has been comprehensively studied and developed for the fabrication of well-controlled MOF thin-films. However, its main utilisations are circled around the paddlewheel-based MOFs, which limits the broad applicability of this technique. Moreover, little attention has been directed towards understanding the underlying mechanisms allowing for fine-tuning of the crystal growth processes and the structuring strategies in order to achieve even greater control over the quality of the resulting films.

Herein, we aim for the fundamental understanding the MOF thin-film fabrication and further exploiting this knowledge to design and modify the properties of MOF thin-films from both perspectives at the molecular assembly level and the mesoscopic architecture to serve the use in practical applications. To achieve these goals, this PhD thesis project is structured around four research questions/objectives (**Q1 to Q4**);

Q1: Understanding the growth mechanism of MOF thin-films fabricated by stepwise LPE method. Extension of the LPE fabrication process towards the other MOF systems beyond the paddlewheel-based MOFs

- How the different types of MOFs form as thin-films on the substrate by employing the stepwise LPE method?
- What we can learn from the in-situ monitoring of QCM frequency change about the growth mechanism of MOF thin-films?
- Are there any possibilities to apply the LPE process to the other MOF types?
- What is the important factors to limit the well-defined growth of MOF thin-films by LPE process to only the paddlewheel-based MOFs?

Q2: Improving the quality of MOF films by modifying the fabrication procedure.

- Since the LPE growth of some MOF systems do not provide the well-defined and highly-oriented films, how can we improve the quality of these LPE-fabricated MOF films?
- What can we learn by integrating the other methodology such as coordination modulation technique, which is known to be an effective method to control the growth of MOF crystals, into the fabrication of MOF thin films by LPE process?
- Is it possible to develop the fabrication process which can provide the high-quality MOF films?

Q3: Structuring and design MOF films towards selective adsorption properties.

- Based on the growth mechanism of the study MOF systems, how can we control the structuring and crystallite orientation as well as fine-tune the properties of the fabricated films?
- If the properties of one MOF is not suitable for the selective adsorption, can we use the LPE process to combine two MOFs into the films, so-called heterostructured MOF-on-MOF films, in order to create the integrated properties such as selective adsorption?
- How we can prove the adsorption selectivity of the heterostructured MOF films?

Q4: Extension the library of LPE-fabricated films to MOFs exhibiting structural flexibility.

- Up to date, most of the MOFs that have been fabricated as thin-films by LPE process exhibit the rigidity of the frameworks. Is it possible to extend the library of MOF systems which can be fabricated by LPE process to the structural-flexible MOFs?
- Once these flexible MOFs can be fabricated as thin-films on the substrate, how the structural flexibility are affected by the anchoring onto the substrate surface?
- Are there any possibilities to control and manipulate the structural flexibility of the MOF films?

1.5 References

1. K. Kaneko, C. Ishii, M. Ruike and H. Kuwabara, *Carbon*, 1992, **30**, 1075–1088.
2. M. C. Ncibi, B. Mahjoub, M. Seffen and S. Gaspard, *Recent Pat. Chem. Eng.*, 2008, **1**, 126–140.
3. M. E. Davis, *Nature*, 2002, **417**, 813–821.
4. P. A. Wright, *Microporous Framework Solids*, Royal Society of Chemistry, Cambridge, 2008.
5. B. Smit and T. L. M. Maesen, *Chem. Rev.*, 2008, **108**, 4125–4184.
6. H. Li, M. Eddaoudi and O. M. Yaghi, *Nature*, 1999, **402**, 276–279.
7. S. R. Batten, N. R. Champness, X.-M. Chen, J. Garcia-Martinez, S. Kitagawa, L. Öhrström, M. O’Keeffe, M. Paik Suh and J. Reedijk, *Pure Appl. Chem.*, 2013, **85**, 1715–1724.
8. O. M. Yaghi, M. O’Keeffe, N. W. Ockwig, H. K. Chae, M. Eddaoudi and J. Kim, *Nature*, 2004, **423**, 705–714.
9. S. Kitagawa, R. Kitaura and S.-i. Noro, *Angew. Chem. Int. Ed.*, 2004, **43**, 2334–2375.
10. G. Férey, *Chem. Soc. Rev.*, 2008, **37**, 191–214.

11. H. Furukawa, K. E. Cordova, M. O’Keeffe and O. M. Yaghi, *Science*, 2013, **341**, 1230444.
12. O. M. Yaghi, *J. Am. Chem. Soc.*, 2016, **138**, 15507–15509.
13. P. Z. Moghadam, A. Li, S. B. Wiggin, A. Tao, A. G. P. Maloney, P. A. Wood, S. C. Ward and F.-D. Jimenez, *Chem. Mater.*, 2017, **29**, 2618–2625.
14. S. Horike, S. Shimomura and S. Kitagawa, *Nature Chem.*, 2009, **1**, 695–704.
15. M. Eddaoudi, J. Kim, N. Rosi, D. Vodak, J. Wachter, M. O’Keeffe and O. M. Yaghi, *Science*, 2002, **295**, 469–472.
16. K. Sumida, D. L. Rogow, J. A. Mason, T. M. McDonald, E. D. Bloch, Z. R. Herm, T.-H. Bae and J. R. Long, *Chem. Rev.*, 2012, **112**, 724–781.
17. Y. He, W. Zhou, G. Qian and B. Chen, *Chem. Soc. Rev.*, 2014, **43**, 5657–5678.
18. T. M. McDonald, J. A. Mason, X. Kong, E. D. Bloch, D. Gygi, A. Dani, V. Crocellà, F. Giordanino, S. O. Odoh, W. S. Drisdell, B. Vlaisavljevich, A. L. Dzubak, R. Poloni, S. K. Schnell, N. Planas, K. Lee, T. Pascal, L. F. Wan, D. Prendergast, J. B. Neaton, B. Smit, J. B. Kortright, L. Gagliardi, S. Bordiga, J. A. Reimer and J. R. Long, *Nature*, 2015, **519**, 303–308.
19. E. Barea, C. Montoro and J. A. R. Navarro, *Chem. Soc. Rev.*, 2014, **43**, 5419–5430.
20. C. A. Trickett, A. Helal, B. A. Al-Maythaly, Z. H. Yamani, K. E. Cordova and O. M. Yaghi, *Nature Rev. Mater.*, 2017, **2**, 17045.
21. J.-R. Li, J. Sculley and H.-C. Zhou, *Chem. Rev.*, 2012, **112**, 869–932.
22. B. van de Voorde, B. Bueken, J. Denayer and D. de Vos, *Chem. Soc. Rev.*, 2014, **43**, 5766–5788.
23. A. J. Brown, N. A. Brunelli, K. Eum, F. Rashidi, J. R. Johnson, W. J. Koros, C. W. Jones and S. Nair, *Science*, 2014, **345**, 72–75.
24. Y. Peng, Y. S. Li, Y. J. Ban, H. Jin, W. M. Jiao, X. L. Liu and W. S. Yang, *Science*, 2014, **346**, 1356–1359.
25. T. Rodenas, I. Luz, G. Prieto, B. Seoane, H. Miro, A. Corma, F. Kapteijn, F. X. L. I. Xamena and J. Gascon, *Nat. Mater.*, 2015, **14**, 48–55.
26. J. E. Bachman, Z. P. Smith, T. Li, T. Xu and J. R. Long, *Nature Mater.*, 2016, **15**, 845–849.

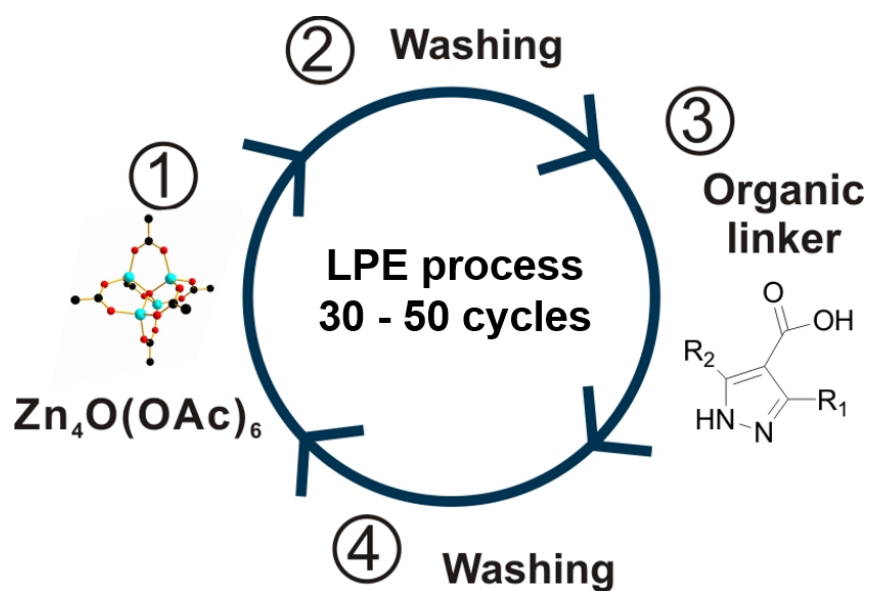
27. Z. Wang, A. Knebel, S. Grosjean, D. Wagner, S. Bräse, C. Wöll, J. Caro and L. Heinke, *Nat. Commun.*, 2016, **7**, 13872–13879.
28. M. Yoon, R. Srirambalaji and K. Kim, *Chem. Rev.*, 2012, **112**, 1196–1231.
29. A. Dhakshinamoorthy and H. Garcia, *Chem. Soc. Rev.*, 2014, **43**, 5750–5765.
30. V. Stavila, A. A. Talin and M. D. Allendorf, *Chem. Soc. Rev.*, 2014, **43**, 5994–6010.
31. I. Strassen, N. Burtch, A. Talin, P. Falcaro, M. Allendorf and R. Ameloot, *Chem. Soc. Rev.*, 2017, **46**, 3185–3241.
32. A. A. Talin, A. Centrone, A. C. Ford, M. E. Foster, V. Stavila, P. Haney, R. A. Kinney, V. Szalai, F. El Gabaly, H. P. Yoon, F. Léonard and M. D. Allendorf, *Science*, 2014, **343**, 66–69.
33. D. Sheberla, J. C. Bachman, J. S. Elias, C.-J. Sun, Y. Shao-Horn and M. Dincă, *Nature Mater.*, 2017, **16**, 220–224.
34. L. E. Kreno, K. Leong, O. K. Farha, M. Allendorf, R. P. van Duyne and J. T. Hupp, *Chem. Rev.*, 2012, **112**, 1105–1125.
35. W. P. Lustig, S. Mukherjee, N. D. Rudd, A. V. Desai, J. Li and S. K. Ghosh, *Chem. Soc. Rev.*, 2017, **46**, 3242–3285.
36. N. Yanai, K. Kitayama, Y. Hijikata, H. Sato, R. Matsuda, Y. Kubota, M. Takata, M. Mizuno, T. Uemura and S. Kitagawa, *Nature Mater.*, 2011, **10**, 787–793.
37. Y. Cui, Y. Yue, G. Qian and B. Chen, *Chem. Rev.*, 2012, **112**, 1126–1162.
38. R. Medishetty, J. K. Zareba, D. Mayer, M. Samoc' and R. A. Fischer, *Chem. Soc. Rev.*, 2017, **46**, 4976–5004.
39. R. Medishetty, V. Nalla, L. Nemeč, S. Henke, D. Mayer, H. Sun, K. Reuter and R. A. Fischer, *Adv. Mater.*, 2017, **29**, 1605637.
40. P. Ramaswamy, N. E. Wong and G. K. H. Shimizu, *Chem. Soc. Rev.*, 2014, **43**, 5913–5932.
41. T. Zhang and W. B. Lin, *Chem. Soc. Rev.*, 2014, **43**, 5982–5993.
42. P. Horcajada, R. Gref, T. Baati, P. K. Allan, G. Maurin, P. Couvreur, G. Férey, R. E. Morris and C. Serre, *Chem. Rev.*, 2012, **112**, 1232–1268.
43. P. Horcajada, T. Chalati, C. Serre, B. Gillet, C. Sebrie, T. Baati, J. F. Eubank, D. Heurtaux, P. Clayette, C. Kreuz, J.-S. Chang, Y. K. Hwang, V. Marsaud, P.-N.

- Bories, L. Cynober, S. Gil, G. Férey, P. Couvreur and R. Gref, *Nature Mater.*, 2010, **9**, 172–178.
44. M. O’Keeffe and O. M. Yaghi, *Chem. Rev.*, 2012, **112**, 675–702.
45. Z. Wang and S. M. Cohen, *J. Am. Chem. Soc.*, 2007, **129**, 12368–12369.
46. Z. Wang and S. M. Cohen, *Angew. Chem. Int. Ed.*, 2008, **47**, 4699–4702.
47. S. M. Cohen, *Chem. Rev.* 2012, **112**, 970–1000.
48. H. Deng, C. J. Doonan, H. Furukawa, R. B. Ferreira, J. Towne, C. B. Knobler, B. Wang and O. M. Yaghi, *Science*, 2010, **327**, 846–850.
49. S. Furukawa, K. Hirai, K. Nakagawa, Y. Takashima, R. Matsuda, T. Tsuruoka, M. Kondo, R. Haruki, D. Tanaka, H. Sakamoto, S. Shimomura, O. Sakata and S. Kitakawa, *Angew. Chem. Int. Ed.*, 2009, **48**, 1766–1770.
50. K. Hirai, S. Furukawa, M. Kondo, H. Uehara, O. Sakata and S. Kitakawa, *Angew. Chem. Int. Ed.*, 2011, **50**, 8057–8061.
51. K. Hirai, S. Furukawa, M. Kondo, M. Meilikhov, Y. Sakata, O. Sakata and S. Kitakawa, *Chem. Commun.*, 2012, **48**, 6472–6474.
52. Z. Fang, B. Bueken, D. E. de Vos and R. A. Fischer, *Angew. Chem. Int. Ed.*, 2015, **54**, 7234–7254.
53. S. Furukawa, J. Reboul, S. Diring, K. Sumida and S. Kitagawa, *Chem. Soc. Rev.*, 2014, **43**, 5700–5734.
54. P. Falcaro, R. Ricco, C. M. Doherty, K. Liang, A. J. Hill and M. J. Styles, *Chem. Soc. Rev.*, 2014, **43**, 5513–5560.
55. S. Henke, R. Schmid, J.-D. Grunwaldt and R. A. Fischer, *Chem. Eur. J.*, 2010, **16**, 14296–14306.
56. S. Henke, A. Schneemann, A. Wütscher and R. A. Fischer, *J. Am. Chem. Soc.*, 2012, **134**, 9464–9474.
57. D. Zacher, O. Shekhah, C. Wöll and R. A. Fischer, *Chem. Soc. Rev.*, 2009, **38**, 1418–1429.
58. O. Shekhah, J. Liu, R. A. Fischer and C. Wöll, *Chem. Soc. Rev.*, 2011, **40**, 1081–1106.
59. A. Bétard and R. A. Fischer, *Chem. Rev.*, 2012, **112**, 1055–1083.
60. D. Bradshaw, A. Garai and J. Huo, *Chem. Soc. Rev.*, 2012, **41**, 2344–2381.

61. K. Otsubo and H. Kitagawa, *APL Mater.*, 2014, **2**, 124105.
62. J. L. Zhuang, A. Terfort and C. Wöll, *Coord. Chem. Rev.*, 2016, **307**, 391–424.
63. J. Liu and C. Wöll, *Chem. Soc. Rev.*, 2017, **46**, 5730–5770.
64. P. Falcaro, K. Okada, T. Hara⁵, K. Ikigaki⁵, Y. Tokudome, A. W. Thornton, A. J. Hill, T. Williams, C. Doonan and M. Takahashi, *Nature Mater.*, 2017, **16**, 342–348.
65. I. Stassen, M. Styles, G. Greci, H. Van Gorp, W. Vanderlinden, S. De Feyter, P. Falcaro, D. De Vos, P. Vereecken and R. Ameloot, *Nature Mater.*, 2016, **15**, 304–310.
66. E. Ahvenniemi and M. Karppinen, *Chem. Mater.*, 2016, **28**, 6260–6265.

Chapter 2

Continuous liquid phase epitaxial growth of moisture-tolerant carboxypyrazolate-based MOF-5 isotype thin films



-
- The results of this chapter are mainly comprised in and reproduced from the following publication, "S. Wannapaiboon, M. Tu and R. A. Fischer, *Adv. Funct. Mater.*, 2014, **24**, 2696-2705" with permission from the Copyright © 2013 WILEY-VCH Verlag GmbH & Co. KGaA.
 - The results of this chapter have been continuously accomplished from the master thesis "S. Wannapaiboon, Deposition of metal—organic framework thin films: their characterizations by X-ray diffraction and accessing the sorption properties by quartz crystal microbalance".

2.1 Introduction and state of the art

2.1.1 Rational design of MOF materials towards real-world utilisation

Metal-organic frameworks (MOFs) are a novel class of porous materials which have been extensively investigated throughout both academic and industrial research during the past decades. The versatility in the range of precursor components that can be used for the molecular assembly of MOFs offers possibilities to precisely manipulate the framework structures, porosities and their associated features.¹⁻³ Hence, recent research has focused on rational design of the pore structure, size, shape and surface functionalities in order to fine-tune and optimise the MOF properties for such specific applications, ranging from gas storage, separation and catalysis towards emerging applications including electronics, sensing, optics and biomedicine.⁴⁻⁷ Apart from exploring the new promising MOF structures, modification of the known frameworks at the molecular-assembly level by altering metal nodes and/or organic linkers could initiate the desired features or even enhance the characteristics of the known MOFs.

$Zn_4O(bdc)_3$ (MOF-5, $bdc = 1,4$ -benzenedicarboxylate)⁸ and its isorecticular MOFs (IRMOFs) family⁹ are the most well-known MOF structures. However, the main drawback of the IRMOFs for practical applications is their moisture sensitiveness, which is a consequence of the easy-hydrolysable Zn—O (carboxylate) coordinated bonds within the framework. In this regard, the crystalline MOF structures are collapsed during the uses at ambient conditions.¹⁰ To improve the moisture stability while still maintain their cubic topology and the relatively-high surface area, an alternative replacement of dicarboxylate linkers by azolate linkers to link with the M_4O clusters ($M = Zn$ or Co) within the frameworks has been introduced. Hou *et al.* reveals that using the stoichiometric-mixed linkers between 3,3',5,5'-tetramethyl-4,4'-bipyrazolate (bpz) and bdc to construct the 3D porous $Zn_4O(bdc)(bpz)_2$ can enhance the hydrophobicity of the framework.¹¹ Specifically, the hydrophobic channels (diameter ~ 8.2 Å) are generated which leads to the favorable adsorption of the hydrophobic probe molecules over the hydrophilic ones. Moreover, the presence of methyl groups of the bpz linker pointing inward to the MOF cavity also help to prevent the interpenetration of the frameworks, of which the specific surface area is not drastically reduced. Unfortunately, the synthesis of the MOF-5 isotype consisting of only

the bipyrazolate linker (so-called $\text{Zn}_4\text{O}(\text{bpz})_3$) is failed to obtain.¹¹ Alternatively, an alteration of the metal source from Zn(II) to Co(II) lead to a successful incorporation of pyrazolate linkers into the MOF-5 analogue framework, namely $\text{Co}^{\text{II}}_4\text{O}(\text{bdpb})_3$ (MFU-1, $\text{bdpb} = 1,4\text{-bis}[(3,5\text{-dimethylpyrazol-4-yl)]\text{benzene}$). Thanks to the thermodynamically-stable complexes between cobalt (II) ions and N-heterocyclic linkers, MFU-1 shows a good performance against hydrolytic decomposition in the presence of water and/or similar protic solvents.¹² However, the thermal stability (up to 390°C) of both MOFs is moderately improved from the MOF-5 parent structure.

2.1.2 Carboxypyrazolate-based MOF-5 isotype MOFs

An enhancement of stability and hydrophobicity of the MOF-5 analogues has been achieved by Montoro et al. by employing the 3,5-dimethyl-4-carboxypyrazole (H_2DM) for the synthesis of robust $\text{Zn}_4\text{O}(\text{DM})_3$ (**Zn-DM**) crystal by refluxing with $\text{Zn}(\text{NO}_3)_2$ in a basic ethanol medium.¹³ The main structural and chemical features of the **Zn-DM** are presented in Figure 2.1A. The structure features tetrahedral $[\text{Zn}_4\text{O}]^{6+}$ units that are bound on average by three carboxylate moieties and three pyrazolate moieties (Fig. 2.1B) that are bridged by the organic linkers to form a cubic network (space group: $Fm-3m$) isorecticular with the well-known MOF-5 framework. However, unlike MOF-5, the presence of the strongly binding pyrazolate moieties provides more robust metal-ligand bonding, and consequently a greater thermal, chemical and mechanical stability. Moreover, a presence of the two methyl groups pointing toward the carboxylate group in the organic linker help to protect the Zn—O bonds from nucleophilic attacks leading to a high degree of hydrophobicity and stability towards moisture. As a highlight, **Zn-DM** exhibits selective captures of chemical warfare gases (*i.e.* analogues of Sarin nerve agent and mustard gas) even in a competition with moisture at ambient conditions.¹³

Building up upon this knowledge, we reported an alternative synthetic procedure to obtain polycrystalline **Zn-DM** powder at relatively low temperature of up to 50°C by employing the controlled secondary building units (SBU) approach (CSA)¹⁴, also called the ligand replacement approach. In the experimental procedure, solutions of metal precursor and organic linker component are prepared separately before mixing them together in the reaction, emphasising a possibility to further apply the optimised synthetic

parameters for the fabrication of MOF thin-films by stepwise deposition process. Herein, the desired MOF framework is formed by the replacement of the acetate ligands in the pre-formed basic zinc acetate cluster ($\text{Zn}_4\text{O}(\text{OAc})_6$) by the DM^{2-} linkers.

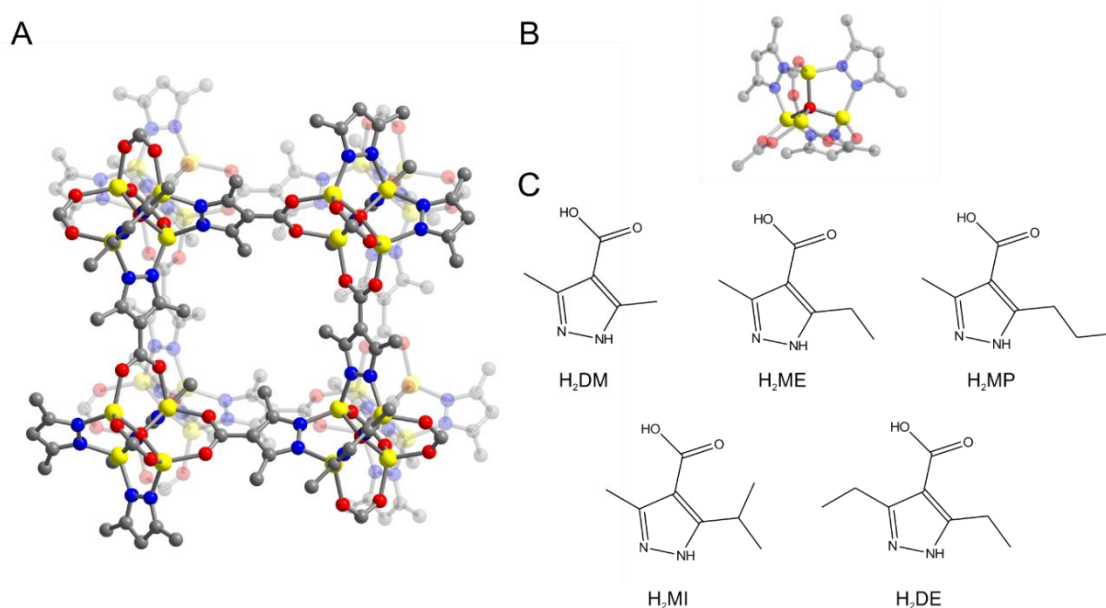


Figure 2.1 (A) A portion of the single-crystal structure of $\text{Zn}_4\text{O}(\text{DM})_3$ (**Zn-DM**) as viewed along the crystallographic *a*-axis; (B) an enlarged view of a $[\text{Zn}_4\text{O}]^{6+}$ unit within the structure; and (C) molecular structures of the five organic linkers employed in this work. Yellow, gray, blue, and red spheres represent Zn, C, N, and O atoms, respectively. Note that, in panels A and B, hydrogen atoms and the disorder in the orientation of the linkers has been omitted for clarity. Reproduced and adapted with permission. Copyright © The Royal Society of Chemistry 2017.³⁵

Moreover, the size of the pore apertures is amenable to fine-tuning via changing the identity of the alkyl substituents on the pyrazolate ring. In this work, we employ the series of analogue linkers to 3,5-dimethyl-4-carboxypyrazolate (DM^{2-}), namely 3-methyl-5-ethyl-4-carboxypyrazolate (ME^{2-}), 3-methyl-5-propyl-4-carboxypyrazolate (MP^{2-}), 3-methyl-5-isopropyl-4-carboxypyrazolate (MI^{2-}) and 3,5-diethyl-4-carboxypyrazolate (DE^{2-}) linkers shown in Fig. 2.1C to demonstrate the broad applicability of the synthetic technique to the **Zn-L** structure type. In order to achieve the phase-pure **Zn-L** powders, the ratio and the type of mixed solvent (ethanol/water system) need to be optimized. Note that, a presence of some amount of water in the reaction mixture enhances the formation of the desired cubic phase of **Zn-L**, while the unknown crystalline phase is formed instead when performing the reaction without water.¹⁵

2.1.3 Fabrication of Zn-L MOF thin-films by static stepwise deposition

The integration of functionalized MOF materials in micro-systems and devices requires the deposition of MOF thin films onto given substrates.¹⁶⁻¹⁷ Thus far, the reported results on this topic indicate potential for various applications, such as chemical sensors,¹⁸⁻¹⁹ separating membranes²⁰⁻²¹ and capillary columns for gas chromatography.²² Most concepts of the bulk MOF synthesis of both single-component and hybrid crystals are transferable to MOF thin-film processing.¹⁶ Stepwise deposition method is one of potential methods for MOF thin-film fabrication. In the ideal case of strictly self-terminated growth kinetics, this method leads to the MOF thin-films with well-defined layer thickness (or crystallite sizes) and controlled crystallographic orientation, so-called surface-mounted MOF thin films (SURMOFs).²³

Combining CSA with stepwise deposition method allows the growth of SURMOFs at relatively low temperature via the sequential contact of the chosen substrates with solutions of the selected inorganic and organic building blocks.²⁴⁻²⁵ In particular, various homo- and heterostructured layered-pillared SURMOFs of M_2L_2P type (M = metal ions, L = layered dicarboxylate linker and P = dinitrogen pillared linker) have been thoroughly investigated and obtained by stepwise deposition method on self-assembled organic monolayer (SAM) modified gold-coated substrates.²⁶⁻²⁸ Unlike bulk crystals, location and distribution of functionalities in the coatings can be designed based on a sequence and a number of deposition cycles of each component. Moreover, the in-situ monitoring of LPE growth by using a quartz crystal microbalance (QCM) instrument²⁶⁻³⁰ or a surface plasmon resonance (SPR) spectroscopy³¹, allows for direct process control and provides insight into the deposition mechanism.

For practical applications of MOFs, including thin films and membranes, chemical, thermal and mechanical stability are required. Moreover, the materials must maintain their adsorptive, selective and separating performances even when operated at ambient conditions. Carboxypyrazolate-based (**Zn-L**) MOF series are one of promising candidates which reveal these desired properties. In our previous work, we fabricated thin films of **Zn-DM** by stepwise deposition method operated in a static mode, i.e. through the batchwise immersion of the substrate into the precursor and washing solutions. The

crystalline **Zn-DM** film was obtained from the static stepwise deposition at a relatively low temperature of 50 °C using an ethanol/water solvent system.¹⁴ According to X-ray diffraction (XRD) data, the **Zn-DM** film exhibited high crystallinity with moderately preferred (100)-related orientation. Nevertheless, the scanning electron microscopic (SEM) images showed a slightly tilted orientation of the cubic MOF crystallites on the substrate (Figure 2.2). This **Zn-DM** film revealed a kinetically size-selective adsorption of alcohol vapours (Figure 2.3A) and *p*-xylene over *m*-/*o*-xylene (Figure 2.3B) as well as a higher affinity of non-polar probe molecules over the polar ones with the same kinetic diameter size (toluene over aniline, Figure 2.3C).¹⁴

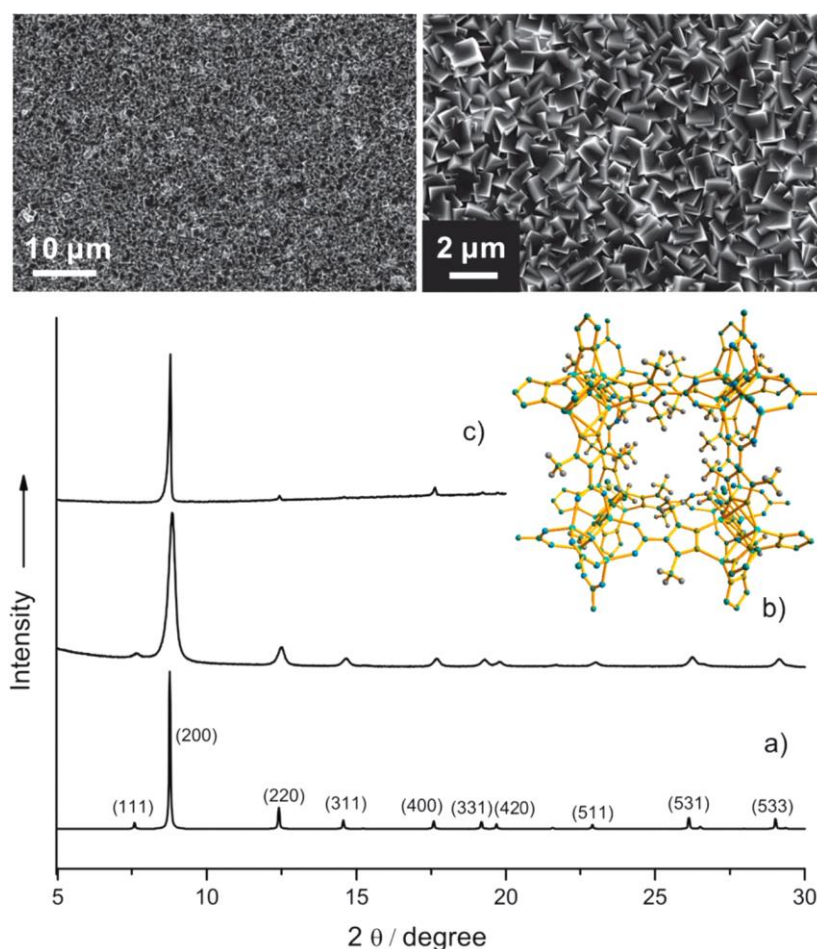


Figure 2.2 (top) SEM micrographs of a 30-cycle **Zn-DM** film grown on COOH-terminated Au-coated substrate. (bottom) Comparison of the X-ray diffraction patterns of (a) simulated pattern from published data, (b) of a powder obtained by the CSA and (c) of a film grown on COOH-functionalized Au-coated substrate by static stepwise deposition. Reprinted with permission. Copyright © The Royal Society of Chemistry 2012.¹⁴

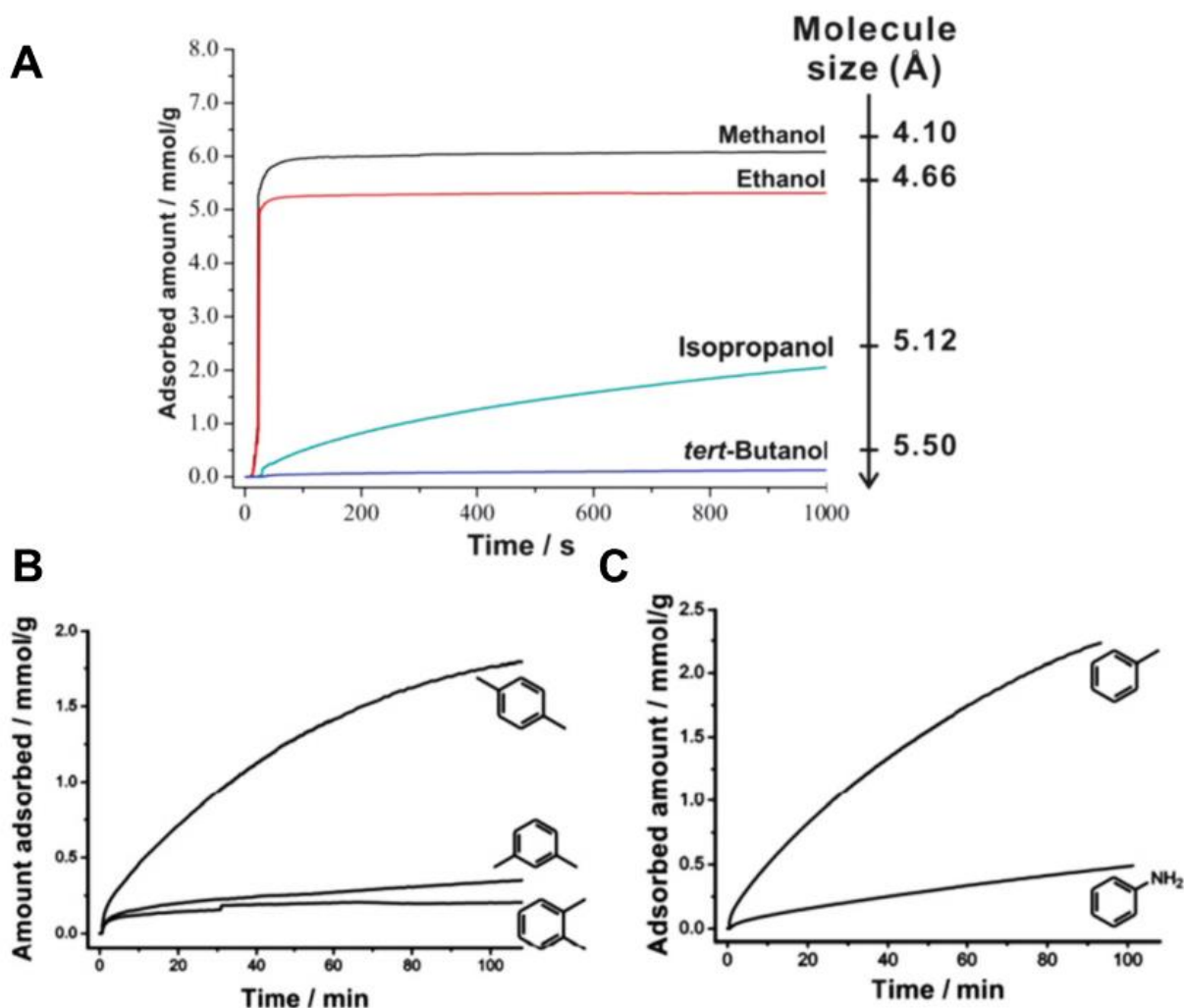


Figure 2.3 Time dependent mass uptake of a **Zn-DM** film illustrating (A) kinetically size-selective adsorption of alcohol vapours, (B) *p*-xylene over *m*-/*o*-xylene and (C) polarity-selective adsorption of toluene over aniline. Reprinted and adapted with permission. Copyright © The Royal Society of Chemistry 2012.¹⁴

However, this non-continuous conduction of the deposition process was found to be of limited versatility because it was difficult (or even impossible) to achieve highly crystalline films of some **Zn-L** MOFs consisting of linker (L) with more-sophisticated alkyl pendant sidechains of the carboxypyrazolate derivatives. Fabrication of **Zn-DM** as a seeding layer (for 1 deposition cycle) was required in order to improve the crystallinity of the analogue **Zn-L** thin-films, indicating the relatively poor nucleation of the analogue **Zn-L** on the substrate surface.¹⁴ An attempt to improve the synthetic procedure in order to achieve **Zn-L** films with better crystallinity and enhanced features is of concern.

2.2 Continuous liquid phase epitaxial growth of Zn-L thin films

Continuous stepwise liquid-phase epitaxial growth (LPE, Figure 2.4) was applied to fabricate thin films of **Zn-L** series. We would first like to note that the applied experimental protocol is characterized by the alternate dosing of solutions of the separated MOF building blocks onto a given substrate in an automated, continuous flow fashion with very small dead volume, which is in contrast to a static (batchwise) stepwise deposition method.¹⁴ The applied growth technique, however, does not imply that the actual film growth kinetics will or should follow a strictly self-terminated layer-by-layer growth mechanism. To avoid any confusion, we do not use the acronym SURMOFs for the MOF thin films discussed in this study and suggest using the definition SURMOF only for those MOF thin films for which the growth mode matches a self-limited mechanism. Herein, we report significant improvement of the quality of such homostructured **Zn-L** films and the fabrication of related heterostructured MOF films **B@A** using the continuous, automated stepwise LPE process, during which the oscillation frequencies of quartz crystal microbalance (QCM) substrates are monitored in-situ.

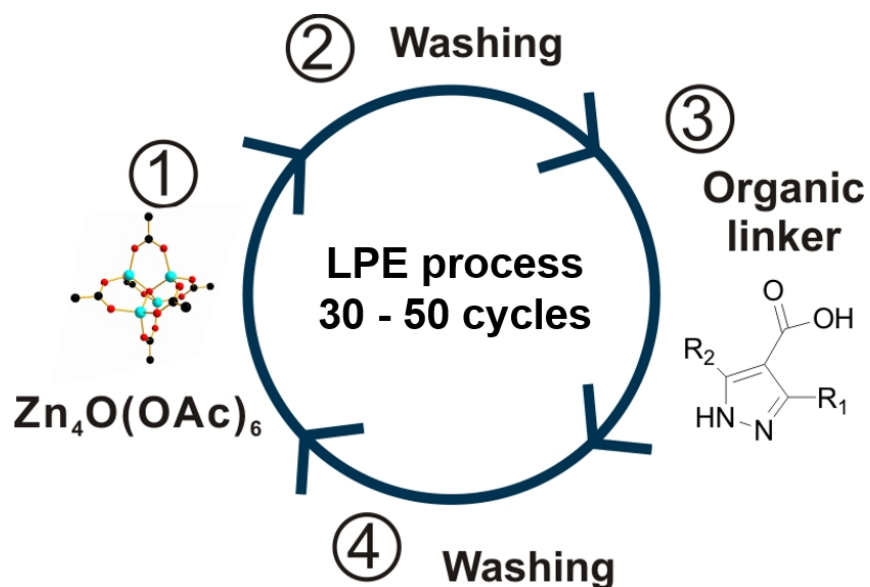


Figure 2.4 Schematic illustration of a continuous stepwise LPE growth of **Zn-L** thin films. Substrate is alternately dosed with solutions of the metal and organic linker building blocks in a continuous flow fashion. In between the precursor dosing steps, substrate is washed with solvent (herein, ethanol). The LPE process is repeated for 30-50 cycles in order to obtain the crystalline **Zn-L** films.

2.2.1 Growth of homostructured Zn-L films

Zn-L MOF series are analogue structures consisting of various alkyl substituents at the 3rd and 5th positions of the 3-alkyl-5-alkyl-4-carboxypyrazolate linkers. Based on the idea of rational synthesis, the pore sizes and pore apertures can be tuned by the choices of the organic linker moieties, while the unit cell parameters either remain unchanged or slightly deviate from the parent **Zn-DM** MOF.

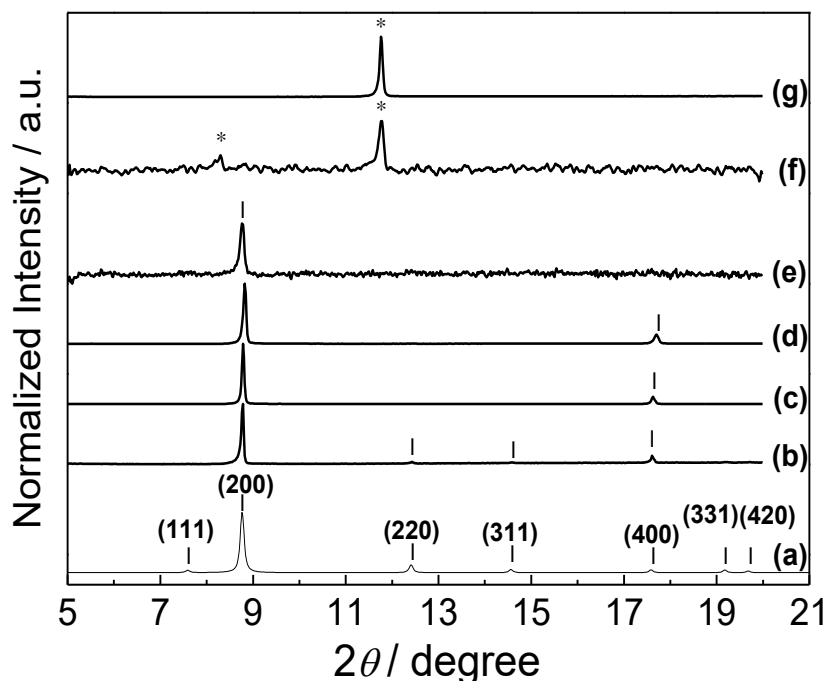


Figure 2.5 (a) Simulated XRD pattern of cubic **Zn-DM** powder according to the published data¹³ (indicated by the | symbol). XRD patterns of the thin films of (b) **Zn-DM**, (c) **Zn-ME**, (d) **Zn-MP** and (e) **Zn-MI** fabricated by the continuous stepwise LPE process at 40°C for 40 cycles on the –COOH functionalized QCM substrates. Each deposition cycle consists of a continuous flow of the basic zinc acetate solution in ethanol 10 min / ethanol 5 min / the H₂L linker in ethanol/water mixture 10 min / and finally ethanol 5 min. Note that, the unknown crystalline phase (indicated by the * symbol) obtained when using (f) H₂MB and (g) H₂DP as the organic linker. Reproduced with permission. Copyright © 2013 WILEY-VCH Verlag GmbH & Co. KGaA.³⁶

Employing continuous stepwise LPE process affords a successful fabrication of crystalline, homostructured **Zn-L** thin-films upon the appropriate selection of the linkers. Excellent crystallinity of these **Zn-L** films as qualitatively judged by the very high signal-

to-noise ratio of the XRD patterns could be achieved when using H₂DM, H₂ME and H₂MP (Figure 2.5 (b) to (d)), whereas a moderate signal-to-noise ratio was observed when using H₂MI (Fig. 2.5 (e)) as the organic linker. However, an attempt to incorporate the H₂L analogues with more sophisticated alkyl substituents e.g. 3-methyl-5-butyl-4-carboxypyrazole (H₂MB) and 3,5-dipropyl-4-carboxypyrazole (H₂DP) disfavoured the formation of the cubic MOF-5 isotype phase under these growth conditions. Instead of the expected cubic **Zn-L** phase, a different crystalline phase was observed, and it appeared to exhibit a so far unknown structure (Figure 2.5 (f) and (g)), showing a limitation for pore size modification in the cubic **Zn-L** system.

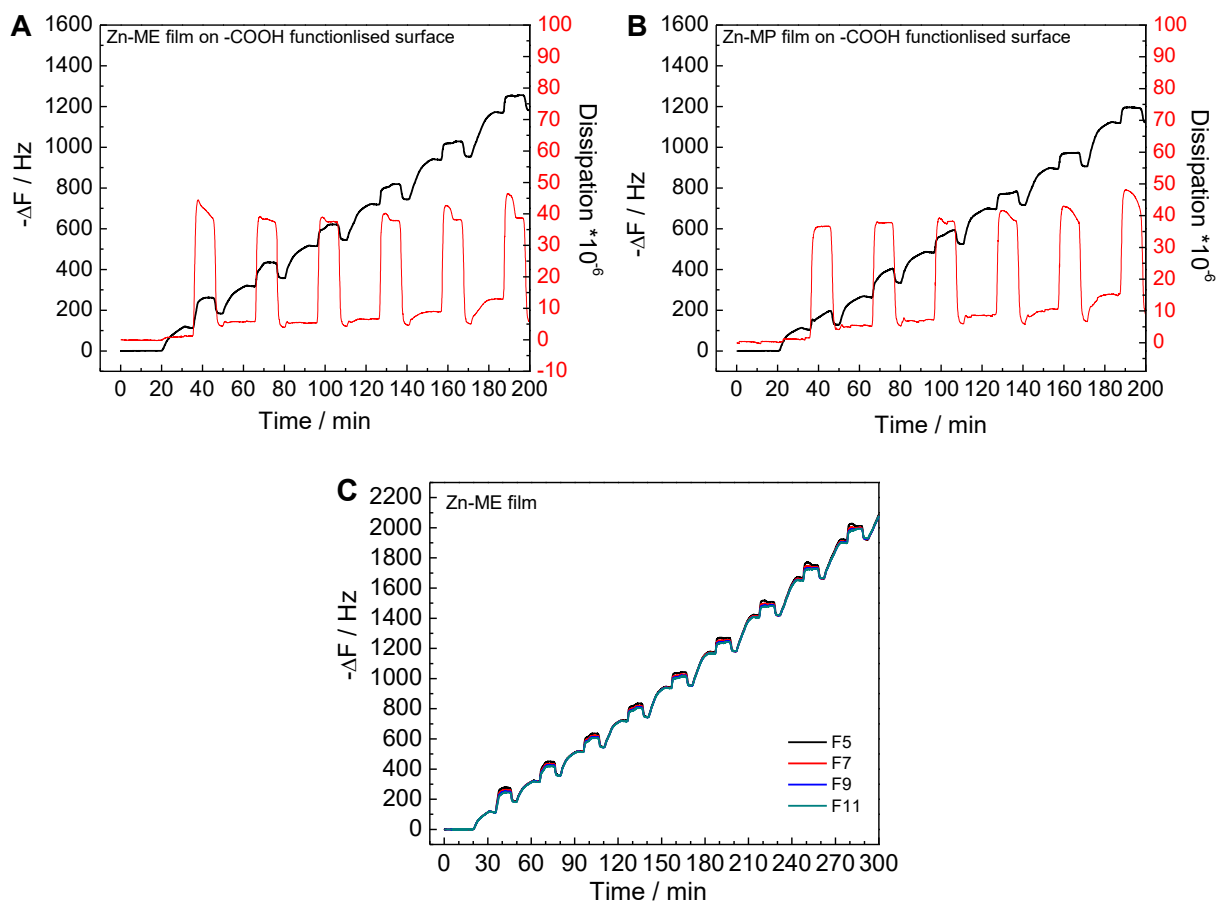


Figure 2.6 In situ monitoring of the change of QCM oscillation frequency and the dissipation parameter (D) as a function of the deposition time of the first 6 deposition cycles of (A) **Zn-ME** and (B) **Zn-MP** films, and (C) the frequency changes in different harmonics show roughly the same value during the fabrication of **Zn-ME** film.

During the film growth by continuous LPE process, the change of QCM oscillation frequency is in-situ monitored as a function of deposition time (corresponding to the number of deposition cycles). The frequency change is proportional to the mass change, according to the Sauerbrey equation³², when the films are thin, rigid and tightly bound to the substrate surface.^{29-31, 33} The similarity of frequency changes in different harmonics and the overall small dissipation after the completion of each deposition cycle are observed in our experiments (as shown the examples in Figure 2.6), which support the applicability of the Sauerbrey equation.

A closer inspection of the QCM frequency changes reveals the information of the particular growth kinetic, and could elucidate the growth mechanism in detail. The overall mass uptakes are determined to be a linear function of the increasing number of deposition cycles, which allows for a precise control of the film growth by the LPE method. Unlike the expected self-terminated growth behaviour as reported in the published SURMOFs (e.g. HKUST-1³⁰ and M₂L₂P MOFs³⁴), the mass deposition on the QCM substrate during the fabrication of **Zn-DM** film (Figure 2.7) increases with each deposition step of the zinc SBU without pronounced a saturation, indicating no self-termination (at least under the chosen conditions). However, the frequency becomes stable after performing the washing step with ethanol, which could correspond to the permanent chemisorption of the zinc SBUs to the substrate surface (indicating by the small dissipation parameter after a completion of the washing step).

In each subsequent deposition step of the H₂L linker solutions, the mass uptake significantly increases until reaching a saturation, after which it decreases and stabilises during the ethanol washing step. Specifically, the rapidly increase of the dissipation parameter at the beginning of the linker deposition step indicates that the linkers are not initially attached in a rigid fashion to the surface. Subsequently, a substitution of the deposited linker to the remaining acetate groups in the previously surface-chemisorbed Zn₄O(OAc)₆ components occurs. Then, the excess amount of the deposited linkers and the substituted acetate units are removed during the following washing step. Finally, it shows a stabilised QCM frequency change with a small value of dissipation due to the permanent chemisorption of the MOF nuclei (or MOF crystallites in the further deposition

cycles). Clearly, the **Zn-DM** film obtained by the continuous stepwise LPE fabrication are not grown via a self-terminated “layer-by-layer” growth mechanism, as found for HKUST-1 (which is the only rigorously investigated case). Instead, an island growth mode in the nucleation stage and the subsequent overgrowth of the pre-formed MOF crystallites on all facets in a core-shell fashion occurs.

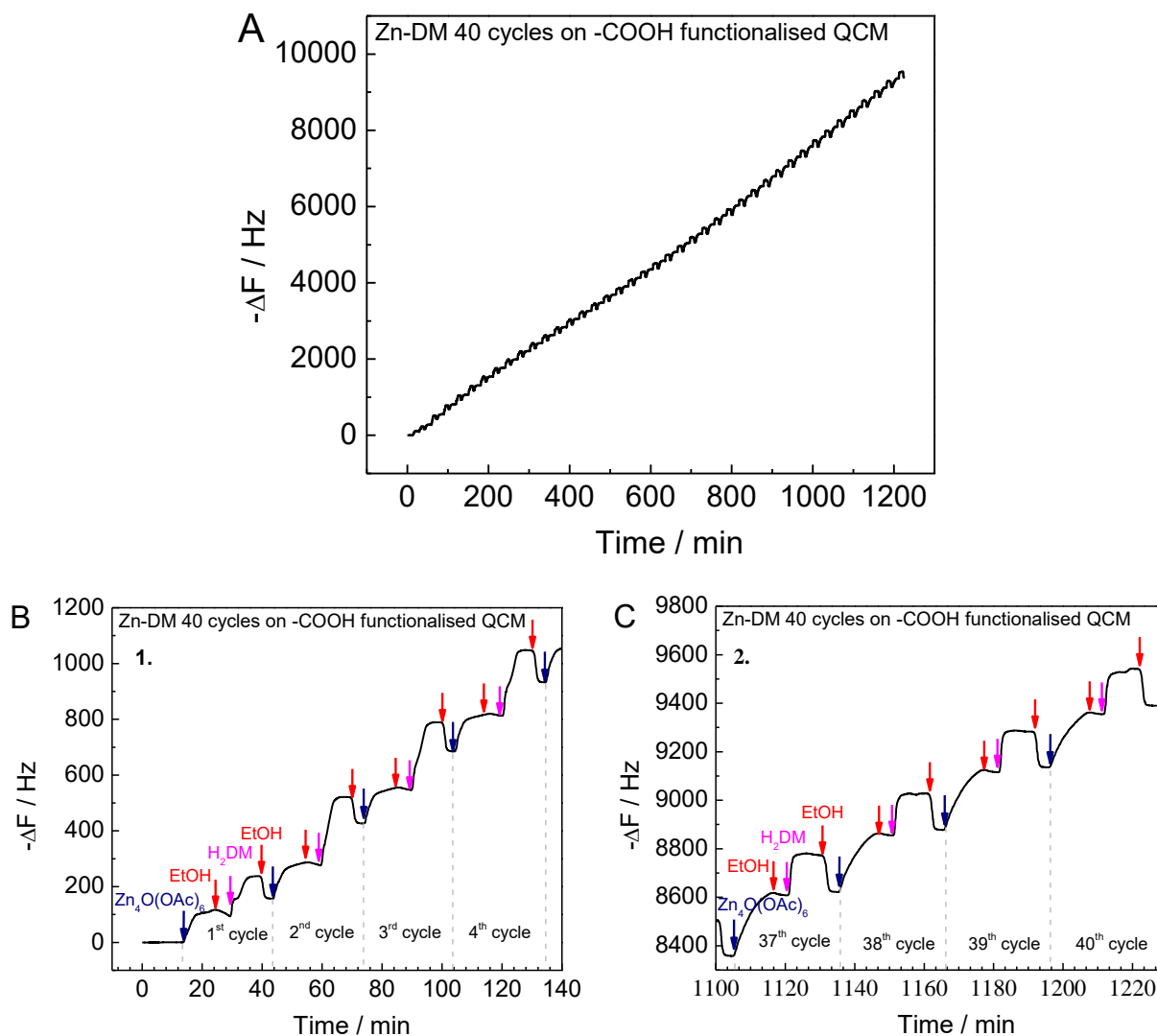


Figure 2.7 (A) In situ monitoring of the QCM oscillation frequency change as a function of deposition time during the continuous stepwise LPE fabrication of **Zn-DM** film at 40°C for total 40 cycles. (B) and (C) The QCM profiles represent the first section and the last section of the **Zn-DM** film growth, respectively.

The QCM frequency change curves during the fabrication of **Zn-ME** (Figure 2.8) and **Zn-MP** films (Figure 2.9) for total 40 cycles show three distinct sections with different growth behaviours. Specifically, the growth behaviour is similar to the growth of the parent **Zn-DM** film during the first few deposition cycles. With increasing number of deposition cycles, the final mass uptake during the deposition of the linker is higher, whereas the uptake of the zinc SBU becomes lower, until showing a tiny uptake at the final section of deposition. This observation may be explained in the following way. The uptake of the zinc SBU plays an important role in the early stage of deposition and is relevant for the control of nucleation and, thus, the formation of the desired MOF nuclei on the functionalized QCM substrate surface. The alteration of the growth mode during the last stage indicates the transition from the nucleation and early crystallite growth stage to the steady-state crystal growth stage, which requires a relatively higher mass uptake of the linker. As a result of this specific growth scheme, the obtained **Zn-ME** and **Zn-MP** films show the excellent crystallinity and the well-defined cubic crystal morphology (Figure 2.10 and 2.11).

Moreover, the two-dimensional grazing incidence X-ray diffraction (2D-GIXRD) patterns of this obtained **Zn-ME** and **Zn-MP** films show discrete diffraction patterns, which indicate the highly preferred orientations of the crystal planes within the MOF films. The out-of-plane cuts from the 2D-GIXRD patterns at the azimuth angle of 0° , corresponding to the lattice planes parallel to the substrate surface, show only the diffraction peaks relating to the [100] orientation with very high intensities. Interestingly, the other lattice planes, *i.e.*, (111), (220) and (311), become significant only in the oblique directions with respect to the substrate surface (Figure 2.12 and 2.13). The 2D-GIXRD data and the SEM images reveal an evidence of the well-oriented, highly-crystalline MOF films. The cubic crystallites attach their bottom (100) facet to the $-\text{COOH}$ terminated substrate surface in the nucleation stage, with the further crystallite growth occurring homoepitaxially along the facets corresponding to the [100] direction of the methyl/ethyl-substituted **Zn-ME** and the methyl/propyl-substituted **Zn-MP** MOFs. Note that, the typical film thickness was approximately $1\ \mu\text{m}$ after a completion of 40 deposition cycles (as shown the examples in Figure 2.14).

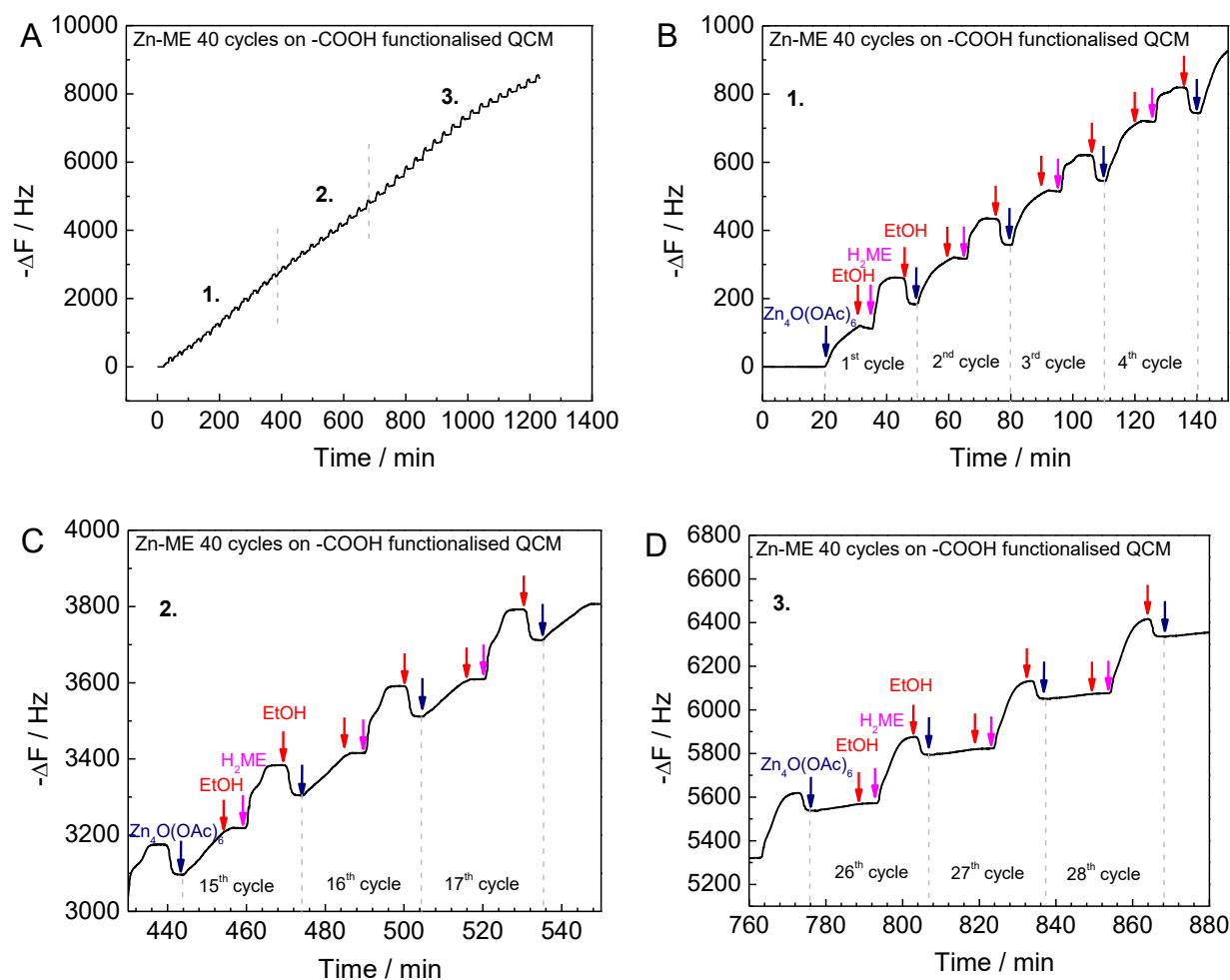


Figure 2.8 (A) In situ monitoring of the QCM frequency as a function of deposition time during the continuous stepwise LPE growth of **Zn-ME** film at 40°C for total 40 cycles. QCM profiles representing the different sections of film growth as depicted in (B) section (1), (C) section (2) and (D) section (3) in Figure 2.8 (A), respectively. Adapted with permission. Copyright © 2013 WILEY-VCH Verlag GmbH & Co. KGaA.³⁶

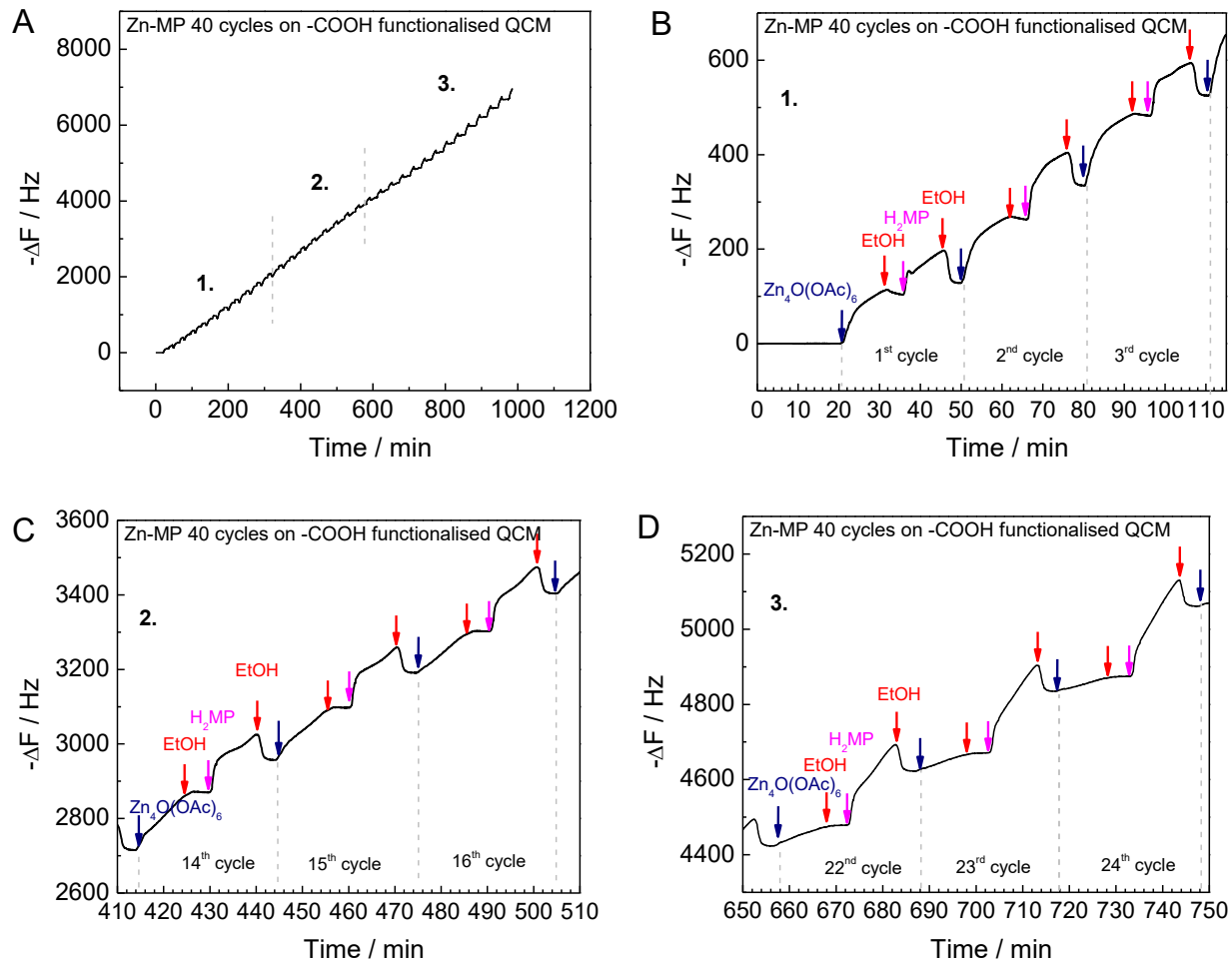


Figure 2.9 (A) In situ monitoring of the QCM frequency as a function of deposition time during the continuous stepwise LPE growth of **Zn-MP** film at 40°C for total 40 cycles. QCM profiles representing the different sections of film growth as depicted in (B) section (1), (C) section (2) and (D) section (3) in Figure 2.9 (A), respectively.

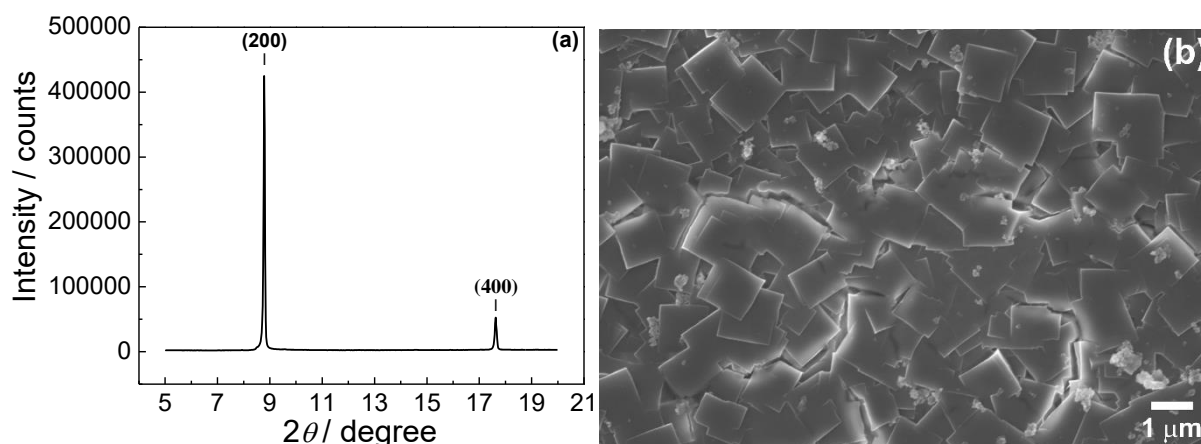


Figure 2.10 (a) The XRD pattern (Bragg-Brentano geometry) and (b) the SEM image of the **Zn-ME** films obtained from the continuous stepwise LPE fabrication at 40°C for 40 cycles indicate a very high crystallinity with preferred orientation along [100]-related direction (attaching the bottom facet of the cubic MOF crystallites onto the substrate surface). Reproduced with permission. Copyright © 2013 WILEY-VCH Verlag GmbH & Co. KGaA.³⁶

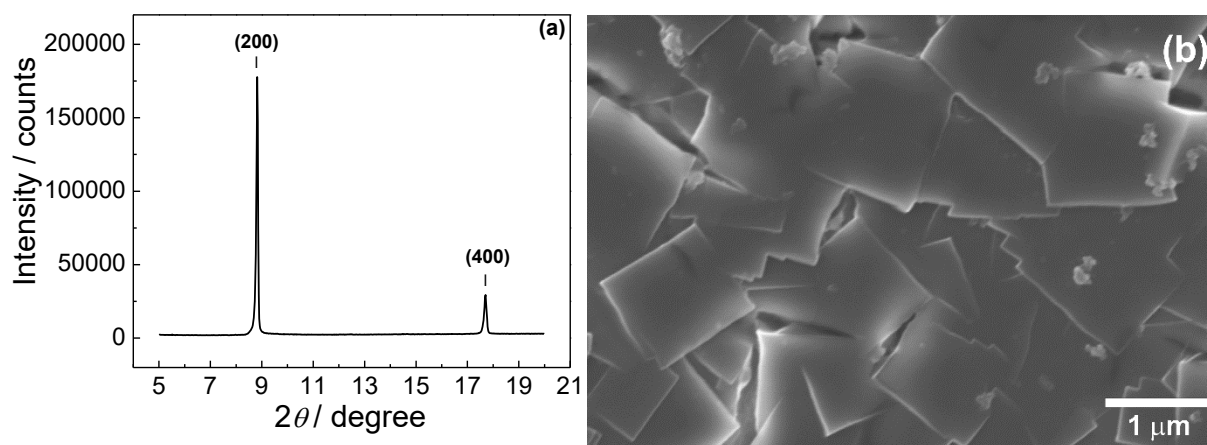


Figure 2.11 (a) The XRD pattern (Bragg-Brentano geometry) and (b) the SEM image of the **Zn-MP** films obtained from the continuous stepwise LPE fabrication at 40°C for 40 cycles indicate a very high crystallinity with preferred orientation along [100]-related direction.

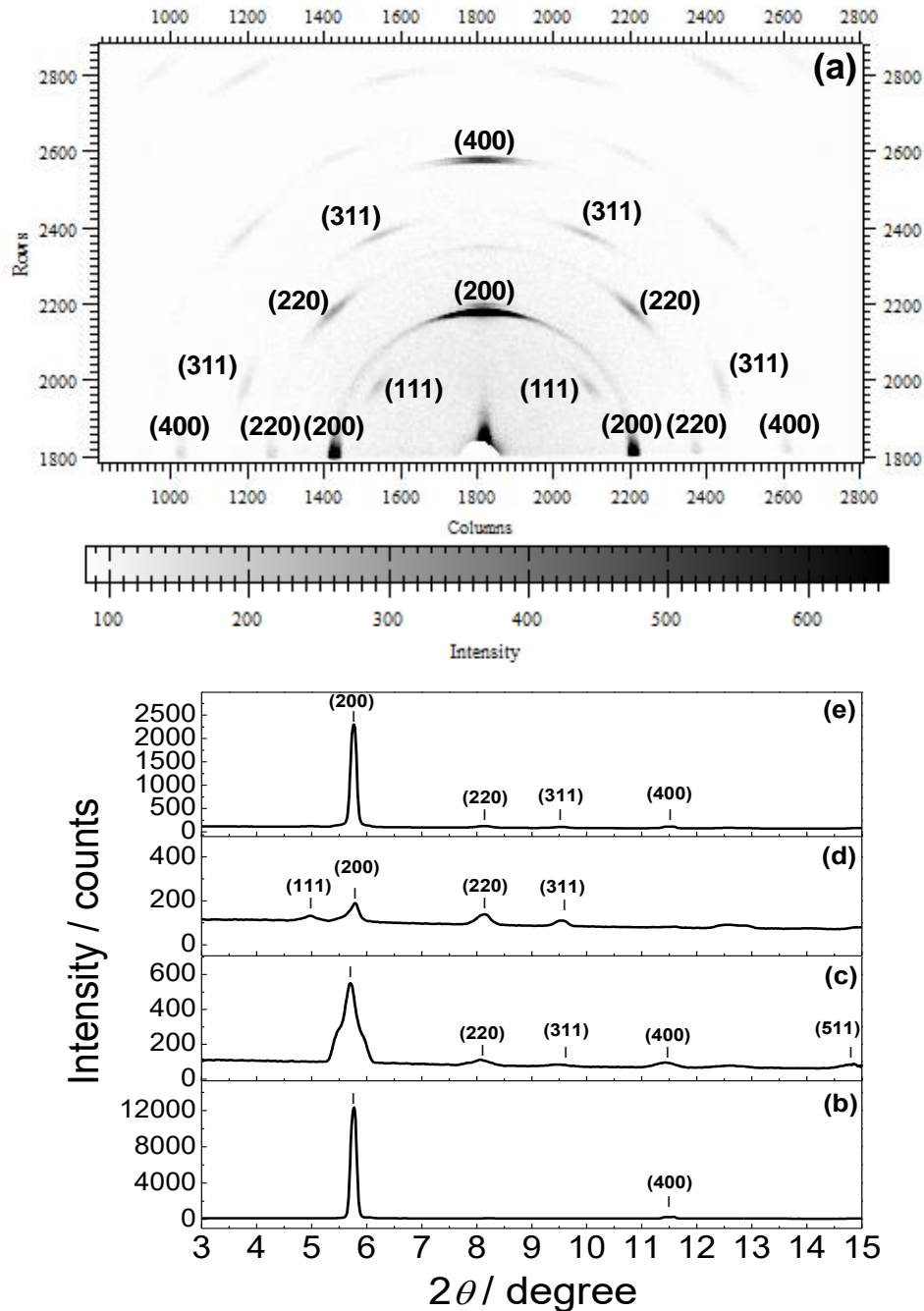


Figure 2.12 (a) 2D-GIXRD pattern of the **Zn-ME** film obtained by using the synchrotron X-ray beam with the wavelength of 1.00 Å. (b) The out-of-plane cut (at azimuth angle of 0°) corresponds to the orientation of lattice planes parallel to the substrate surface (or perpendicular to the film growth direction) showing a preferred orientation in the [100]-related direction. (c) The in-plane cut (at azimuth angle of 90°) corresponding to the orientation of lattice planes perpendicular to the substrate surface. (d) The integrated 1D-line profile at the azimuth angles from 25 to 75° shows the lattice planes that are oblique with respect to the substrate surface. (e) The average integrated 1D line profile.

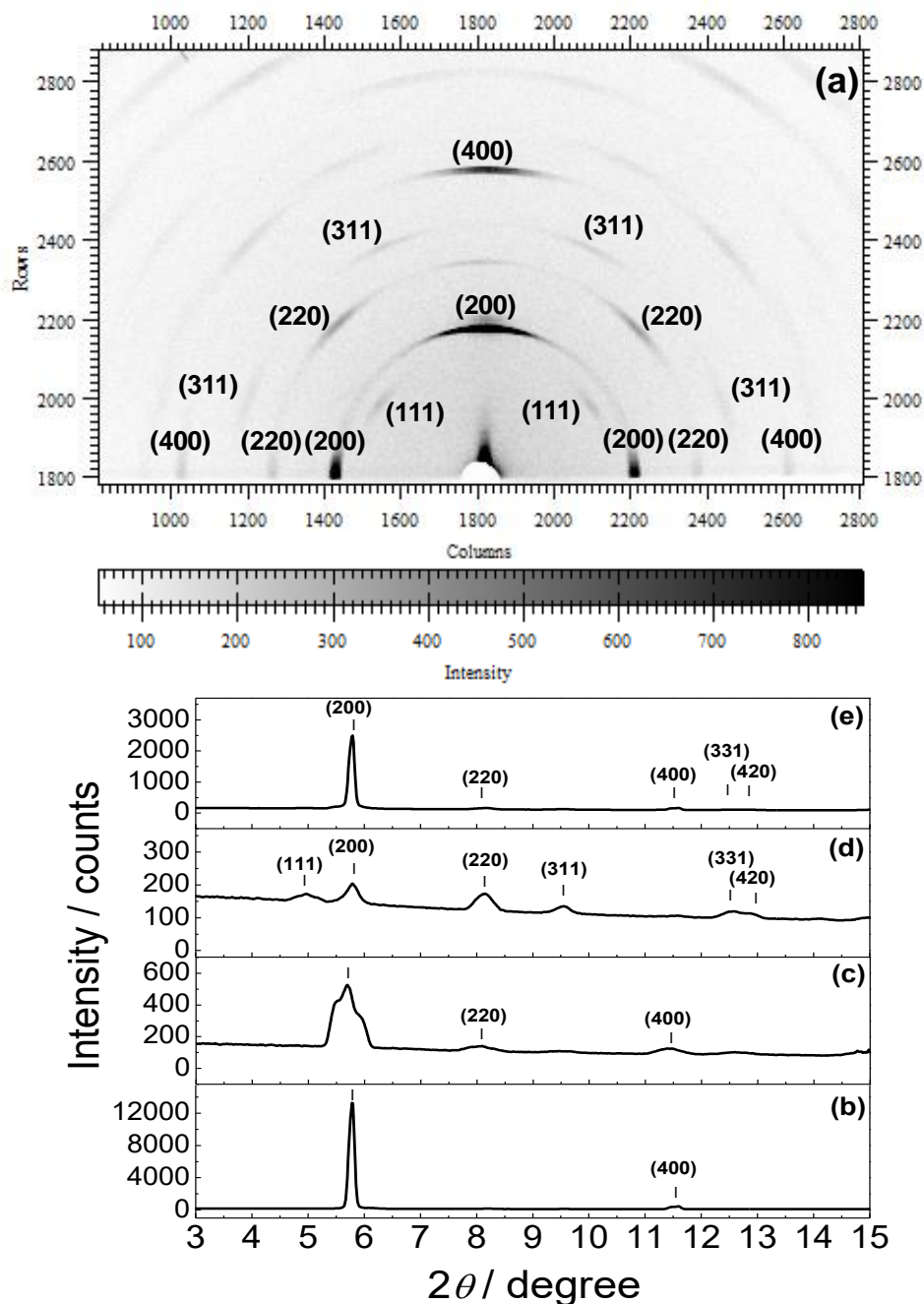


Figure 2.13 (a) 2D-GIXRD pattern of the **Zn-MP** film obtained by using the synchrotron X-ray beam with the wavelength of 1.00 Å. (b) The out-of-plane cut (at azimuth angle of 0°) corresponds to the orientation of lattice planes parallel to the substrate surface (or perpendicular to the film growth direction) showing a preferred orientation in the [100]-related direction. (c) The in-plane cut (at azimuth angle of 90°) corresponding to the orientation of lattice planes perpendicular to the substrate surface. (d) The integrated 1D-line profile at the azimuth angles from 25 to 75° shows the lattice planes that are oblique with respect to the substrate surface. (e) The average integrated 1D line profile.

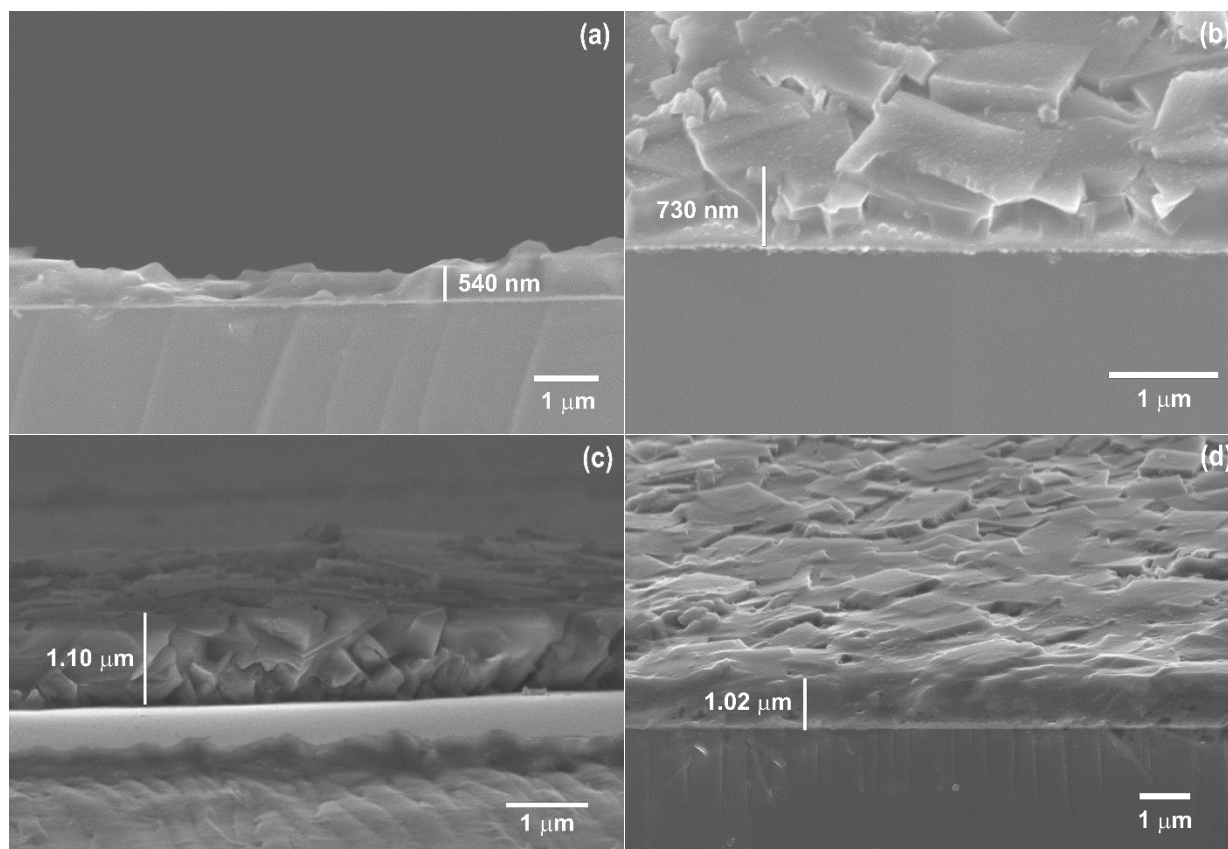


Figure 2.14 Cross-sectional view SEM images of the **Zn-L** MOF films obtaining from the continuous stepwise LPE fabrication at 40°C of **Zn-DM** (a) 20 cycles, (b) 30 cycles, (c) 40 cycles and (d) **Zn-MP** 40 cycles.

Based on the conversion between the frequency change and the mass uptake by Sauerbrey equation, the LPE thin-film growth of **Zn-DM**, **Zn-ME** and **Zn-MP** reveal the calculated mass uptake of approximately $0.70 \text{ nmol}\cdot\text{cm}^{-2}$ per deposition cycle, whereas the significantly lower uptake of $0.19 \text{ nmol}\cdot\text{cm}^{-2}$ per deposition cycle is observed in case of **Zn-MI** film. Moreover, only moderate crystallinity of the **Zn-MI** films was observed (see also Figure 2.5). The in-situ monitored growth behaviour (Figure 2.15) reveals the increased mass uptake during the exposure of the QCM substrates to the zinc SBU solution, as expected. Again, the frequency becomes stable after performing the washing step with ethanol corresponding to the permanent chemisorption of the zinc SBUs to the substrate surface. Subsequently, the rapidly increase of the uptake at the early stage of the H_2MI linker deposition is observed. Nevertheless, and in contrast to the previous

cases, almost all of the applied H_2MI linkers are removed during the washing step with ethanol, indicating poor nucleation and inefficient crystal growth of the methyl/isopropyl-substituted **Zn-MI** MOF as thin-film on the substrate. Accordingly, the obtained **Zn-MI** film shows the lowest crystallinity (poor signal-to-noise ratio of the XRD pattern) among all of the deposited **Zn-L** MOFs in this study. A highly efficient crystal growth stage after the prior nucleation stage is required to achieve excellent crystallinity of the MOF films.

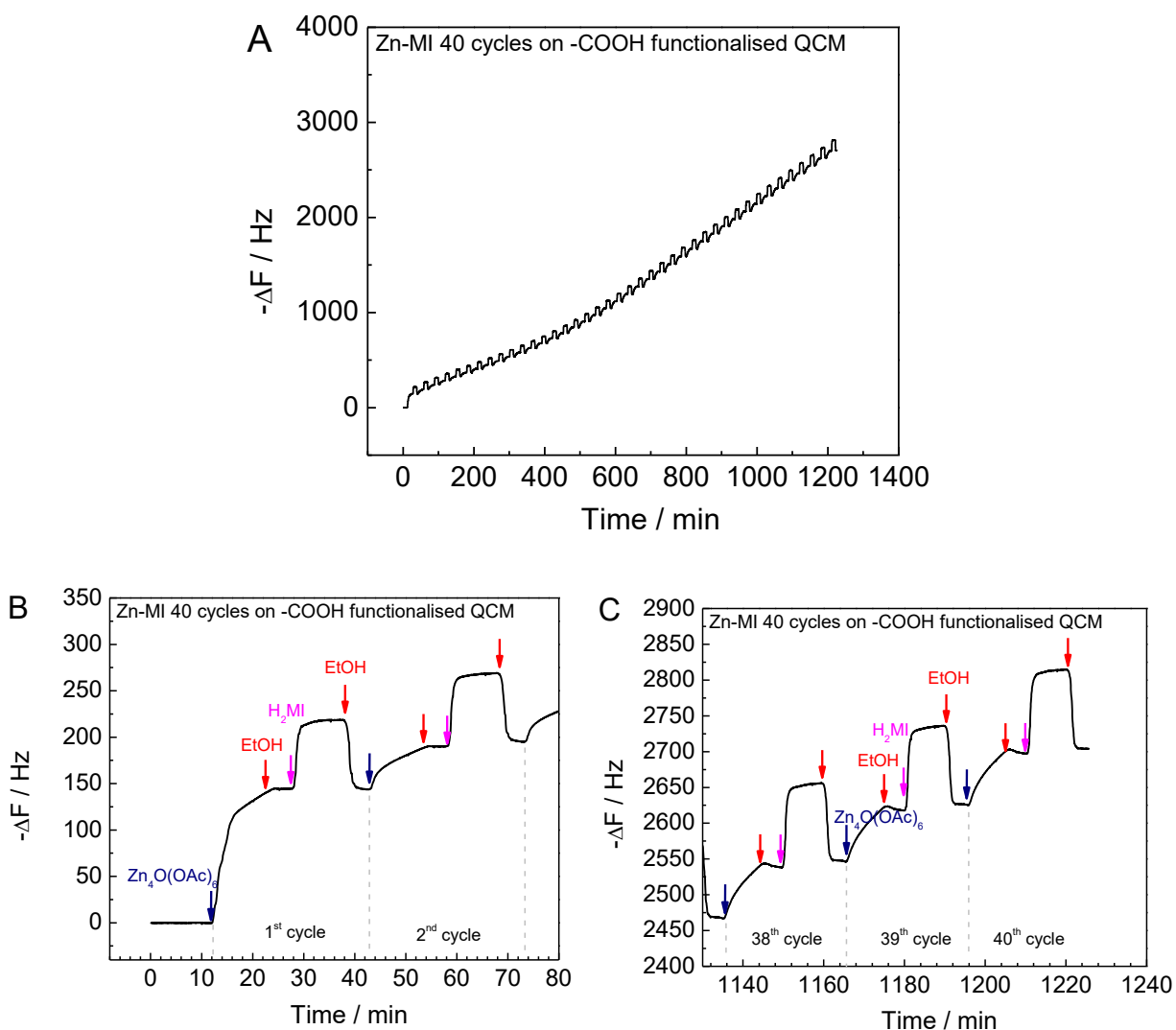


Figure 2.15 (A) In situ monitoring of the QCM oscillation frequency change as a function of deposition time during the continuous stepwise LPE fabrication of **Zn-MI** film at 40°C for total 40 cycles. (B) and (C) The QCM profiles represent the first section and the last section of the **Zn-DM** film growth, respectively.

2.2.2 Adsorption properties of homostructured Zn-L films

Since the **Zn-L** films are fabricated on QCM sensors by the continuous LPE process, it allows to investigate the sorption properties of the films by employing the measurements with an environmentally controlled QCM instrument. The methanol sorption isotherms at 25°C exhibit the expected Langmuir type I isotherm shape without hysteresis, which characteristically illustrates a presence of microporosity in the **Zn-L** films (Figure 2.16). The kinetic diameter size of the methanol molecule (4.10 Å) is smaller than the pore opening windows for the entire **Zn-L** series; therefore, the amount of methanol adsorbed at relative vapour pressure (P/P_0) of 0.90 to 0.95 (approximately, the saturated vapour pressure of methanol at 25 °C and 1 atm) is used to calculate the accessible pore volume of the **Zn-L** films (details are presented in Table 2.1).

The increased bulkiness of the substituents at the carboxypyrazolate linkers in the series $H_2DM \rightarrow H_2ME \rightarrow H_2MP$ results in a reduction of the saturation uptake of methanol and, therefore, the total pore volume of the MOFs. However, the dramatic decrease in the methanol total uptake observed in the **Zn-MI** film is explained by the much lower crystallinity of this particular film. Therefore, the effective pore volume derived for the homostructured **Zn-MI** film is not comparable with the expected value deduced from the respective, idealized MOF structure. The MOF film fabrication needs to be modified to achieve the expected adsorption capacity of the **Zn-MI** film, which is discussed in section 2.2.3. In comparison to the films fabricated using the static stepwise deposition method reported in our previous work,¹⁴ the **Zn-L** films obtained using the continuous stepwise LPE process show a significant increase of methanol uptake by 7% to 55% depending on the type of MOFs. This observation is attributed to the improved crystallinity of the films (less amorphous components), especially in the cases of **Zn-ME** and **Zn-MP**.

The specific methanol saturation uptake for **Zn-DM** films is almost independent from the number of deposition cycles (ranging from 20, 30 to 40 cycles) and only slightly increase proportional to the crystallite dimension (Figure 2.17A). This result indicates that **Zn-DM** films achieve high crystallinity as being accompanied with high porosity from the continuous LPE fabrication of at least 20 cycles. However, in case of the derivatives i.e. **Zn-ME** (showing the unique three-different growth phases), the dependence of a specific

methanol uptake on the total number of deposition cycles is somewhat more pronounced. Herein, the 40-cycles **Zn-ME** film shows an increase of the total methanol uptake by about 10 % with respect to the 30-cycles **Zn-ME** film (Figure 2.17B).

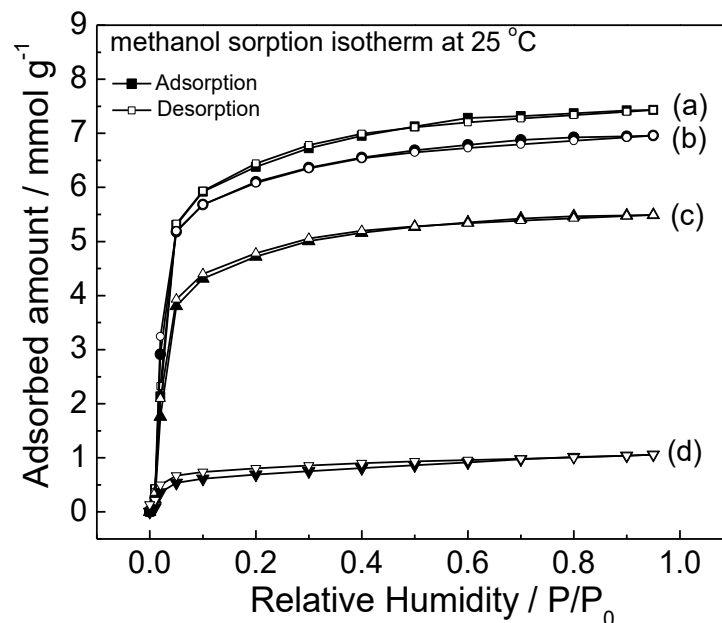


Figure 2.16 Methanol sorption isotherm at 25°C using an environmentally controlled QCM (BEL-QCM-4 instrument) of the homostructured **Zn-L** films of (a) **Zn-DM** (b) **Zn-ME** (c) **Zn-MP** and (d) **Zn-MI** fabricated by the continuous stepwise LPE fabrication process at 40°C for total 40 cycles on the –COOH functionalized QCM substrates. Reprinted with permission. Copyright © 2013 WILEY-VCH Verlag GmbH & Co. KGaA.³⁶

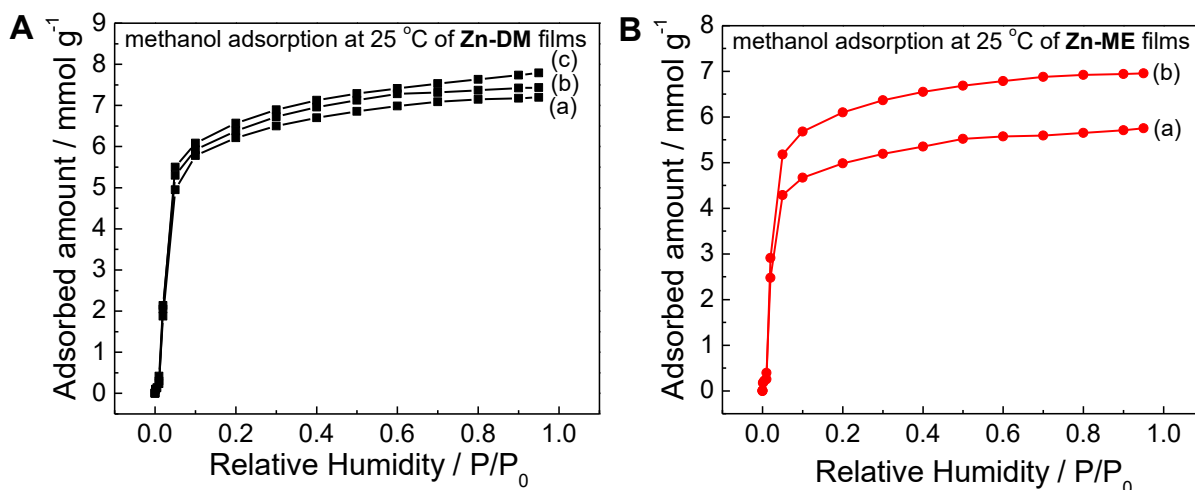


Figure 2.17 Methanol sorption isotherm at 25°C of (A) **Zn-DM** films fabricated by the continuous LPE process for (a) 20, (b) 30 and (c) 40 cycles, and (B) **Zn-ME** films for (a) 30 and (b) 40 cycles* (* showing the unique three-different growth behaviours).

Table 2.1 The unit cell parameter and the calculated volume of the **Zn-L** films and the corresponding accessible pore volume calculated based on their methanol sorption isotherms using an environmentally controlled QCM instrument at 25 °C

Zn-L films	Unit cell parameter [Å] ^[a]	Volume [cm³ mol⁻¹]	Methanol adsorbed amount [mol MeOH mol⁻¹ MOF]	Accessible pore volume [cm³ cm⁻³ MOF]
Zn-DM	20.036	605.46	5.391	0.360
Zn-ME	20.104	611.64	5.107	0.338
Zn-MP	20.036	605.46	4.262	0.285
Zn-MI	20.150	615.85	0.822 ^[b]	0.054 ^[b]

[a] The unit cell parameter is refined from the XRD patterns of the synthesized **Zn-L** films.

[b] The value is relatively low due to the moderate crystallinity of the film. The reasonable adsorption capacity of **Zn-MI** may be calculated from the methanol adsorbed amount of the heterostructured **Zn-MI-on-Zn-DM** film (3.668 mol MeOH mol⁻¹), which shows the accessible pore volume of 0.241 cm³ per cm³ of MOF.

Using slightly larger adsorbents than methanol with similar chemical functionality, such as ethanol and isopropanol, the effective pore opening window of the **Zn-L** MOFs can be probed (Figure 2.18). The highly crystalline films of **Zn-DM** and **Zn-ME** show almost the same adsorption amounts, indicating nearly equal pore openings of both MOFs, which also allow for the accommodation of isopropanol. Interestingly, after achieving a saturated loading of isopropanol into the **Zn-MP** films, the adsorbed isopropanol is hardly desorbed out of the MOF pore, as observed by the difference (hysteresis) between the adsorption and desorption isotherms. From this phenomenon, the effective pore opening window of the **Zn-MP** was estimated to be approximately 5.1 Å, matching with the kinetic diameter size of isopropanol. We must note that the homostructured **Zn-MI** film shows no uptake of isopropanol, which attracted our interest to fabricate this particular MOF film as a sorption selective layer, expressing the potential model for further separating applications (see section 2.2.3, below). Note that, all of the MOF films (**Zn-MP** in particular) can be fully re-activated after the adsorption/desorption measurements by exchanging the adsorbed or remaining alcohol guests within the pore

with methanol for at least 24 h and further applying an in-situ activation protocol by heating at 70°C for 2 h under a dry Helium gas flow (quantitative desorption of methanol) before performing the next adsorption measurement.

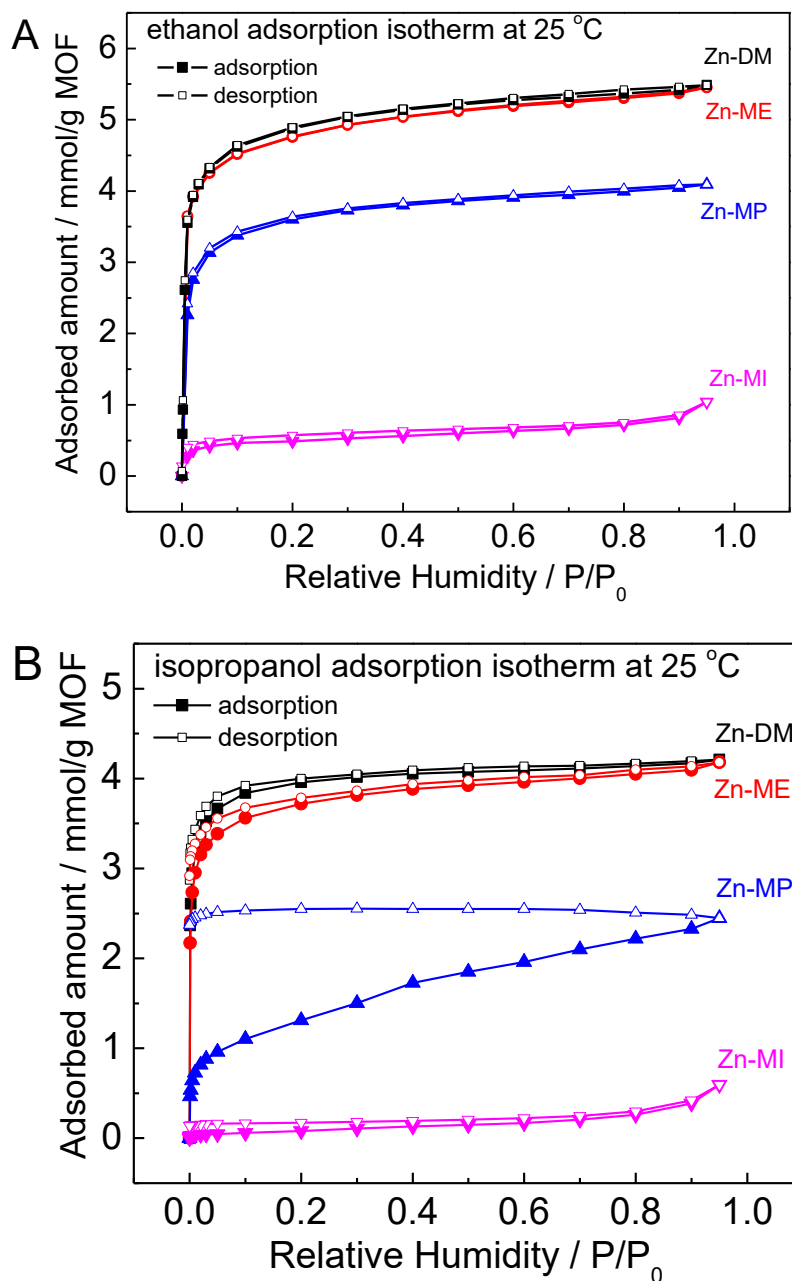


Figure 2.18 (A) Ethanol sorption isotherm and (B) isopropanol sorption isotherm at ambient temperature (25°C) using environmentally controlled BEL-QCM-4 equipment of the **Zn-DM**, **Zn-ME**, **Zn-MP** and **Zn-MI** films fabricated by the continuous stepwise LPE deposition at 40°C for total 40 cycles on the $-\text{COOH}$ functionalized QCM substrates.

2.2.3 Fabrication of heterostructured Zn-L films

In the previous section, an attempt to achieve highly crystalline homostructured **Zn-MI** film is failed. To overcome this problem, the concept of heteroepitaxial growth *via* the continuous stepwise LPE method of one MOF **B** on the surface of a previously-deposited, highly-crystalline seed MOF **A** was applied. As a model for separating applications, the smaller pore opening analogue was chosen as the particular MOF **B**, and it was fabricated on top of some larger pore opening analogue (MOF **A**) to obtain the hybrid function of size exclusion in adsorption process.

Herein, **Zn-DM** (or **Zn-ME**) was selected as the core MOF **A** component because of the favourable continuous LPE growth behaviour, as described above, combined with the wider pore opening window in comparison to the other MOF analogues. After 20 initial deposition cycles of the wide pore core component **A**, the narrower pore shell component **B** (**Zn-ME**, **Zn-MP** and) **Zn-MI** was deposited on top of the pre-deposited **A** (**Zn-DM**) for an additional 20 cycles. This resulted in 40-cycles **B@A** heterostructured **Zn-L** films (which exhibit similar overall thickness as the 40-cycles homostructured reference **Zn-DM** film discussed in the previous section). The XRD patterns of the heteroepitaxial **B@A** films (Figure 2.19) show a high signal-to-noise ratio, which indicates the high degree of crystallinity. According to the same unit cell parameter of the two analogous MOF components **A** and **B**, a single phase is indexed in the XRD patterns, which agrees with the idea of lattice matching in the heteroepitaxial growth.

In-situ monitoring of the QCM frequency changing as a function of the LPE deposition time illustrates the total growth behaviour of the heteroepitaxial **B@A** films. A continuous linear growth is observed if the bulkiness of the substituent groups at the H₂L linkers within the core (**A**) and the shell (**B**) are only slightly different (for example, **Zn-ME@Zn-DM**). Two distinct linear-growth regimes (different slopes) are found if the bulkiness of the linkers within the core and the shell MOF are more different. Interestingly, the film growth rate of **Zn-MI** on the pre-deposited **Zn-DM** (or **Zn-ME**) film is increased approximately two-fold with respect to the homostructured **Zn-MI** film deposited without seeding layer (Figure 2.20). This observation highlights the enhanced MOF film growth by means of the heteroepitaxial growth on the highly-crystalline, pre-formed MOF film.

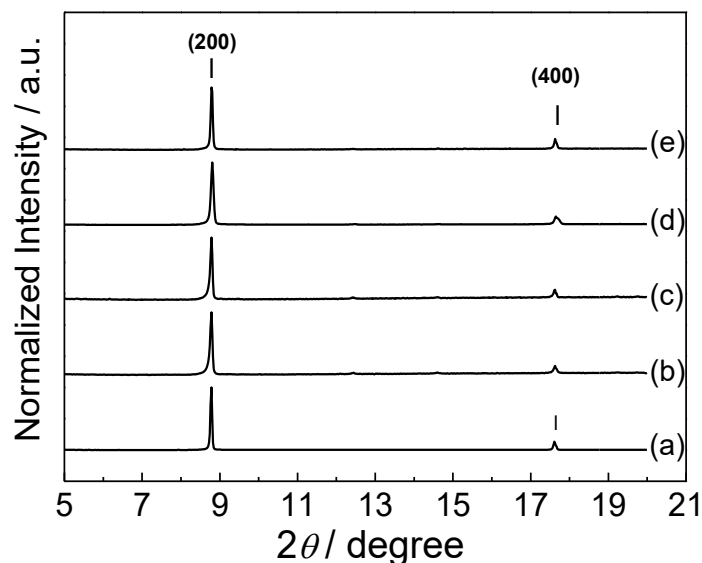


Figure 2.19 XRD patterns of the heteroepitaxial **B@A Zn-L** films (indexed by the \mid symbol) fabricated by the continuous stepwise deposition of **B** 20 cycles on top of pre-deposited **A** 20 cycles at 40°C on the $-\text{COOH}$ functionalized QCM substrates of (a) **Zn-ME@Zn-DM**, (b) **Zn-MP@Zn-DM**, (c) **Zn-MI@Zn-DM**, (d) **Zn-MP@Zn-ME** and (e) **Zn-MI@Zn-ME**. Each deposition cycle consists of a continuous flow of the solutions of zinc SBU 10 min/ethanol 5 min/ H_2L linker 10 min/ethanol 5 min.

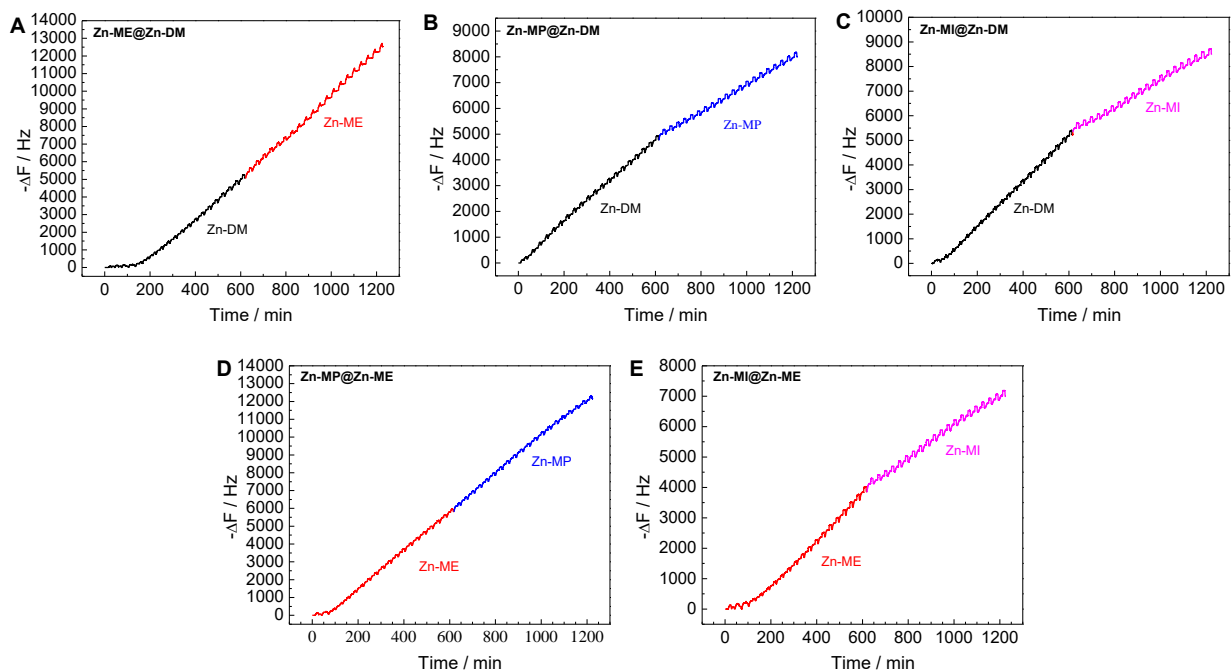


Figure 2.20 In situ monitoring of the QCM frequency changing as a function of deposition time during the continuous stepwise deposition of the heteroepitaxial **B@A Zn-L** films corresponding to the XRD patterns in Figure 2.19.

Closer inspection to the heteroepitaxial growth of an example of heterostructured **Zn-MP@Zn-DM** film, intensity of the 200 XRD peak of the **Zn-MP@Zn-DM** film (**B@A**) is increased from the 20-cycles pre-deposited, homostructured **Zn-DM** film (**A**) indicates the successful formation of the desired **B@A** film (Figure 2.21a). An inspection of the SEM image of the core MOF **A** after 20 deposition cycles reveals the (expected) incomplete surface coverage of the seed crystals as a result of the island growth mode (Figure 2.21b). The subsequent heteroepitaxial growth (20 cycles) of the shell component **B** can occur at all facets of the seeding core crystals **A** as a consequence of the isotropic cubic lattice of the **Zn-L** MOFs. Consequently, the seeding MOF **A** as a core is completely overgrown by the MOF **B** as a shell resulting in the increasing of the crystallite particle sizes. Eventually, full surface coverage of the MOF crystallites on the substrate is achieved (intergrown MOF **B** shell crystals; Figure 2.21c). Moreover, the orientation of the shell part **B** maintains the (100)-related preferred orientation of the MOF **A**.

These results nicely emphasize the advantage of the continuous stepwise LPE method in the fabrication of the hybridized **B@A** films consisting of some MOF component **B** (e.g. **Zn-MI**), which is difficult (or even impossible) to deposit as phase-pure and highly-crystalline homostructured component **A** (as discussed in section 2.2.1) In other words, certain nucleation problems of some MOF **B** on a given substrate can be overcome by selecting an appropriate seed MOF **A**.

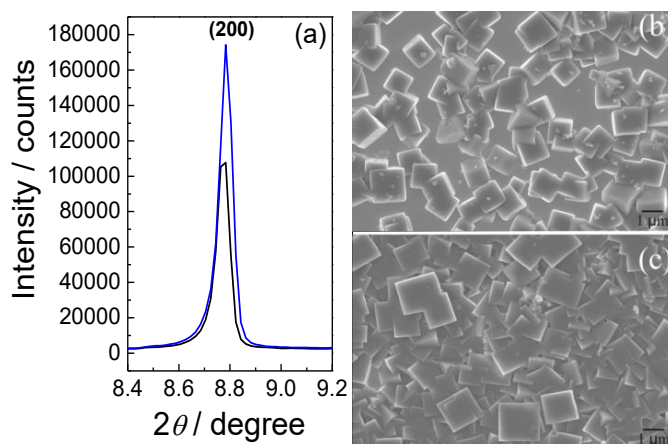


Figure 2.21 (a) Intensity comparison at the (200) XRD diffraction of the homostructured 20-cycles **Zn-DM** film (black) and the heterostructured 20-cycles **Zn-MP** on the pre-deposited 20-cycles **Zn-DM** film (blue); (b) and (c) show the corresponding SEM images. Reprinted with permission. Copyright © 2013 WILEY-VCH Verlag GmbH & Co. KGaA.³⁶

2.2.4 Adsorption properties of heterostructured Zn-L films

An environmentally-controlled QCM instrument is used to investigate the sorption properties of the heterostructured **B@A Zn-L** films and the results are compared with the corresponding homostructured film component for clarification. In general, the alcohol sorption isotherm curves (i.e. methanol, ethanol and isopropanol) of the films match the expected Langmuir type I isotherm shape (characteristic microporosity) if the size of the adsorbed alcohol molecules is smaller than the pore opening window of the MOF. If the size of the adsorbed molecules is bigger than the pore opening window of the MOF, there is no significant adsorption is observed.

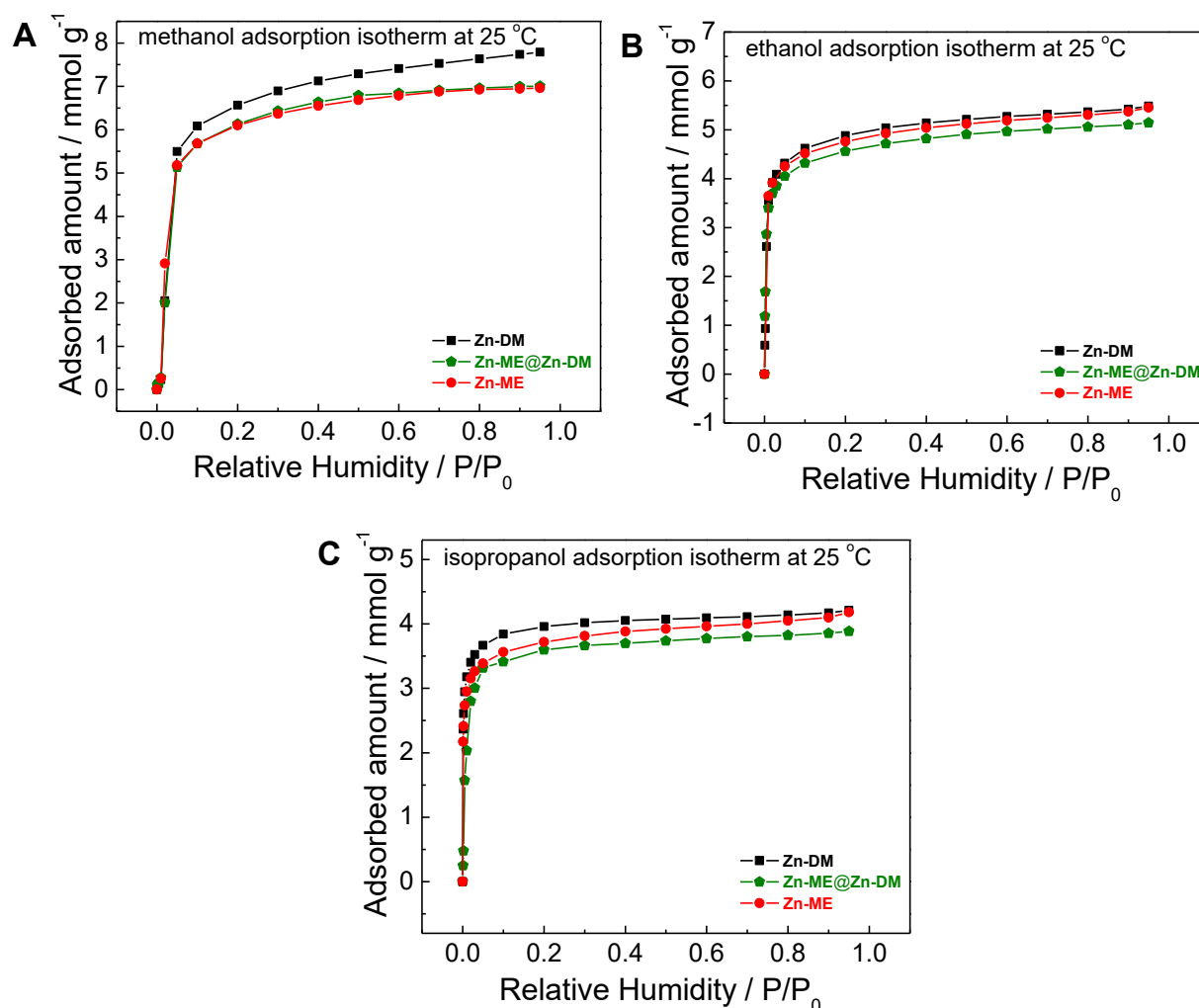


Figure 2.22 (A) methanol (B) ethanol and (C) isopropanol adsorption isotherm at 25 °C using an environmentally controlled QCM of the heteroepitaxial **Zn-ME@Zn-DM** film in comparison with its corresponding homostructured-film components.

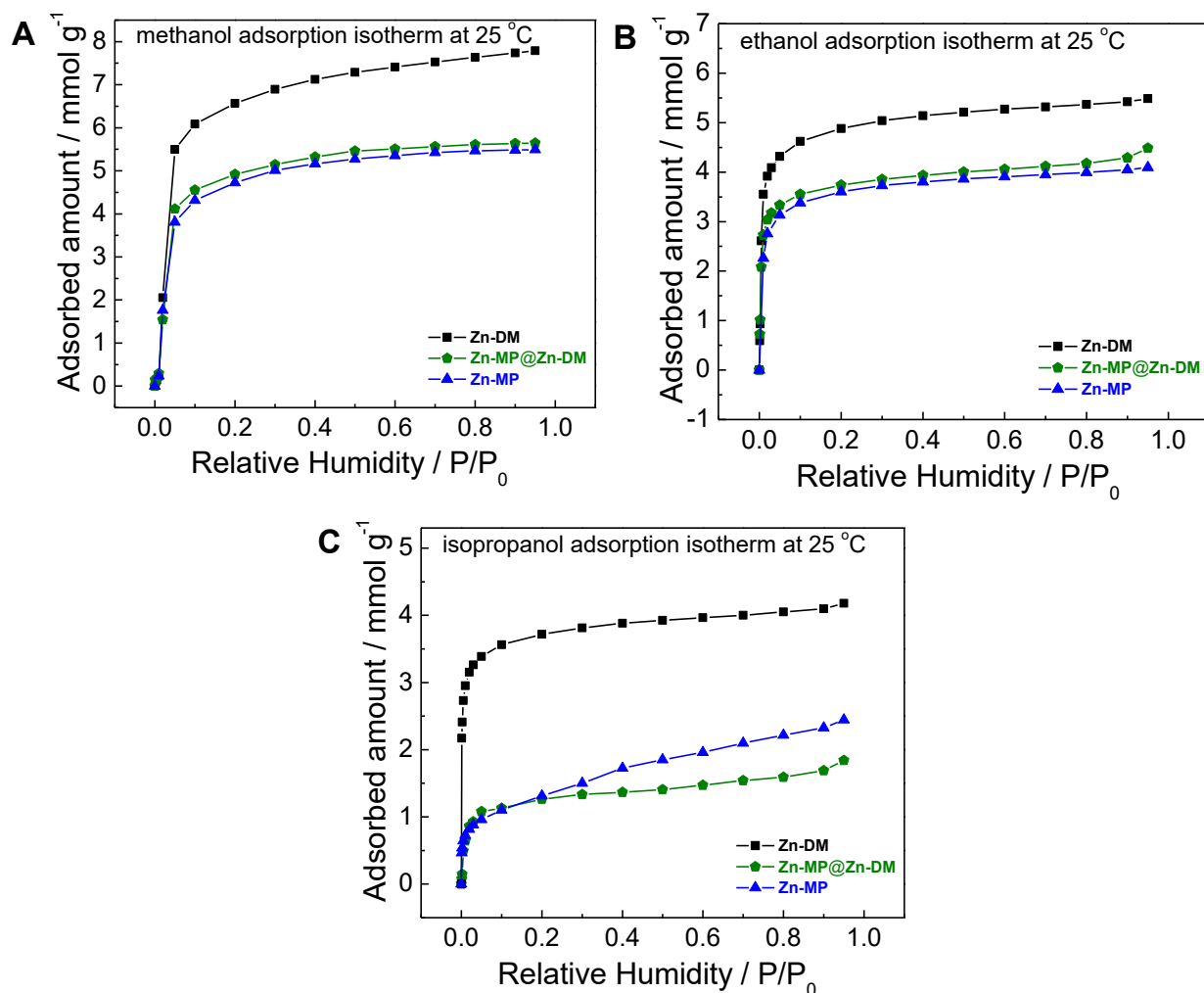


Figure 2.23 (A) methanol (B) ethanol and (C) isopropanol adsorption isotherm at 25 °C using an environmentally controlled QCM of the heteroepitaxial **Zn-MP@Zn-DM** film in comparison with its corresponding homostructured-film components.

For the heterostructured **Zn-ME@Zn-DM** and **Zn-MP@Zn-DM** films, which both components exhibit a high crystallinity when fabricated as such homostructured films, the alcohol adsorptions of these **B@A** films do not fall between the properties of the respective homostructured core and shell MOF films, as observed in the cases of the corresponding heterostructured layer-pillar-type SURMOFs in our recent work.³⁴ Instead, the saturation amounts of these **B@A** films are approximately equal to the saturation amount of the respective homostructured shell component MOF (**B**) (Figure 2.22 and 2.23). At present, we do not have additional evidence suitable for an explanation as to

why the saturation uptakes of the **Zn-ME@Zn-DM** and **Zn-MP@Zn-DM** films are dominated by the property of the shell component **Zn-ME** and **Zn-MP**, respectively. However, it may be related to an enhanced heteroepitaxial growth rate of the **Zn-ME** and **Zn-MP** films from the further growth from the pre-formed nucleation of the **Zn-DM** seeding (core) layer, leading to the more contribution of the shell components within the heterostructured films.

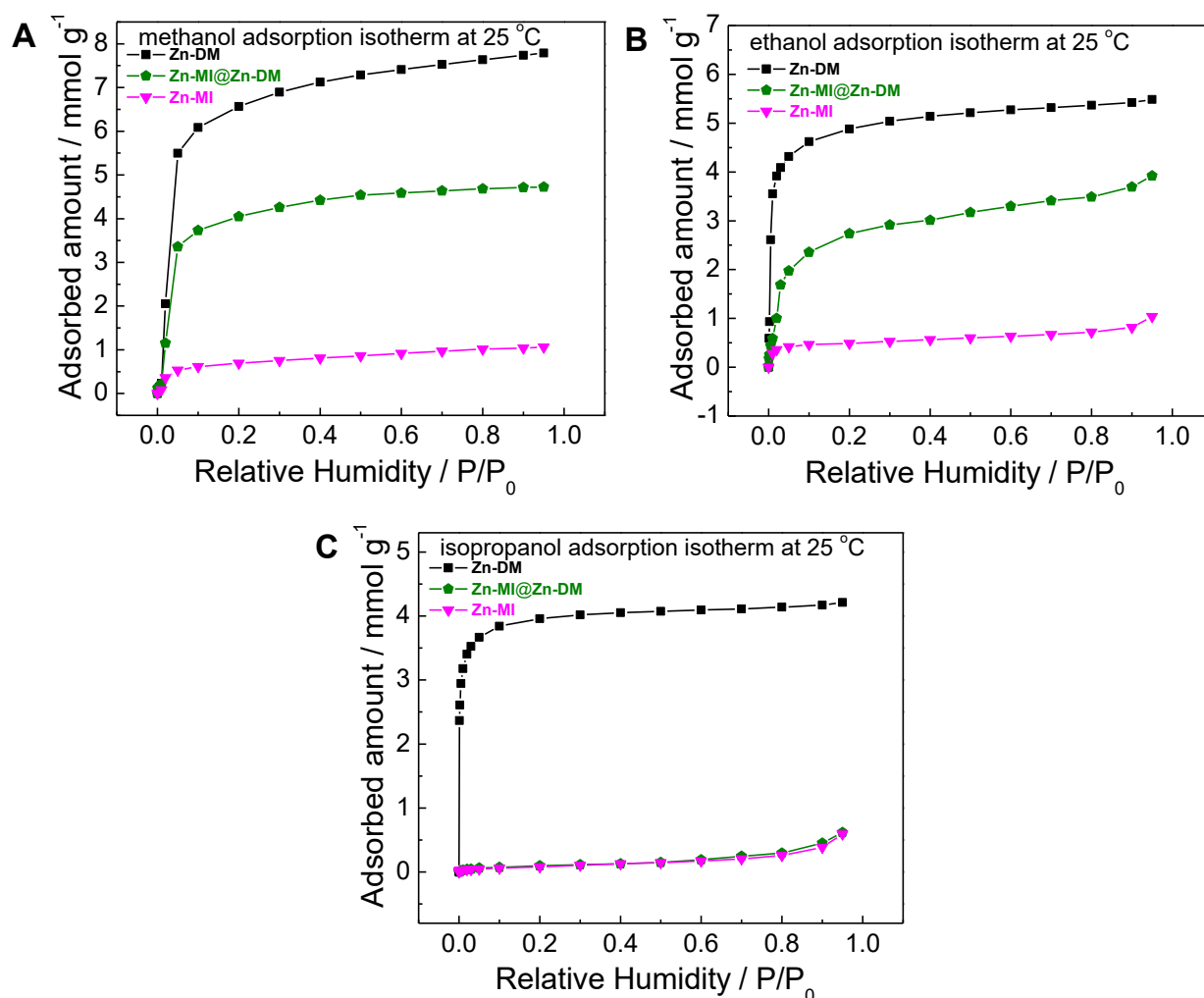


Figure 2.24 (A) methanol (B) ethanol and (C) isopropanol adsorption isotherm at 25 °C using an environmentally controlled QCM of the heteroepitaxial **Zn-MI@Zn-DM** film in comparison with its corresponding homostructured-film components.

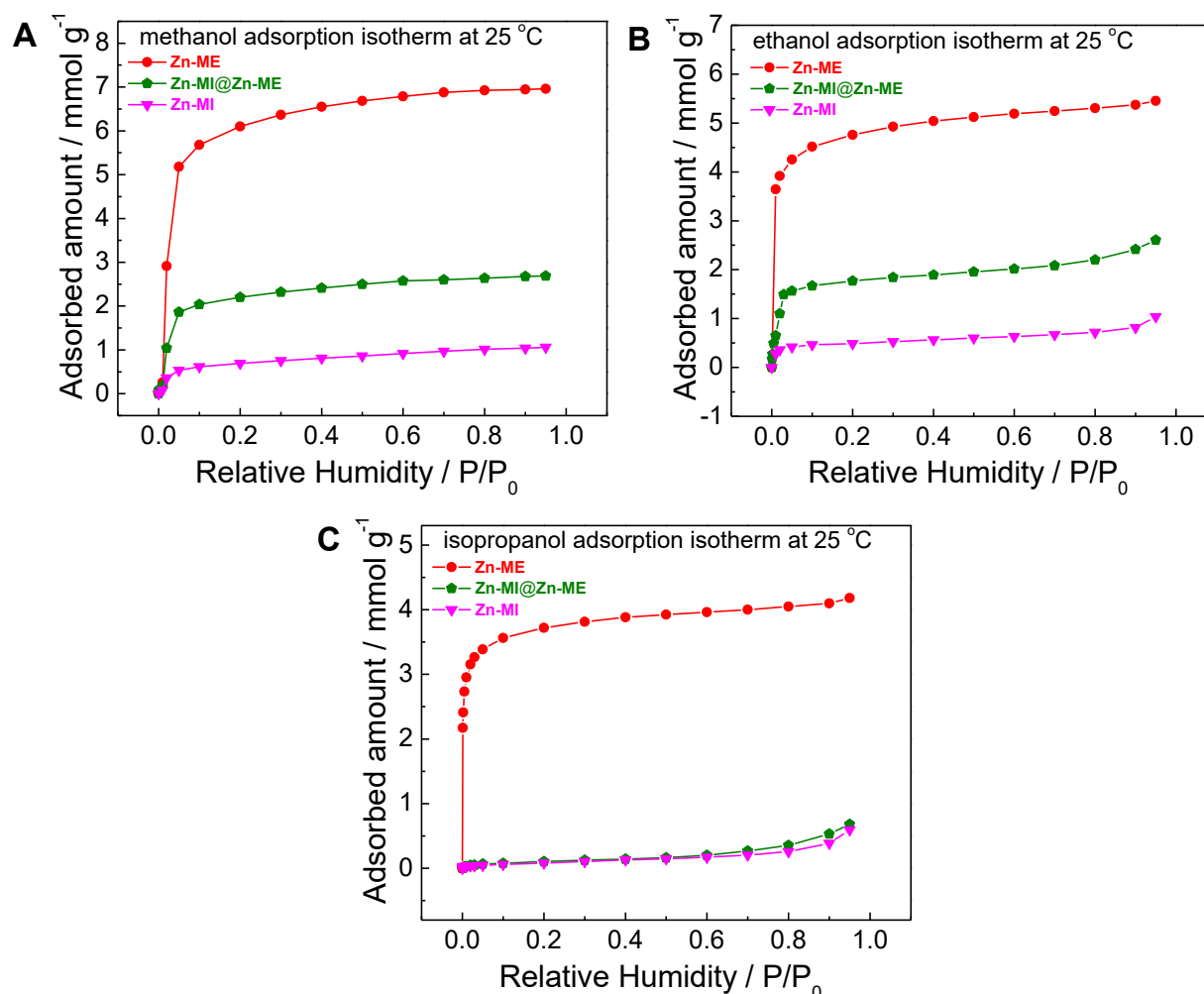


Figure 2.25 (A) methanol (B) ethanol and (C) isopropanol adsorption isotherm at 25 °C using an environmentally controlled QCM of the heteroepitaxial **Zn-MI@Zn-ME** film in comparison with its corresponding homostructured-film components.

In the cases of **Zn-MI@Zn-DM** and **Zn-MI@Zn-ME** films (Figure 2.24 and 2.25), the alcohol adsorptions of the heterostructured films are ranged in between the adsorption of the homostructured components. It is noteworthy that the total methanol (and ethanol) adsorption capacity of **Zn-MI@Zn-DM** and **Zn-MI@Zn-ME** films is significantly higher than the total adsorption of the homostructured **Zn-MI** film, highlighting the improvement of crystallinity by mean of the heteroepitaxial growth. Interestingly, these **Zn-MI@Zn-DM** and **Zn-MI@Zn-ME** films allow methanol and ethanol molecules but not isopropanol molecules to be adsorbed, indicating the molecular sieve function of the outer component

Zn-MI when grown in high crystallinity. Herein, the adsorption data clearly indicate the successful fabrication of a very high crystallinity **Zn-MI** (MOF **B**) by the heteroepitaxial growth on top of the existing crystalline seed **Zn-DM** or **Zn-ME** (MOF **A**) in the core-shell **B@A** fashion, but not as a mixing of separate crystals of the two components on the substrate surface. In other words, the core MOF **A** is nicely imbedded into a matrix of densely intergrown MOF **B** shell crystals without the presence of separate crystals **A** or **B** or **B@A** islands or platelets on the substrate surface. From the adsorption data, we conclude that the larger pore opening windows present in MOF film **A** are fully covered by the smaller pore opening windows of MOF film **B**. Only in such a case can one expect the proper function of the shell MOF **B** as the selective layer to allow size exclusion and only small enough probe molecules to be adsorbed inside the MOF films. For more details in selective adsorption properties of the heterostructured **Zn-L** films are discussed further in Chapter 4.

2.2.5 Moisture Tolerance of Zn-L films

For practical use as MOF-based devices, the stability of MOF materials over moisture at ambient conditions is one of important concerns. Herein, the homostructured **Zn-DM** (**A**) and the heterostructured **Zn-MI@Zn-DM** (**B@A**) films are selected as representatives for the moisture tolerant test of the fabricated **Zn-L** films by performing a series of water vapour sorption isotherm measurements at 25°C using the QCM instrument. Both of the **Zn-DM** and the **Zn-MI@Zn-DM** films exhibit type III isotherms, indicating that water molecules are not adsorbed up to the P/P_0 of 0.6 (60% relative humidity). However, the multilayer condensation is observed when operating at higher relative humidity than 60% (Figure 2.26). There are no significant differences in the crystallinity of the **Zn-L** films after two complete adsorption/desorption treatments with water vapour at 60% relative humidity (Figure 2.27). These results suggest the robustness of the **Zn-L** films over moisture, which provides the possibility for practical applications at ambient conditions (relative humidity up to 60 % at room temperature).

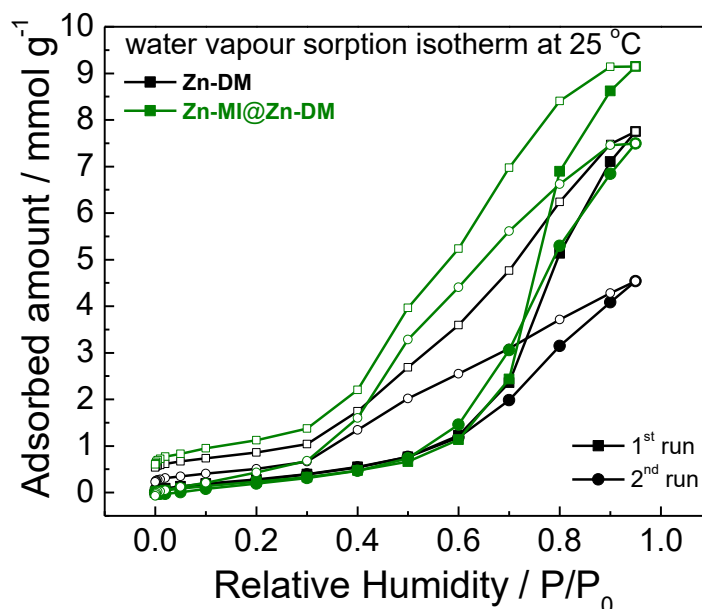


Figure 2.26 Water vapour sorption isotherm at 25°C of the homostructured **Zn-DM** (black curves) and the heterostructured **Zn-MI@Zn-DM** films (green curves). The square and the circle symbols represent the first and the second run of the water vapour isotherms, respectively. The closed and open symbols indicate the adsorption and desorption measurements, respectively.

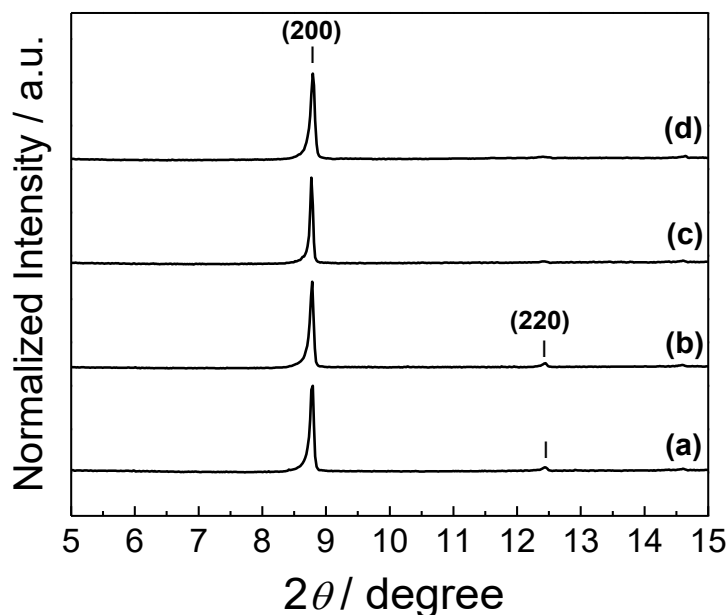


Figure 2.27 XRD patterns of the homostructured **Zn-DM** after (a) the first run and (b) the second run of water vapour sorption isotherm and the heterostructured **Zn-MI@Zn-DM** film after (c) the first run and (b) the second run of water vapour sorption isotherm indicate the maintain of the crystalline **Zn-L** thin films (indexed by the \mid symbol).

However, after the moisture treatment at a high relative humidity of 95%, the methanol uptake of the reference homostructured **Zn-DM** film was reduced to approximately 48% of the total adsorbed amount observed prior to the moisture treatment (Figure 2.28). This reduction in adsorption capacity can be explained by the gradual hydrolysis of the Zn—O coordinative bonds and, hence, by partial framework collapse. Interestingly, the heteroepitaxial **Zn-MI@Zn-DM** film shows the reduction of methanol adsorption capacity of only 20% after the moisture treatment at 95% relative humidity, indicating the higher stability over moisture of **Zn-MI** than **Zn-DM** as the outer component within the films. Due to the bulkier alkyl substituents located at the pyrazolate ring and pointing towards the labile Zn—O coordinative bonds of the H₂MI linker, the better protection against nucleophilic attacks (e.g. hydrolysis with water) can be observed. This investigation again emphasizes the merits of fabricating the hybrid **B@A** MOF films.

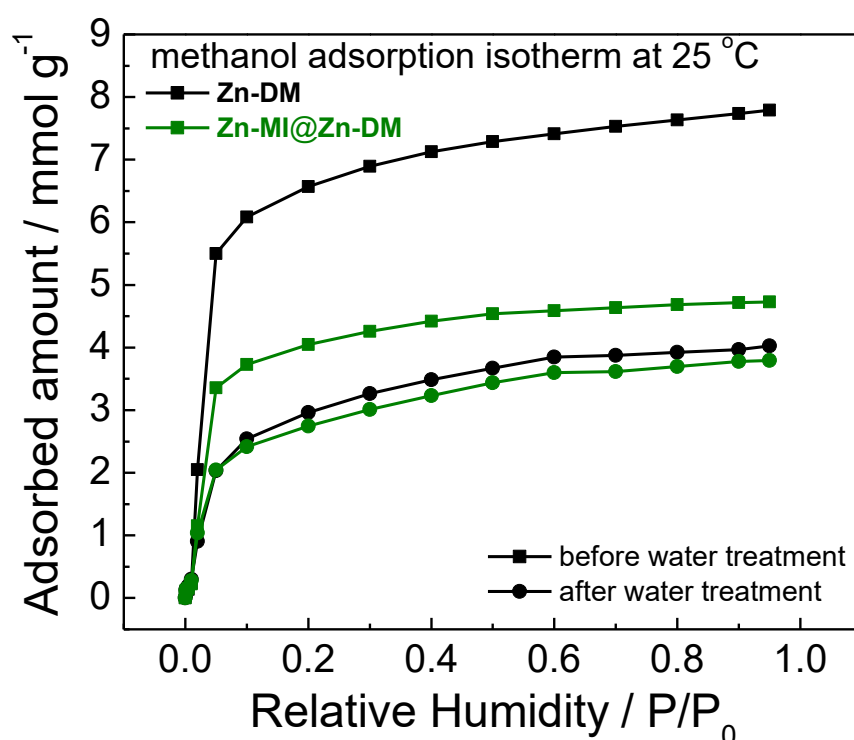


Figure 2.28 Methanol sorption isotherm at 25°C of the selected homostructured **Zn-DM** (black curves) and the heterostructured **Zn-MI@Zn-DM** films (green curves) after two-completed cycles of water vapour sorption isotherm treatments in comparison with the corresponding isotherms before the treatment.

2.3 Summary

The continuous stepwise LPE process provides an outstanding improvement in the crystallinity of the MOF-5 isotype carboxypyrazolate-type **Zn-L** thin films. The in-situ monitoring of the mass uptake during LPE growth by QCM serves as a guideline for control of the film growth, which strongly influences the observed crystallinity of the products. The schematic illustration (Figure 2.29) describes the summarized messages of the fabrication of both the homostructured films **A** and the heteroepitaxial **B@A** films using the continuous stepwise LPE method. **Zn-MI** films, which exhibit a moderate crystallinity when grown as a homostructured film **A**, can be deposited with very high crystallinity using the heteroepitaxial growth of this MOF as component **B** on top of the previously deposited highly crystalline component **A**. The outer component **B** begins to grow on all facets of the seeding component **A** until providing the fully covered core-shell heteroepitaxial **B@A** films. By selection of the MOF components, the heterostructured **Zn-MI@Zn-DM** film reveals hybrid functionality and exhibits good adsorption selectivity based on the size selection by the small pore opening window of **Zn-MI** as the shell component. Therefore, methanol and ethanol are selectively adsorbed over isopropanol. Moreover, the adsorbed molecules can be stored with higher capacity within the heterostructured film as a result of the excellent crystallinity of both core and shell components compared to the poor crystallinity of the **Zn-MI** deposited as a single, homostructured film. This heterostructured **Zn-L** film could be one of the promising candidates for use in selective adsorption applications because of its reasonable adsorption capacity, excellent size-selective adsorption of different alcohols and high degree of moisture-tolerance. Based on the lattice matching concept of the stepwise heteroepitaxial growth, more complex structured multi-functionalized MOF films could be achieved in this well-controlled manner, which open the path for specific applications.

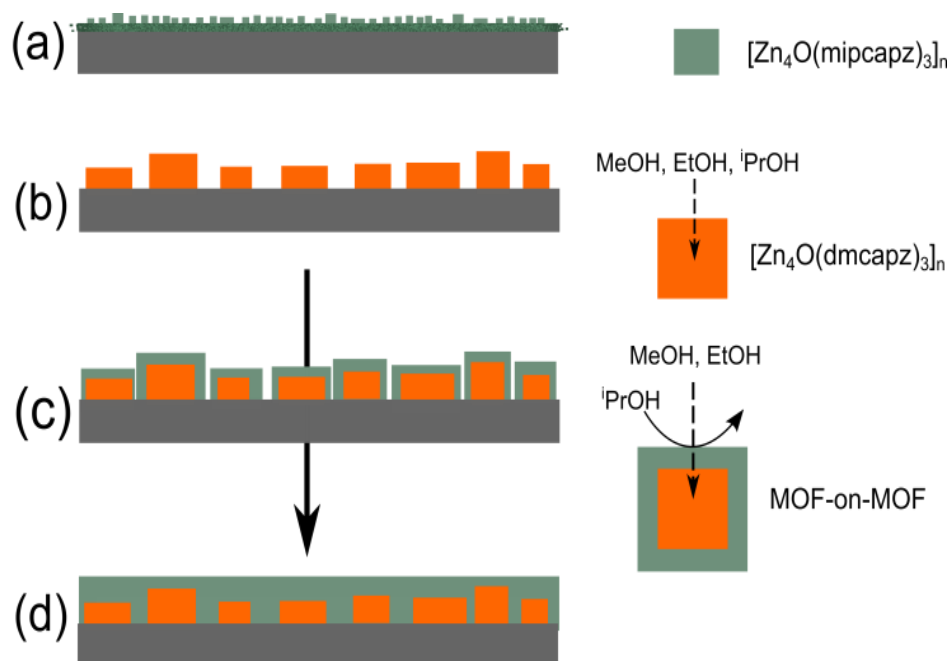


Figure 2.29 The schematic illustration of the **Zn-L** film growths by the continuous stepwise LPE deposition indicates (a) the moderately crystalline homostructured **Zn-MI** film after 40 deposition cycles, (b) the highly crystalline **Zn-DM** film after 20 deposition cycles acting as the pre-deposited core component, (c) the early stage of a heteroepitaxial growth of the **Zn-MI** shell component on top of the **Zn-DM** core and (d) the fully covered heteroepitaxial **Zn-MI@Zn-DM** films showing high crystallinity and selective adsorption of methanol and ethanol over isopropanol molecules based on the size selection by the pore opening window of the shell **Zn-MI** component. Copyright © 2013 WILEY-VCH Verlag GmbH & Co. KGaA.³⁶

2.4 References

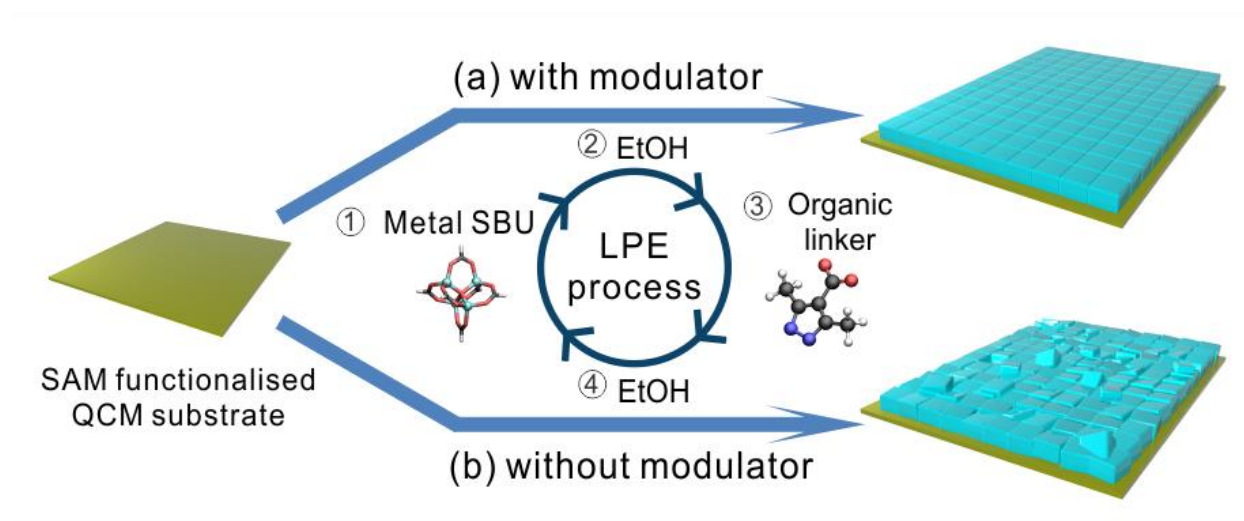
1. O. M. Yaghi, M. O'Keeffe, N. W. Ockwig, H. K. Chae, M. Eddaoudi and J. Kim, *Nature*, 2003, **423**, 705–714.
2. S. Kitagawa, R. Kitaura and S.-i. Noro, *Angew. Chem. Int. Ed.*, 2004, **43**, 2334–2375.
3. G. Férey, C. Mellot-Draznieks, C. Serre and F. Millange, *Acc. Chem. Res.*, 2005, **38**, 217–225.
4. Metal Organic Frameworks Themed Issue, *Chem. Soc. Rev.*, 2009, **38**, 1201–1508.
5. 2012 Metal Organic Frameworks Issue, *Chem. Rev.*, 2012, **112**, 673–1268.

6. Metal–Organic Frameworks (MOFs), *Chem. Soc. Rev.*, 2014, **43**, 5415–6172.
7. Metal-organic frameworks and porous polymers – current and future challenges, *Chem. Soc. Rev.*, 2017, **46**, 3097–3484.
8. H. Li, M. Eddaoudi, M. O’Keeffe and O. M. Yaghi, *Nature*, 1999, **402**, 276–279.
9. M. Eddaoudi, J. Kim, N. Rosi, D. Vodak, J. Wachter, M. O’Keeffe and O.M. Yaghi, *Science*, 2002, **295**, 469–472.
10. J. A. Greathouse and M. D. Allendorf, *J. Am. Chem. Soc.*, 2006, **128**, 10678–10679.
11. L. Hou, Y.-Y. Lin and X.-M. Chen, *Inorg. Chem.*, 2008, **47**, 1346–1351.
12. M. Tonigold, Y. Lu, B. Bredenkötter, B. Rieger, S. Bahnmüller, J. Hitzbleck, G. Langstein and D. Volkmer, *Angew. Chem. Int. Ed.*, 2009, **48**, 7546–7550.
13. C. Montoro, F. Linares, E. Q. Procopio, I. Senkovska, S. Kaskel, S. Galli, N. Masciocchi, E. Barea and J. A. R. Navarro, *J. Am. Chem. Soc.*, 2011, **133**, 11888–11891.
14. A. Bétard, S. Wannapaiboon and R. A. Fischer, *Chem. Commun.*, 2012, **48**, 10493–10495.
15. S. Wannapaiboon, “Deposition of metal—organic framework thin films: their characterizations by X-ray diffraction and accessing the sorption properties by quartz crystal microbalance”, Ruhr-University of Bochum, 2013.
16. A. Bétard and R. A. Fischer, *Chem. Rev.*, 2012, **112**, 1055–1083.
17. O. Shekhah, J. Liu, R. A. Fischer and C. Wöll, *Chem. Soc. Rev.*, 2011, **40**, 1081–1106.
18. M. D. Allendorf, R. J. T. Houk, L. Andruszkiewicz, A. A. Talin, J. Pikarsky, A. Choudhury, K. A. Gall and P. J. Hesketh, *J. Am. Chem. Soc.*, 2008, **130**, 14404–14405.
19. G. Lu and J. T. Hupp, *J. Am. Chem. Soc.*, 2010, **132**, 7832–7833.
20. J. Gascon and F. Kapteijn, *Angew. Chem. Int. Ed.*, 2010, **49**, 1530–1532.
21. A. Bétard, H. Bux, S. Henke, D. Zacher, J. Caro and R. A. Fischer, *Microporous Mesoporous Mater.*, 2012, **150**, 76–82.
22. A. S. Münch, J. Seidel, A. Obst, E. Weber and F. O. R. L. Mertens, *Chem. Eur. J.*, 2011, **17**, 10958–10964.

23. B. Liu, M. Ma, D. Zacher, A. Bétard, K. Yussenko, N. Metzler-Nolte, C. Wöll and R. A. Fischer, *J. Am. Chem. Soc.*, 2011, **133**, 1734–1737.
24. O. Shekhah, H. Wang, D. Zacher, R. A. Fischer and C. Wöll, *Angew. Chem. Int. Ed.*, 2009, **48**, 5038–5041.
25. D. Zacher, R. Schmid, C. Wöll and R. A. Fischer, *Angew. Chem. Int. Ed.*, 2011, **50**, 176–199.
26. D. Zacher, K. Yussenko, A. Bétard, S. Henke, M. Molon, T. Ladnorg, O. Shekhah, B. Schüpbach, T. de los Arcos, M. Krasnopolski, M. Meilikhov, J. Winter, A. Terfort, C. Wöll and R. A. Fischer, *Chem. Eur. J.*, 2011, **17**, 1448–1455.
27. B. Liu, M. Tu, D. Zacher and R. A. Fischer, *Adv. Funct. Mater.*, 2013, **23**, 3790–3798.
28. M. Meilikhov, S. Furukawa, K. Hirai, R. A. Fischer and S. Kitagawa, *Angew. Chem. Int. Ed.*, 2013, **52**, 341–345.
29. O. Zybaylo, O. Shekhah, H. Wang, M. Tafipolsky, R. Schmid, D. Johannsmann and C. Wöll, *Phys. Chem. Chem. Phys.*, 2010, **12**, 8092–8097.
30. V. Stavila, J. Volponi, A. M. Katzenmeyer, M. C. Dixon and M. D. Allendorf, *Chem. Sci.*, 2012, **3**, 1531–1540.
31. O. Shekhah, K. Hirai, H. Wang, H. Uehara, M. Kondo, S. Diring, D. Zacher, R. A. Fischer, O. Sakata, S. Kitagawa, S. Furukawa, C. Wöll, *Dalton Trans.*, 2011, **40**, 4954–4958.
32. G. Sauerbrey, *Z. Phys.*, 1959, **155**, 206–222.
33. H. Uehara, S. Diring, S. Furukawa, Z. Kalay, M. Tsotsalas, M. Nakahama, K. Hirai, M. Kondo, O. Sakata and S. Kitagawa, *J. Am. Chem. Soc.*, 2011, **133**, 11932–11935.
34. M. Tu, S. Wannapaiboon and R. A. Fischer, *Dalton Trans.*, 2013, **42**, 16029–16035.
35. S. Wannapaiboon, K. Sumida, K. Dilchert, M. Tu, S. Kitagawa, S. Furukawa and R. A. Fischer, *J. Mater. Chem. A*, 2017, **5**, 13665–13673.
36. S. Wannapaiboon, M. Tu and R. A. Fischer, *Adv. Funct. Mater.*, 2014, **24**, 2696–2705.

Chapter 3

Enhanced properties of MOF thin-films fabricated via a coordination modulation-controlled layer-by-layer process



- The results of this chapter are mainly comprised in and reproduced from the following publication, "S. Wannapaiboon, K. Sumida, K. Dilchert, M. Tu, S. Kitagawa, S. Furukawa and R. A. Fischer, *J. Mater. Chem. A*, 2017, **5**, 13665-13673" with permission from the Copyright © The Royal Society of Chemistry 2017

3.1 Introduction and state of the art

3.1.1 Integration of MOFs with devices by stepwise LPE method and its limitation

Tremendous diversity of components that can be used to construct MOF materials provides opportunities for precise, bottom-up design of both the framework structure and the chemical properties of the pore surfaces.¹⁻³ The potential to incorporate MOFs within functional devices has resulted in their investigation with respect to a wide variety of emerging applications⁴, including electronics and optoelectronics,⁵ proton conduction,⁶ photocatalysis,⁷ sensing,⁸ optics,^{9,10} and biomolecular medicine.¹¹ One of the primary challenges facing the integration of MOFs with real-world technologies is the development of enhanced fabrication techniques that allow MOFs to be structuralized into mesoscopic and macroscopic forms that maximise compatibility with the specific device configurations.¹²⁻¹⁴ Furthermore, a more detailed knowledge regarding the influence of such processing on the properties of MOFs is needed in order to ensure that the performance profile of the bulk material is maintained (or even improved upon) under real-world operation conditions.

In the area of MOF thin-film deposition, stepwise liquid-phase epitaxy (LPE, or layer-by-layer deposition) has emerged as an important concept and method for depositing films on a variety of substrate types. In this technique, solutions containing the metal ion source and organic linkers are alternately provided to a crystal growth surface to allow the MOF to grow with a well-controlled film thickness, surface coverage, and crystal orientation via the ability to explicitly program the number of growth cycles associated with the deposition process.¹⁵⁻¹⁷ Although the utility of this technique has been demonstrated via the successful deposition of several MOF systems, a well-controlled self-terminated “*layer-by-layer*” film growth and high crystal orientation has remained elusive to date for MOF systems beyond the paddlewheel-based MOFs.¹⁸⁻²⁵

Moreover, little attention has been directed toward understanding the underlying mechanisms allowing for fine-tuning of the crystal growth processes in order to achieve even greater control over the quality of the resulting films. Specifically, the application of synthetic strategies known to manipulate the growth of bulk MOF crystals in the context

of thin-film fabrication protocols, and the elucidation of how such optimisations can influence the performance of the resulting films would greatly advance the prospects for the use of MOF-based thin-films in the types of applications mentioned above.

3.1.2 Improvement of MOF features at the molecular self-assembly level by coordination modulation method

Among the synthetic methods available for controlling the growth of MOF crystals, the coordination modulation technique is particularly effective in providing control over the resulting crystal size and the crystal morphology. Here, the addition of a coordination modulator (also called as additive or capping agent), which typically bears the same coordinating functional group as organic linker used to construct the framework (e.g. a carboxylate moiety), gives rise to competitive phenomena in solution as well as alters the coordination equilibrium between the metal-containing node and the organic linker. Consequently, it influences both the crystal nucleation and growth processes.²⁶

The extent to which these processes are affected can be controlled via the coordinating strength of the modulator, as well as through the quantity introduced to the reaction mixture. Indeed, a systematic and rational control over the crystal size across the nanometre-to-micrometre size regimes has been demonstrated in a variety of systems, including $\text{Cu}_3(\text{btc})_2$ (HKUST-1; btc^{3-} = 1,3,5-benzene tricarboxylate),^{27,28} $\text{Cu}_2(\text{bdc})_2(\text{bipy})$ (bdc^{2-} = 1,4-benzenedicarboxylate and bipy = 4,4'-bipyridine),²⁹ $\text{Zn}(\text{Melm})_2$ (ZIF-8; Melm^- = 2-methyl imidazolate),³⁰⁻³² $\text{Zr}_6\text{O}_4(\text{OH})_4(\text{bdc})_6$ (UIO-66)³³⁻³⁴ and its analogues,³⁵ $\text{Zn}_4\text{O}(\text{bdc})_3$ (MOF-5),³⁶ and $(\text{Fe}_3\text{O}_4\text{H})_2(\text{C}_{16}\text{H}_6\text{N}_2\text{O}_8)_3$ (PCN-250; $\text{C}_{16}\text{H}_6\text{N}_2\text{O}_8^{4-}$ = azobenzenetetracarboxylate), and its analogues.³⁷ Note that, the effects of coordination modulator on MOF nucleation and crystal growth rather depend on the type of MOFs and the associated coordination geometry and coordination mode of the metal nodes, especially at the crystal surface. As examples, modulator selectively impedes the coordination equilibrium and framework extension at the functional-related coordination mode leading to the anisotropic growth of $\text{Cu}_2(\text{ndc})_2(\text{dabco})$ (ndc = naphthalene-1,4-dicarboxylate, dabco = 1,4-diazabicyclo[2.2.2]octane), and

consequently different crystal size and morphology. Specifically, nanorod, nanosheet and nanocube crystals are successfully synthesised by adding acetic acid, pyridine and both modulators to the solvothermal reaction mixture, respectively.³⁸ Moreover, the downsizing of MOF crystal by coordination modulation method can regulate the structural flexibility and generate a new intrinsic phenomenon in the coordination frameworks so-called a shape-memory effect.²⁹

Various characterisation methods are conducted in order to get insight into the influences of modulator on the nucleation and crystal growth mechanism. Monte Carlo simulation of Gibbs free energy of the attachment of the coarse-grain standard unit (defined by the shape of the main pore) to form the HKUST-1 framework indicates the design of particles morphology (octahedron, cuboctahedron or cube) and particles size by optimising the amount of modulator (i.e. n-dodecanoic acid).²⁷ Moreover, the in-situ study of MOF formation by time-resolved light scattering^{30,39} and time-resolved X-ray diffraction^{32,35} proposes the modulation mechanisms depending on the types of modulator. The use of modulator with related functionality to the framework linker shows the retardation of coordination and reduces the nucleation rate, so-called “coordination modulation”,³⁵ whereas the other modulator acts as base to accelerate the deprotonation of organic linkers and enhance the nucleation rate, so-called “deprotonation modulation”.³²

The broad applicability of the coordination modulation approach highlights the versatility of the technique, although its utility beyond bulk crystallization solutions, such as in thin-film formation processes, is currently not well established.⁴⁰ According to the literature reported so far, the MOF films have been fabricated via a spin-coating⁴¹ or a dip-coating³⁶ using the pre-formed MOF nanocrystals synthesised by coordination modulation method. However, formation of cracks due to the absence of strong chemical bonds between the MOF nanocrystals and the substrate as well as the poor control of crystal orientation are still the disadvantages of these thin-film processing.^{36,41} The coordination

modulation-assisted solvothermal synthesis provides an improvement of crystal orientation.^{34,40,42} However, only with the intergrowth between MOF particles can lead to fully surface-coverage films. Therefore, studies directed toward assessing the use of coordination modulation as a tool for tuning the properties of thin-films, as well as developing a more thorough understanding of how the modulation process affects the properties of the film are necessary.

3.2 Preparation of bulk Zn-L powders via coordination modulation

In order to evaluate the compatibility of the coordination modulation technique in LPE processing, its success in manipulating the growth of bulk crystals of the $Zn_4O(L)_3$ (**Zn-L**) structure type⁴³⁻⁴⁵ (L^{2-} = 3,5-dialkyl-4-carboxypyrazolate, structure type is firstly demonstrated. In conventional syntheses, the **Zn-L** frameworks are obtained by the reaction of $Zn(NO_3)_2 \cdot 6H_2O$ with the organic linker, H_2L , under reflux in a basic ethanol medium.⁴³ The same frameworks can be prepared by a ligand replacement reaction starting with a solution of pre-formed $Zn_4O(OAc)_6$ clusters, followed by addition of a linker solution to induce framework assembly.⁴⁴ Note that in this case, however, the obtained powders have a comparatively low crystallinity that, for the **Zn-DM** system, yields a significantly lower BET surface area⁴⁵ ($470 \text{ m}^2/\text{g}$) compared to the conventional synthesis ($840 \text{ m}^2/\text{g}$).⁴³

Owing to its experimental convenience and previous successful implementation in the LPE-based deposition of other MOF systems, the ligand replacement approach is selected for further development and integration of the coordination modulation process. Here, the acetic acid modulator is incorporated into the metal cluster solution prior to combination with the organic linker, with the ratio of modulator relative to a fixed concentration of the organic linker (r_L) being varied from $r_L = 1$ to 30. An initial screening shows that in each of the three systems, **Zn-DM**, **Zn-ME**, and **Zn-DE**, the powder X-ray diffraction (PXRD) patterns confirm the formation of the expected framework structure, but with increasing crystallinity and crystallite size (smaller full width at half maximum intensity according to Scherrer Equation) with respect to increasing r_L (see Figure 3.1 – Figure 3.3).

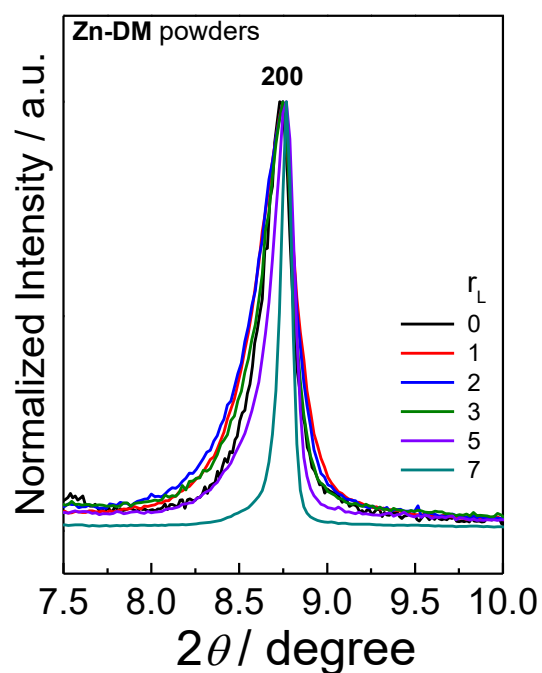
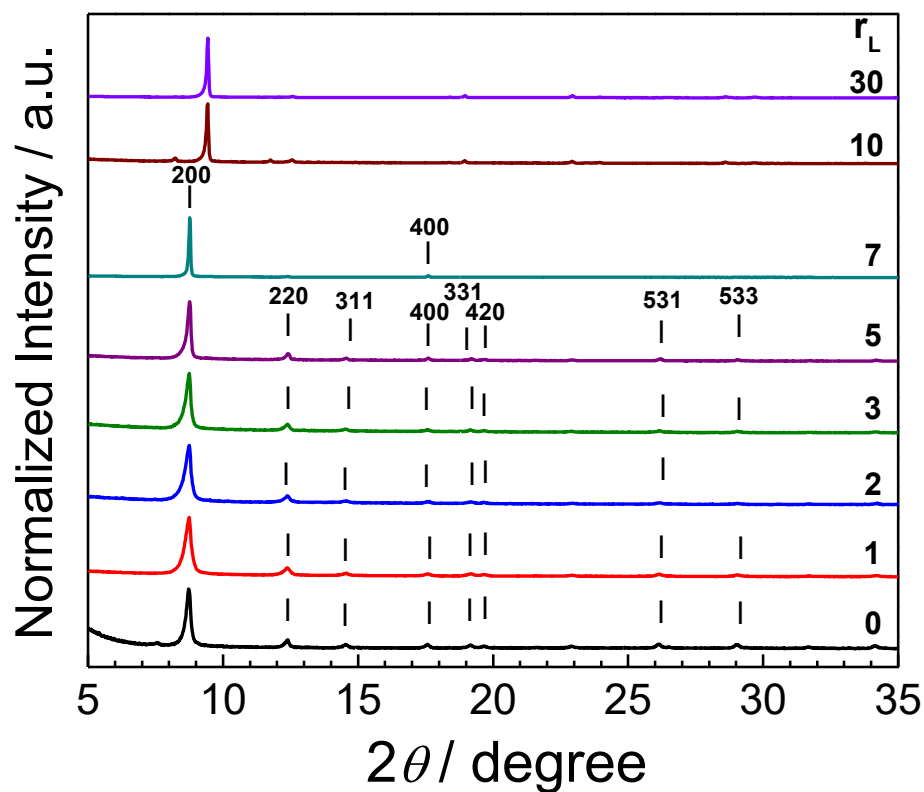


Figure 3.1 PXR D patterns for **Zn-DM** powders synthesized by combining coordination modulation with ligand replacement approach at 50 °C using acetic acid as the modulator with $r_L = 0 - 30$. The numbers in the figure indicate the Miller indices of the diffractions.

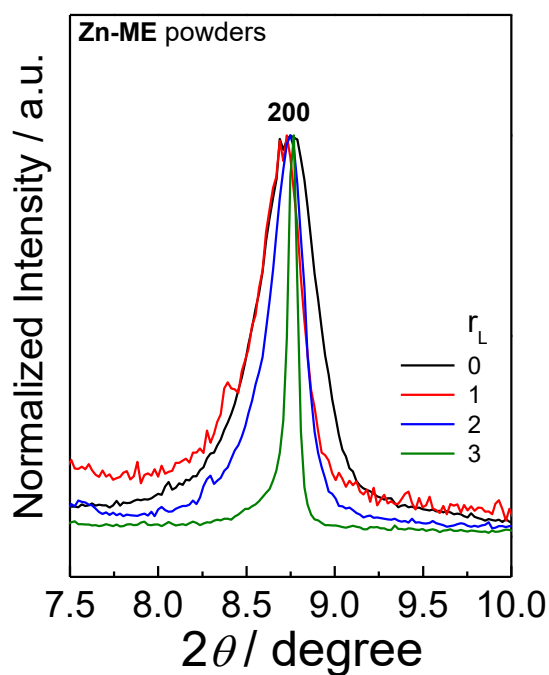
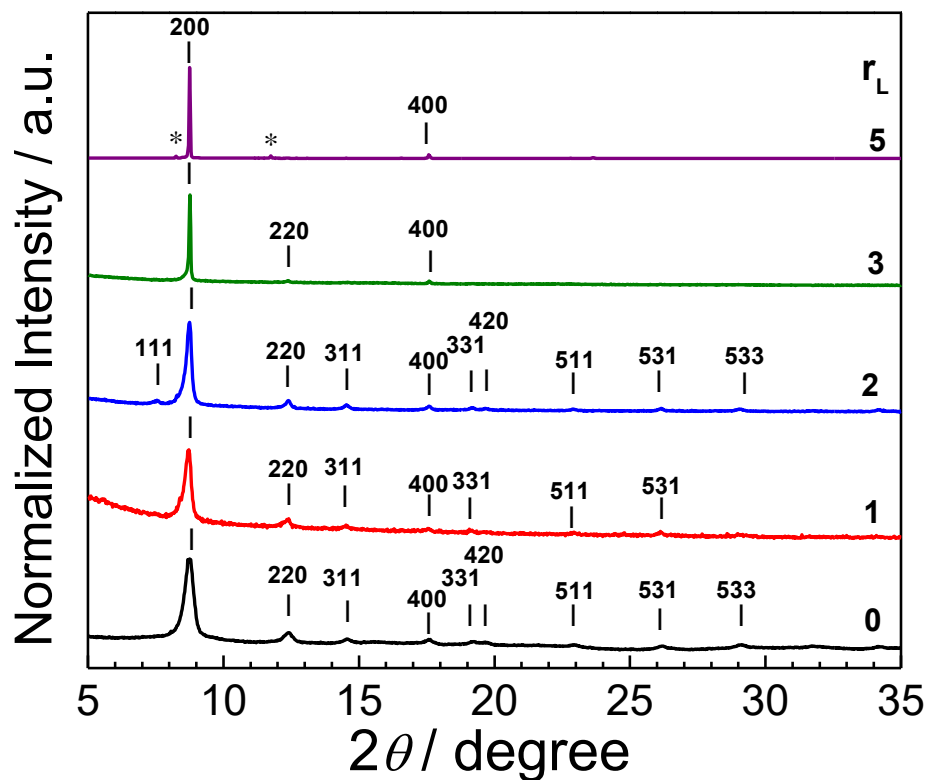


Figure 3.2 PXR D patterns for **Zn-ME** powders synthesized by combining coordination modulation with ligand replacement approach at 50 °C using acetic acid as the modulator with $r_L = 0 - 5$. The numbers in the figure indicate the Miller indices of the diffractions.

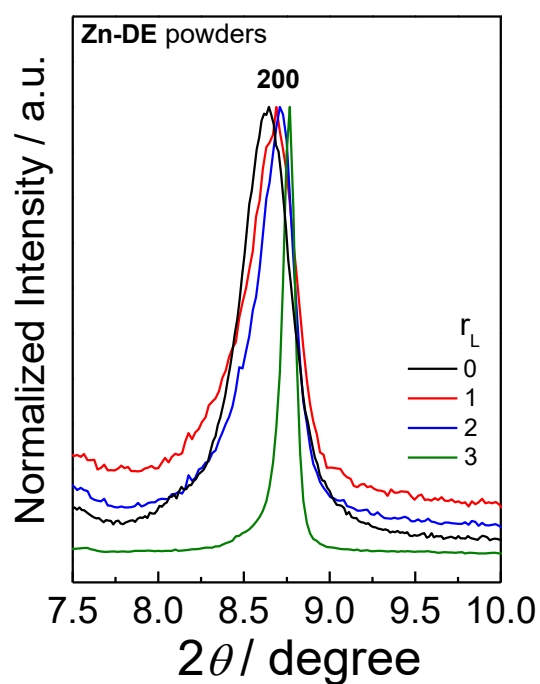
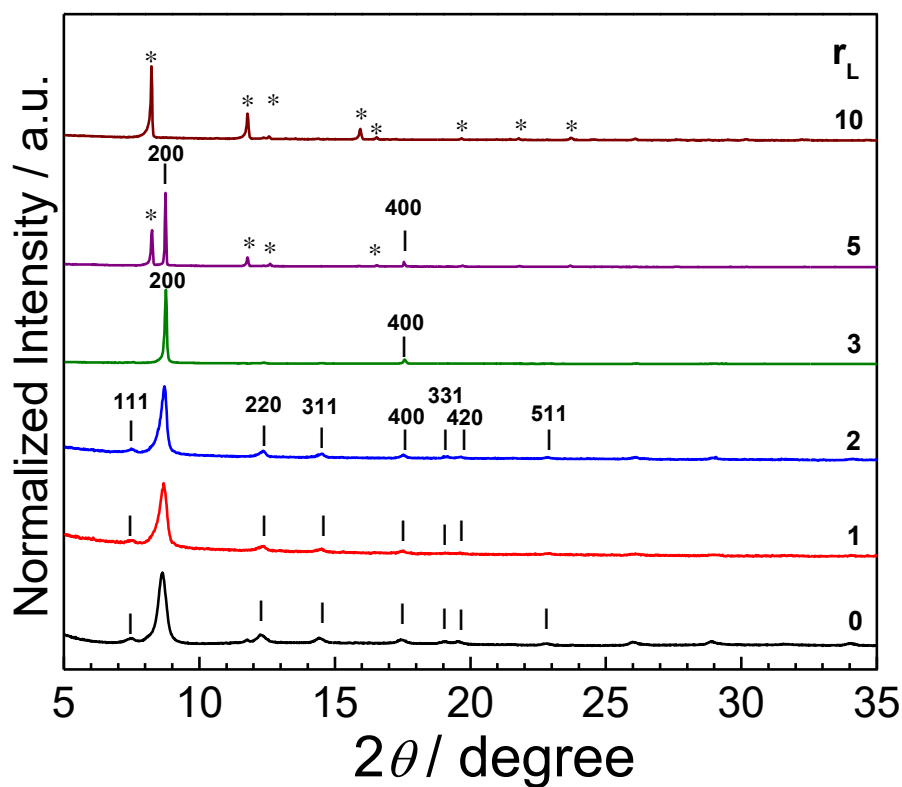


Figure 3.3 PXR D patterns for **Zn-DE** powders synthesized by combining coordination modulation with ligand replacement approach at 50 °C using acetic acid as the modulator with $r_L = 0 - 10$. The numbers in the figure indicate the Miller indices of the diffractions.

Note that, beyond certain levels of modulator addition ($r_L = 7$ for **Zn-DM**, $r_L = 3$ for **Zn-ME** and **Zn-DE**), an uncharacterized impurity phase emerges. The more sophisticated of the side chains at the linkers is, the less amount of acetic acid can be used as modulator to control the formation of phase-pure **Zn-L** powders. This observation potentially arises due to the more prevalent modulator component affecting carboxylate and pyrazolate binding unequally, thereby leading to anisotropic (and lower-symmetry) phases becoming the preferred product.

The enhanced crystallinity is also supported by scanning electron microscopy (SEM), which reveals an increase in the crystal size from the nanometre to micrometre regime, as well as the emergence of crystals exhibiting a well-defined cubic morphology (Figure 3.4 – Figure 3.6), upon increasing r_L . The agreement of XRD and SEM data indicates the role of acetic acid as a coordination modulator which competes with the organic linkers to coordinate with the metal SBU in the equilibrium state. Hence, the degree of nucleation is slowed down and then leads to the further growth of the pre-formed nuclei into the well-crystalline MOF particles.

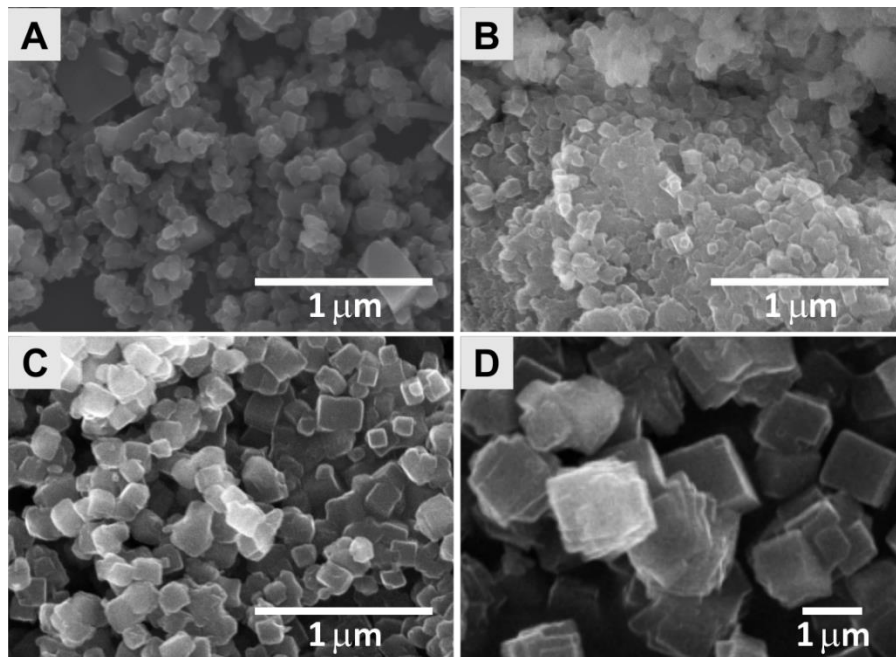


Figure 3.4 SEM images of **Zn-DM** powders synthesized at 50°C by (A) ligand replacement approach without using the modulator ($r_L = 0$) comparing with **Zn-DM** powders synthesized by integrating coordination modulation into the procedure using acetic acid as the modulator with r_L of (B) 1, (C) 3 and (D) 5.

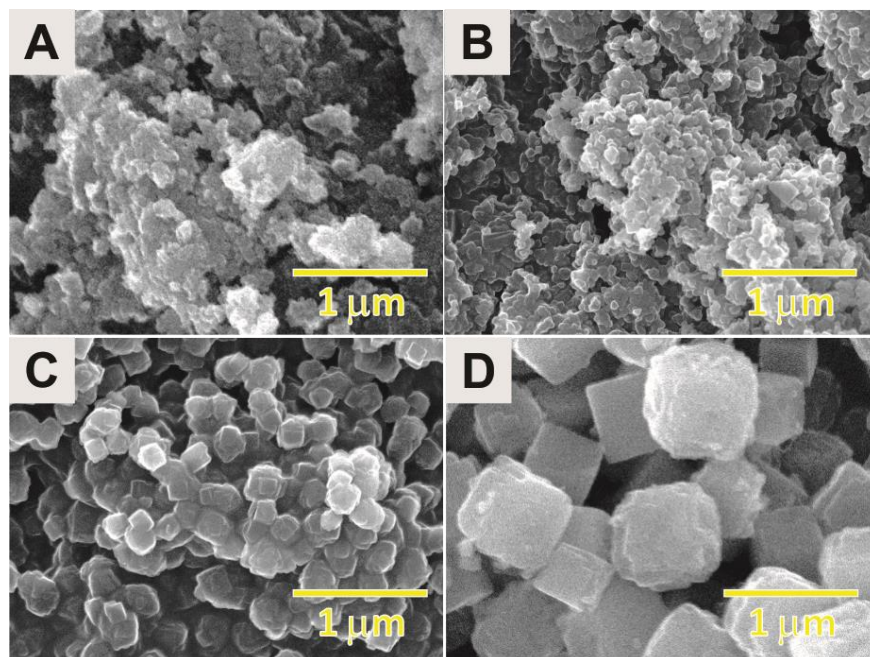


Figure 3.5 SEM images of **Zn-ME** powders synthesized at 50°C by (A) ligand replacement approach without using the modulator ($r_L = 0$) comparing with **Zn-ME** powders synthesized by integrating coordination modulation into the procedure using acetic acid as the modulator with r_L of (B) 1, (C) 2 and (D) 3.

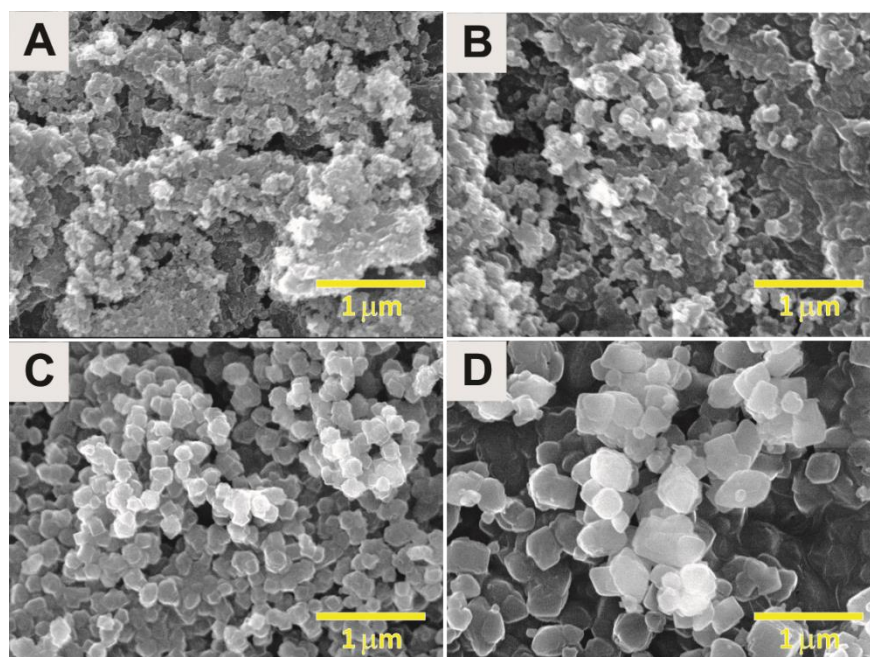


Figure 3.6 SEM images of **Zn-DE** powders synthesized at 50°C by (A) ligand replacement approach without using the modulator ($r_L = 0$) comparing with **Zn-DE** powders synthesized by integrating coordination modulation into the procedure using acetic acid as the modulator with r_L of (B) 1, (C) 2 and (D) 3.

Notably, the BET surface area (calculated according to the N₂ adsorption isotherm at 77 K, see Figure 3.7 – Figure 3.9) is significantly boosted upon introduction of the modulator to the synthetic protocol (see Table 1). In the case of **Zn-DM**, intermediate concentration of the modulator ($r_L = 3$) optimizes the BET surface area to a level even higher than that has been achieved via the conventional synthetic technique mentioned above (940 m²/g), reinforcing the promise in integrating the coordination modulation technique in LPE-based processing of high-quality MOF thin-films. Moreover, the **Zn-L** powders obtained at the use of higher r_L show the less degree of surface condensation at the higher relative pressure ($P/P_0 > 0.8$) due to the bigger and well-defined particles.

Table 1. BET surface areas for **Zn-L** frameworks synthesized in bulk form with variation of the modulator-to-linker ratio (r_L).

Compound	r_L	BET surface area (m² g⁻¹)
Zn-DM	0	470
	1	740
	3	940
	5	920
Zn-ME	0	250
	2	670
Zn-DE	0	180
	1	210
	3	370

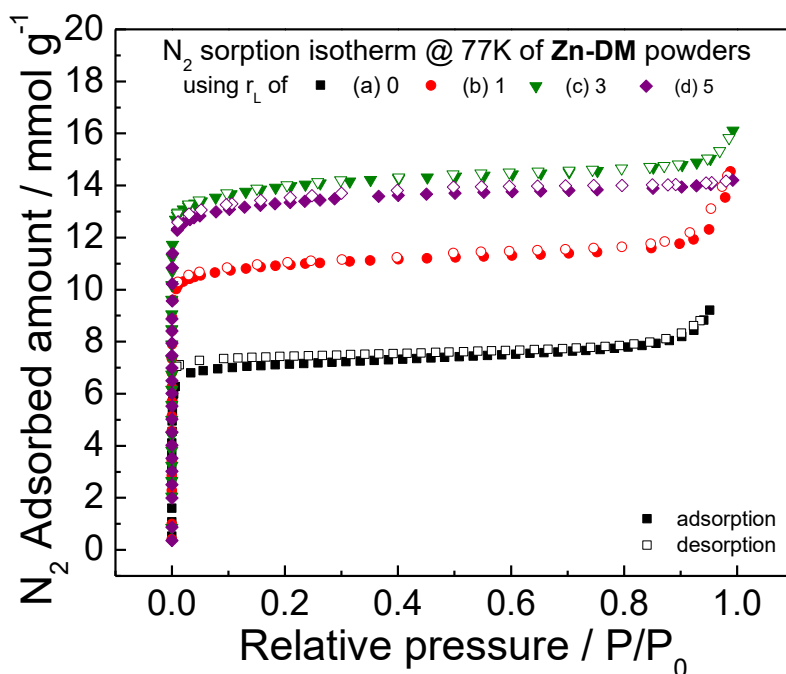


Figure 3.7 N_2 sorption isotherm at 77 K of the **Zn-DM** powders synthesized at 50°C by integrating coordination modulation with the ligand replacement approach using r_L ratio of (a) 0, (b) 1, (c) 3 and (d) 5.

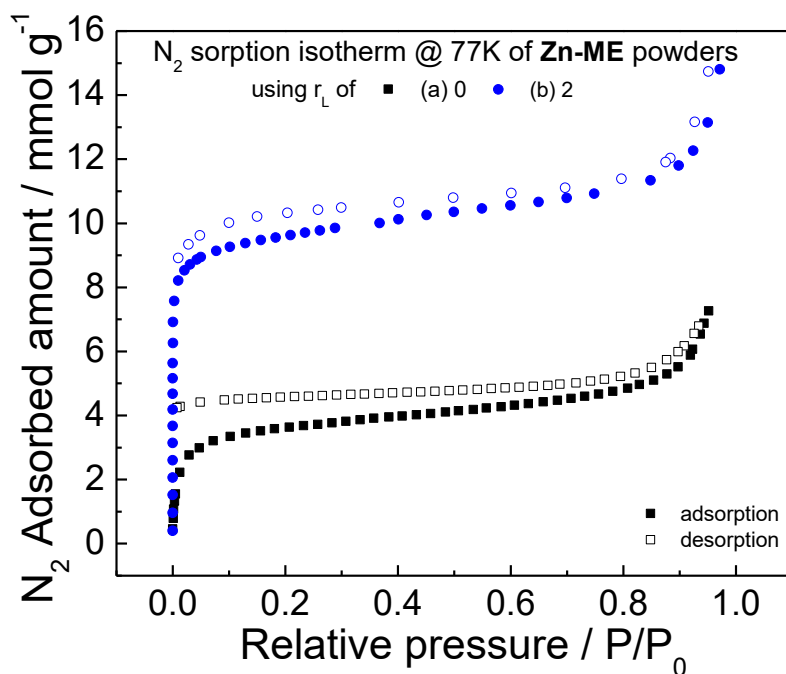


Figure 3.8 N_2 sorption isotherm at 77 K of the **Zn-ME** powders synthesized at 50°C by integrating coordination modulation with the ligand replacement approach using r_L ratio of (a) 0 and (b) 2.

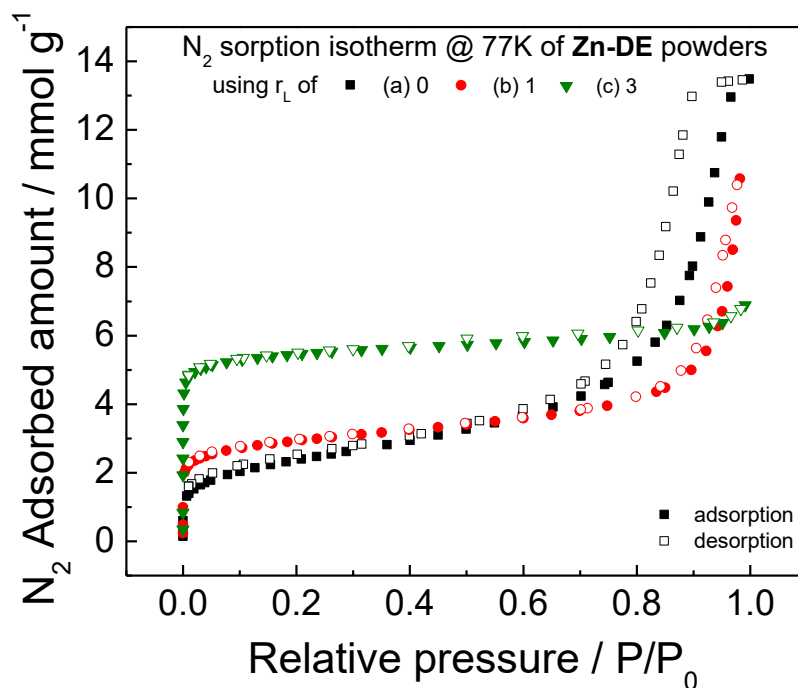


Figure 3.9 N_2 sorption isotherm at 77 K of the **Zn-DE** powders synthesized at 50°C by integrating coordination modulation with the ligand replacement approach using r_L ratio of (a) 0, (b) 1 and (c) 3.

3.3 Integration of coordination modulation in the LPE-based fabrication of Zn-L films

In the present work, we explore the use of the coordination modulation technique in an LPE-based process, with an object of assessing its potential utility in enhancing the quality and performance of MOF-based thin-films, using the **Zn-L** type MOFs as a model system due to their previous success in being processed via a conventional LPE route.

3.3.1 Coordination modulation in LPE-based growth of Zn-DM films

Given the success of coordination modulation in controlling the size and enhancing the properties of bulk crystals of **Zn-DM**, the analogous approach is then employed for LPE-based fabrication of thin-films of the same compound. In a typical preparation, the Au-coated QCM substrate (pre-functionalized with a monolayer of 16-mercaptohexadecanoic acid (MHDA) to anchor the MOF crystals)

is alternately dosed with the metal cluster ($\text{Zn}_4\text{O}(\text{OAc})_6$) and the organic linker (H_2DM) solutions in a continuous flow mode, with an ethanol washing step between precursor dosing steps. During the fabrication process, the QCM frequency change, which directly correlates with the mass of the deposited thin-film according to Sauerbrey equation, is monitored in real-time to confirm the progress of film growth. In a conventional LPE-based fabrication of **Zn-DM** (without modulator) the quantity of MOF deposited is observed to linearly increase with the cycling frequency. Note that, the **Zn-DM** compound and its analogues exhibit an island growth mode involving a relatively small number of initial MOF nuclei on the substrate surface, followed by subsequent growth into larger crystallites.⁴⁵ Although this facilitates the growth of **Zn-DM** films with micrometre thickness, the extent to which the control of crystal orientation and the overall film quality is limited, highlighting a challenge associated with typical LPE processes of the MOF systems beyond the paddlewheel-based MOFs.⁴⁵

The influence of coordination modulation on thin-film growth is then investigated by varying the concentration of the modulator (herein, acetic acid) relative to the concentration of $\text{Zn}_4\text{O}(\text{OAc})_6$ in the metal precursor solution (expressed via the ratio r_M) in an otherwise identical LPE-based process. Note that for the LPE-based fabrication, the parameter r_M is more relevant than r_L as described for bulk syntheses, since the modulator is added to the metal precursor solution and a washing step exists between metal and organic linker dosing steps. The QCM data stemming from deposition processes using r_M values ranging from 0 to 5 is presented in Figure 3.10. In all cases, the quantity of **Zn-DM** deposited on the substrate increases as a function of the cycling frequency, as reflected by the decrease in oscillation frequency (F) as a function of time.⁴⁶ However, the quantity deposited *per step* is significantly affected by r_M , which is ascribed to the modulator influencing the nucleation and growth phases of thin-film growth.

Closer inspection of the QCM frequency data reveals that, in the initial stages of deposition (<10 deposition cycles; Figure 3.10, inset), the quantity of MOF grown on the surface is significantly reduced for $r_M \geq 3$, suggesting the

disruption of the initial nucleation process (as observed in the case of bulk MOF systems) at high modulator concentrations.^{27,28} At lower levels ($r_M \leq 2$), the influence of the modulator is found to be limited over the same period. However, beyond this nucleation stage (Figure 3.10, main panel), the deposited mass per deposition cycle is enhanced for $r_M = 1$ and 2, as indicated by the steeper (negative) slope in the frequency change profile relative to the conventional process ($r_M = 0$).

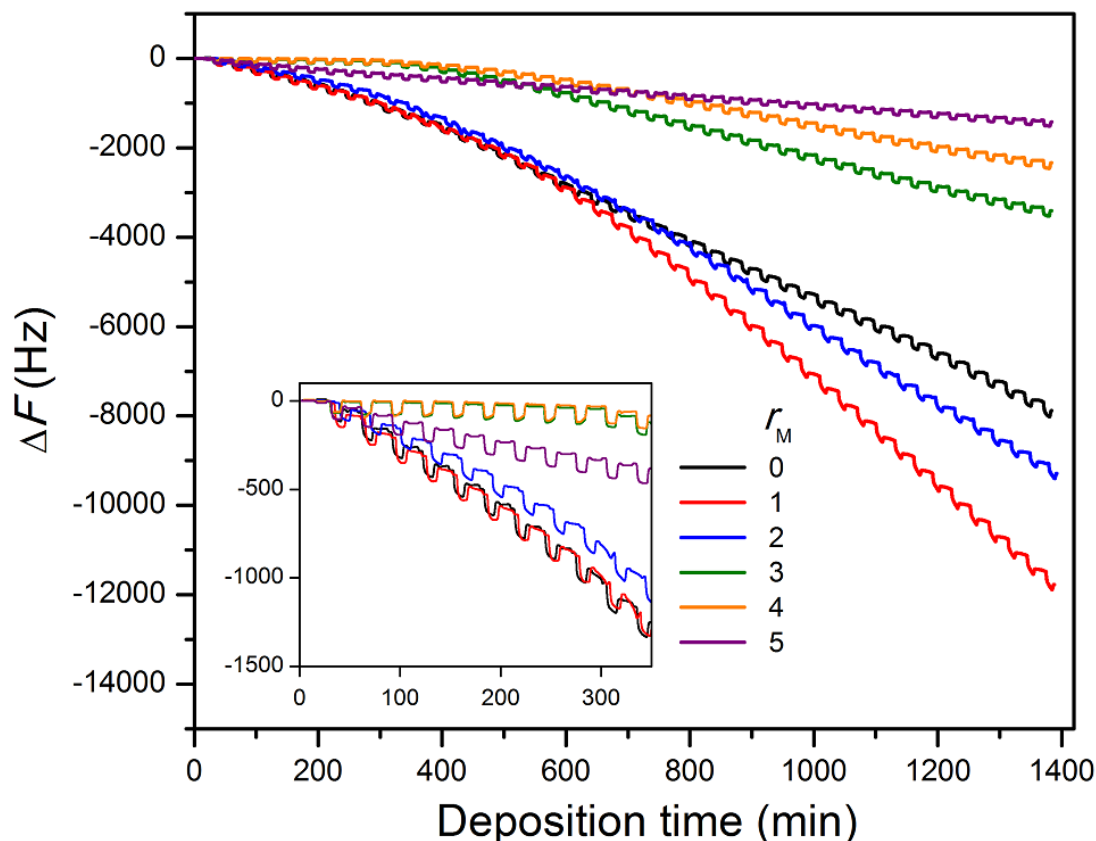


Figure 3.10 Plots showing changes in QCM oscillator frequency (F) as a function of time during the fabrication of **Zn-DM** films with variation of the modulator-to-metal cluster ratio (r_M). Reproduced with permission. Copyright © The Royal Society of Chemistry 2017.⁴⁷

This can be rationalized by the fact that larger crystals are likely to emerge upon addition of the modulator, whose growth surfaces, at which additional metal clusters and linker molecules can attach to effect further growth, will be larger than in the absence of modulator. Thus, the limited perturbation of the initial nucleation at low modulator concentrations coupled with growth of larger crystallites leads to more rapid growth of

these films over the timeframe studied. At higher modulator concentrations ($r_M \geq 3$), the significant disruption to the nucleation process leads to fewer available growth sites, leading to slower overall growth and a lower mass of material deposited on the surface. Note that, while the QCM platform provides a highly sensitive quantitative method of observing the deposition of thin-films, it does not provide information regarding the composition or morphology of the materials. Thus, full characterization of the films is carried out in order to ascertain the influence of the modulator on the film growth and characteristics of the films.

Detailed analysis of the composition of the deposited films were carried out via PXRD experiments (see Figure 3.11). In each case, a good match with the simulated pattern of bulk **Zn-DM** was obtained, indicating phase-pure **Zn-DM** was deposited on the QCM substrate surface. Interestingly, the addition of modulator during the deposition led to a pronounced preferred crystal orientation in the [100] direction, as evidenced by an increased intensity in the $h00$ reflections (e.g. at $2\theta = 8.8^\circ$ and 17.6°). In contrast, the **Zn-DM** films fabricated in the absence of the modulator ($r_M = 0$) showed the remainder of the expected diffraction peaks (e.g. 220 and 311), which is consistent with a slightly random orientation of the crystallites.

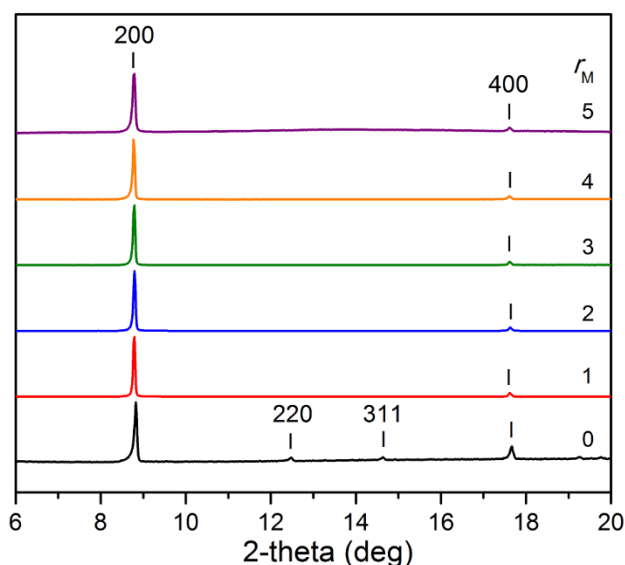


Figure 3.11 Powder X-ray diffraction (PXRD) patterns of the **Zn-DM** films fabricated by the LPE process with variation of the modulator-to-metal cluster ratio (r_M). Reproduced with permission. Copyright © The Royal Society of Chemistry 2017.⁴⁷

To probe the orientation of the films further, two-dimensional grazing incidence X-ray diffraction (2D-GIXRD) data were collected for a **Zn-DM** films fabricated using $m = 0$ to 5 (Figure 3.12). In the absence of the modulator (Figure 3.12A), the broad ring-like profile of the diffraction peaks is indicative of a limited control over the growth orientation of the crystals. However, the incorporation of the modulator during growth revealed discrete reflections in the corresponding data (Figure 3.12B to 3.12F), which indicate that the films are oriented in the film growth direction (normal to the substrate surface). This ability to tune both the crystallinity and crystal orientation illustrate a clear advantage of incorporating coordination modulation in an LPE-based fabrication protocol.

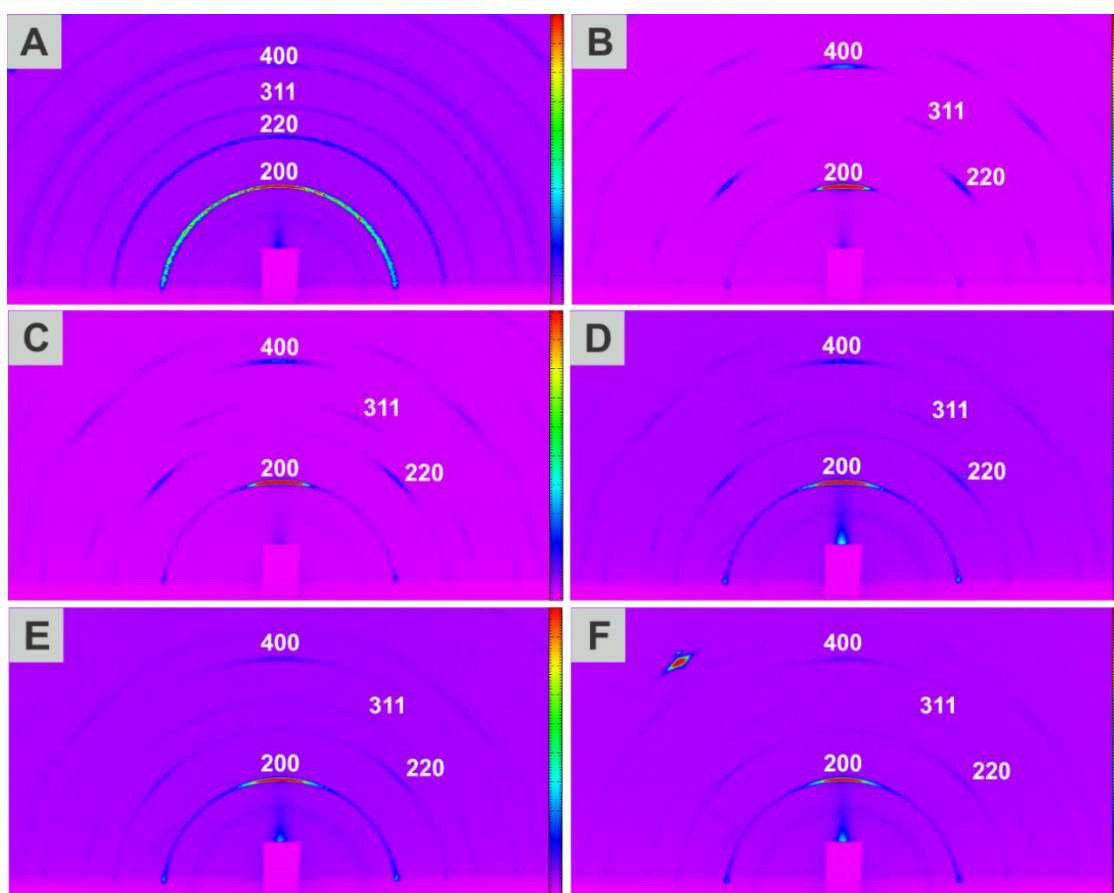


Figure 3.12 Two-dimensional grazing incidence X-ray diffraction patterns (2D-GIXRD) of **Zn-DM** films fabricated at 40 °C via integration of coordination modulation with LPE fabrication process; using $\text{Zn}_4\text{O}(\text{OAc})_6$ 0.5 mM, H_2DM 0.5 mM as precursor solutions and acetic acid as coordination modulator by mixing it with the $\text{Zn}_4\text{O}(\text{OAc})_6$ solutions with $m =$ (A) 0, (B) 1, (C) 2, (D) 3, (E) 4 and (F) 5. The synchrotron parameters are X-ray wavelength 1.0013 Å, incidence angle 0.6° and refined sample-to-detector distance 440.0 mm. The color of each pixel reflects the intensity from low (magenta) to high (red).

To further probe the influence of coordination modulation on the crystal orientation and morphology of the deposited MOF thin-films, top (Figure 3.13) and cross-sectional (Figure 3.14) views of the **Zn-DM** films are obtained via scanning electron microscopy (SEM). In the absence of the modulator (Fig. 3.13A), crystals with square facets are observed with a broad range of crystal sizes and orientations. This reflects the limitation of control over the nucleation and crystal growth using a conventional LPE-based fabrication process. However, addition of a small amount of modulator ($r_M = 1$ and 2) led to the formation of larger, square plate-like crystals with a denser packing and consistent orientation (Figure 3.13B and 3.13C). Further increases in the modulator concentration ($r_M \geq 3$) led to a reduction in the crystal size and an incomplete surface coverage (Figure 3.13D to 3.13F and see also Figure 3.14). These observations are consistent with the QCM frequency data presented in Figure 3.10, which displayed the most rapid overall deposition of the film for $r_M = 1$ and 2, and reduced nucleation and growth at $r_M \geq 3$.

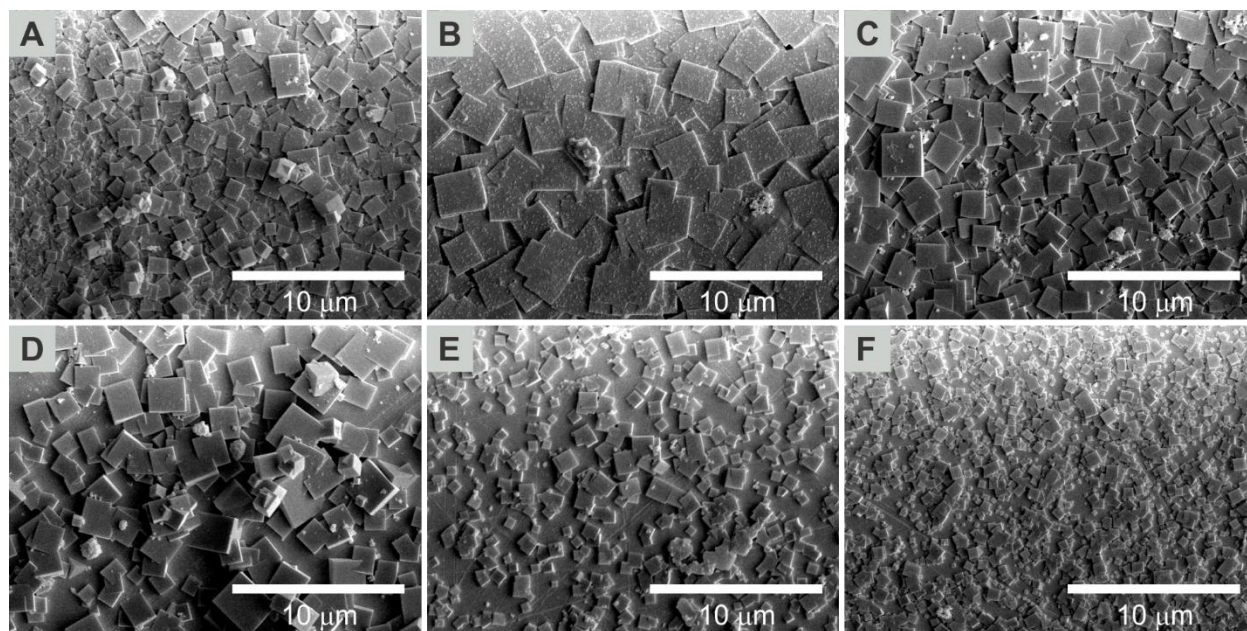


Figure 3.13 SEM images of the surfaces of **Zn-DM** films fabricated coordination modulation-assisted LPE-based process using modulator-to-metal cluster ratios (r_M) of (A) 0; (B) 1; (C) 2; (D) 3; (E) 4; and (F) 5. Reproduced and Adapted with permission. Copyright © The Royal Society of Chemistry 2017.⁴⁷

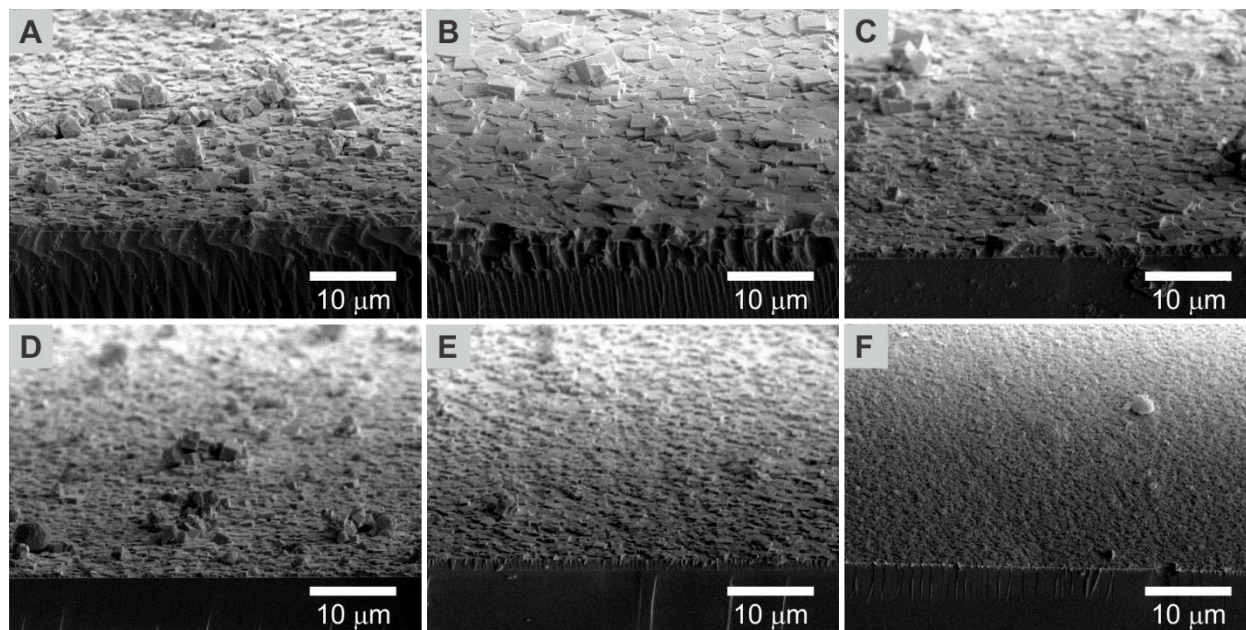


Figure 3.14 Cross-sectional SEM images of the **Zn-DM** films fabricated coordination modulation-assisted LPE-based process using modulator-to-metal cluster ratios (r_M) of (A) 0; (B) 1; (C) 2; (D) 3; (E) 4; and (F) 5, corresponding to the top-view images in Figure 3.13.

The influence of coordination modulation on the films fabricated by the LPE-based protocol is tested via methanol adsorption experiments. Here, a helium gas flow containing a controlled partial pressure of methanol vapor is introduced to a quartz crystal microbalance (QCM) cell held at a constant temperature of 25 °C, and the mass of methanol adsorbed is recorded following stabilization of the QCM substrate frequency. The methanol adsorption data for the **Zn-DM** thin-films fabricated using different r_M values is presented in Figure 3.15. Addition of modulator during the film fabrication process enhances the methanol adsorption capacity from 7.40 mmol/g ($r_M = 0$) to 10.43 mmol/g ($r_M = 2$) at $P/P_0 = 0.95$ (Figure 3.15), which is likely a direct consequence of the enhanced crystallinity and packing of the film, and a decrease in the amount of amorphous, non-porous phases and low-porosity regions of the MOF film. The adsorption capacity is maximized in the range of $r_M = 2$ to 4, after which the capacity decreases due to a significantly lower micropore density, which may be associated with lower-quality pore formation associated with a significantly smaller crystal size compared to the other

samples examined in these experiments. Note that the introduction of non-periodic defects (e.g. linker absences) can also boost the adsorption capacity of MOFs in some cases. However, infrared spectroscopy (Figure 3.16) reveals little difference in composition for samples fabricated at different r_M values, while the pore size distributions also appear unchanged based on the similarity in the form of the adsorption profiles and the kinetic (diffusion) data for methanol adsorption (Figure 3.17). Therefore, the boost in adsorption capacity presumably arise via the elimination of low-crystallinity or amorphous portions of the film that accommodate a lower gravimetric capacity for guest molecules compared to the pristine regions of the MOF film.

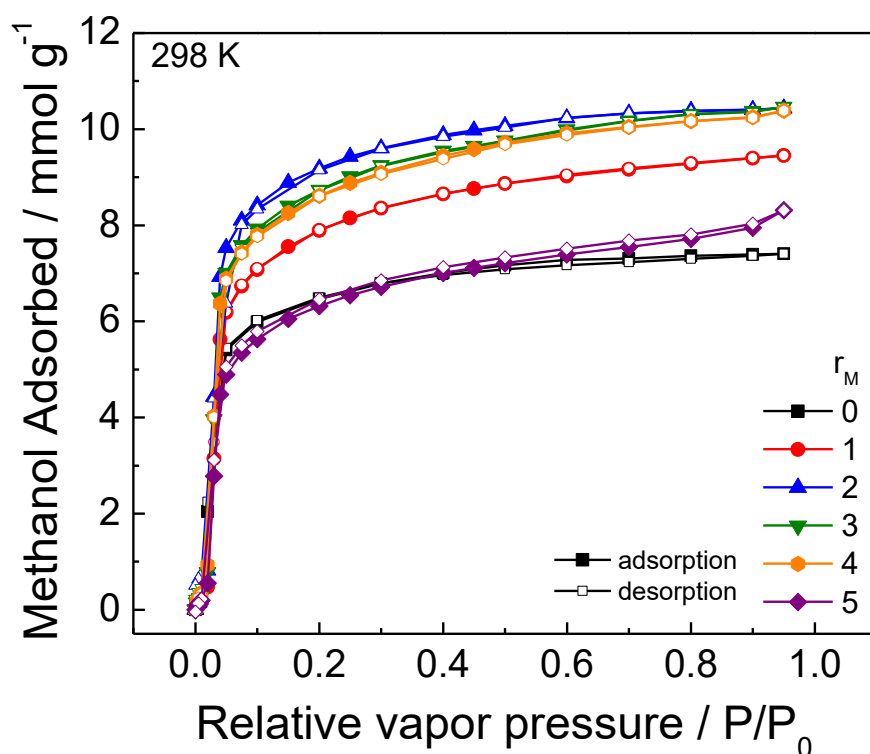


Figure 3.15 Methanol sorption isotherms at 25 °C measured using the environmentally controlled QCM of **Zn-DM** films fabricated at 40 °C via integration of coordination modulation with LPE fabrication process; using $Zn_4O(OAc)_6$ 0.5 mM, H_2DM 0.5 mM as precursor solutions and acetic acid as coordination modulator by mixing it with the $Zn_4O(OAc)_6$ solutions with $r_M = 0 - 5$.

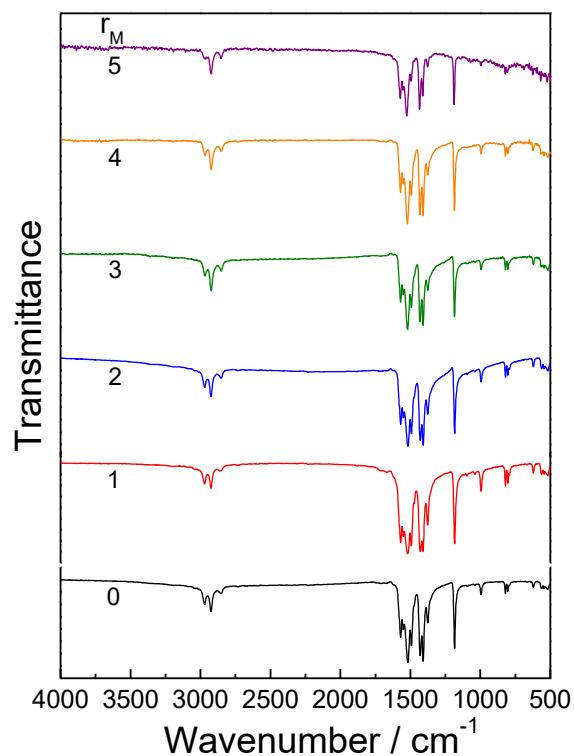


Figure 3.16 Infrared reflection absorption spectra (IRRAS) of **Zn-DM** films fabricated at 40 °C via integration of coordination modulation with LPE-based fabrication process with $r_M = 0 - 5$.

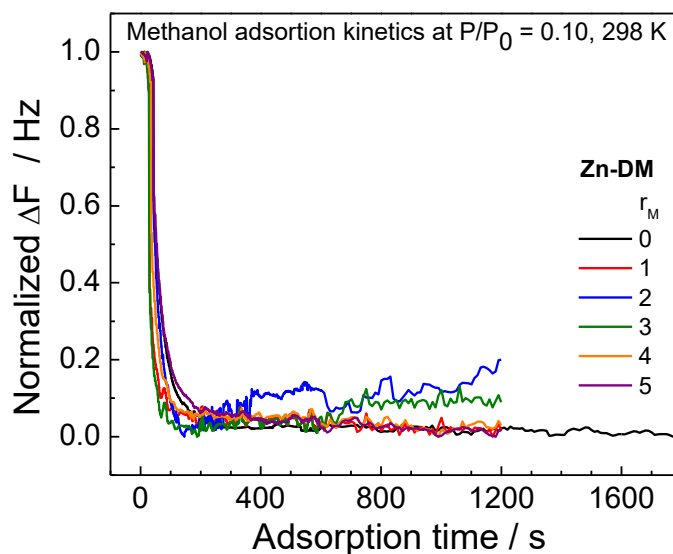


Figure 3.17 Methanol adsorption kinetics at P/P_0 of 0.10 of **Zn-DM** films fabricated at 40 °C via integration of coordination modulation with LPE-based protocol with $r_M = 0 - 5$.

3.3.2 Coordination modulation in LPE-based growth of Zn-ME films

A similar optimization procedure was carried out using the organic linker H₂ME to test the utility of coordination modulation with respect to the LPE-based fabrication of **Zn-ME** films. The analogous deposition protocol in the absence of the modulator ($r_M = 0$) led to the expected formation of **Zn-ME** as indicated by PXRD (Figure 3.18). Interestingly, introduction of the modulator during the deposition process enhances the orientation of the films which exhibit the [100]-related crystallite orientation along the film growth direction (Figure 3.18). Moreover, the 2D-GIXRD data shown in Figure 3.19 clearly illustrate the discrete reflections which are observed as a characteristic of the preferred-oriented crystalline film. SEM data (Figure 3.20 and 3.21) reveal the appearance of square, plate-like crystals approximately 1 μm in size of the **Zn-ME** films fabricated by integration of coordination modulation into the LPE-based protocol.

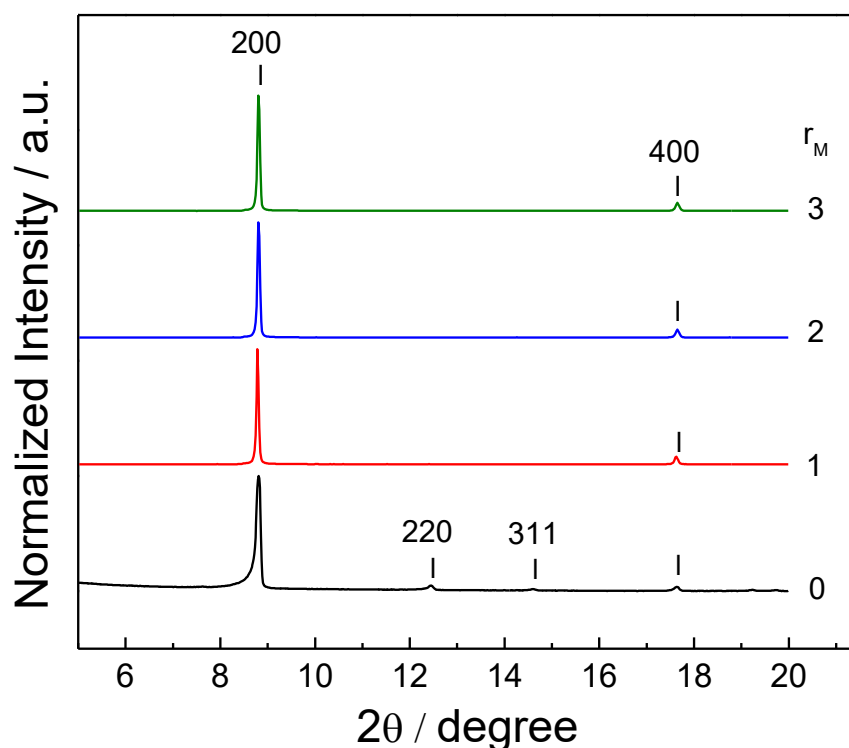


Figure 3.18 Powder X-ray diffraction patterns (XRD) of **Zn-ME** films fabricated at 40 °C via integration of coordination modulation with LPE fabrication process; using $\text{Zn}_4\text{O}(\text{OAc})_6$ of 0.5 mM, H₂ME 0.5 mM as precursor solutions and acetic acid as coordination modulator by mixing it with the $\text{Zn}_4\text{O}(\text{OAc})_6$ solutions with $r_M = 0 - 3$.

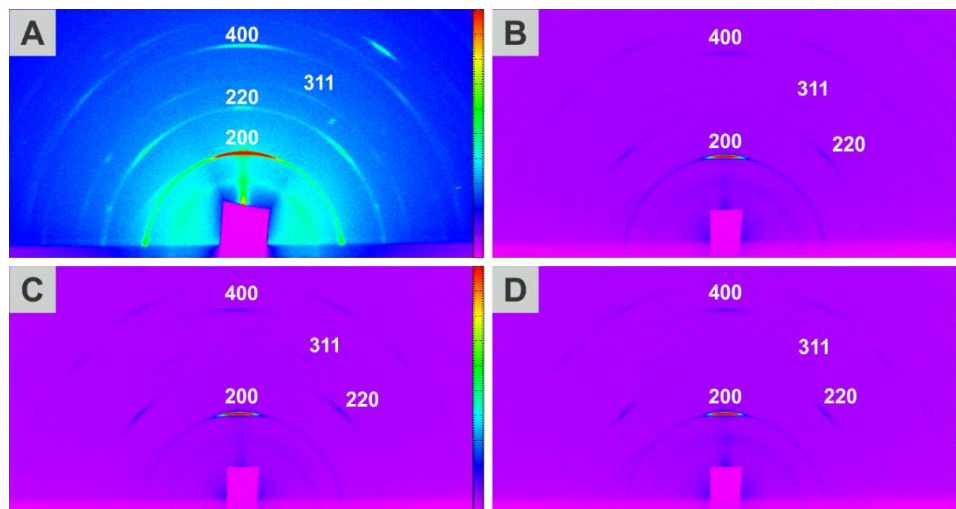


Figure 3.19 2D-GIXRD of **Zn-ME** films fabricated at 40 °C via integration of coordination modulation with LPE fabrication process; using $\text{Zn}_4\text{O}(\text{OAc})_6$ 0.5 mM, H_2ME 0.5 mM as precursor solutions and acetic acid as coordination modulator by mixing it with the $\text{Zn}_4\text{O}(\text{OAc})_6$ solutions with $r_M =$ (A) 0, (B) 1, (C) 2 and (D) 3. The synchrotron parameters are X-ray wavelength 1.0013 Å, incidence angle 0.6° and refined sample-to-detector distance 440.0 mm. The color of each pixel reflects the diffraction intensity from low (magenta) to high (red).

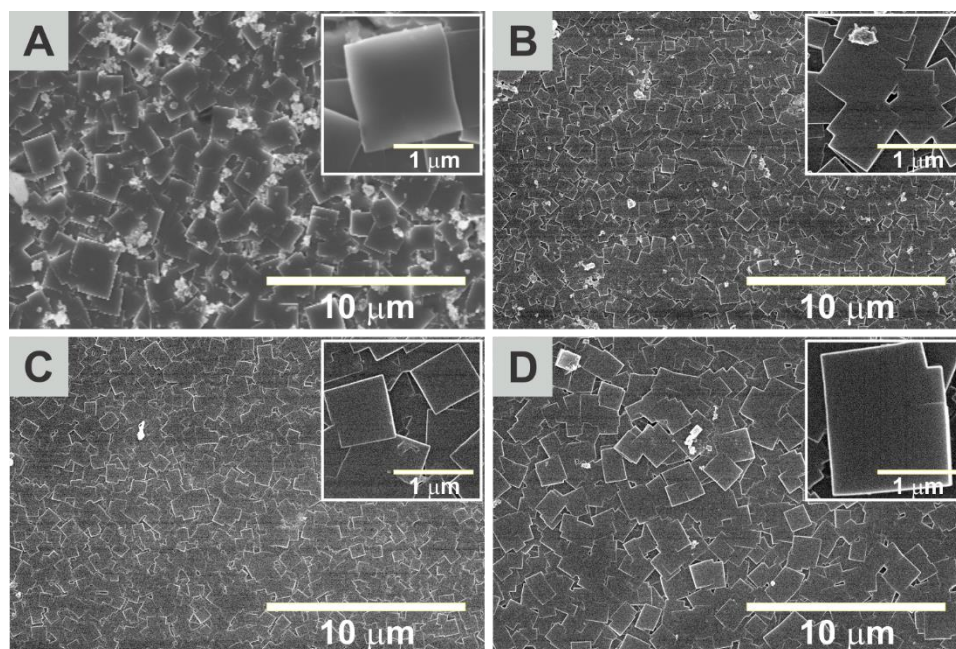


Figure 3.20 SEM images of the surfaces of **Zn-ME** films fabricated at 40 °C via integration of coordination modulation with LPE fabrication process; using $\text{Zn}_4\text{O}(\text{OAc})_6$ 0.5 mM, H_2ME 0.5 mM and acetic acid as coordination modulator by mixing it with the $\text{Zn}_4\text{O}(\text{OAc})_6$ solutions with $r_M =$ (A) 0, (B) 1, (C) 2 and (D) 3.

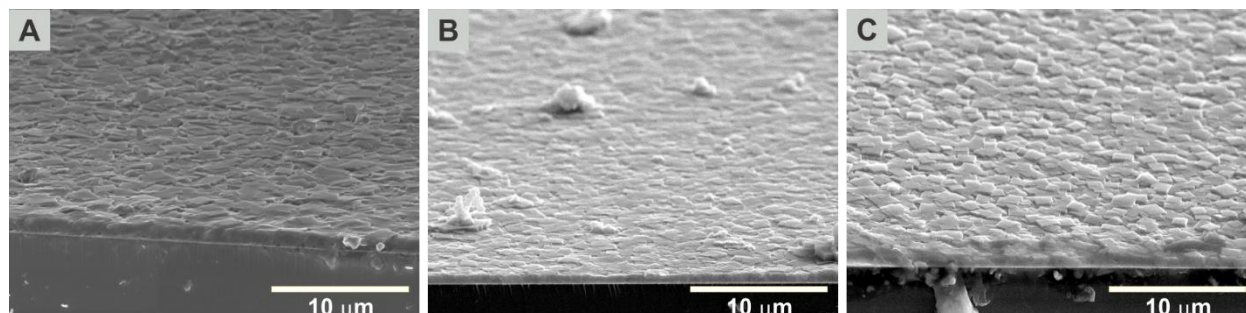


Figure 3.21 Cross-sectional SEM images of **Zn-ME** films fabricated via integration of coordination modulation with LPE fabrication process using $r_M =$ (A) 0, (B) 1 and (C) 2.

Further, although less pronounced relative to the case of **Zn-DM**, the enhanced crystallinity and preferred orientation result in a marginal enhancement in the adsorption capacity of methanol (increase of 15% for $r_M = 3$ at $P/P_0 = 0.95$ relative to the $r_M = 0$ case, see Figure 3.22). Again, the kinetic diffusion data for methanol adsorption of **Zn-ME** films (Figure 3.23) show the similar trend regardless on the increasing of r_M used in this fabrication experiment, confirming that the enhanced adsorption is not due to the non-periodic defects but rather due to the enhanced crystallinity. Therefore, it further confirms the benefit of the addition of a small quantity of a modulator during the film growth.

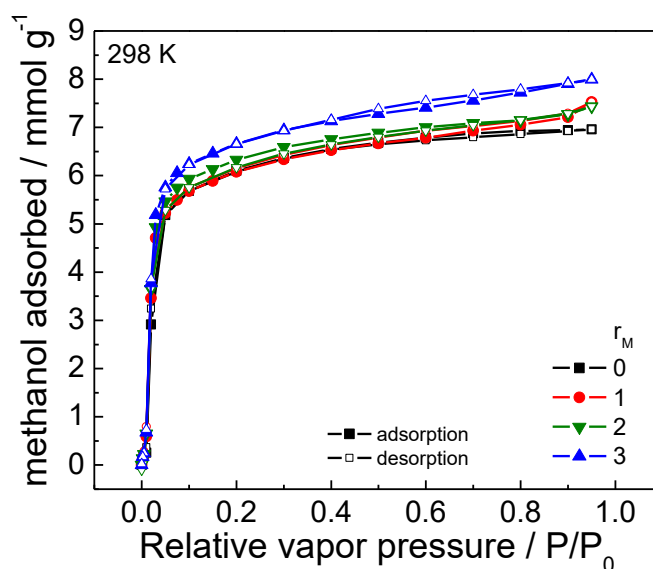


Figure 3.22 Methanol sorption isotherms at 25 °C using QCM of **Zn-ME** films fabricated at 40 °C via integration of coordination modulation with LPE fabrication process; using $\text{Zn}_4\text{O}(\text{OAc})_6$ 0.5 mM, H_2ME 0.5 mM as precursor solutions and acetic acid as coordination modulator by mixing it with the $\text{Zn}_4\text{O}(\text{OAc})_6$ solutions with $r_M = 0 - 3$.

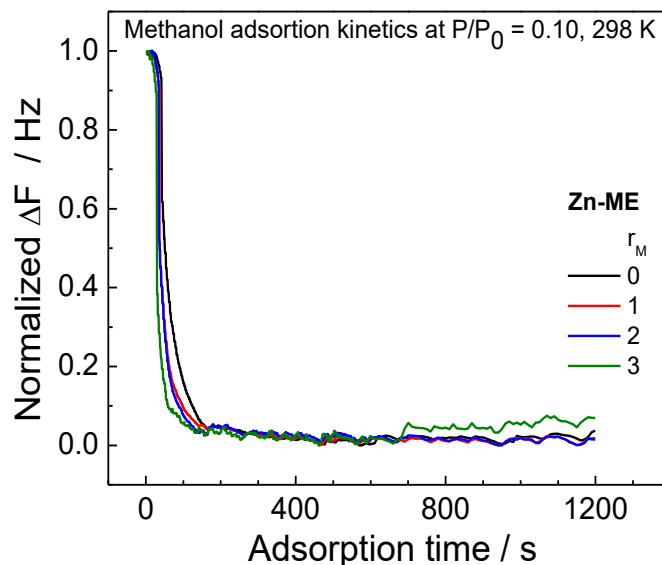


Figure 3.23 Methanol adsorption kinetics at P/P_0 of 0.10 of **Zn-ME** films fabricated at 40 °C via integration of coordination modulation with LPE-based protocol with $r_M = 0 - 3$.

3.3.3 Coordination modulation in LPE-based growth of Zn-DE films

The deposition of the **Zn-DE** framework could also be readily optimized via the same fabrication protocols using the linker H_2DE . In a similar manner to both **Zn-DM** and **Zn-ME**, a conventional LPE-based deposition process afforded the expected **Zn-DE** framework (Figure 3.24 and 3.25), which exhibited a square plate-like morphology (Figure 3.26) and dense film packing (Figure 3.27). The addition of small quantities of modulator (up to $r_M = 3$) provided enhanced crystallinity and film orientation as confirmed by 2D-GIXRD data (Figure 3.25).

Interestingly, upon characterization of the adsorption properties of the films, a considerable enhancement in the methanol adsorption capacity was observed for films derived using $r_M = 2$ and 3, which exhibited increases of 69% and 120% at $P/P_0 = 0.95$ relative to the $r_M = 0$ case, respectively (Figure 3.28). This boost in adsorption capacity, and overall benefit of the coordination modulation approach, is likely particularly pronounced compared to the other frameworks due to the more sterically demanding nature of the organic linker (possessing two ethyl groups on the pyrazolate backbone, rather than methyl groups), where the overall properties

are more sensitive to blockages and pore clogging as a result of lattice defects or low-crystallinity portions of the film. According to the kinetic adsorptions of methanol at P/P_0 of 0.10 (Figure 3.29), the **Zn-DE** films fabricated using the integration of coordination modulation with the LPE process adsorb methanol vapour with significantly faster rate than the **Zn-DE** film fabricated via the typical LPE process. This observation highlights that the film fabricated using modulator show a homogeneous pore size distribution due to the high degree of crystallinity, and consequently leads to the fast-kinetic adsorption.

Thus, the enhanced crystallinity and preferred orientation of the films fabricated in the presence of the modulator (and elimination of low-porosity components with little or no crystallinity) facilitates the formation of more periodic, uniform pores, which in turn allows the surface area to be maximized. In all, for **Zn-DM**, **Zn-ME** and **Zn-DE**, the use of coordination modulation during the metal dosing step provides enhancements in the film properties, highlighting the success of this integrated approach.

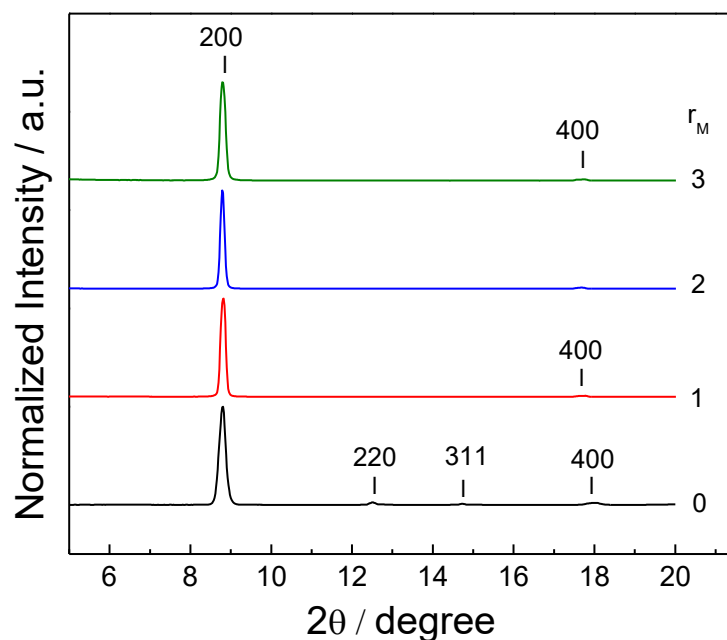


Figure 3.24 PXRD patterns of **Zn-DE** films fabricated at 40 °C via integration of coordination modulation with LPE fabrication process; using $\text{Zn}_4\text{O}(\text{OAc})_6$ 0.5 mM, H_2DE 0.5 mM as precursor solutions and acetic acid as coordination modulator by mixing it with the $\text{Zn}_4\text{O}(\text{OAc})_6$ solutions with $r_M = 0 - 3$.

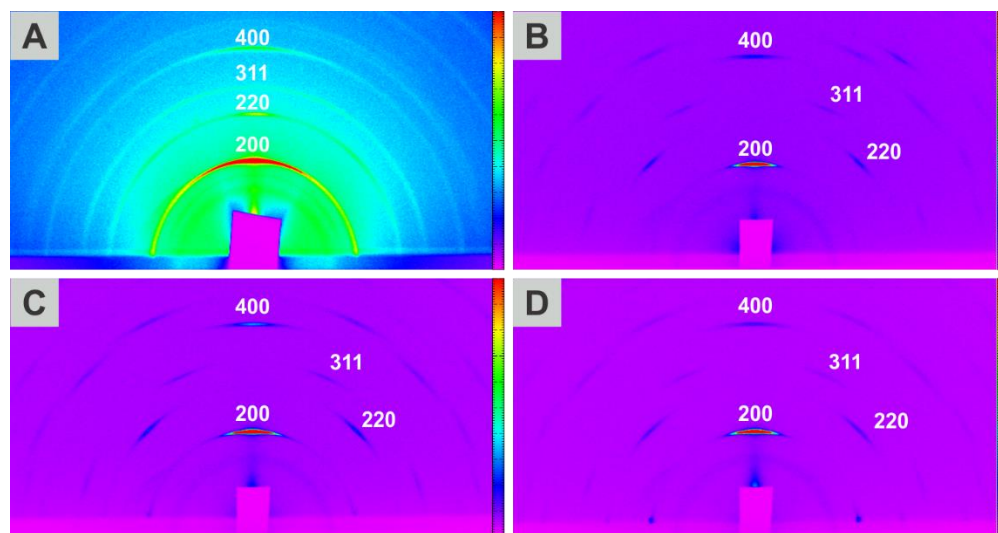


Figure 3.25 2D-GIXRD patterns of **Zn-DE** films fabricated at 40 °C via integration of coordination modulation with LPE-based process; using $\text{Zn}_4\text{O}(\text{OAc})_6$ 0.5 mM, H_2DE 0.5 mM and acetic acid as coordination modulator by mixing it with the $\text{Zn}_4\text{O}(\text{OAc})_6$ solutions with $m =$ (A) 0, (B) 1, (C) 2 and (D) 3. The synchrotron parameters are X-ray wavelength 1.0013 Å, incidence angle 0.6° and refined sample-to-detector distance 440.0 mm.

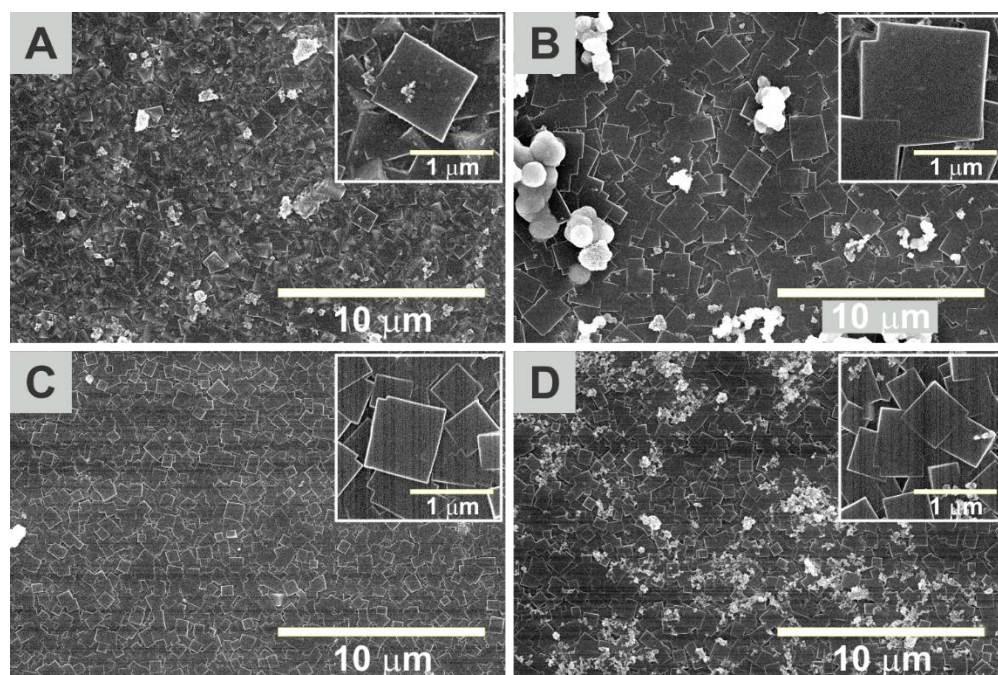


Figure 3.26 SEM images of the surfaces of **Zn-DE** films fabricated at 40 °C via integration of coordination modulation with LPE fabrication process using $m =$ (A) 0, (B) 1, (C) 2 and (D) 3.

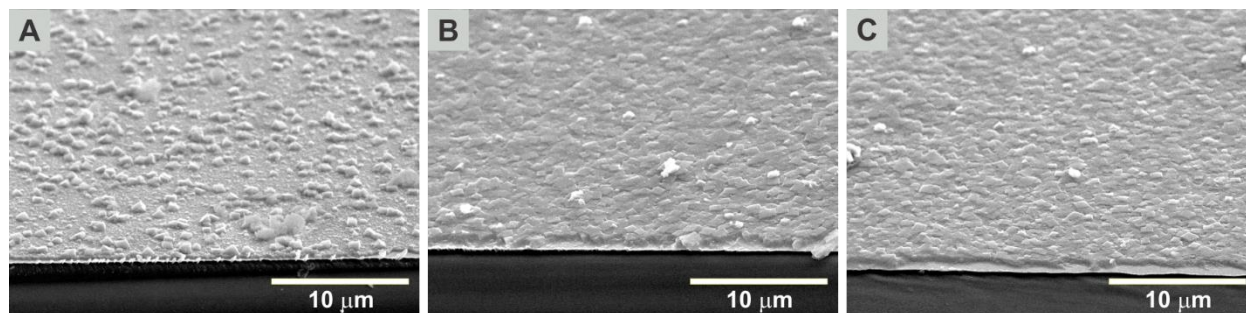


Figure 3.27 Cross-sectional SEM images of **Zn-DE** films fabricated via integration of coordination modulation with LPE fabrication process using $r_M =$ (A) 0, (B) 1 and (C) 2, corresponding to the top view images in Figure 3.26.

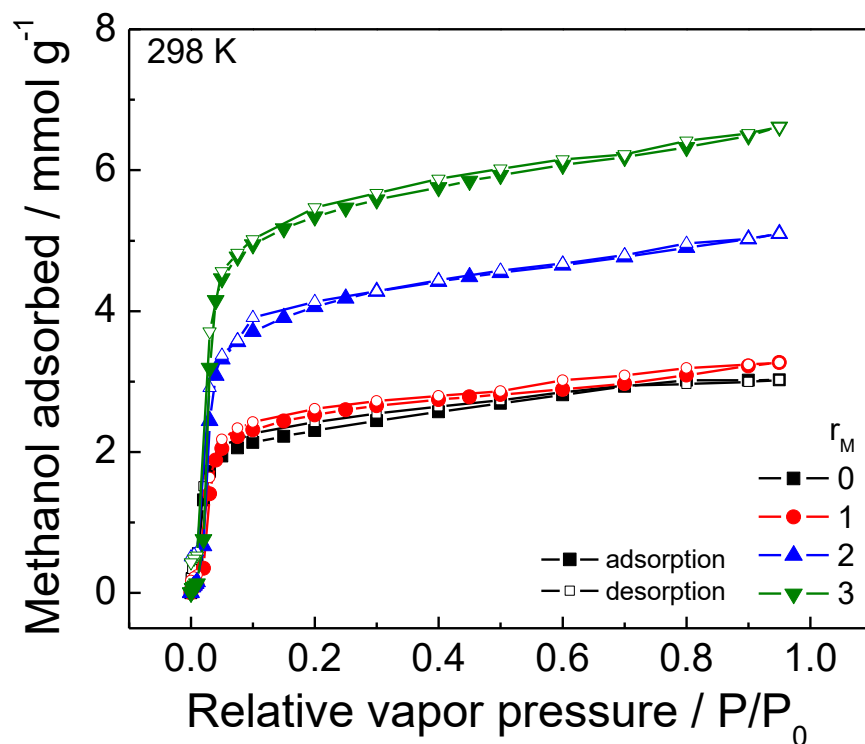


Figure 3.28 Methanol sorption isotherms at 25 °C measured by QCM of **Zn-DE** films fabricated at 40 °C via integration of coordination modulation with LPE fabrication process; using $\text{Zn}_4\text{O}(\text{OAc})_6$ 0.5 mM, H_2DE 0.5 mM and acetic acid as coordination modulator by mixing it with the $\text{Zn}_4\text{O}(\text{OAc})_6$ solutions with $r_M = 0 - 3$.

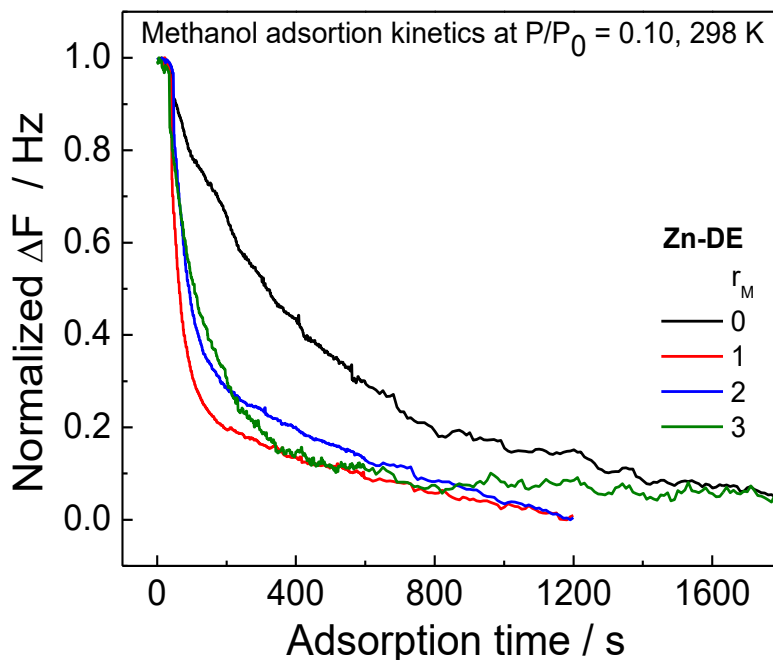
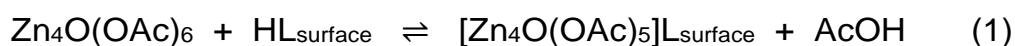


Figure 3.29 Methanol adsorption kinetics at P/P_0 of 0.10 of **Zn-DE** films fabricated at 40 °C via integration of coordination modulation with LPE-based protocol with $r_M = 0 - 3$.

3.4 Probing the role of coordination modulation in optimizing LPE fabrication

3.4.1 Film nucleation and growth

The success of the coordination modulation approach in enhancing the growth rate and properties of the **Zn-L** films prompts more detailed investigation regarding the influence of the modulator on the molecular interactions during the fabrication process. Herein, the presence of acetic acid modulator within the metal cluster-containing solution suggests its importance on the metal precursor dosing step of the fabrication process, and hence it is postulated that variation of the value of r_M exerts changes in the affinity of the $[Zn_4O]^{6+}$ clusters toward the QCM substrate surface via manipulations of a solution/surface equilibrium of the type shown in Equation 1.



In such a system, there is an equilibrium between $\text{Zn}_4\text{O}(\text{OAc})_6$ molecules in the bulk solution and those that are bound to carboxylate moieties of the organic ligands or the initially deposited carboxylate-terminated SAM (denoted by L_{surface}). The binding of the cluster to L_{surface} liberates an acetic acid molecule, and hence the addition of excess modulator molecules is expected to shift this equilibrium toward the reactants (left shift), resulting in less metal clusters binding to the surface. This is expected to contribute to lower initial crystal nucleation, and slower overall film growth as observed in the in-situ QCM frequency change in Figure 3.10.

In order to probe this effect, a metal cluster solution without modulator ($r_M = 0$) is firstly delivered to the QCM surface to facilitate the attachment of $[\text{Zn}_4\text{O}]^{6+}$ clusters to the substrate. This is then followed by treatment of the substrate with the modulator solutions of various concentrations (0.5, 1.0, and 2.0 mM acetic acid in ethanol), and the relative quantities of the metal clusters attached to the surface upon reaching equilibrium are analysed by the frequency changes in the quartz oscillator (according to Sauerbrey equation). Figure 3.30 illustrates the QCM data for the three modulator concentrations collected over four cycles (where each cycle represents metal cluster dosing, followed by treatment with the modulator solution). At the lower concentrations of 0.5 (red) and 1.0 (blue) mM, the switching of the treatment solution from the metal solution to the modulator solution (indicated by the vertical red dashed lines in Figure 3.30) results in minimal changes in the QCM frequency, indicating that the metal clusters are retained on the QCM surface. However, upon increasing the modulator concentration to 2.0 mM (orange), which approximately correlates with $r_M = 4$ in the fabrication studies described above, a complete detachment of the surface-bound $\text{Zn}_4\text{O}(\text{OAc})_6$ clusters from the substrate is observed due to the frequency returning to the baseline. Therefore, higher modulator concentrations restrict the quantity of metal cluster deposition on the substrate surface, which in turn reduces crystal nucleation and opportunities for further film growth. This is consistent with the trends in the rate of overall deposition of the **Zn-L** films as shown above (Figure 3.10), which demonstrates that precise tuning of the modulator concentration can achieve control over the film growth rate via tuning of the quantity of the metal cluster deposited on the film surface.

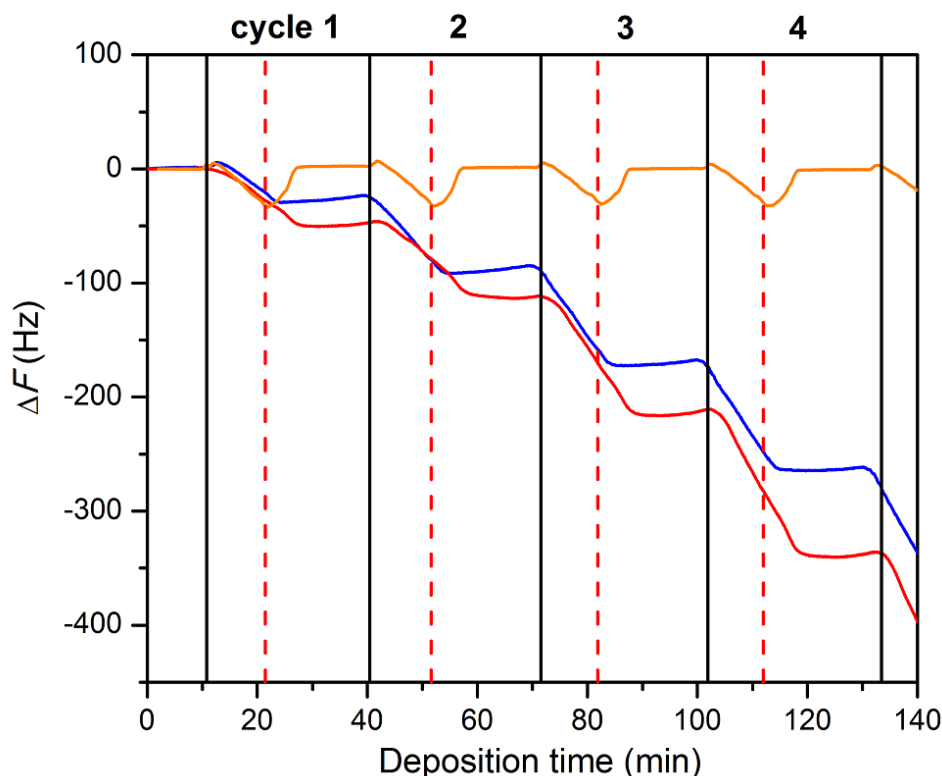


Figure 3.30 QCM data showing frequency changes of the oscillator as a function of time over four metal cluster dosing cycles. Here, each cycle represents the treatment of the substrate with a metal cluster solution (0.5 mM), followed by washing using the modulator-containing solutions having concentrations of 0.5 mM (red), 1.0 mM (blue), and 2.0 mM (orange). The beginning and end of each cycle is represented by vertical solid black lines, while the timing of the modulator addition is indicated by the vertical dashed red lines. Reproduced with permission. Copyright © The Royal Society of Chemistry 2017.⁴⁷

3.4.2 Film crystallinity and preferred orientation

As shown above, the rate of the initial stages of film growth is highly dependent on the concentration of the modulator, which is directly correlated to the quantity of the metal cluster that is deposited on the growth surface. Since the **Zn-L** films deposited in presence of the modulator also feature enhanced crystallinity and orientation, this observation suggests that the first few growth cycles also play an important role in determining these features of the product films. In order to probe this in more detail, the properties of a **Zn-DM** film prepared via a conventional LPE process ($r_M = 0$) for the first five cycles followed by further LPE-based growth

in the presence of the acetic acid modulator with various r_M are compared with those employing coordination modulations for all deposition cycles of the fabrication process (starting from the first LPE deposition cycle). In-situ monitoring of QCM frequency change during the fabrication process (Figure 3.31) indicates the significant alteration of the deposited mass on QCM surface when starting to introduce the modulator in the fabrication (herein, starting from the 6th deposition cycle). The higher modulator ratio (r_M), the slower growth rate and hence the less deposited mass per deposition cycle, similarly to the previous section when using the precursor solution with the modulator from the first fabrication cycle.

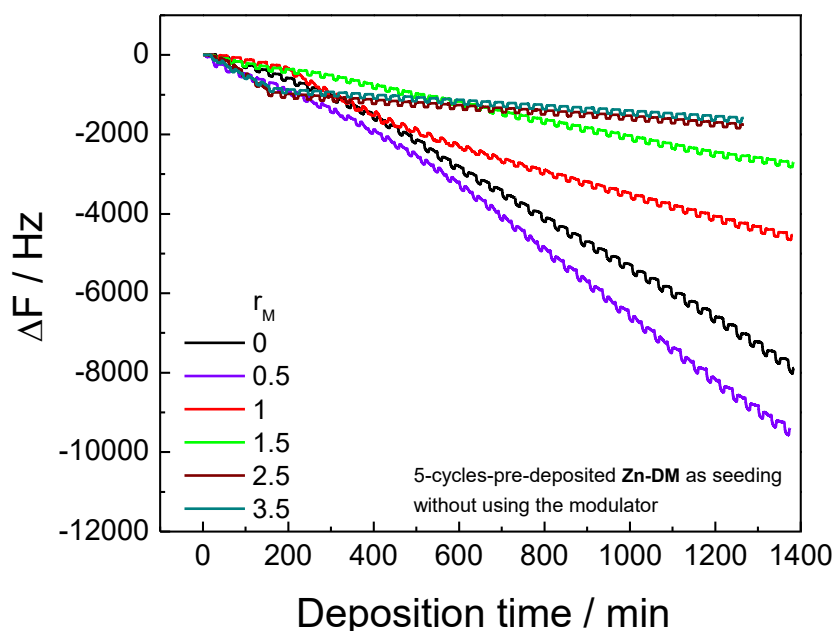


Figure 3.31 In-situ monitoring of QCM frequency during the fabrication of **Zn-DM** films at 40 °C via integration of coordination modulation with LPE fabrication process on the 5-cycles-pre-deposited **Zn-DM** films fabricated without using modulator as a self-seeding layer; using $\text{Zn}_4\text{O}(\text{OAc})_6$ 0.5 mM, H_2DM 0.5 mM as precursor solutions and acetic acid as coordination modulator by mixing it with the $\text{Zn}_4\text{O}(\text{OAc})_6$ solutions with $r_M = 0 - 3.5$.

The 2D-GIXRD patterns in the former case exhibited a small 220 diffraction peak in the out-of-plane direction (90° line cut), illustrating a more randomized orientation of the MOF crystals along the film growth direction (Figure 3.32). This observation is agreed well with the top-view SEM images in Figure 3.33. An

enhancement of the methanol adsorption capacity is also observed when using the acetic acid modulator in the LPE fabrication process after fabricating the 5-cycles pre-deposited **Zn-DM** layer without modulator (Figure 3.34); however, these enhanced adsorptions are still slightly lower than the cases of using the modulator from the first deposition cycle. This confirms that the presence of the modulator in the initial deposition cycles is crucial in determining the crystal orientation of the resulting films, and reveals that the quality of the nucleation process is propagated to the uniformity of the orientation of product films despite the use of coordination modulation in the later stages of film fabrication.

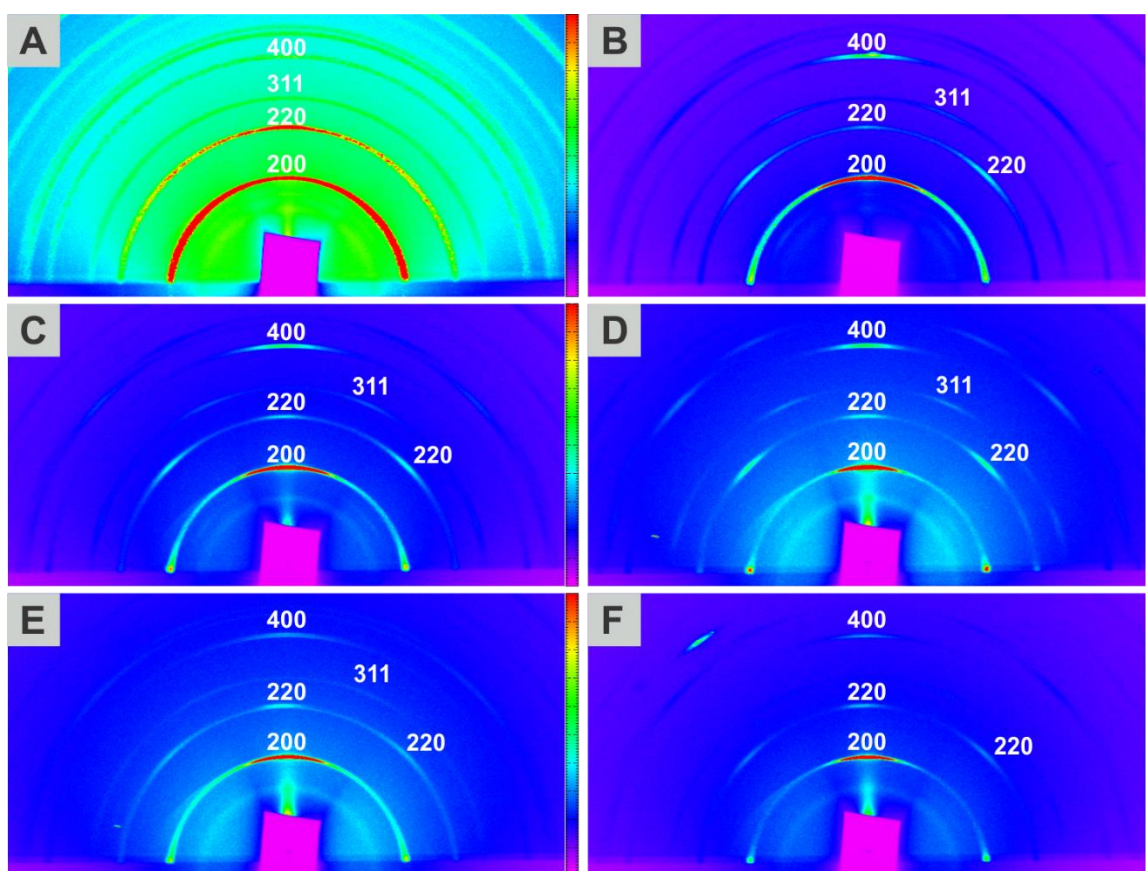


Figure 3.32 GIXRD patterns of **Zn-DM** films fabricated at 40 °C with various M ratio of (A) 0, (B) 0.5, (C) 1, (D) 1.5, (E) 2.5 and (F) 3.5 by employing coordination modulation method in conjunction with LPE process on the 5-cycles pre-deposited, self-seeding **Zn-DM** layer fabricated without using the modulator. Synchrotron parameters are X-ray wavelength 1.0013 Å, incidence angle 0.6° and refined sample-to-detector distance 487.3 mm.

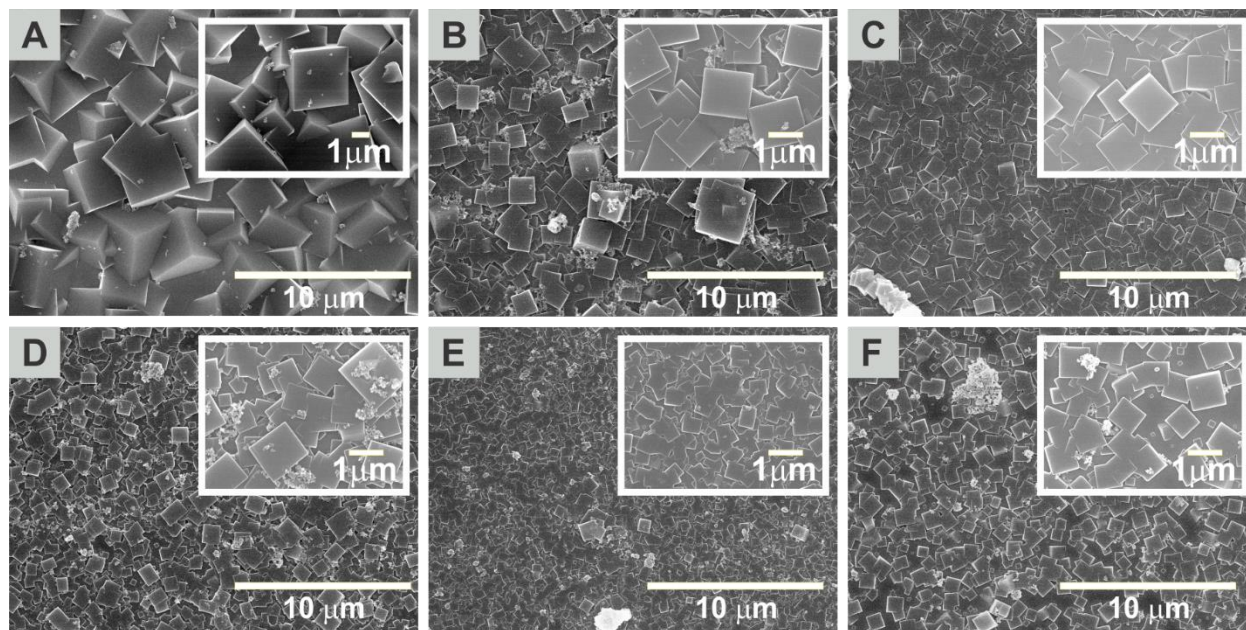


Figure 3.33 SEM images of the surfaces of **Zn-DM** films fabricated at 40 °C with various r_M ratio via integration of coordination modulation with LPE fabrication process on the pre-deposited, self-seeding **Zn-DM** layer fabricated without using the modulator for 5 cycles.

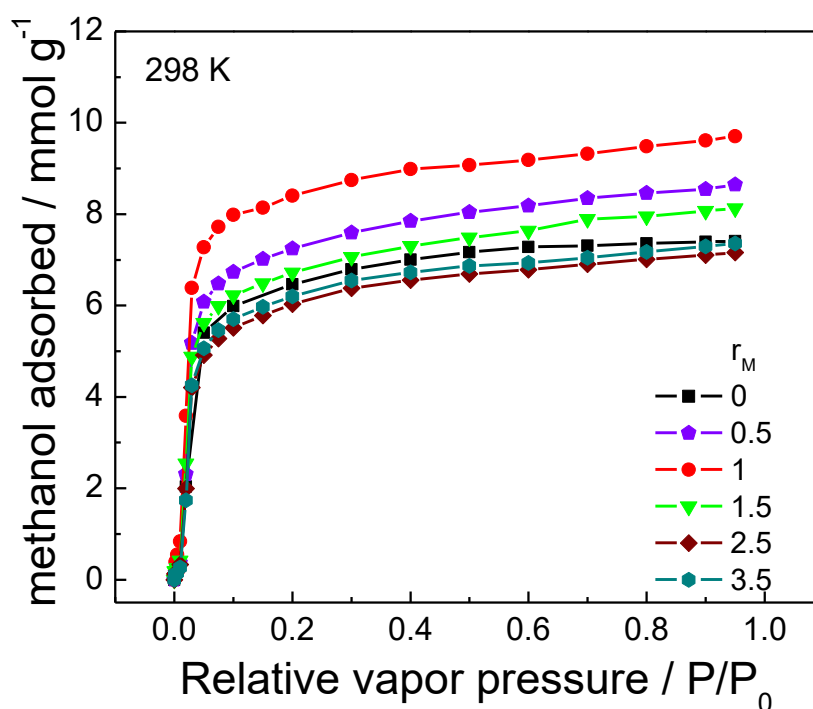


Figure 3.34 Methanol adsorption isotherms at 25 °C using the environmentally controlled quartz crystal microbalance (QCM) of **Zn-DM** films fabricated at 40 °C with various r_M ratio via integration of coordination modulation with LPE fabrication process on the self-seeding **Zn-DM** layer fabricated without using the modulator for 5 cycles

The influence of modulator addition to organic linker solutions, rather than the metal solutions, is also probed to ascertain whether the enhancement in film properties is unique to protocols incorporating the modulator in the metal cluster deposition step of the LPE process. In this case, the in-situ observation of QCM frequency change (Figure 3.35) shows no significant difference of the growth rate with respect to the increasing of r_M (also similar to r_L). Interestingly, in all cases where the modulator is incorporated in the organic linker solutions, 220 and 311 diffraction peaks are observed in the PXRD patterns (Figure 3.36), indicating a reduced uniformity in the crystal orientation. Further, these films display no significant enhancement in their methanol adsorption capacity, suggesting that the film quality is not enhanced above those prepared in the absence of the modulator (Figure 3.37). This indicates that the presence of the modulator during metal cluster deposition is crucial in order to achieve high-quality **Zn-DM** films.

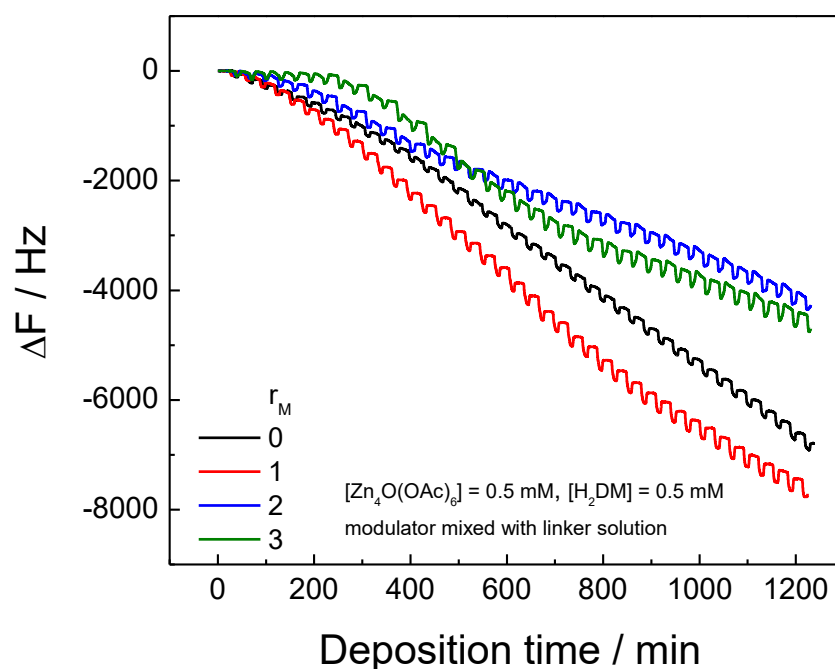


Figure 3.35 In-situ monitoring of QCM frequency during the fabrication of **Zn-DM** films at 40 °C via integration of coordination modulation with LPE fabrication process without seeding layer; using $Zn_4O(OAc)_6$ 0.5 mM and H_2DM 0.5 mM as precursor solutions, and acetic acid as coordination modulator by mixing it with the H_2DM solutions with various r_M ratio

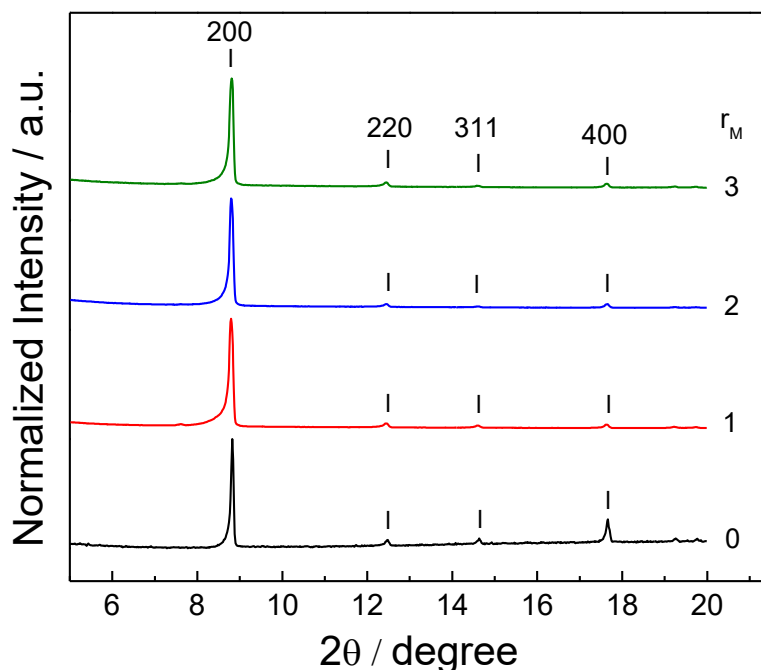


Figure 3.36 XRD patterns of **Zn-DM** films fabricated at 40 °C via integration of coordination modulation with LPE fabrication process; mixing acetic acid with the H_2DM solutions with various r_M ratio (corresponding with the growth data in Figure 3.35)

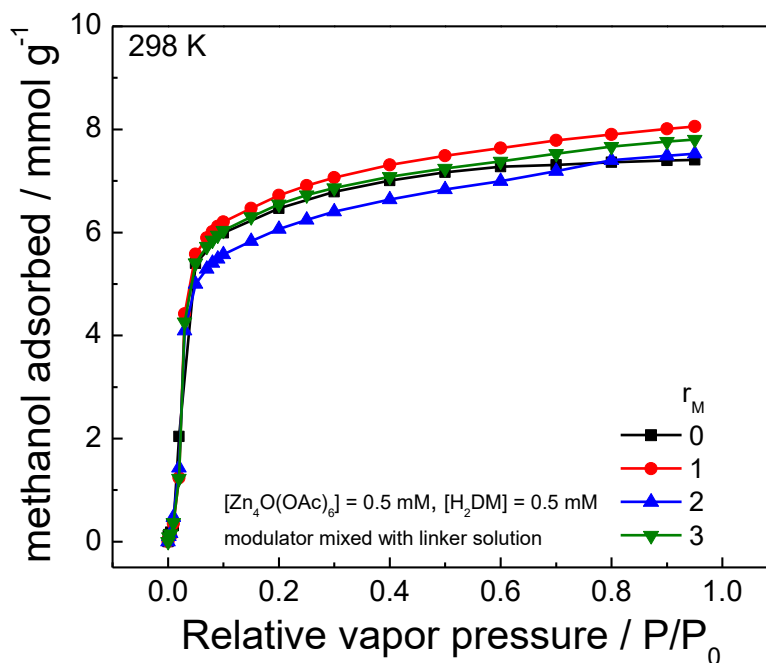


Figure 3.37 Methanol adsorption isotherms at 25 °C using QCM of **Zn-DM** films fabricated at 40 °C via integration of coordination modulation with LPE fabrication process; mixing acetic acid modulator with the H_2DM solution with various r_M ratio

Although detailed molecular-level insights of the origins of this observation are not yet available, it is likely that only the most strongly bound, and therefore the most thermodynamically stable, conformations of cluster binding on the surface are present in upon addition of the modulator (i.e. weaker, loosely bound clusters are removed from the surface). This presumably reduces the number of possible coordination modes of the cluster on the surface, which allows the films to grow in a more uniform and oriented fashion.

The mechanism of film growth by integration of coordination modulation with LPE fabrication is therefore proposed as following. (1) First, acetic acid controls the deposited amount and the orientation of $Zn_4O(OAc)_6$ on the substrate surface. (2) Then, the H_2DM linker is dosed to the substrate leading to an exchange with the acetate groups in the pre-deposited metal SBU. The coordination of the organic linker to the metal node creates the MOF nuclei on the substrate, of which the amount is controlled by the amount of pre-deposited metal SBU in the previous dosing step. (3) Next, the presence of acetic acid in the following deposition step of $Zn_4O(OAc)_6$ modulates the coordination equilibrium between the dosing metal SBU and the free-coordinated groups of the organic linker within the MOF nuclei anchored on the surface and hence leads to the further growth to the bigger MOF crystals with a controlled crystal orientation. (4) Acetic acid prevents the formation of new MOF nuclei with undesired orientation on the surface. In all, the repeating depositions of the fabrication process leads to the further growth of well-defined MOF crystals on the surface and finally creates the oriented and dense MOF films.

3.5 Summary

One of the primary challenges facing the integration of metal-organic frameworks (MOFs) with real-world technologies is the development of enhanced fabrication processes that maximize compatibility with specific device configurations, while maintaining or even improving the performance profile relative to bulk MOF materials. Stepwise liquid-phase epitaxy (LPE) has emerged as an

important method for depositing MOF thin-films on variety of substrate types, although current limitations include challenges in obtaining well-oriented and highly-crystalline thin-films, and the applicability of the technique beyond the most common MOF structure types (e.g. paddlewheel-based MOFs). The foregoing has demonstrated that the integration of coordination modulation with an LPE-based fabrication protocol can provide a significant enhancement in the quality of MOF-based thin films (Figure 3.38). In the **Zn-L** system investigated in this study, addition of even small quantities of a modulator during the metal cluster dosing step has been demonstrated as being beneficial in achieving more crystalline and oriented, high-density MOF thin-films that offer a boost in adsorption capacities of polar adsorbates such as methanol. Such enhancements are expected to be crucial in applications such as molecular sensing, where higher film quality can directly enhance detection limits, response times, estimation of analyte concentrations, and device lifetimes. It is expected that, in a similar fashion to the preparation of bulk MOF crystals, coordination modulation will be applicable to LPE-based thin-film deposition protocols of a wide variety of MOF structure types. The current challenge lies in more fully understanding the molecular interactions that dictate the final properties of the film, and studies that address the deposition of a greater variety of MOFs using a broader scope of modulator types are currently underway.

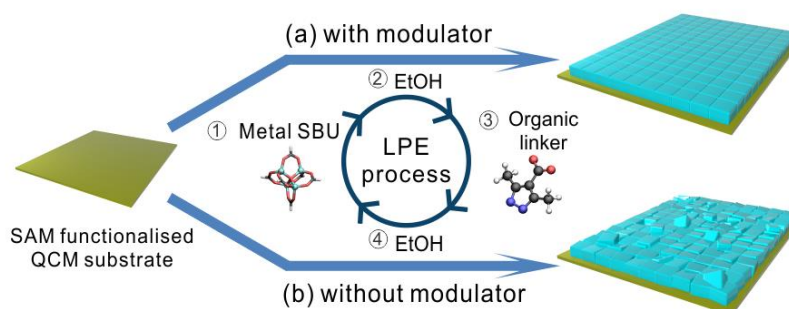


Figure 3.38 Schematic illustration of fabrication of **Zn-DM** films and its analogues by (a) employing coordination modulation method in conjunction with LPE process comparing with (b) by LPE process indicating impact of coordination modulation on the crystal growth and crystal orientation of the films.

3.6References

1. O. M. Yaghi, M. O'Keeffe, N. W. Ockwig, H. K. Chae, M. Eddaoudi and J. Kim, *Nature*, 2003, **423**, 705–714.
2. S. Kitagawa, R. Kitaura and S.-i. Noro, *Angew. Chem. Int. Ed.*, 2004, **43**, 2334–2375.
3. G. Férey, C. Mellot-Draznieks, C. Serre and F. Millange, *Acc. Chem. Res.*, 2005, **38**, 217–225.
4. R. Ricco, C. Pfeiffer, K. Sumida, C. J. Sumby, P. Falcaro, S. Furukawa, N. R. Champness and C. J. Doonan, *CrystEngComm*, 2016, **18**, 6532–6542.
5. V. Stavila, A. A. Talin and M. D. Allendorf, *Chem. Soc. Rev.*, 2014, **43**, 5994–6010.
6. P. Ramaswamy, N. E. Wong and G. K. H. Shimizu, *Chem. Soc. Rev.*, 2014, **43**, 5913–5932.
7. T. Zhang and W. Lin, *Chem. Soc. Rev.*, 2014, **43**, 5982–5993.
8. L. E. Kreno, K. Leong, O. K. Farha, M. Allendorf, R. P. van Duyne and J. T. Hupp, *Chem. Rev.*, 2012, **112**, 1105–1125.
9. Z. Hu, B. J. Deibert and J. Li, *Chem. Soc. Rev.*, 2014, **43**, 5815–5840.
10. Y. Cui, Y. Yue, G. Qian and B. Chen, *Chem. Rev.*, 2012, **112**, 1126–1162.
11. P. Horcajada, R. Gref, T. Baati, P. K. Allan, G. Maurin, P. Couvreur, G. Férey, R. E. Morris and C. Serre, *Chem. Rev.*, 2012, **112**, 1232–1268.
12. S. Furukawa, J. Reboul, S. Diring, K. Sumida and S. Kitagawa, *Chem. Soc. Rev.*, 2014, **43**, 5700–5734.
13. P. Falcaro, R. Ricco, C. M. Doherty, K. Liang, A. J. Hill and M. J. Styles, *Chem. Soc. Rev.*, 2014, **43**, 5513–5560.
14. K. Sumida, K. Liang, J. Reboul, I. A. Ibarra, S. Furukawa and P. Falcaro, *Chem. Mater.*, 2017, **29**, 2626–2645.
15. L. Heinke, M. Tu, S. Wannapaiboon, R. A. Fischer and C. Wöll, *Microporous Mesoporous Mat.*, 2015, **216**, 200–215.
16. M. Tu, S. Wannapaiboon and R. A. Fischer, *Inorg. Chem. Front.*, 2014, **1**, 442–463.

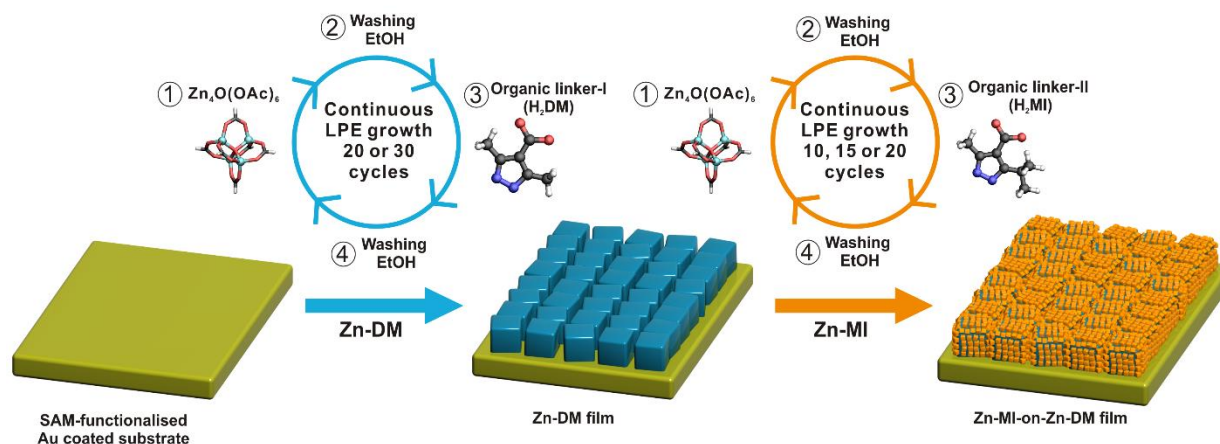
17. L. Heinke, H. Gliemann, P. Tremouilhac and C. Wöll, *The Chemistry of Metal–Organic Frameworks: Synthesis, Characterization, and Applications*, Wiley-VCH, Weinheim, Germany, 2016, pp. 523–550.
18. O. Shekhah, H. Wang, S. Kowarik, F. Schreiber, M. Paulus, M. Tolan, C. Sternemann, F. Evers, D. Zacher, R. A. Fischer and C. Wöll, *J. Am. Chem. Soc.*, 2007, **129**, 15118–15119.
19. O. Shekhah, H. Wang, D. Zacher, R. A. Fischer and C. Wöll, *Angew. Chem. Inter. Ed.*, 2009, **48**, 5038–5041.
20. D. Zacher, K. Yussenko, A. Bétard, S. Henke, M. Molon, T. Lahnorg, O. Shekhah, B. Schüpbach, T. de los Arcos, M. Krasnopolski, M. Meilikhov, J. Winter, A. Terfort, C. Wöll and R. A. Fischer, *Chem. Eur. J.*, 2011, **17**, 1448–1455.
21. O. Shekhah, H. K. Arslan, K. Chen, M. Schmittel, R. Maul, W. Wenzel and C. Wöll, *Chem. Commun.*, 2011, **47**, 11210–11212.
22. B. Liu, M. Tu, D. Zacher and R. A. Fischer, *Adv. Funct. Mater.*, 2013, **23**, 3790–3798.
23. M. Tu, S. Wannapaiboon and R. A. Fischer, *Dalton Trans.*, 2013, **42**, 16029–16035.
24. Z. Wang, J. Liu, B. Lukose, Z. Gu, P. G. Weidler, H. Gliemann, T. Heine and C. Wöll, *Nano Lett.*, 2014, **14**, 1526–1529.
25. L. Heinke, M. Cakici, M. Dommaschk, S. Grosjean, R. Herges, S. Bräse and C. Wöll, *ACS Nano*, 2014, **8**, 1463–1467.
26. T. Tsuruoka, S. Furukawa, Y. Takashima, K. Yoshida, S. Isoda and S. Kitagawa, *Angew. Chem. Inter. Ed.*, 2009, **48**, 4739–4743.
27. A. Umemura, S. Diring, S. Furukawa, H. Uehara, T. Tsuruoka and S. Kitagawa, *J. Am. Chem. Soc.*, 2011, **133**, 15506–15513.
28. S. Diring, S. Furukawa, Y. Takashima, T. Tsuruoka and S. Kitagawa, *Chem. Mater.*, 2010, **22**, 4531–4538.
29. Y. Sakata, S. Furukawa, M. Kondo, K. Hirai, N. Horike, Y. Takashima, H. Uehara, N. Louvain, M. Meilikhov, T. Tsuruoka, S. Isoda, W. Kosaka, O. Sakata and S. Kitagawa, *Science*, 2013, **339**, 193–196.

30. J. Cravillon, R. Nayuk, S. Springer, A. Feldhoff, K. Huber and M. Wiebcke, *Chem. Mater.*, 2011, **23**, 2130–2141.
31. N. Yanai, M. Sindoro, J. Yan and S. Granick, *J. Am. Chem. Soc.*, 2013, **135**, 34–37.
32. J. Cravillon, C. A. Schroder, H. Bux, A. Rothkirch, J. Caro and M. Wiebcke, *CrystEngComm*, 2012, **14**, 492–498.
33. A. Schaate, P. Roy, A. Godt, J. Lippke, F. Waltz, M. Wiebcke and P. Behrens, *Chem. Eur. J.*, 2011, **17**, 6643–6651.
34. H. Fei, S. Pullen, A. Wagner, S. Ott and S. M. Cohen, *Chem. Commun.*, 2015, **51**, 66–69.
35. G. Zahn, P. Zerner, J. Lippke, F. L. Kempf, S. Lilienthal, C. A. Schroder, A. M. Schneider and P. Behrens, *CrystEngComm*, 2014, **16**, 9198–9207.
36. H. Guo, M. Wang, J. Liu, S. Zhu and C. Liu, *Microporous Mesoporous Mat.*, 2016, **221**, 40–47.
37. D. Feng, K. Wang, Z. Wei, Y.-P. Chen, C. M. Simon, R. K. Arvapally, R. L. Martin, M. Bosch, T.-F. Liu, S. Fordham, D. Yuan, M. A. Omary, M. Haranczyk, B. Smit and H.-C. Zhou, *Nat. Commun.*, 2014, **5**:5723.
38. M.-H. Pham, G.-T. Vuong, F.-G. Fontaine and T.-O. Do, *Cryst. Growth Des.*, 2012, **12**, 3091–3095.
39. S. Hermes, T. Witte, T. Hikov, D. Zacher, S. Bahnmüller, G. Langstein, K. Huber and R. A. Fischer, *J. Am. Chem. Soc.*, 2007, **129**, 5324–5325.
40. H. Uehara, S. Diring, S. Furukawa, Z. Kalay, M. Tsotsalas, M. Nakahama, K. Hirai, M. Kondo, O. Sakata and S. Kitagawa, *J. Am. Chem. Soc.*, 2011, **133**, 11932–11935.
41. H. Guo, Y. Zhu, S. Qiu, J. A. Lercher and H. Zhang, *Adv. Mater.*, 2010, **22**, 4190–4192.
42. M. Miyamoto, S. Kohmura, H. Iwatsuka, Y. Oumi and S. Uemiyama, *CrystEngComm*, 2015, **17**, 3422–3425.
43. C. Montoro, F. Linares, E. Q. Procopio, I. Senkovska, S. Kaskel, S. Galli, N. Masciocchi, E. Barea and J. A. R. Navarro, *J. Am. Chem. Soc.*, 2011, **133**, 11888–11891.

44. A. Bétard, S. Wannapaiboon and R. A. Fischer, *Chem. Commun.*, 2012, **48**, 10493-10495.
45. S. Wannapaiboon, M. Tu and R. A. Fischer, *Adv. Funct. Mater.*, 2014, **24**, 2696-2705.
46. G. Sauerbrey, *Z. Phys.*, 1959, **155**, 206-222.
47. S. Wannapaiboon, K. Sumida, K. Dilchert, M. Tu, S. Kitagawa, S. Furukawa and R. A. Fischer, *J. Mater. Chem. A*, 2017, **5**, 13665-13673.

Chapter 4

Hierarchical structuring of MOF thin-films on quartz crystal microbalance substrates for selective adsorption applications



- The results of this chapter are mainly comprised in and reproduced from the following publication, “S. Wannapaiboon, M. Tu, K. Sumida, K. Khaletskaia, S. Furukawa, S. Kitagawa, and R. A. Fischer, *J. Mater. Chem. A*, 2015, **3**, 23385–23394.” with permission from the Copyright © The Royal Society of Chemistry 2015
- Part of the introduction of this chapter are comprised in the review, “L. Heinke, M. Tu, S. Wannapaiboon, R. A. Fischer and C. Wöll, *Microporous Mesoporous Mater.*, 2015, **216**, 200–215.” with permission from the Copyright © 2015 Elsevier Inc.

4.1 Introduction and state of the art

4.1.1 Functionalisation of bulk MOFs

Functionalisation of MOFs with defined physical and chemical properties has become an important issue for the development of MOF-integrating devices.¹ The versatility in the range of precursor components that can be used at the molecular-assembly scale to construct MOF materials offers possibilities for precise manipulation of MOF features such as pore topology, size, shape as well as the coordination space and the reactive centres within the frameworks.² A rational design of the MOF components prior to the direct incorporation into the frameworks via solvothermal synthesis is a straightforward way to introduce functionalities into MOFs and to tailor the desired properties. However, the direct incorporation of some sophisticated functional groups is limited under solvothermal synthetic conditions, and certain substituents at the linker components may hinder the formation of desired MOFs as a result of interference with the desired coordination chemistry of the metal nodes. Post-synthetic modification (PSM) circumvents this limitation by employing an interchange of the functional groups at the organic linkers within the pre-formed MOF structure into the desired functionalities via organic chemical reactions (such as amide-, urea-, and thiourea formations as well as click chemistry) after the MOF formation without deconstruction of the frameworks.³⁻⁷ Hence, various functionalities can be introduced into the MOF structures.

In addition to tuning of the composition of MOFs at the molecular-assembly scale, control and structuring of their physical forms in the mesoscopic and macroscopic scales is known to uniquely affect their properties.⁸⁻¹² The hierarchical ordering of more than one MOF within a single, mesoscopic superstructure (as a so-called *heterostructure*) provides further opportunities to manipulate the characteristics of the system,¹³⁻¹⁷ particularly when a single MOF does not offer all required features for a specific application. Here, heteroepitaxial growth has been used for the deposition of one MOF onto different but structurally-related MOF to produce various heterostructured systems.¹³ This form of heteroepitaxy has been applied successfully in a number of cases. Due to the good lattice matching between both MOF structures, heterometallic core-shell layered-pillared MOF crystals¹³ and core-shell IRMOF crystals consisting of different linkers¹⁴ have been

successfully synthesized. In the case of layered-pillared MOFs, the use of two pillar linkers with different lengths allow the heteroepitaxial growth of the selective overlaying MOFs only at the lattice-matching facets of the pre-formed seeding MOF. In this example, the epitaxy occurs through the connection of the metal-dicarboxylate layered structures with the extended pillar linkers along the *c*-axis, which results in the hybrid BAB-type, rod-like crystals. The matching of the lattice parameters and the coordination chemistry is critical for the heteroepitaxial growth to succeed under solvothermal conditions.¹⁵

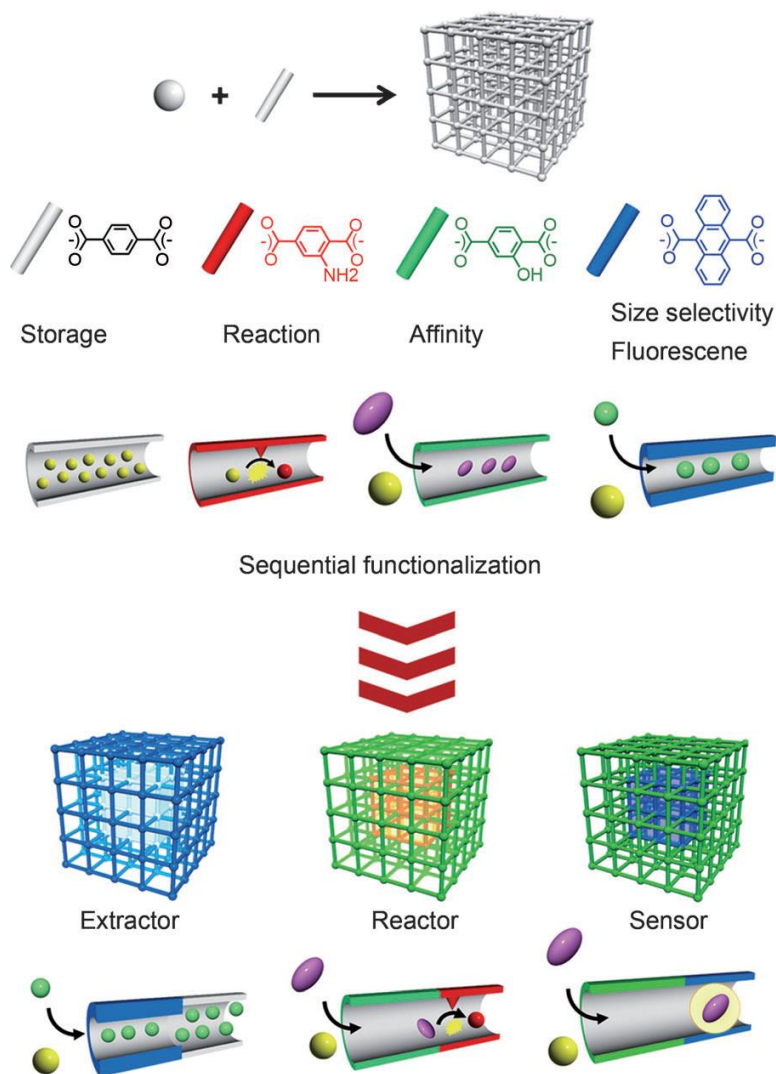


Figure 4.1 Conceptual illustration of sequential (or spatial-controlled) functionalization of multi-component MOF crystals indicate the synergistic features of the hybrid systems for various applications. Reprint with permission. Copyright © 2011 WILEY-VCH Verlag GmbH & Co. KGaA.¹⁶

These multi-component MOFs offer functionalities resulting both from the simple addition of the components' features (characteristics of each MOF component) and from a synergistic combination, which is achieved through a controlled spatial arrangement of the MOF components (Figure 4.1).¹⁶⁻¹⁷ For example, the variation of the size of the organic linkers in the core-shell layered-pillared MOF leads to such promising characteristics of the hybrid MOF crystal, exhibiting the size-selective separation (molecular sieve) by the shell MOF component (with smaller pore opening window) and the preservation of a high-capacity storage container by the core MOF component (with larger pore opening and volume).¹⁶ Furthermore, the combination of PSM into this epitaxial growth of the multi-component MOFs leads to the spatially-specific modification only at the targeted MOF component consisting of the reactive groups for PSM (in this case, the shell component).¹⁷ As a result, the PSM-modified core-shell MOF crystal provides a selective adsorption of guest molecules with different size and/or chemical functionalities, which do not be observed in the pre-modified case. These achievements enlarge the potential for MOF applications.

4.1.2 Stepwise LPE process as a tool for functionalisation of MOF films

The structuring of MOFs in two-dimensional superstructures (e.g. thin films) is an emerging field that has received an increased attention over the last few years due to their potential use in membranes, coatings, quartz crystal microbalance (QCM)-based and microcantilever-based sensors.¹⁸⁻²⁰ Various methods have been developed to integrate MOF materials into devices by processing MOFs as thin films on various substrates and patterning them for specific applications.²¹ In particular, stepwise liquid-phase epitaxial (LPE) growth technique (also known as layer-by-layer deposition)²² is a potentially versatile method for preparing MOF thin films. In LPE fabrication process, the substrate is alternately dosed with metal and organic precursor solutions leading to a systematic control of MOF thin-film properties by optimising the crystallisation conditions and the number of growth cycles.^{23,24} The overall performance of MOF materials including thin films could be improved by such a proper selection of functionalities within the frameworks, which could be tailored in both microscopic molecular-assembly level and in mesoscopic structuring-architecture scale. Stepwise LPE growth strategy is an attractive

method to transfer the concepts of functionalisation from bulk MOF synthesis to thin-film processing.

Concerning the **microscopic molecular-assembly level**, a straightforward way to functionalise MOF thin-films is a use of pre-designed MOF precursor components e.g. the metal secondary building units (SBUs) and the functionalised organic linkers in the LPE fabrication process, so-called controlled-SBU approach. Moreover, the PSM is also applied to modify the functionalities of the LPE-fabricated MOF films at both the internal and external surfaces. Firstly, the organic linkers containing the reactive groups for PSM such as amino- or azido- pendent sidechains are incorporated into the MOF films by the LPE process. Further, the LPE-fabricated MOF films are exposed to the PSM reagents resulting in a modification of chemical functions within the framework structures. For examples, the LPE-fabricated $\text{Cu}_2(\text{NH}_2\text{-bdc})_2(\text{dabco})$ film ($\text{NH}_2\text{-bdc}$ = 2-amino-benzene-1,4-dicarboxylate, dabco = 1,4-diazabicyclo-(2.2.2)-octane) is post-synthetic modified by exposing to isocyanates and/or isothiocyanates vapour at room temperature. The free amino pendent sidechains in the MOF framework are reacted with the PSM reagents and form strong covalent urea and thiourea bonds, leading to a chemical modification of the internal surface within the MOF film.²⁵ Interestingly, the use of PSM reagent so-called 1-ferrocenylmethylisocyanate provides an opportunity to modify the MOF film by mean of grafting the ferrocene moieties into the framework which can be used for electrochemical applications.²⁶ Moreover, the click chemistry is also applied for PSM of the MOF films consisting of azido pendent groups of the organic linkers e.g. $\text{Zn}_2(\text{N}_3\text{-bdc})_2(\text{dabco})$ film ($\text{N}_3\text{-bdc}$ = 2-azido-benzene-1,4-dicarboxylate) by using the selected alkynes as the PSM reagents.²⁷ PSM can be also used to modify the MOF film only at the external surface in order to alter the surface properties (such as hydrophilicity/hydrophobicity and affinity) while maintain the adsorption capacity of the inner pore space (Figure 4.2).²⁸ In this case, the organic linkers containing reactive groups are incorporated into the MOF film at the latest step of LPE fabrication. Then, the fabricated film is exposed to the PSM reagent with a larger size than the pore opening of MOF to modify the framework only at the outer surface without any change in the internal surface. In general, the crystallinity and orientation of the SURMOFs is not affected by performing the PSM reaction (no significantly change in the XRD data).

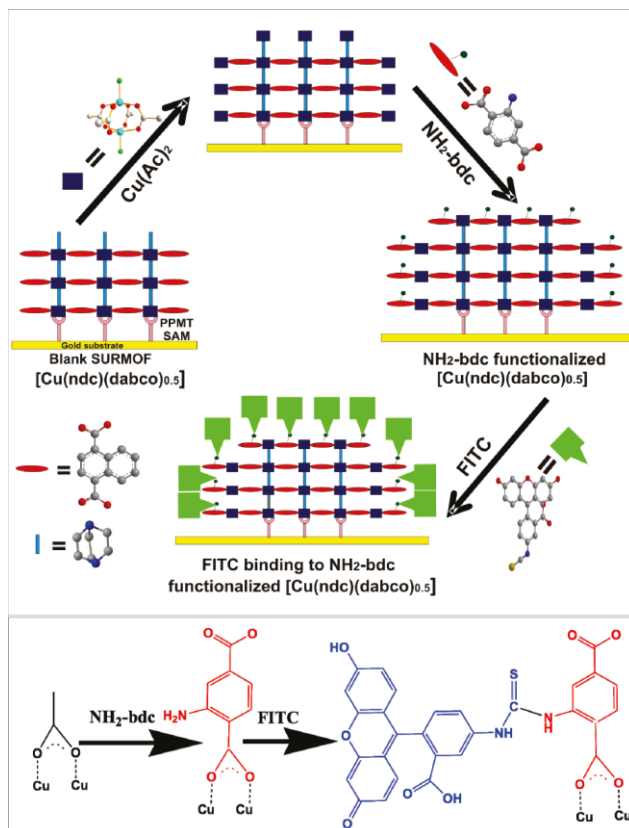


Figure 4.2 Stepwise approach for external surface functionalisation of $\text{Cu}_2(\text{ndc})_2(\text{dabco})$ (top), the incorporation of reactive organic linker $\text{NH}_2\text{-bdc}$ at the latest step of LPE process (middle) and the PSM reaction of $\text{NH}_2\text{-bdc}$ with fluorescein isothiocyanate (FITC) (bottom). Reprint with permission. Copyright © 2011 American Chemical Society.²⁸

In the **mesoscopic structuring-architecture scale**, the stepwise LPE growth strategy is an attractive method for the fabrication of heterostructured MOF films, since the precursors can be switched between those at a defined step for the formation of different MOFs during the film fabrication process.^{29,30} Unlike the solvothermal syntheses of bulk crystals, LPE provides a straightforward control of location and distribution of the added functionalities through the variation of deposition sequences and the number of repeated cycles. Hence, heterostructured MOF films can be fabricated with a controlled distribution of the functionalities along the growth direction. Using this LPE method, several structurally-related MOFs,²⁹⁻³¹ and even some MOFs with significantly mismatched lattice parameters³² and incompatible network structures³³ have been prepared with a precise spatial control via an appropriate programming of the sequence and cycling frequency of the deposition process.

4.1.3 Growth and Functions of paddlewheel-based heterostructured MOF films

Paddlewheel-based layered-pillared MOFs of the type $M_2(L)_2(P)$ (M = paddlewheel-based metal ion e.g. Cu^{2+} and Zn^{2+} , L = anionic dicarboxylate layer linkers and P = neutral bidentate nitrogen pillar linkers) have known as the well-investigated systems in MOF thin-film (also called as surface-mounted MOFs or SURMOFs) research, especially using the stepwise LPE method as the fabrication process. Mesoscopic structuring of two or three paddlewheel-based MOFs as heterostructured SURMOFs with a precise spatial control of the components have been thoroughly investigated. Various analogues of dicarboxylate linkers and metals are integrated in the heterostructured SURMOFs e.g. $Cu_2(F_4bdc)_2(dabco)$ -on- $Cu_2(ndc)_2(dabco)$, $Zn_2(BME-bdc)_2(dabco)$ -on- $Cu_2(ndc)_2(dabco)$ ²⁹ and $Zn_2(ndc)_2(dabco)$ -on- $Cu_2(ndc)_2(dabco)$ ³⁰ (note that, F_4bdc = tetrafluorobenzene-1,4-dicarboxylate, $BME-bdc$ = 2,5-bis(2-methoxyethoxy)-1,4-benzene dicarboxylate, and ndc = naphthalene-1,4-dicarboxylate) have been successfully fabricated by the LPE process.

An increase of the intensity at 001 diffraction-peak without a presence of additional XRD peaks implies that the heteroepitaxial growth maintains the crystal orientation of the pre-formed SURMOF.^{29,30} Moreover, the perfect orientation along the growth direction (perpendicular to the substrate surface) could be shown by using a four-circle synchrotron X-ray diffractometer for scanning the heterostructured SURMOF along the perpendicular direction to the sample stage (χ scan).³⁰ The existence of the heterostructured components are further examined by means of an increase of the water contact angle due to a presence of the fluorinated (thus hydrophobic) top layer,²⁹ an increase of film thickness observed by the change of refractive index unit (RIU) based on *in-situ* surface plasmon resonance (SPR) spectroscopy as well as the atomic force microscopy (AFM),³⁰ and the combined characteristic signals from the two MOF components in the X-ray photoelectron (XPS) and the infrared reflection absorption (IRRAS) spectra.^{29,30} These studies have demonstrated that LPE allows fabricating heterostructured SURMOFs with a control on a mesoscopic and microscopic scale to obtain well-defined thin-film topologies with specific crystallographic orientations.

Apart from the aforementioned heterostructured SURMOFs consisting of the lattice-matching MOF layers, the LPE technique has been extensively used to grow MOF films with different lattice parameters and topologies on top of each other to form coherent heterostructured SURMOFs. For example, heterostructured SURMOF comprising three layers of distinct isorecticular SURMOF-2 structures – despite the large lattice mismatches of about 20% has been successfully fabricated by the LPE spraying procedure. The XRD patterns from this hybrid material show a perfect [001]-related crystal orientation for all SURMOF layers. The selective loading of $\text{Eu}(\text{bzac})_3\text{bipy}$ compound (bzac = 1-benzoylacetone and bipy = 4,4'-bipyridine) allows to differentiate the different layers by generating the contrast in the SEM images. Quantum theoretical analysis has provided justification for the unexpected formation of heterostructured SURMOFs with large lattice-mismatch. Possible vacancies at the MOF—MOF interface resulting from lattice mismatch can be capped by coordination with residual acetate groups. Moreover, the low elastic constant of the MOF materials can facilitate the delocalization of the mismatch, resulting in a distribution of the total stress over a large area in order to produce a small local stress within the material.³²

Moreover, two different MOFs with incompatible network structures can be also combined as a unit by applying the LPE procedure. $\text{Cu}_3(\text{btc})_2$ (also known as HKUST-1) with a face-centred-cubic structure (space group $Fm\bar{3}m$) can be fabricated on top of the pre-deposited, specific-oriented film of a type $\text{Cu}_2(\text{ndc})_2(\text{dabco})$ with a tetragonal symmetry (space group $P4/mmm$).³³ In details, $\text{Cu}_2(\text{ndc})_2(\text{dabco})$ is firstly grown on a pyridyl-terminated substrate, which allows the MOF film to preferably grow along the [001] direction and provide a dabco-pillared terminated layer at the outer surface of the fabricated film. This top layer further acts like a pyridyl-terminated surface, which is used to seed the nucleation of the $\text{Cu}_3(\text{btc})_2$ films and direct their growth along the [111] direction. The presence of these two crystalline MOF films as a synergistic heterostructure is confirmed by cross-sectional SEM images and by XRD measurements which reveal the peaks related to the [001]-orientation of $\text{Cu}_2(\text{ndc})_2(\text{dabco})$ and to the [111]-orientation of $\text{Cu}_3(\text{btc})_2$. Both films contribute to the gas adsorption properties of the material, albeit the top film is exposed first and may block any uptake by the core layer, as shown by QCM.³³

Multiple functionalities can be integrated into heterostructured SURMOFs which are of interest for a large field of promising applications, especially in sensing and separation.²⁴ However, some functional building blocks can hinder the formation of MOF when directly used in the LPE fabrication process. Hence, PSM is applied to specifically tune some components within the pre-formed heterostructured SURMOFs in order to obtain the desired functionalities.³¹ For example, Liu *et al.* incorporated reactive -NH_2 -functional groups at a controlled depth in highly oriented heterostructured SURMOFs resulting in core-shell (A-B) and core-shell-shell (A-B-C) SURMOF structures (A: $\text{Cu}_2(\text{bdc})_2(\text{dabco})$, B: $\text{Cu}_2(\text{NH}_2\text{-bdc})_2(\text{dabco})$ and C: $\text{Cu}_2(\text{ndc})_2(\text{dabco})$). The presence of -NH_2 groups within the heterostructured SURMOFs is identified by the N-H vibration bands using IRRAS (at 3500 and 3380 cm^{-1}). These -NH_2 groups within the B layer allow a localized PSM by using 4-fluorophenyl isothiocyanate (FPI). The isothiocyanate groups of FPI molecules react with the -NH_2 groups to form robust thiourea bonds and hence modify the frameworks only at the B layer. By *in-situ* QCM measurements during the FPI loading, complex kinetic uptake behaviours by the heterostructured SURMOFs could be revealed. The fine tuning of the pore structure within the material by the combined hetero-LPE-PSM methodology can have great effects on the kinetic uptake of guest molecules.³¹

Moreover, in the case of combining MOFs possessing different pore properties, the spatial control can lead to enhanced characteristics compared to a simple physical mixture of the same frameworks in a random fashion. For example, the spatial-controlled structuring of heterostructured SURMOFs facilitates such a promising function for selective adsorption and diffusion into the materials.^{34,35} Tu *et al.* have used the LPE-PSM method to functionalize heterostructured SURMOFs for selective adsorptions. B@A heterostructured SURMOF of $\text{Cu}_2(\text{NH}_2\text{-bdc})_2(\text{dabco})@\text{Cu}_2(\text{bdc})_2(\text{dabco})$ have been fabricated and subsequently modified by PSM with *tert*-butyl isothiocyanate (tBITC). Here, the PSM leads to the chemical modification of the outer layer (B) of the heterostructured SURMOF (Figure 4.3), and induces the size-selective adsorption of methanol and hexane over cyclohexane. Moreover, the total uptake of hexane in the tBITC@B@A SURMOF is higher than for a tBITC@B SURMOF of comparable thickness, owing the contribution of the larger pore volume of the unmodified core component (A). This results again emphasize the advantages of heterostructured SURMOFs.³⁴

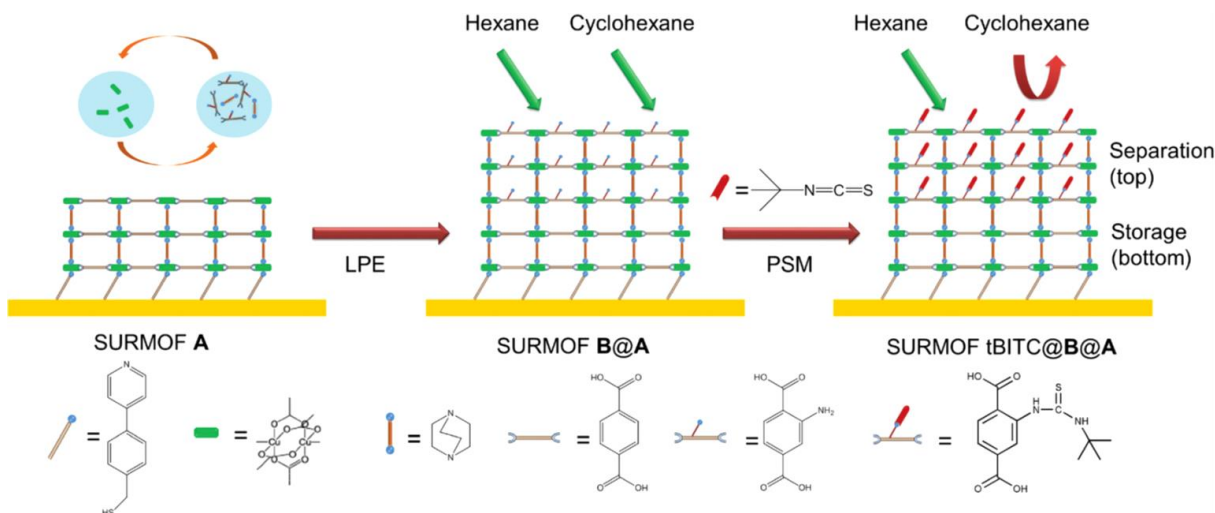


Figure 4.3 Schematic illustration of programmed functionalization of SURMOFs via LPE-PSM procedure: Initially, SURMOF $\text{Cu}_2(\text{bdc})_2(\text{dabco})$ (A) was deposited on pyridyl-terminated SAM on Au covered QCM substrates using the LPE method. Sequentially, SURMOF $\text{Cu}_2(\text{NH}_2\text{-bdc})_2(\text{dabco})$ (B) was deposited on A using the LPE procedure giving rise to SURMOF B@A. Finally, SURMOF B@A was modified by PSM with tert-butyl isothiocyanate (tBITC). Reprint with permission. Copyright © The Royal Society of Chemistry 2013.³⁴

The influence of the spatial arrangement of each component within the heterostructured SURMOFs on the integrated properties of materials has been highlighted by the work of Meilikhov *et al.*³⁵ Two layered-pillared SURMOF-on-SURMOF structures, in which one component contain the $-\text{NH}_2$ pendent groups within the organic linker (B) and one without the reactive groups (A), have been fabricated by the same combined LPE-PSM method but with the inversed spatial ordering. The PSM with succinic acid anhydride modifies the $-\text{NH}_2$ containing SURMOF block (change from B to C) leading to a reduction of the pore openings. After LPE-PSM process, two types of SURMOFs-on-SURMOFs with the same components but inversed ordering are obtained, in which the reduced-pore component is at the shell (C@A) and at the core (A@C), respectively. Probing the two type films with multiple volatile organic vapours (VOCs) adsorptions using QCM instrument, the C@A SURMOF exhibit a selective adsorption of methanol from the mixture of methanol/hexane, whereas no selectivity is observed in the case of A@C SURMOF. This stresses the role of the spatial arrangement of the components within the heterostructured SURMOFs on the adsorption properties.³⁵

Remote control is one of the key challenges for intelligent, functional materials. A very promising opportunity for the realization of the remote-controllable switching of physical and chemical properties is the incorporation of photoswitchable molecules, like azobenzene, into the MOFs structure. Using LPE process photo-switchable pendant groups are incorporated into the outer layer of a film and indicates a pathway to control the adsorption permeability by light irradiation. In this way, a two-layered heterostructured SURMOF consisting of a passive bottom layer $\text{Cu}_2(\text{bpdc})_2(\text{bipy})$ and a photoswitchable top layer $\text{Cu}_2(\text{azo-bpdc})_2(\text{bipy})$ (bpdc = 4,4'-biphenyldicarboxylate and azo-bpdc: 3-azobenzene-4,4'-biphenyldicarboxylate) was prepared by LPE process. It can be demonstrated that the permeability of the top-layer can be changed by switching the azobenzene groups from its basic *trans* state to the *cis* state by UV light and back by red light. This means the bottom layer acts as a molecular container and the top layer acts as valve which can open and close the container. The release of a probe molecule (1,4-butanediol) could be initiated by illuminating the sample with light and switching the azobenzene side groups in the top layer from *cis* to *trans*.³⁶

Despite this emerging interest in heterostructured MOF thin-films, fundamental investigations into their adsorptive properties still remains limited to a small number of systems, and the versatility of the LPE growth technique for the fabrication of heterostructured systems is currently not well established. In order to advance both these aspects, we have selected the robust $\text{Zn}_4\text{O}(\text{L})_3$ -based MOF series (**Zn-L**, L = 3-alkyl-5-alkyl-4-carboxypyrazolate),³⁷ for which the stepwise LPE method has been previously used (in both static batch-wise immersion³⁸ and a continuous flow mode³⁹) to generate pure (single-phase) MOF thin-films integrated with QCM. Thus, we herein fabricate heterostructured **Zn-L** films with an object of achieving high adsorption selectivity via hierarchical positioning of the isostructures. The growth of a MOF with smaller pore openings as a shell layer is shown to provide adsorptive selectivity, while the presence of a larger-pore MOF as a core layer provides a high storage capacity of guest molecules. The LPE fabrication parameters (i.e. number of fabrication cycles for each individual MOF component) are systematically optimised to obtain well-defined core-shell architectures of the heterostructured films that provide a high adsorptive selectivity and a specific molecular recognition of the adsorbed guest.⁴⁰

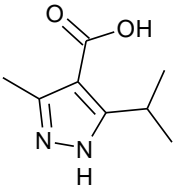
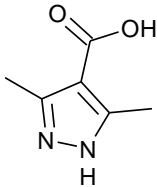
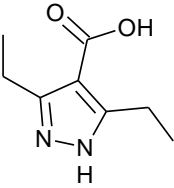
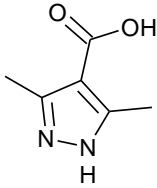
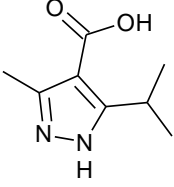
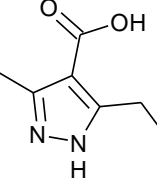
4.2 Hierarchical structuring of heterostructured Zn-L thin-films

Stepwise LPE growth is an attractive method for introducing the concepts of heterostructured bulk MOFs to thin films via sequential and controlled deposition cycles of the metal and the organic precursors to the substrate.²⁹ The precursors can be changed at any time (to introduce a functionalised analogue of an organic linker for example) during the thin-film fabrication at a pre-programmed point to induce growth of other MOFs on a pre-deposited parent MOF film. However, the range of MOFs that have been processed via the LPE method is very limited mainly of the layered-pillared SURMOFs (discussed in the previous section), and warrants further studies to understand its versatility. Here, size-based adsorption permeability was demonstrated via post-synthetic modification of the amino-containing SURMOF outer layer.^{34,35} However, the films were not chemically robust (particularly in the presence of moisture), limiting their potential for practical uses under ambient conditions.²¹ This has prompted investigations of a similar type in the context of other more stable materials that could be amenable for use under biologically or industrially relevant conditions.

In this work, we selected the more-chemically-robust, MOF-5-isotype $\text{Zn}_4\text{O}(\text{3,5-dimethyl-4-carboxypyrazolate})_3$ (**Zn-DM**) and its 3,5-dialkyl substituted analogues for fabrication as heterostructured MOF thin-films on QCM substrates by LPE method. Based on our previous work, the formation of thin-films of **Zn-DM** and its isostructural thin-films was proposed to occur via an island growth mode during the nucleation stage, followed by an overgrowth of the pre-formed MOF crystallites to form dense MOF films.³⁹ Therefore, we surmise that heterostructured thin-films could be formed with a variety of isostructural compounds in a core-shell architecture. Herein, the LPE fabrication process is optimised to achieve a well-controlled hierarchical arrangement of individual MOF components within heterostructured films. In particular, the small-pore $\text{Zn}_4\text{O}(\text{3-methyl-5-isopropyl-4-carboxypyrazolate})_3$ (**Zn-MI**) and $\text{Zn}_4\text{O}(\text{3,5-diethyl-4-carboxypyrazolate})_3$ (**Zn-DE**) frameworks are respectively deposited as a size selective layer upon larger-pore **Zn-DM** and $\text{Zn}_4\text{O}(\text{3-methyl-5-ethyl-4-carboxypyrazolate})_3$ (**Zn-ME**) layers. Three different types of the shell-on-core heterostructured films were produced: **Zn-MI-on-Zn-DM**, **Zn-DE-on-Zn-DM** and **Zn-MI-on-Zn-ME** (see the summary in Table 4.1). The number of

deposition cycles of each individual MOF component was varied from 10 to 30 cycles. In the following discussion, we employ the notation “MOF(x)-on-MOF(y)”, where x and y represent the number of deposition cycles carried out in forming the shell and core MOFs, respectively. For example, **Zn-MI(20)-on-Zn-DM(20)** heterostructured film refers to a sample in which **Zn-DM** is fabricated for 20 cycles on a functionalised QCM substrate, followed by **Zn-MI** for 20 cycles (Figure 4.4). During thin-film fabrication, the change in QCM frequency was recorded in-situ in order to monitor the film growth. The performance of these films in the context of selective adsorption properties are then systematically investigated using a QCM apparatus, demonstrating unique properties stemming from the nature of the structuring.

Table 4.1 Heterostructured shell-on-core **Zn-L** thin-films reported in this study

Heterostructured shell-on-core MOF films	Organic linkers used for the thin film fabrication at	
	Shell (outer layer)	Core (inner layer)
1. Zn-MI-on-Zn-DM		
<ul style="list-style-type: none"> • Zn-MI(10)-on-Zn-DM(20) • Zn-MI(15)-on-Zn-DM(20) • Zn-MI(20)-on-Zn-DM(20) • Zn-MI(10)-on-Zn-DM(30) • Zn-MI(15)-on-Zn-DM(30) • Zn-MI(20)-on-Zn-DM(30) 		
2. Zn-DE-on-Zn-DM		
<ul style="list-style-type: none"> • Zn-DE(10)-on-Zn-DM(20) • Zn-DE(20)-on-Zn-DM(20) • Zn-DE(10)-on-Zn-DM(30) • Zn-DE(20)-on-Zn-DM(30) 		
3. Zn-MI-on-Zn-ME		
<ul style="list-style-type: none"> • Zn-MI(20)-on-Zn-ME(20) • Zn-MI(20)-on-Zn-ME(30) 		

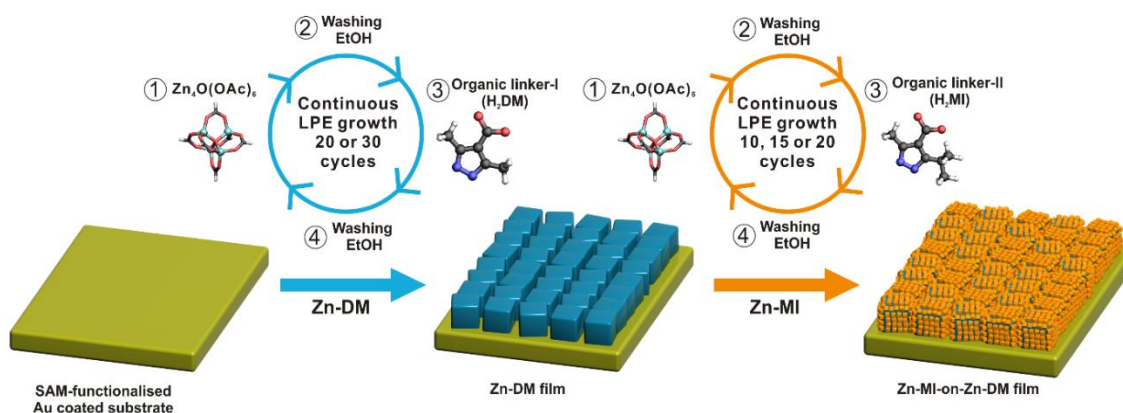


Figure 4.4 Schematic illustration of the continuous stepwise LPE fabrication of heterostructured **Zn-L** thin films. Note that while a **Zn-MI-on-Zn-DM** heterostructure is used as an example, the other systems described in this work follow the same basic procedure. A SAM-functionalised Au-coated substrate is alternately exposed to solutions of $Zn_4O(OAc)_6$ (Step 1) and 3,5-dimethyl-4-carboxypyrazole (H_2DM) (Step 3) with an intermediate EtOH washing step (Step 2 and 4) to induce a uniform film of **Zn-DM** (illustrated in blue colour). Then, the same procedure is repeated using 3-methyl-5-isopropyl-4-carboxypyrazole (H_2MI) to further grow a **Zn-MI** layer (illustrated in orange colour) on the original film, resulting in a **Zn-MI-on-Zn-DM** heterostructured film. Reprint with permission. Copyright © The Royal Society of Chemistry 2015.⁴⁰

4.2.1 Stepwise LPE growth of Zn-L heterostructured films

During the fabrication procedure of the heterostructured **Zn-L** films by stepwise LPE method at 40 °C, the QCM frequency change (which is proportional to the mass uptake on QCM substrate based on Sauerbrey equation⁴¹) was monitored. The temporal frequency change during growth for **Zn-MI-on-Zn-DM** films using various deposition cycle counts for each component are presented in Figure 4.5. The overall mass of the respective MOF components linearly increases with the number of deposition cycles. However, the change in the rate of frequency change upon switching the linker suggests that the growth rate of the **Zn-DM** inner layer is significantly higher than that of the **Zn-MI** outer layer, presumably due to the different growth behaviour of the two MOFs.³⁹ Note that, there is a deviation of the deposited amount of the same MOF film (e.g **Zn-DM**) in different experiments, which could be attributed to the non- self-terminated “layer-by-layer” growth mechanism of these MOF films under this chosen LPE condition (Figure 4.6) as well as the quality of the functionalised substrate.

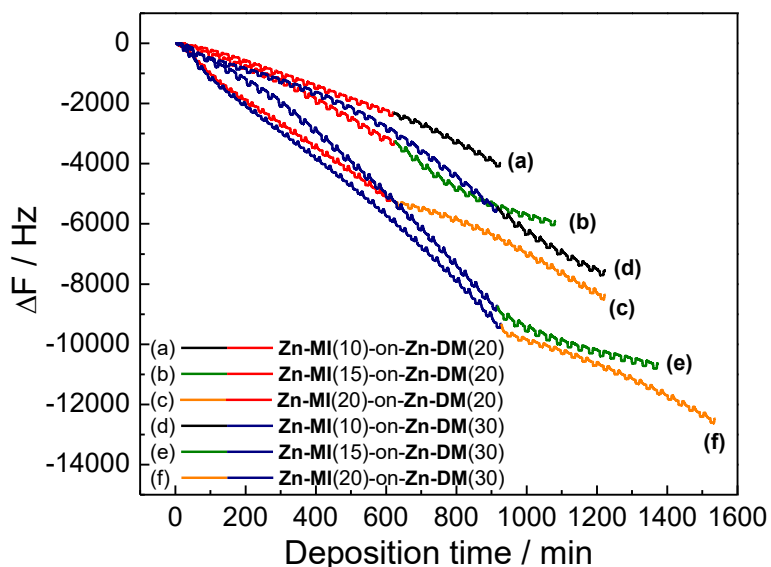


Figure 4.5 In-situ monitoring of the QCM frequency change as a function of deposition time during the continuous LPE growths of the **Zn-MI-on-Zn-DM** heterostructured films with various number of deposition cycles in each MOF component.

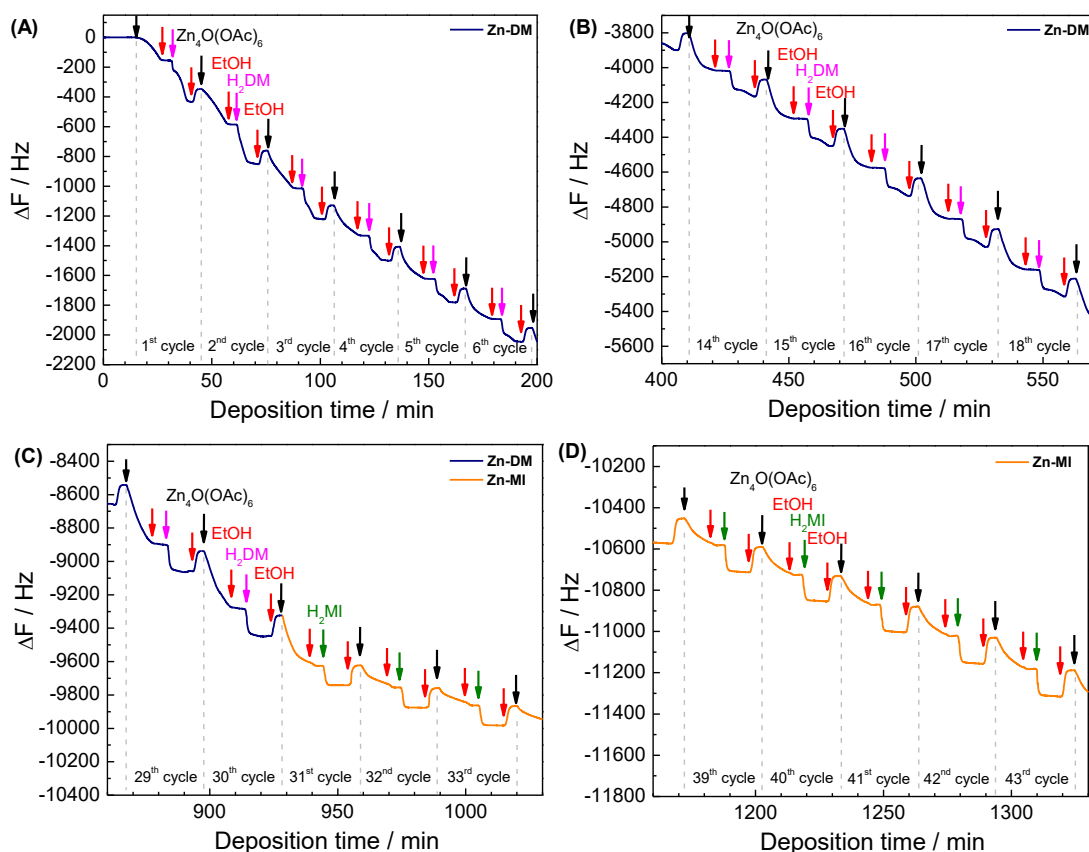


Figure 4.6 In-situ monitoring of the QCM frequency change as a function of deposition time during the continuous LPE growth of the **Zn-MI(20)-on-Zn-DM(30)** heterostructured film at different sections corresponding to the growth curve in Figure 4.5(f).

4.2.2 Characterisations of LPE-fabricated Zn-L heterostructured films

The crystallinity of the heterostructured MOF thin films was characterised by grazing incidence X-ray diffraction (GIXRD) using a synchrotron X-ray source ($\lambda = 1.00130 \text{ \AA}$). The out-of-plane cuts of the obtained GIXRD patterns for different compositions of the **Zn-MI-on-Zn-DM** thin-films are shown in Figure 4.7. The corresponding data for the **Zn-MI-on-Zn-ME** and **Zn-DE-on-Zn-DM** systems are also displayed in Figure 4.8. These data indicate the formation of highly-crystalline films with a preferential orientation in the [100] direction, corresponding with the attachment of the crystallites to the substrate via one of their cubic facets. The isostructural nature of the two components within the heterostructured films (and almost identical unit cell dimensions³⁹; **Zn-DM**: $a = 20.036 \text{ \AA}$, **Zn-MI**: $a = 20.150 \text{ \AA}$) leads to just a single set of peaks that are well-matched with the diffraction peak positions for the phase-pure **Zn-DM** material.

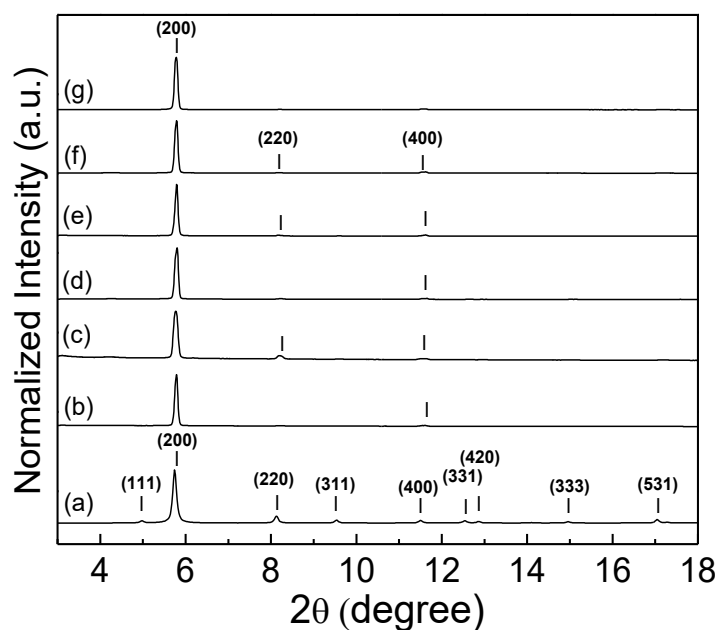


Figure 4.7 (a) Simulated powder X-ray diffraction pattern for bulk **Zn-DM** ($\lambda = 1.00130 \text{ \AA}$); and out-of-plane cuts from 2D-GIXRD patterns (corresponding to the crystalline structure along the film growth direction) using a synchrotron X-ray source of $\lambda = 1.00130 \text{ \AA}$ for (b) **Zn-MI(10)-on-Zn-DM(20)**, (c) **Zn-MI(15)-on-Zn-DM(20)**, (d) **Zn-MI(20)-on-Zn-DM(20)**, (e) **Zn-MI(10)-on-Zn-DM(30)**, (f) **Zn-MI(15)-on-Zn-DM(30)**, (g) **Zn-MI(20)-on-Zn-DM(30)**. The numbers within the parentheses in the figure indicate the Miller indices of the crystal planes. Reprint with permission. Copyright © The Royal Society of Chemistry 2015.⁴⁰

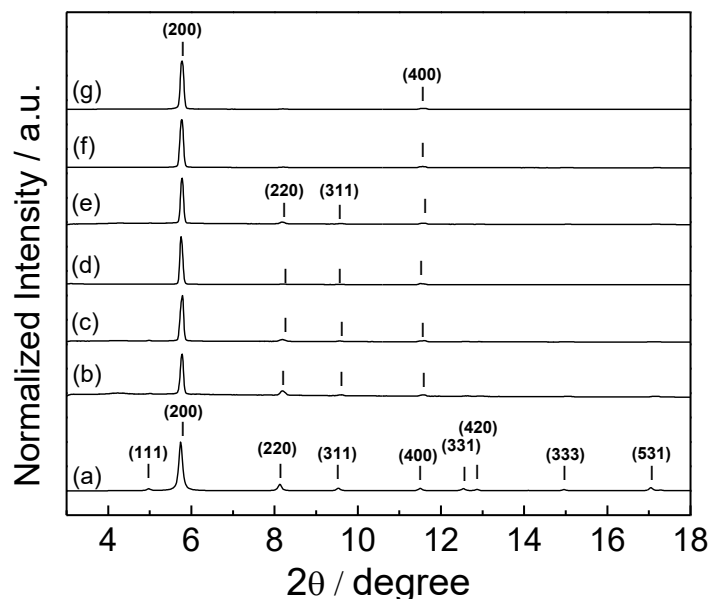


Figure 4.8 (a) Simulated powder X-ray diffraction pattern for bulk **Zn-DM** ($\lambda = 1.00130 \text{ \AA}$); and out-of-plane cuts from 2D-GIXRD patterns using a synchrotron X-ray source of $\lambda = 1.00130 \text{ \AA}$ for (b) **Zn-MI(20)-on-Zn-ME(20)**, (c) **Zn-MI(20)-on-Zn-ME(30)**, (d) **Zn-DE(10)-on-Zn-DM(20)**, (e) **Zn-DE(20)-on-Zn-DM(20)**, (f) **Zn-DE(10)-on-Zn-DM(30)**, and (g) **Zn-DE(20)-on-Zn-DM(30)**. The numbers within the parentheses in the figure indicate the Miller indices of the crystal planes.

In order to demonstrate the presence of both MOF components, infrared reflection absorption spectra (IRRAS) were collected for the heterostructured films (Figure 4.9 to Figure 4.11). The transmittance bands belonging to both components (grey bands) are observed at the same frequencies in both the homostructured and heterostructured films. However, the intensity ratio of these transmittance bands in the heterostructured films is deviated from the one observed in each single-component film, highlighting the combining of the signal from both MOF components. Moreover, the IR bands, which are characteristic to each MOF component (highlighted as blue and yellow bands), are synergistically presented in the heterostructured films (see Figure 4.10 for the data corresponding to **Zn-DE-on-Zn-DM** films). This observation indicates the existence of both MOF components within the thin-films. Importantly, this data, taken together with the X-ray diffraction data described above, illustrate the formation of preferred oriented heterostructured films for each of the combination of MOF components surveyed in this research work.

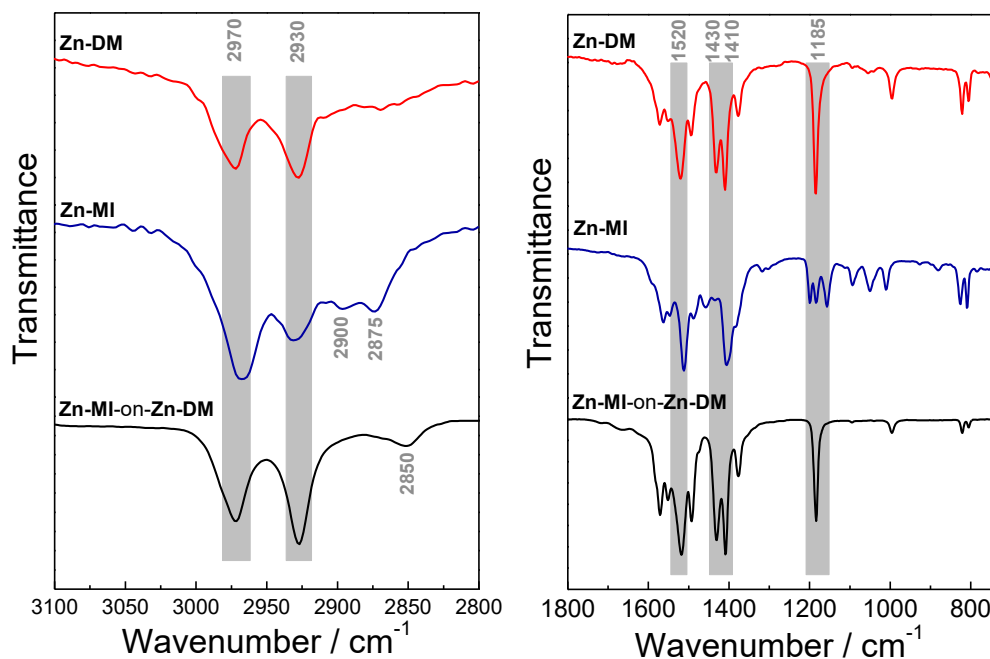


Figure 4.9 Example of IRRAS spectra of **Zn-MI-on-Zn-DM** heterostructured films indicates the position of the IR vibrational signals and the variation of relative transmittance at some wave numbers as a combination between the IRRAS spectra of the corresponding **Zn-DM** and **Zn-MI** MOF films.

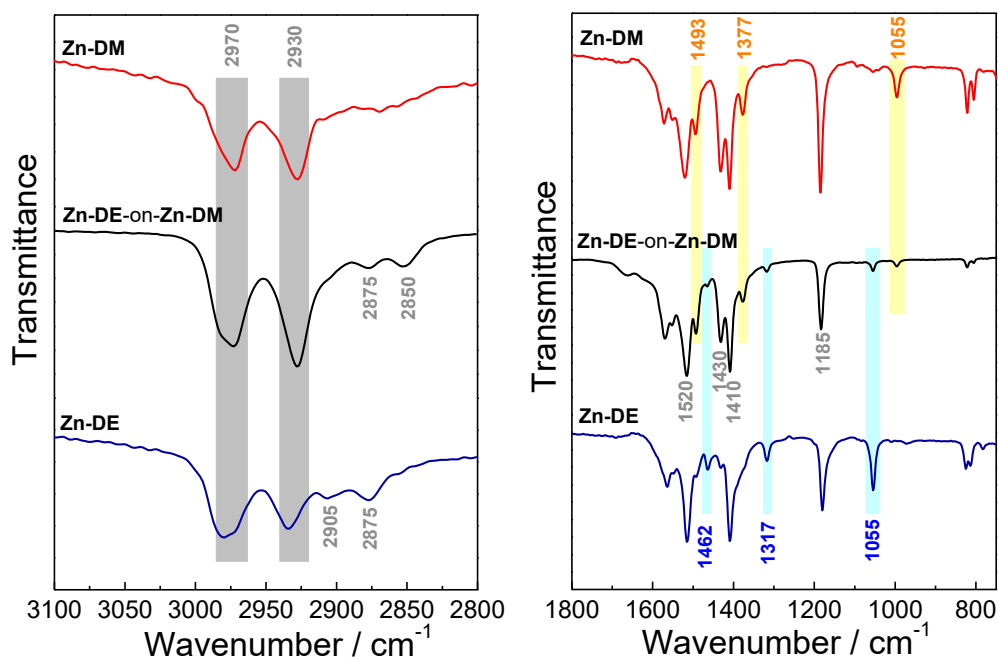


Figure 4.10 Example of IRRAS spectra of **Zn-DE-on-Zn-DM** heterostructured films indicates the position of the IR vibrational signals and the variation of relative transmittance at some wave numbers as a combination between the IRRAS spectra of the corresponding **Zn-DM** and **Zn-DE** MOF films.

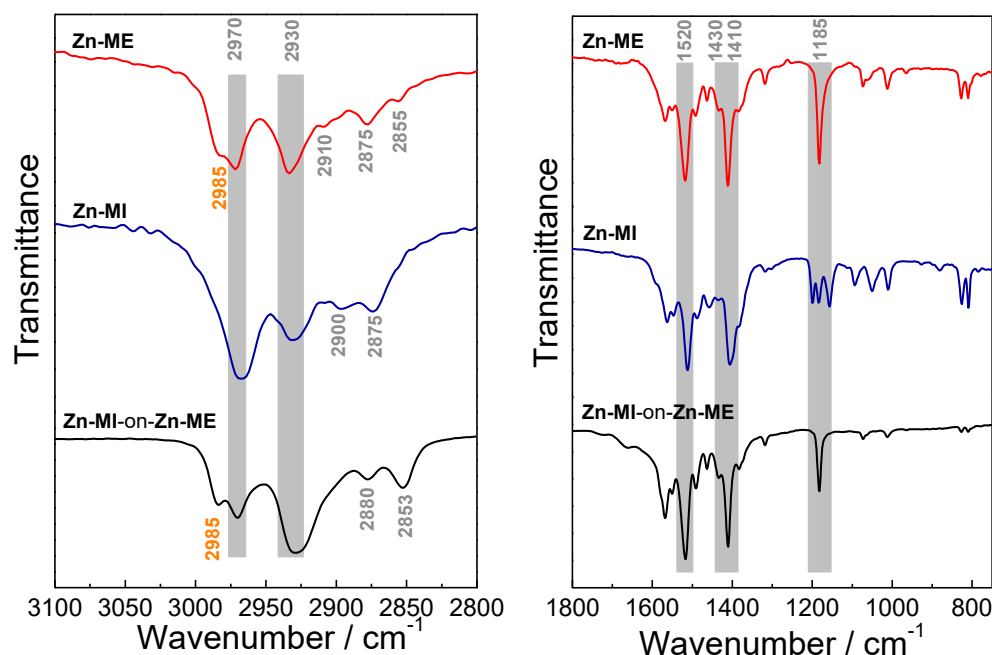


Figure 4.11 Example of IRRAS spectra of **Zn-MI-on-Zn-ME** heterostructured films indicates the position of the IR vibrational signals and the variation of relative transmittance at some wave numbers as a combination between the IRRAS spectra of the corresponding **Zn-ME** and **Zn-MI** MOF films.

To obtain insight into the morphology and surface coverage of the heterostructured MOF films, the samples are characterised by scanning electron microscopy (SEM). Figure 4.12 shows the SEM images of the top-view surfaces of a pure **Zn-DM(20)** film (Figure 4.12A), **Zn-MI(x)-on-Zn-DM(20)** films (Figure 4.12B – 4.12D), a pure **Zn-DM(30)** film (Figure 4.12E), and **Zn-MI(x)-on-Zn-DM(30)** films (Figure 4.12F – 4.12H). As can be understood from the images of the pure **Zn-DM** films (Figure 4.12A and 4.12E), LPE fabrication leads to cubic crystallites that are anchored to the –COOH terminated surface via one of their facets. Increasing the number of growth cycles is shown to increase the crystal size, with the **Zn-DM(30)** film exhibiting a crystal size of approximately 2 μm and a greater surface coverage of the Au substrate. For the heterostructured films, the size of the **Zn-MI** crystallites is significantly smaller than that of the **Zn-DM** particles, potentially due to the different growth behaviour of the two MOFs. As observed for pure films of the two compounds, while a greater number of LPE growth cycles leads growth of the **Zn-DM** into larger crystals, additional nucleation is more preferable in the case of **Zn-MI**. This leads to the formation of a large number of **Zn-MI** nanocrystals, which is corroborated by

the **Zn-MI-on-Zn-DM** heterostructured films exhibiting rougher surfaces due to the attachment of the **Zn-MI** nanocrystals to the smooth facets of the cubic **Zn-DM** crystallites in a core-shell fashion.

The number of LPE fabrication cycles required to achieve a dense surface coverage of the thin-film on the substrate, and a fully-covered shell-on-core heterostructure, is optimised for the respective MOF components. While a **Zn-MI(10)-on-Zn-DM(20)** sample does not afford full surface coverage of the MOF film (Figure 4.12B), increasing the number of shell-component **Zn-MI** fabrication cycles to at least 15 cycles (Figure 4.12C and 4.12D) and/or increasing the core-component **Zn-DM** fabrication cycles to 30 cycles (Figure 4.12F to 4.12H) give enhanced surface coverage. The cross-sectional SEM images of the **Zn-MI-on-Zn-DM** films (Figure 4.13) indicate the formation of dense MOF thin films on the functionalised Au-coated QCM substrate, except in the case of the **Zn-MI(10)-on-Zn-DM(20)** film, for which full surface coverage is not observed as mentioned above. According to the SEM images, the **Zn-MI-on-Zn-ME** and **Zn-DE-on-Zn-DM** systems show similar characteristics as the **Zn-MI-on-Zn-DM** films (see Figure 4.14). These data suggest that the **Zn-L** films are formed by the overgrowth of the island MOF nuclei in a core-shell fashion, with further intergrowth to form dense films.

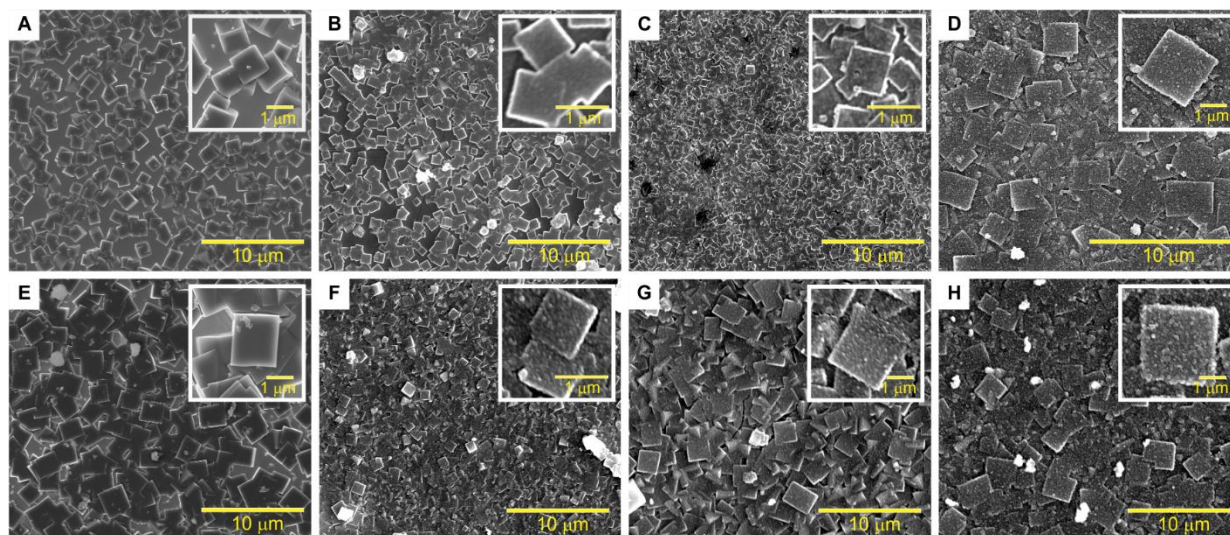


Figure 4.12 SEM images of the surfaces of (A) **Zn-DM(20)**, (B) **Zn-MI(10)-on-Zn-DM(20)**, (C) **Zn-MI(15)-on-Zn-DM(20)**, (D) **Zn-MI(20)-on-Zn-DM(20)**, (E) **Zn-DM(30)**, (F) **Zn-MI(10)-on-Zn-DM(30)**, (G) **Zn-MI(15)-on-Zn-DM(20)**, and (H) **Zn-MI(20)-on-Zn-DM(30)** films. Reprint with permission. Copyright © The Royal Society of Chemistry 2015.⁴⁰

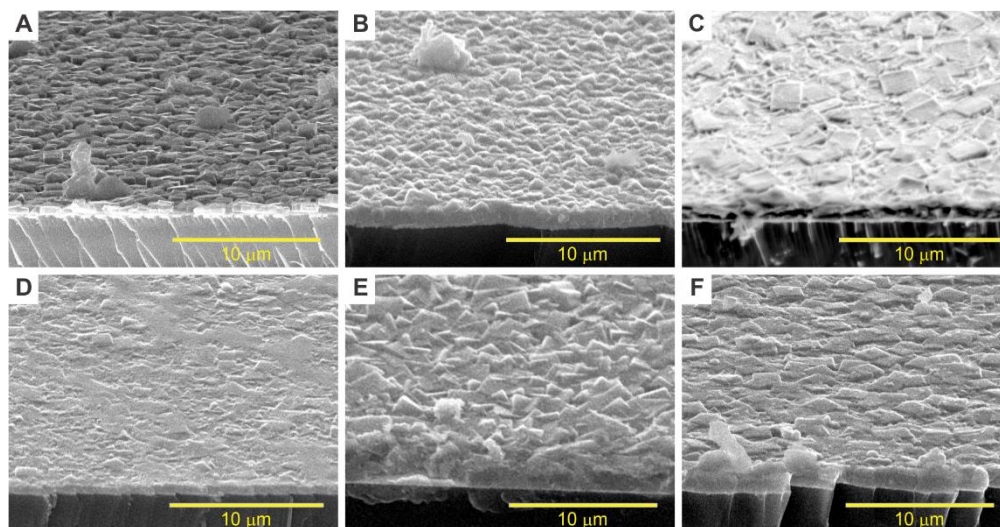


Figure 4.13 Cross-sectional SEM images of the **Zn-MI-on-Zn-DM** heterostructured thin-films with different number of deposition cycles in each MOF component: (A) **Zn-MI(10)-on-Zn-DM(20)**, (B) **Zn-MI(15)-on-Zn-DM(20)**, (C) **Zn-MI(20)-on-Zn-DM(20)**, (D) **Zn-MI(10)-on-Zn-DM(30)**, (E) **Zn-MI(15)-on-Zn-DM(30)** and (F) **Zn-MI(20)-on-Zn-DM(30)**.

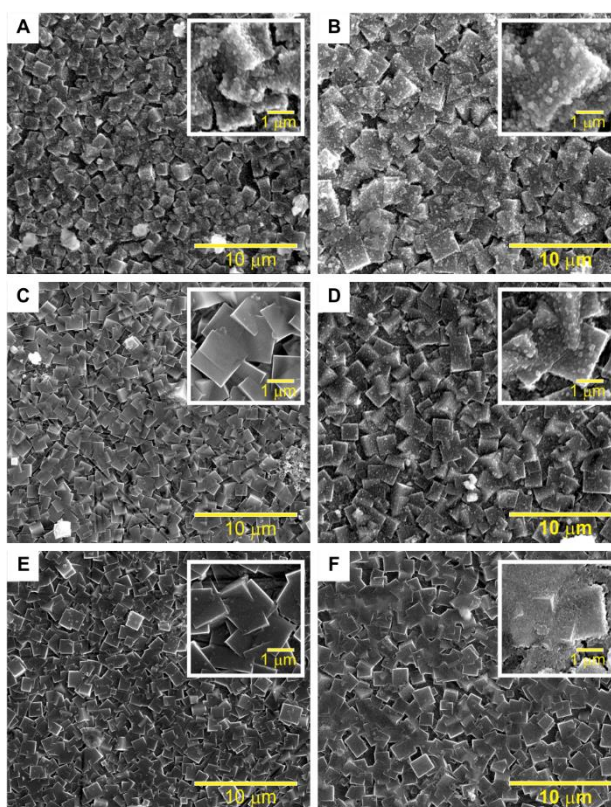


Figure 4.14 Top-view SEM images of the heterostructured (A) **Zn-MI(20)-on-Zn-ME(20)**, (B) **Zn-MI(20)-on-Zn-ME(30)**, (C) **Zn-DE(10)-on-Zn-DM(20)**, (D) **Zn-DE(20)-on-Zn-DM(20)**, (E) **Zn-DE(10)-on-Zn-DM(30)** and (F) **Zn-DE(20)-on-Zn-DM(30)** thin-films.

4.3 Sorption properties of heterostructured Zn-L thin-films

The sorption properties of the heterostructured MOF thin films were studied at 25 °C by an environmental-controlled QCM (BEL-QCM-4 equipment, BEL Japan) equipped with two vaporisers for different volatile organic compounds (VOCs) with their own set of mass flow controllers (see Chapter 6). Herein, two alcohols of different kinetic diameter (i.e. methanol: 3.6 Å and isopropanol: 4.7 Å) as well as water were selected as probe volatile compounds. As described below, both single- and multiple-components adsorption experiments were carried out to characterise the storage capacity of the films and the possibility for selective adsorption applications.

Prior to the sorption experiments, the samples were activated by exchanging the adsorbed solvent molecules within the pores with dichloromethane for 24 h followed by in-situ activation in the BEL-QCM instrument at 70 °C under a dry helium gas flow (100 sccm) for 2 h until the QCM frequency was stable (± 5 Hz over 20 min). The mass of the deposited MOF thin film was calculated by the difference in the fundamental QCM oscillation frequency and the frequency after final activation of the sample. Single-component adsorption isotherms of each probe compound were collected using a single vaporiser. The desired relative vapour pressure (P/P_0) of saturated organic vapour in helium gas was varied between 0.0~95.0%, and the specific adsorption amount was calculated from the observed QCM frequency according to the Sauerbrey equation (see Chapter 6). For mixed-components adsorption, the experiments were performed using two different probe compounds. Here, the P/P_0 of one probe compound was kept constant at a certain amount (maximum 45% P/P_0), while the other was varied between 0~45% P/P_0 . The total gas flow through the system was fixed at 100 sccm, with mixing of the two components in the manifold prior to exposure to the QCM cell.

4.3.1 Single-component alcohol adsorption

The single-component alcohol adsorption data collected at 25 °C for the **Zn-MI-on-Zn-DM** heterostructured films and their pure counterparts are presented in Figure 4.15. The methanol adsorption data for the **Zn-MI-on-Zn-DM** heterostructured films exhibit a Type-I isotherm typical of a microporous solid in a similar manner to the pure **Zn-DM** film (see Figure 4.15A). Here, the normalised total methanol adsorption capacity is greatest

for the pure **Zn-DM** film, and decreases as the proportion of **Zn-MI** increases in the heterostructured films. This is due to the lower surface area of **Zn-MI** (BET surface area $200 \text{ m}^2 \text{ g}^{-1}$) compared to **Zn-DM** (BET surface area $640 \text{ m}^2 \text{ g}^{-1}$) resulting from the bulkier alkyl chains present in the organic linker.³⁹ Most notably, increasing the fabrication cycles of **Zn-DM** from 20 to 30 leads to a significant increase in the methanol adsorption capacity when the number of **Zn-MI** cycles is held constant (i.e. when y is increased, but x remains unchanged). Referring to the in-situ QCM frequency changes (Figure 4.5) discussed in the previous section, the total composition of the heterostructured MOF film is dominated by the **Zn-DM** core component. Moreover, the **Zn-DM(30)** film features a well-defined morphology and high crystallinity, which is also likely of benefit to the adsorption capacity. Similar trends were observed for the methanol adsorptions within the **Zn-DE-on-Zn-DM** (Figure 4.16A) and **Zn-MI-on-Zn-ME** (Figure 4.17A) films, wherein the adsorption predominantly arises from the highly-crystalline **Zn-DM** and **Zn-ME** core components, respectively. However, the overvalued methanol adsorbed amount in the **Zn-DE(10)-on-Zn-DM(20)** film is observed due to the very low amount of **Zn-DE** shell component in the heterostructured film (featuring rather smooth facets of cubic MOF particles akin to the homostructured **Zn-DM** film, SEM image in Figure 4.14C).

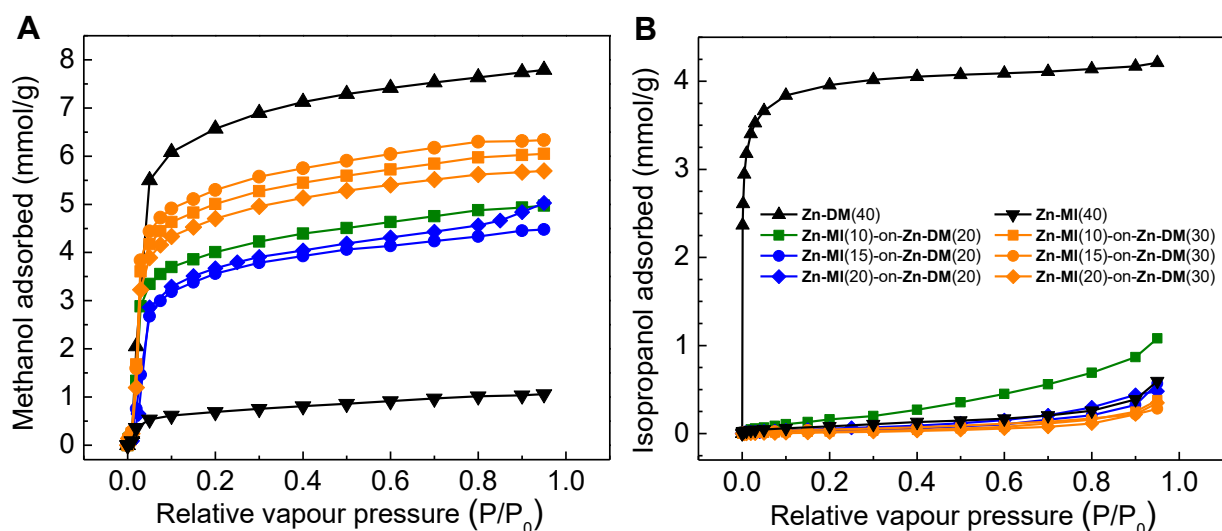


Figure 4.15 Single-component (A) methanol and (B) isopropanol adsorption isotherms at $25 \text{ }^\circ\text{C}$ for **Zn-MI**(x)-on-**Zn-DM**(y) heterostructured films and **Zn-MI** and **Zn-DM** recorded using an environmental-controlled QCM. Note that x and y represents the number of deposition cycles for **Zn-MI** and **Zn-DM**, respectively. Reprint with permission. Copyright © The Royal Society of Chemistry 2015.⁴⁰

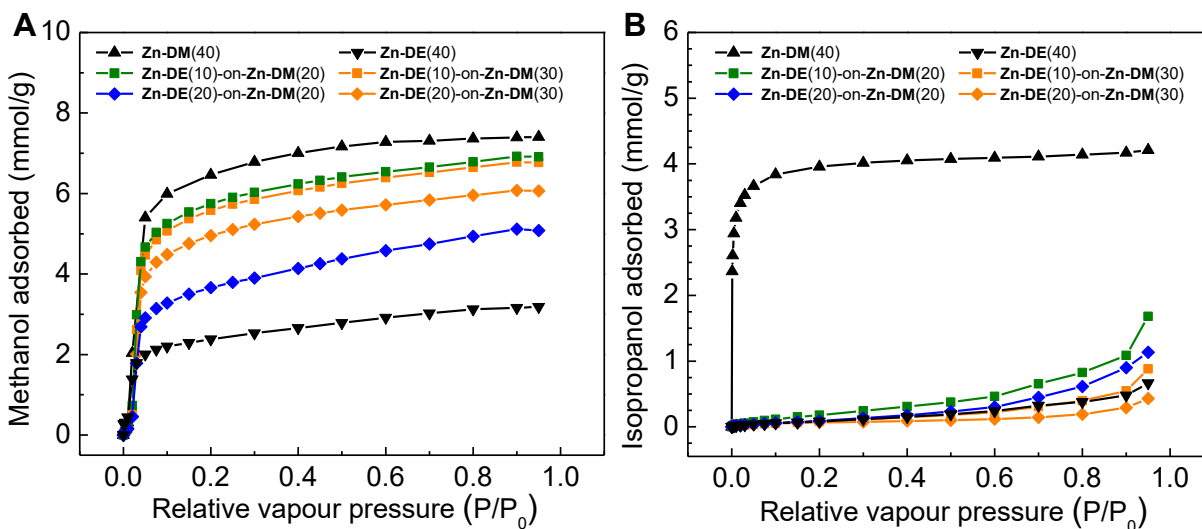


Figure 4.16 Single-component (A) methanol and (B) isopropanol adsorption isotherm at 25°C using the environmentally controlled QCM of the **Zn-DE-on-Zn-DM** heterostructured films with various deposition cycles in each component in comparison with the corresponding **Zn-DM** and **Zn-DE** homostructured films.

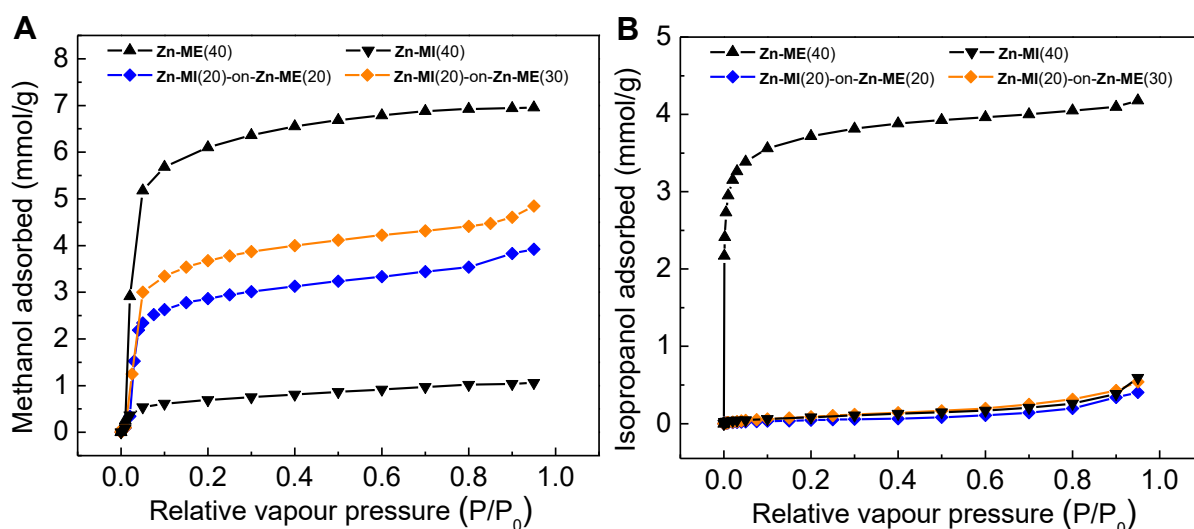


Figure 4.17 Single-component (A) methanol and (B) isopropanol adsorption isotherm at 25°C using the environmentally controlled QCM of the **Zn-MI-on-Zn-ME** heterostructured films with various deposition cycles in each component in comparison with the corresponding **Zn-ME** and **Zn-MI** homostructured films.

The isopropanol adsorption isotherms of the **Zn-MI-on-Zn-DM** films (Figure 4.15B) were collected for the same set of samples at 25 °C (the corresponding data for the **Zn-DE-on-Zn-DM** and **Zn-MI-on-Zn-ME** films are displayed in Figure 4.16B and 4.17B, respectively). Here, it is clearly observed that isopropanol, which features a larger molecular diameter, is adsorbed inside the pores of the homostructured **Zn-DM** (or **Zn-ME**) film, but not in the homostructured **Zn-MI** (or **Zn-DE**) film.

In the heterostructured films, there is also no significant uptake of isopropanol upon formation of the smaller-pore shell layer, except at the lowest coverage of **Zn-MI(10)-on-Zn-DM(20)** (adsorption curves labelled in green in Figure 4.15). This can be attributed to a fully-covered shell-on-core structure at higher coverages, as evidenced by the SEM data, which achieves exclusion of isopropanol from the core **Zn-DM** layer. At lower coverages, diffusion pathways still exist to the core layer, which is not desired from the viewpoint of obtaining a size-based selective adsorption profile. Optimisation of the number of fabrication cycles for the **Zn-DM** and **Zn-MI** components reveals that at least 15 fabrication cycles of **Zn-MI** are required for complete coverage of the **Zn-DM** layer formed by a 20- or 30-cycle LPE-fabrication process.

From the perspective of achieving selective adsorption properties, all of the films featuring a sufficient coverage of **Zn-MI** as the shell layer display size-selective adsorption of methanol over isopropanol. This can be ascribed to the small pore apertures of **Zn-MI**, which inhibit access of the isopropanol to the **Zn-DM** phase. Meanwhile, although the adsorption capacity of a **Zn-MI(40)** displays a small (< 1 mmol/g) uptake for methanol, the pores are sufficiently large to facilitate diffusion of the molecules through its pores to the higher-capacity **Zn-DM** phase. Hence, controlled hierarchical structuring that integrates the two MOFs is crucial not only for achieving selective adsorption, but also for increasing the total adsorption capacity of the integrated system. In other words, the smaller-pore **Zn-MI** (or **Zn-DE**) shell layer contributes toward the adsorption selectivity, while the larger-pore **Zn-DM** (or **Zn-ME**) core layer plays a dominant role in dictating the total adsorption capacity.⁴⁰

4.3.2 Size-selective adsorption of alcohols

The size-based adsorptive selectivity of the films was further examined via multiple-component adsorptions experiments using methanol and isopropanol as adsorbates. Here, all whole adsorption experiments were performed at 25 °C with a fixed total gas flow of 100 sccm. In a typical experiment, the composition of one of the alcohols was kept constant (either 30% or 45% P/P_0), while the quantity of the other was varied in a range from 0 to 45% P/P_0 . The streams of the two probe compounds were mixed in a dedicated manifold prior to being introduced into the QCM sample cell, and the adsorption quantities were computed after stabilisation of the oscillation frequency.

The comparison between the multiple-component adsorption data and the corresponding single-component (methanol and isopropanol) adsorption data for a **Zn-MI(20)-on-Zn-DM(20)** film are shown as an example in Figure 4.18 (see Appendix section 4.5 for corresponding data for other film compositions). An experiment performed under a variable methanol concentration (varied P/P_0 from 0-45%) in the presence of 30% and 45% P/P_0 isopropanol concentration (blue and orange plots in Figure 4.18A), revealed a mass uptake profile almost indistinguishable from that of the single-component methanol adsorption isotherm (black plot in Figure 4.18A). This suggests that the pores are free from adsorbed molecules under the original isopropanol flow, and only methanol molecules are adsorbed as its concentration is increased. Note that, a deviation at the end of the curve of the methanol adsorption in the presence of 45% P/P_0 of isopropanol (orange plot) from the single-component methanol adsorption isotherm (black plot) can be explained by the surface condensation phenomena due to the near total saturation of alcohol vapour molecules in the gas flow.

In contrast, the analogous experiment using a variable isopropanol adsorption in the presence of a constant 45% methanol concentration shows a large uptake of approximately 0.13 g/g prior to the introduction of isopropanol. Subsequent introduction of isopropanol to the 45% concentration of methanol leads to little additional uptake (see green plot, Figure 4.18B). This nearly constant total adsorption amount is approximately equal to the total adsorption amount at 45% methanol concentration in the single-component methanol adsorption isotherm. This suggests that the isopropanol permeation

into the MOF film is blocked by the **Zn-MI** shell component. Based on these data, it can be directly concluded that the **Zn-MI(20)-on-Zn-DM(20)** heterostructured film exhibits selective adsorption of methanol over isopropanol even under mixed component conditions.

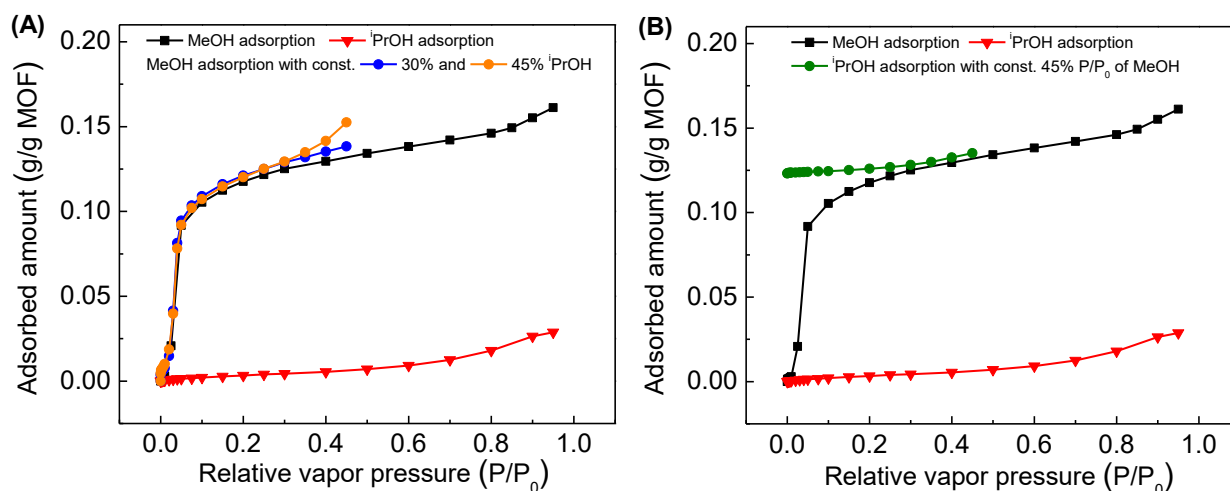


Figure 4.18 Methanol/isopropanol single- and multi-component adsorption at 25 °C for a heterostructured **Zn-MI(20)-on-Zn-DM(20)** film. The individual plots represent (A) variable methanol concentration in the presence of an isopropanol concentration of 30% (blue) and 45% (orange); (B) variable isopropanol adsorption in the presence of a methanol concentration of 45% (green). In both plots, the single-component methanol (black) and isopropanol (red) adsorption isotherms for the same sample are included for reference. Reprint with permission. Copyright © The Royal Society of Chemistry 2015.⁴⁰

In the cases of the **Zn-MI(10)-on-Zn-DM(20)** and **Zn-DE(10)-on-Zn-DM(20)** films (see section 4.5), the multi-component adsorption curve for a variable methanol concentration under a fixed 30% concentration isopropanol shows a substantial deviation from the single-component methanol adsorption curve. The higher total adsorption capacity can be ascribed to both methanol and isopropanol molecules being adsorbed in these two heterostructured MOF films. This confirms the presence of just a partial shell-on-core ordering within these films, which allow isopropanol molecules to permeate into the MOF film via regions where **Zn-DM** is directly exposed as the external layer (no **Zn-MI** covering layer on top), leading to the limited adsorption selectivity. This also further emphasises the importance of optimising the number of LPE fabrication cycles for each MOF component in order to obtain a fully heterostructured film.

4.3.3 Molecular recognition of methanol over water

The multiple-component QCM apparatus was also employed to test the methanol/water selectivity of the heterostructured films. In a similar manner to the methanol/isopropanol mixed-component experiments described above, the films were tested by varying the concentration of one of the components (methanol or water) under a fixed concentration of the other adsorbate.

The multiple-component adsorption profile at 25 °C for a **Zn-MI(20)-on-Zn-DM(30)** film using a variable methanol concentration under a constant water vapour concentration of 20% is shown in Figure 4.19 (blue plot). Here, the heterostructured MOF film shows a similar isotherm shape and saturation adsorption capacity to the single-component methanol adsorption isotherm (black plot). In contrast, when the water vapour concentration is varied under a constant methanol concentration of 45% (green plot), a large mass increase is observed prior to the introduction of water vapour. Increasing the concentration of water vapour from 0% to 45% under these conditions does not provide a significant increase in the total uptake. This lack of permeation of water molecules into the films is surprising, although the kinetic diameter of water (2.6 Å) is smaller in comparison with methanol (3.6 Å). This observation could be rationalised due to the hydrophobicity of the frameworks, which prevents water from being adsorbed within the pores, providing adsorptive selectivity toward methanol molecules. This suggests that in addition to the size-based (kinetic) selectivity observed for the alcohols, the films also possess an adsorptive selectivity based on a molecular recognition mechanism. Thus, from a practical perspective, these heterostructured MOF films coupled with QCM sensors can be used for selective adsorption of alcohol vapours even in the presence of relatively high levels of humidity. This concept of hierarchically structuring MOF thin films could provide possibilities for further development in MOF-based sensing applications via control over specific responses to certain probe molecules facilitated by selective adsorption.

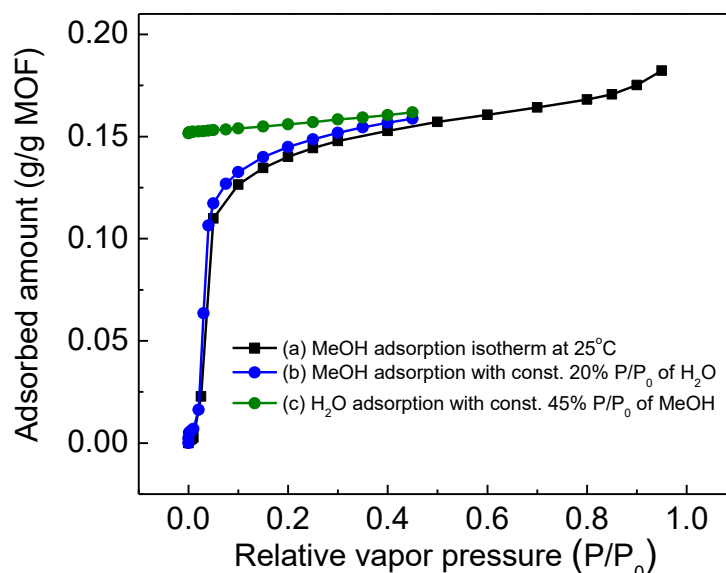


Figure 4.19 Methanol and methanol/water multi-component mass uptake profiles recorded at 25 °C for a heterostructured **Zn-MI(20)-on-Zn-DM(30)** film. The individual plots represent (a) a single-component methanol adsorption isotherm, (b) variable methanol concentration in the presence of a 20% water concentration (blue); and (c) variable water concentration in the presence of a 45% methanol concentration (green). Reprint with permission. Copyright © The Royal Society of Chemistry 2015.⁴⁰

4.4 Summary

The effective continuous stepwise LPE growth procedure is used for hierarchically structuring MOF materials as thin films on QCM sensors. A specific spatially-controlled ordering of two structurally-related **Zn-L**-based thin films with different pore features in a core-shell fashion, which combines the MOF with smaller pore as a shell layer and the one with larger pore as a core layer, reveals promising selective adsorption properties. Optimisation of the number of LPE fabrication cycles for each individual MOF component is required to achieve a full coverage of the MOF shell layer on the pre-deposited core MOF layer. In the heterostructured films studied here, the smaller-pore **Zn-MI** and **Zn-DE** shell components demonstrate size-based selectivity, while the **Zn-DM** and **Zn-ME** core components significantly dictate the overall adsorption capacity (acting as a storage container), highlighting a creation of synergistic functionality by means of mesoscopic-scale architecture. Hence, the size-selective adsorptions of alcohols as well as the molecular recognition of alcohol over water can both be achieved by these

heterostructured MOF thin-films. The excellent adsorptive selectivity and high storage capacity combined with a high robustness toward moisture presents these heterostructured **Zn-L** thin films as a promising candidate for practical use in MOF-based devices. For widespread industrial use, greater control over the uniformity of the MOF thin film on larger substrates (as well as spatial localisation of the MOF film to small working units within specific devices), as well as investigations directed toward understanding the mechanical stability will provide an additional perspective toward developing these materials within next-generation devices.

4.5 Appendix: multi-component adsorptions

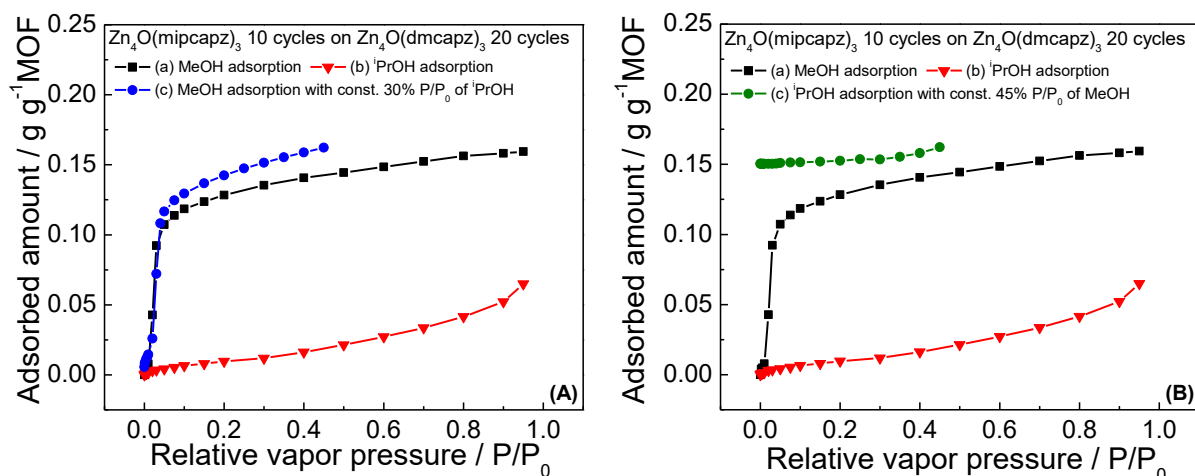


Figure 4.20 Methanol/isopropanol multi-components adsorption of the heterostructured **Zn-MI(10)-on-Zn-DM(20)** film at 25°C; (A) Methanol adsorption (P/P_0 varied from 0 to 45%) in the presence of constant 30% P/P_0 of isopropanol (blue) and (B) Isopropanol adsorption (P/P_0 varied from 0 to 45%) in the presence of constant 45% P/P_0 of methanol (green) in comparison with the single-component methanol (black) and isopropanol (red) adsorption isotherm at 25°C of the same sample.

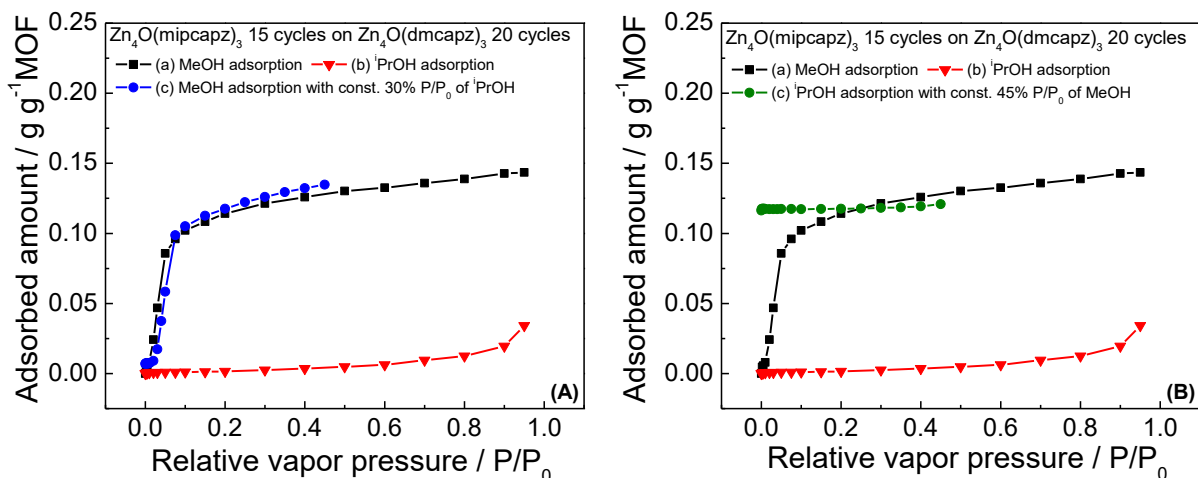


Figure 4.21 Methanol/isopropanol multi-components adsorption of the heterostructured **Zn-MI(15)-on-Zn-DM(20)** film at 25°C; (A) Methanol adsorption (P/P_0 varied from 0 to 45%) in the presence of constant 30% P/P_0 of isopropanol (blue) and (B) Isopropanol adsorption (P/P_0 varied from 0 to 45%) in the presence of constant 45% P/P_0 of methanol (green) in comparison with the single-component methanol (black) and isopropanol (red) adsorption isotherm at 25°C of the same sample.

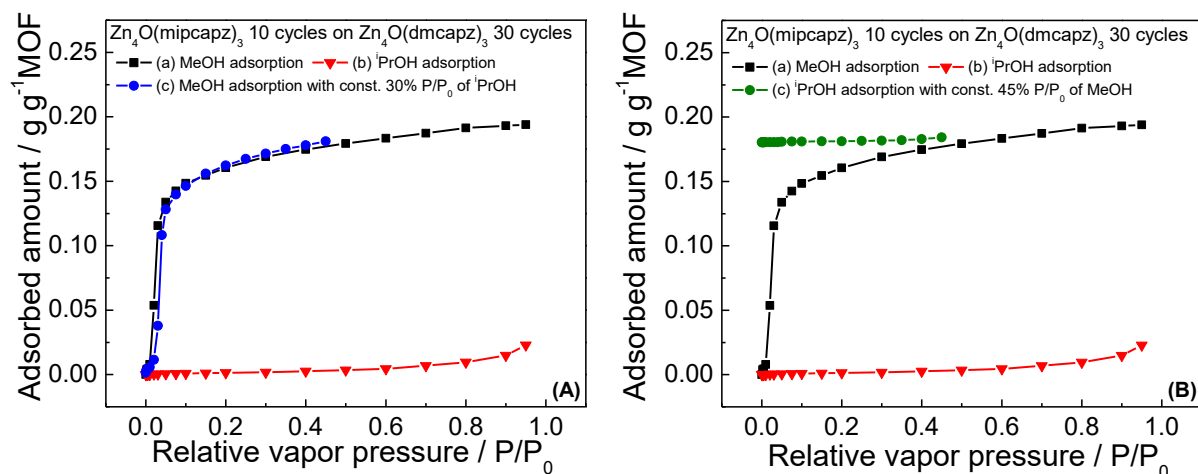


Figure 4.22 Methanol/isopropanol multi-components adsorption of the heterostructured **Zn-MI(10)-on-Zn-DM(30)** film at 25°C; (A) Methanol adsorption (P/P_0 varied from 0 to 45%) in the presence of constant 30% P/P_0 of isopropanol (blue) and (B) Isopropanol adsorption (P/P_0 varied from 0 to 45%) in the presence of constant 45% P/P_0 of methanol (green) in comparison with the single-component methanol (black) and isopropanol (red) adsorption isotherm at 25°C of the same sample.

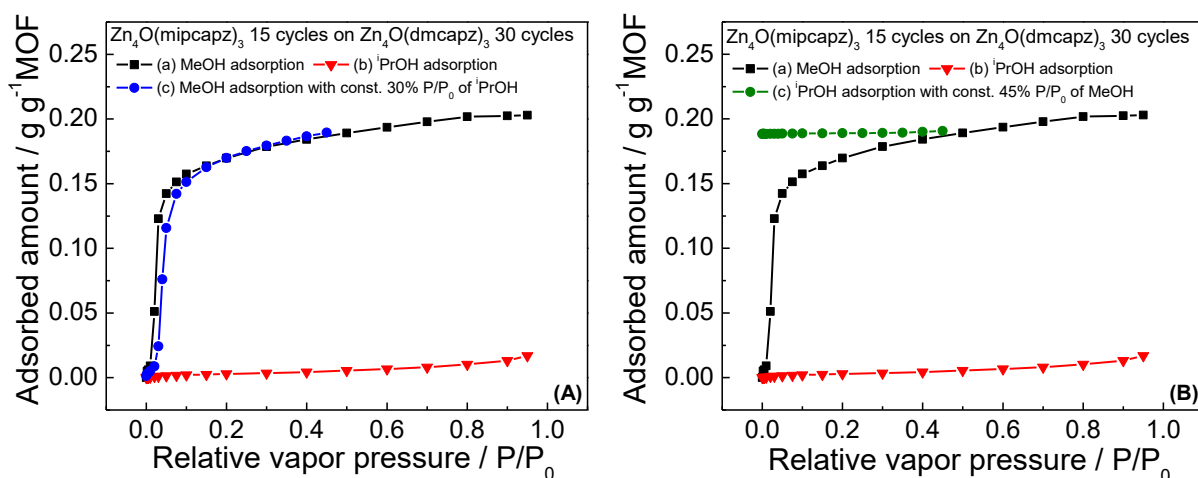


Figure 4.23 Methanol/isopropanol multi-components adsorption of the heterostructured Zn-MI(15)-on-Zn-DM(30) film at 25°C; (A) Methanol adsorption (P/P_0 varied from 0 to 45%) in the presence of constant 30% P/P_0 of isopropanol (blue) and (B) Isopropanol adsorption (P/P_0 varied from 0 to 45%) in the presence of constant 45% P/P_0 of methanol (green) in comparison with the single-component methanol (black) and isopropanol (red) adsorption isotherm at 25°C of the same sample.

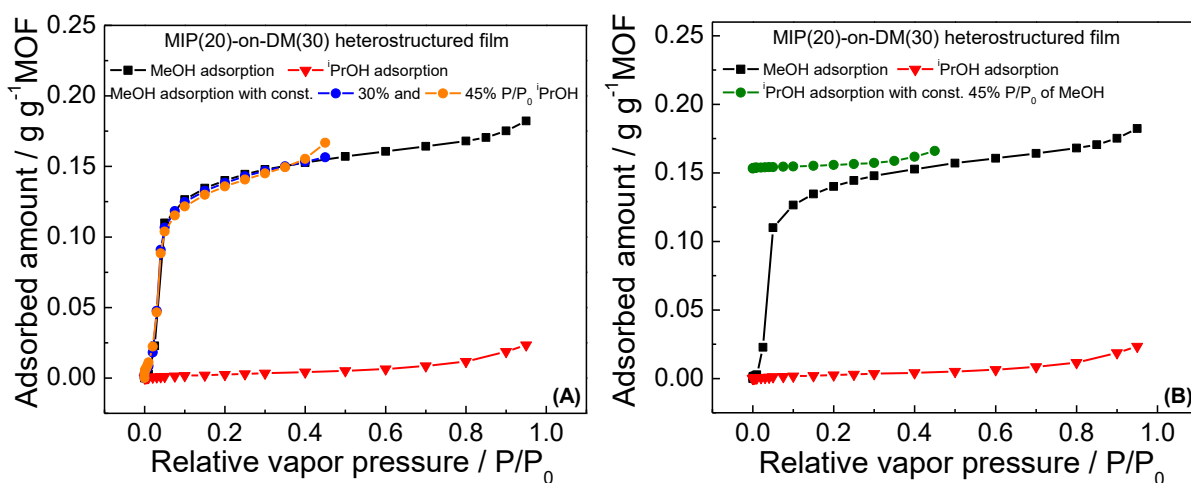


Figure 4.24 Methanol/isopropanol multi-components adsorption of the heterostructured Zn-MI(20)-on-Zn-DM(30) film at 25°C; (A) Methanol adsorption (P/P_0 varied from 0 to 45%) in the presence of constant 30% P/P_0 (blue) and 45% P/P_0 (orange) of isopropanol and (B) Isopropanol adsorption (P/P_0 varied from 0 to 45%) in the presence of constant 45% P/P_0 of methanol (green) in comparison with the single-component methanol (black) and isopropanol (red) adsorption isotherm at 25°C of the same sample.

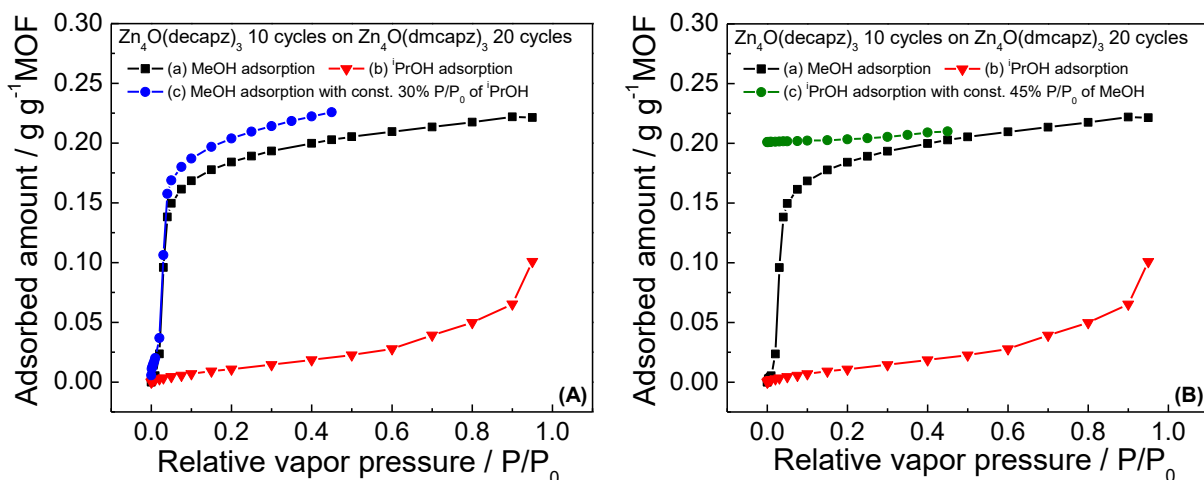


Figure 4.25 Methanol/isopropanol multi-components adsorption of the heterostructured Zn-DE(10)-on-Zn-DM(20) film at 25°C; (A) Methanol adsorption (P/P_0 varied from 0 to 45%) in the presence of constant 30% P/P_0 of isopropanol (blue) and (B) Isopropanol adsorption (P/P_0 varied from 0 to 45%) in the presence of constant 45% P/P_0 of methanol (green) in comparison with the single-component methanol (black) and isopropanol (red) adsorption isotherm at 25°C of the same sample.

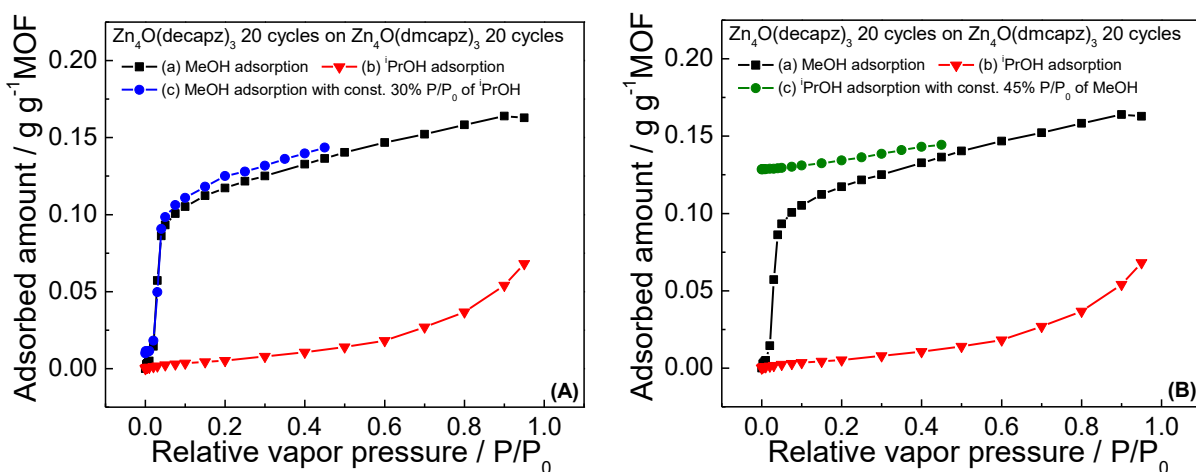


Figure 4.26 Methanol/isopropanol multi-components adsorption of the heterostructured Zn-DE(20)-on-Zn-DM(20) film at 25°C; (A) Methanol adsorption (P/P_0 varied from 0 to 45%) in the presence of constant 30% P/P_0 of isopropanol (blue) and (B) Isopropanol adsorption (P/P_0 varied from 0 to 45%) in the presence of constant 45% P/P_0 of methanol (green) in comparison with the single-component methanol (black) and isopropanol (red) adsorption isotherm at 25°C of the same sample.

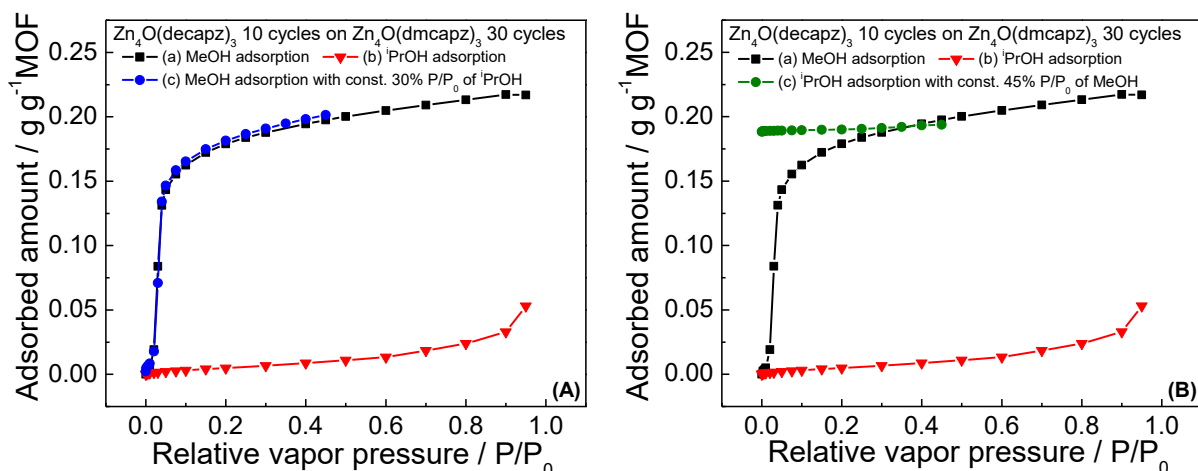


Figure 4.27 Methanol/isopropanol multi-components adsorption of the heterostructured **Zn-DE(10)-on-Zn-DM(30)** heterostructured film at 25°C; (A) Methanol adsorption (P/P_0 varied from 0 to 45%) in the presence of constant 30% P/P_0 of isopropanol (blue) and (B) Isopropanol adsorption (P/P_0 varied from 0 to 45%) in the presence of constant 45% P/P_0 of methanol (green) in comparison with the single-component methanol (black) and isopropanol (red) adsorption isotherm at 25°C of the same sample.

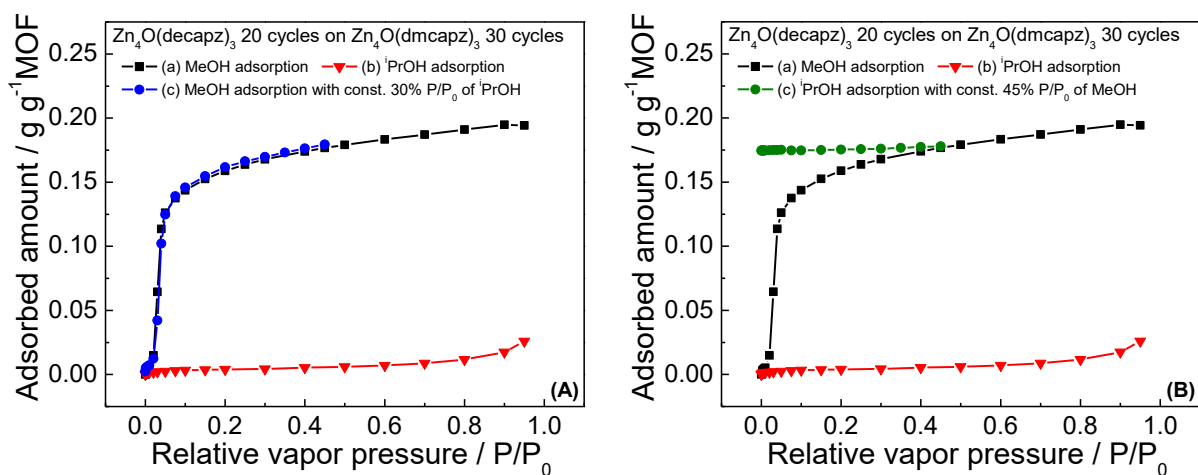


Figure 4.28 Methanol/isopropanol multi-components adsorption of the heterostructured **Zn-DE(20)-on-Zn-DM(30)** film at 25°C; (A) Methanol adsorption (P/P_0 varied from 0 to 45%) in the presence of constant 30% P/P_0 of isopropanol (blue) and (B) Isopropanol adsorption (P/P_0 varied from 0 to 45%) in the presence of constant 45% P/P_0 of methanol (green) in comparison with the single-component methanol (black) and isopropanol (red) adsorption isotherm at 25°C of the same sample.

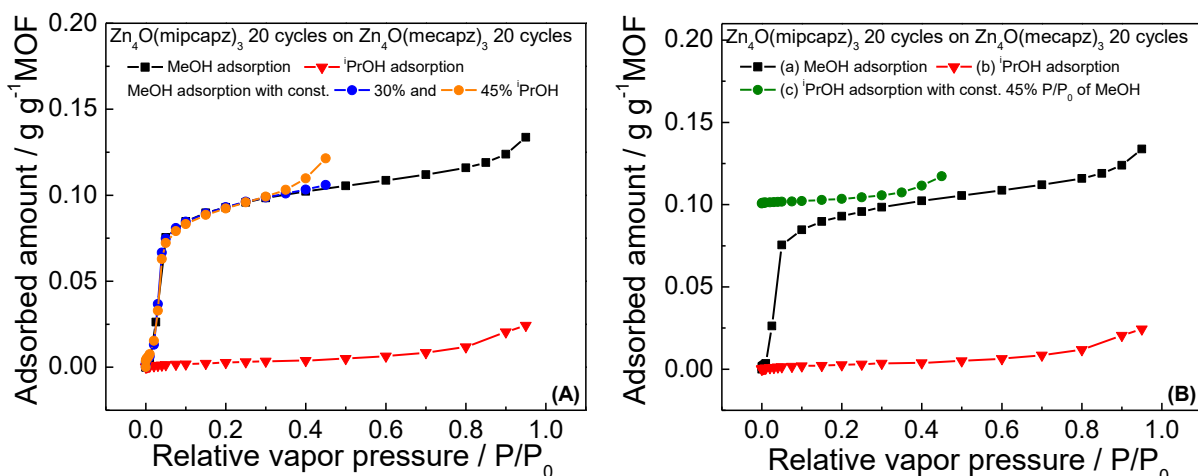


Figure 4.29 Methanol/isopropanol multi-components adsorption of the heterostructured **Zn-MI(20)-on-Zn-ME(20)** film at 25°C; (A) Methanol adsorption (P/P_0 varied from 0 to 45%) in the presence of constant 30% P/P_0 (blue) and 45% P/P_0 (orange) of isopropanol and (B) Isopropanol adsorption (P/P_0 varied from 0 to 45%) in the presence of constant 45% P/P_0 of methanol (green) in comparison with the single-component methanol (black) and isopropanol (red) adsorption isotherm at 25°C of the same sample.

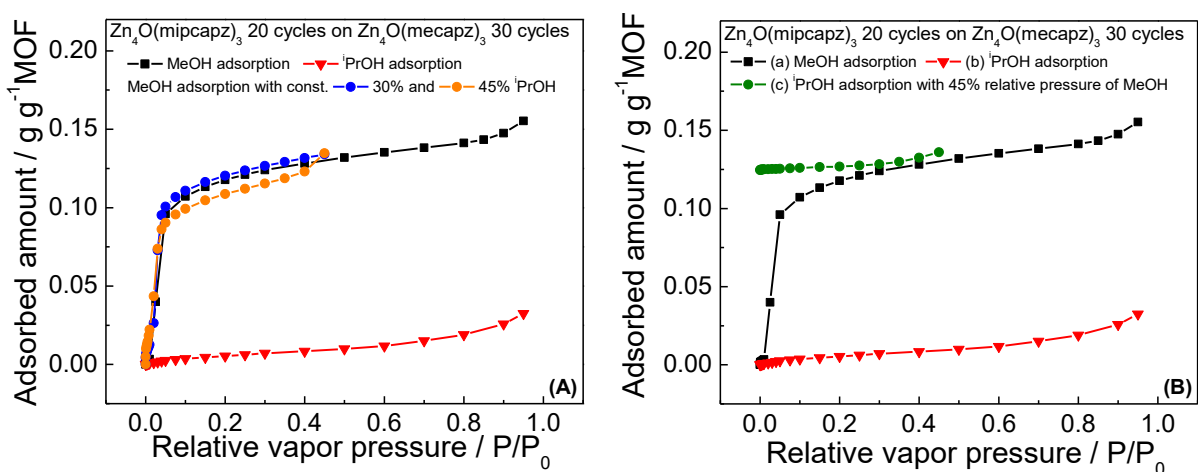


Figure 4.30 Methanol/isopropanol multi-components adsorption of the heterostructured **Zn-MI(20)-on-Zn-ME(30)** film at 25°C; (A) Methanol adsorption (P/P_0 varied from 0 to 45%) in the presence of constant 30% P/P_0 (blue) and 45% P/P_0 (orange) of isopropanol and (B) Isopropanol adsorption (P/P_0 varied from 0 to 45%) in the presence of constant 45% P/P_0 of methanol (green) in comparison with the single-component methanol (black) and isopropanol (red) adsorption isotherm at 25°C of the same sample.

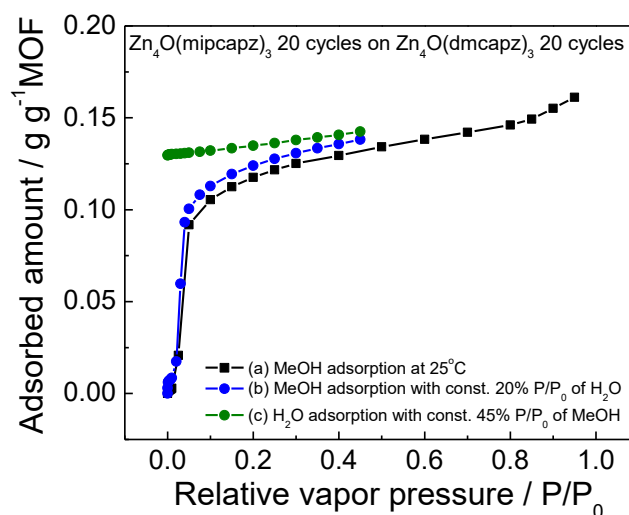


Figure 4.31 Methanol/moisture multi-components adsorption of the heterostructured **Zn-MI(20)-on-Zn-DM(20)** film at 25°C. Using the same sample, (a) single-component methanol (black) adsorption isotherm at 25°C, (b) methanol adsorption (P/P_0 varied from 0 to 45%) in the presence of constant 20% P/P_0 of moisture (blue) and (c) moisture adsorption (P/P_0 varied from 0 to 45%) in the presence of constant 45% P/P_0 of methanol (green) are compared.

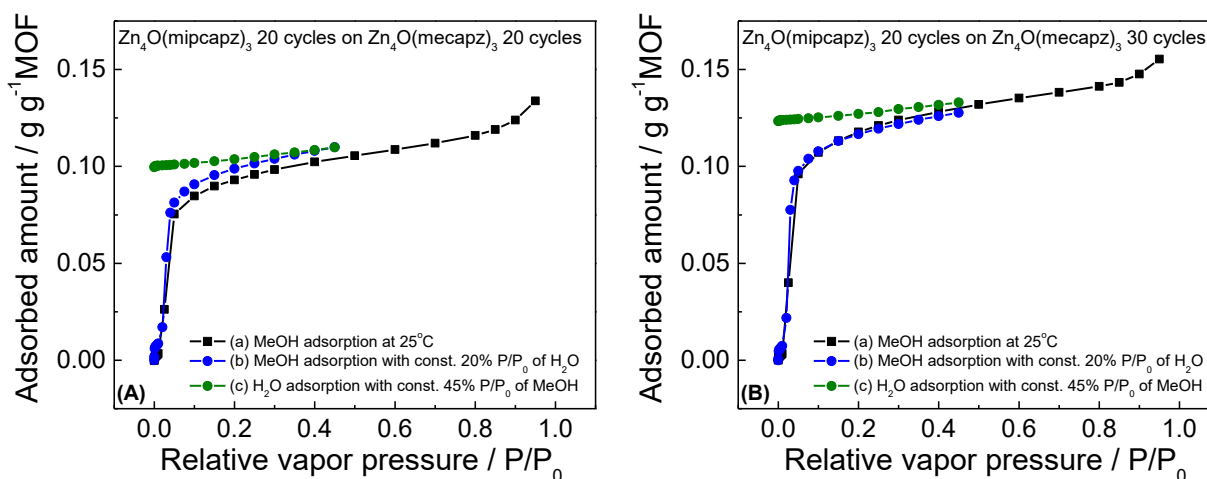


Figure 4.32 Methanol/moisture multi-components adsorption of the heterostructured (A) **Zn-MI(20)-on-Zn-ME(20)** and (B) **Zn-MI(20)-on-Zn-ME(30)** heterostructured film at 25°C. Using the same sample, (a) single-component methanol (black) adsorption isotherm at 25°C, (b) methanol adsorption (P/P_0 varied from 0 to 45%) in the presence of constant 20% P/P_0 of moisture (blue) and (c) moisture adsorption (P/P_0 varied from 0 to 45%) in the presence of constant 45% P/P_0 of methanol (green) are compared.

4.6 References

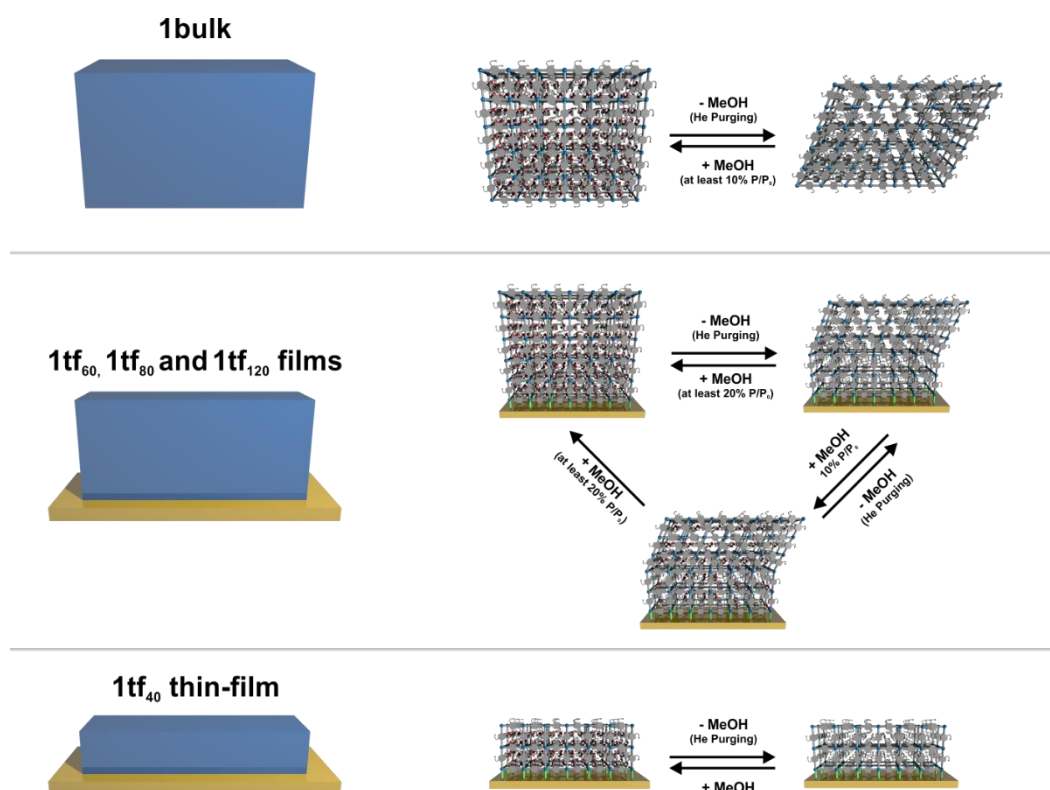
1. M. D. Allendorf, A. Schwartzberg, V. Stavila and A. A. Talin, *Chem. A Eur. J.*, 2011, **17**, 11372–11388.
2. M. Eddaoudi, J. Kim, N. Rosi, D. Vodak, J. Wachter, M. O'Keeffe and O. M. Yaghi, *Science*, 2002, **295**, 469–472.
3. Z. Wang and S. M. Cohen, *J. Am. Chem. Soc.*, 2007, **129**, 12368–12369.
4. Z. Wang and S. M. Cohen, *Angew. Chem. Int. Ed.*, 2008, **47**, 4699–4702.
5. T. Gadzikwa, O. K. Farha, C. D. Malliakas, M. G. Kanatzidis, J. T. Hupp and S. T. Nguyen, *J. Am. Chem. Soc.*, 2009, **131**, 13613–13615.
6. H.-L. Jiang, D. Feng, T.-F. Liu, J.-R. Li and H.-C. Zhou, *J. Am. Chem. Soc.*, 2012, **134**, 14690–14693.
7. S. M. Cohen, *Chem. Rev.*, 2012, **112**, 970–1000.
8. S. Furukawa, J. Reboul, S. Diring, K. Sumida and S. Kitagawa, *Chem. Soc. Rev.*, 2014, **43**, 5700–5734.
9. E. A. Flugel, A. Ranft, F. Haase and B. V. Lotsch, *J. Mater. Chem.*, 2012, **22**, 10119–10133.
10. Y. Sakata, S. Furukawa, M. Kondo, K. Hirai, N. Horike, Y. Takashima, H. Uehara, N. Louvain, M. Meilikhov, T. Tsuruoka, S. Isoda, W. Kosaka, O. Sakata and S. Kitagawa, *Science*, 2013, **339**, 193–196.
11. K. Sumida, N. Moitra, J. Reboul, S. Fukumoto, K. Nakanishi, K. Kanamori, S. Furukawa and S. Kitagawa, *Chem. Sci.*, 2015, **6**, 5938–5946.
12. S. Furukawa, J. Reboul, S. Diring, K. Sumida and S. Kitagawa, *Chem. Soc. Rev.*, 2014, **43**, 5700–5734.
13. S. Furukawa, K. Hirai, K. Nakagawa, Y. Takashima, R. Matsuda, T. Tsuruoka, M. Kondo, R. Haruki, D. Tanaka, H. Sakamoto, S. Shimomura, O. Sakata and S. Kitagawa, *Angew. Chem. Int. Ed.*, 2009, **48**, 1766–1770.
14. K. Koh, A. G. Wong-Foy and A. J. Matzger, *Chem. Commun.*, 2009, 6162–6164.
15. S. Furukawa, K. Hirai, Y. Takashima, K. Nakagawa, M. Kondo, T. Tsuruoka, O. Sakata and S. Kitagawa, *Chem. Commun.*, 2009, 5097–5099.
16. K. Hirai, S. Furukawa, M. Kondo, H. Uehara, O. Sakata and S. Kitagawa, *Angew. Chem. Int. Ed.*, 2011, **50**, 8057–8061.

17. K. Hirai, S. Furukawa, M. Kondo, M. Meilikhov, Y. Sakata, O. Sakata and S. Kitagawa, *Chem. Commun.*, 2012, **48**, 6472–6474.
18. D. Zacher, O. Shekhah, C. Wöll and R. A. Fischer, *Chem. Soc. Rev.*, 2009, **38**, 1418–1429.
19. O. Shekhah, J. Liu, R. A. Fischer and C. Wöll, *Chem. Soc. Rev.*, 2011, **40**, 1081–1106.
20. A. Bétard and R. A. Fischer, *Chem. Rev.*, 2012, **112**, 1055–1083.
21. P. Falcaro, R. Ricco, C. M. Doherty, K. Liang, A. J. Hill and M. J. Styles, *Chem. Soc. Rev.*, 2014, **43**, 5513–5560.
22. O. Shekhah, H. Wang, S. Kowarik, F. Schreiber, M. Paulus, M. Tolan, C. Sternemann, F. Evers, D. Zacher, R. A. Fischer and C. Wöll, *J. Am. Chem. Soc.*, 2007, **129**, 15118–15119.
23. M. Tu, S. Wannapaiboon and R. A. Fischer, *Inorg. Chem. Front.*, 2014, **1**, 442–463.
24. L. Heinke, M. Tu, S. Wannapaiboon, R. A. Fischer and C. Wöll, *Microporous Mesoporous Mater.*, 2015, **216**, 200–215.
25. O. Shekhah, H. K. Arslan, K. Chen, M. Schmittel, R. Maul, W. Wenzel and C. Wöll, *Chem. Commun.*, 2011, **47**, 11210–11212.
26. L. Heinke and C. Wöll, *Phys. Chem. Chem. Phys.*, 2013, **15**, 9295–9299.
27. Z. Wang, J. Liu, H. K. Arslan, S. Grosjean, T. Hagendorn, H. Gliemann, S. Braese and C. Wöll, *Langmuir*, 2013, **29**, 15958–15964.
28. B. Liu, M. Ma, D. Zacher, A. Bétard, K. Yussenko, N. Metzler-Nolte, C. Wöll and R. A. Fischer, *J. Am. Chem. Soc.*, 2011, **133**, 1734–1737.
29. D. Zacher, K. Yussenko, A. Bétard, S. Henke, M. Molon, T. Lahnorg, O. Shekhah, B. Schüpbach, T. de los Arcos, M. Krasnopolski, M. Meilikhov, J. Winter, A. Terfort, C. Wöll and R. A. Fischer, *Chem. Eur. J.*, 2011, **17**, 1448–1455.
30. O. Shekhah, K. Hirai, H. Wang, H. Uehara, M. Kondo, S. Diring, D. Zacher, R. A. Fischer, O. Sakata, S. Kitagawa, S. Furukawa and C. Wöll, *Dalton Trans*, 2011, **40**, 4954–4958.
31. B. Liu, M. Tu, D. Zacher and R. A. Fischer, *Adv. Funct. Mater.*, 2013, **23**, 3790–3798.

32. Z. Wang, J. Liu, B. Lukose, Z. Gu, P. G. Weidler, H. Gliemann, T. Heine and C. Wöll, *Nano Lett*, 2014, **14**, 1526–1529.
33. M. Tu and R. A. Fischer, *J. Mater. Chem. A*, 2014, **2**, 2018–2022.
34. M. Tu, S. Wannapaiboon and R. A. Fischer, *Dalton Trans*, 2013, **42**, 16029–16035.
35. M. Meilikhov, S. Furukawa, K. Hirai, R.A. Fischer and S. Kitagawa, *Angew. Chem. Int. Ed.*, 2013, **52**, 341–345.
36. L. Heinke, M. Cakici, M. Dommaschk, S. Grosjean, R. Herges, S. Bräse and C. Wöll, *ACS Nano*, 2014, **8**, 1463–1467.
37. C. Montoro, F. Linares, E. Q. Procopio, I. Senkovska, S. Kaskel, S. Galli, N. Masciocchi, E. Barea and J. A. R. Navarro, *J. Am. Chem. Soc.*, 2011, **133**, 11888–11891.
38. A. Betard, S. Wannapaiboon and R. A. Fischer, *Chem. Commun.*, 2012, **48**, 10493–10495.
39. S. Wannapaiboon, M. Tu and R. A. Fischer, *Adv. Funct. Mater.*, 2014, **24**, 2696–2705.
40. S. Wannapaiboon, M. Tu, K. Sumida, K. Khaletskaya, S. Furukawa, S. Kitagawa, and R. A. Fischer, *J. Mater. Chem. A*, 2015, **3**, 23385–23394.
41. G. Sauerbrey, *Z. Phys.*, 1959, **155**, 206–222.

Chapter 5

Systematic control of structural flexibility of MOF crystallites anchored at surfaces



- S. Wannapaiboon, A. Schneemann, I. Hante, M. Tu, K. Epp, C. Sternemann, M. Paulus, G. Kieslich and R. A. Fischer, 2017, *manuscript in preparation*.

5.1 Introduction and state of the art

5.1.1 Stimuli-responsive materials and the attempt to combine flexibility in crystalline solid materials

Responsiveness to specific external stimuli at a certain threshold by undergoing structural reformation and selective recognition reveals a breakthrough in research and development of novel materials, so-called flexible materials. The potential utility of biological flexible materials has been perceived for centuries, *i.e.* the production of the first hygrometer by Leonardo da Vinci, employing the flexible properties of human hair upon adsorption and release of water from air. Structural flexibility is frequently observed in biomimetic and organic-based materials such as enzymes, biomolecules as well as organic oligomers and polymers, which can rearrange their forms and shapes in response to stimuli with a multifaceted character.¹⁻⁶ Specifically, responsive polymer materials can adapt their structures to surrounding environments and change their surface properties such as wettability and adhesion of different species depended on external stimuli. Moreover, stimuli-responsive polymeric materials can provide the interconversion of chemical and biochemical signals into optical, electrical, thermal and mechanical signals, leading to a variety of applications such as “smart” optical systems, biosensors, drug delivery and microelectromechanical systems.⁶ However, introducing such softness and flexibility within crystalline solid materials still remains a challenge, since the components are closely packed and hence create such a long-range order of crystallinity, which consequently lead to less freedom of motion for reorganisation. The attempt to combine rigidity and regularity of crystalline materials with flexibility and responsivity of enzyme-like materials has attracted significant attention.⁷

A novel class of porous materials so-called metal—organic frameworks (MOFs), formed by a combination of metal ion based nodes and multitopic organic bridging linkers,⁸ is among the promising candidates to fulfil the aim for such integrated attributes. Thanks to the versatility of the precursor components, MOFs reveal broad perspectives for systematic designs and fine tunings of the framework structures, characteristic features and chemical properties of the pore surfaces.⁹⁻¹¹ Control and alteration of the attractive forces used for assembly of the porous scaffolds as well as the internal

interactions within the networks by specific design of the building blocks lead to the discovery of MOFs which possess structural dynamic behaviours (coined as flexible MOFs or soft porous crystals).^{7,12-15} Upon physical and chemical stimuli (i.e. guest introduction/removal, photochemical-, thermal- and pressure-induced stimuli), flexible MOFs undergo reversible crystal-to-crystal, crystal-to-less crystalline, or even crystal-to-amorphous phase transitions. Depending on the applied stimuli and the characteristic features of MOFs, various modes of structural flexibility i.e. breathing,¹⁶ swelling,¹⁷ linker rotation¹⁸ and subnetwork displacement^{19,20} have been observed (Figure 5.1). The achievement to create these stimuli-responsive, crystalline porous materials highlights potential applications for selective gas storage (or gas capture),²¹⁻²⁴ effective gas separation²⁵ and controlled drug release.²⁶

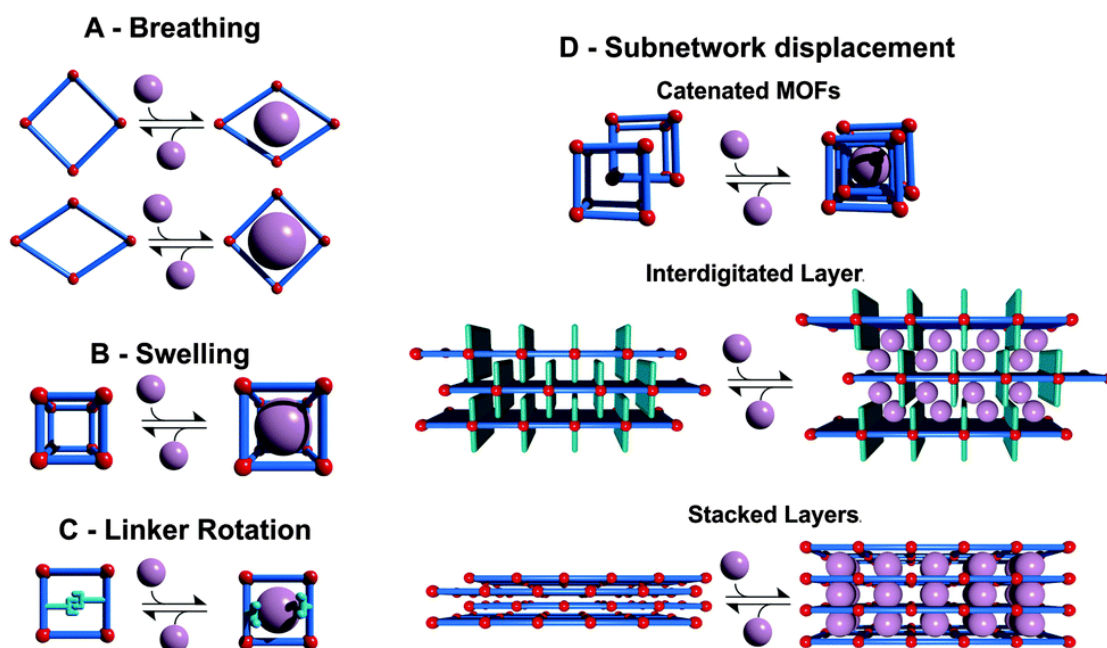


Figure 5.1 Schematic representation of different flexibility modes of MOFs; (A) breathing is defined by a change in unit cell volume ($\Delta V \neq 0$) and characteristic distances and angles of the unit cell, and maybe a difference of crystallographic space groups of the two distinct phases. (B) swelling is defined by a (gradual) enlargement of the unit cell volume ($\Delta V \neq 0$) without a change in the unit cell shape and space group. (C) linker rotation is defined as a (continuous) transition of a spatial arrangement of a linker by turning around the rotational axis ($\Delta V = 0$). (D) subnetwork displacement is defined by a drift, relocate, or shift of the individual subnets (which are not connected to each other by chemical bonds but rather by weak forces) in regard to each other. Reprinted with permission. Copyright © The Royal Society of Chemistry 2014.¹³

5.1.2 Flexible MOFs and how to fine tune structural flexibility

Among about 20,000 coordination network structures listed in the Cambridge Structural Database (CSD) which are classified as MOFs, only less than 100 compounds exhibit considerable structural transformation as responsivity to external stimuli.¹³ MIL (Materiaux Institute Lavoisier) systems are the well-known systems, of which structural flexibilities have been systematically investigated, especially M(bdc)(OH) (MIL-53, M = Al, Fe, Cr, Sc, Ga and In, bdc = benzene-1,4-dicarboxylate)^{16,27-32} and $M_3O(X)(H_2O)_2(L)_3$ (MIL-88, M = Fe³⁺ or Cr³⁺, X = F⁻ or OH⁻ and L = dicarboxylate linkers e.g. fumarate (MIL-88A), bdc (MIL-88B), 2,6-naphthalenedicarboxylate (2,6-ndc, MIL-88C) as well as 4,4'-biphenyl dicarboxylate (bpdc, MIL-88D)) family.^{17,33} Specifically, MIL-53 is the prototypical system exhibiting the so-called breathing transition, while MIL-88 possesses swelling mode upon introduction and removal of guest molecules as well as the external physical stimuli such as temperature and mechanical stress.

Closer inspection on the structural transformation phenomena, the degree of flexibility in MOFs is a correlative effect of both the inorganic node and the organic linker, which can be fine-tuned and controlled at the molecular assembly level by pre-designing of the precursor components as well as by post-synthetic modification of the chemical functionalities within the frameworks.¹³ For example, variation of the metal nodes in MIL-53 system shows a significant difference of the unit cell volumes of the obtained MIL-53 analogues and can lead to the different responsiveness upon solvent uptake and removal; i.e. MIL-53(Fe) and MIL-53(Sc) show a pore contraction upon activation (empty pore) which are contrary to the other analogues.²⁷⁻³² Changing in valency of the metal node (i.e. from typical M³⁺ in MIL-53 to V⁴⁺ in the analogue MIL-47) results in the retardation of the framework breathing during the adsorption of polar guests.³⁴ Interestingly, the use of V³⁺ and the protonated bridging OH groups in the metal node regains the framework flexibility again.³⁵ Moreover, functionalisation of the bdc linker has been found to comprehensively influence the breathing transitions in MIL-53(Al)³⁶ and MIL-53(Fe)³⁷. Variation in the breathing behaviour is attributed to the modulated electronic properties of the μ^2 -OH groups within the framework due to the modified interaction with the implemented dangling groups at the bdc linkers (which are related to their size and

polarity). Hence, the interaction of the MIL frameworks with guest molecules is changed and consequently alters the flexibility upon the adsorption/desorption of the same guest molecules.^{36,37} In addition, mixing of the different metal nodes or the different linkers so-called multivariate MOFs (e.g. in the MIL-53 systems) can tune the adsorption characteristics as well as generate such a unique adsorption behaviour differing for the single MOF components.³⁸⁻⁴⁰ However, the influence on flexibility is not always a linear effect with respect to the varied compositions. Systematic optimisation in each case is still required in order to understand and control the flexible phenomena.

Apart from the well-known MIL systems, layered-pillared MOFs (M_2L_2P ; M = metal centre; L = linear dicarboxylate linker; P = neutral nitrogen donor pillar) are another interesting class of MOFs which possess a variety of structural transformations. $Zn_2(bdc)_2(dabco)$ (dabco = 1,4-diazabicyclo[2.2.2]octane) is the prototypical example of such a system that provides a framework flexibility upon activation and solvent infiltration.⁴¹ Here, the deformation of the paddle-wheel $Zn_2(bdc)_2$ grids (especially, the O-Zn-O adjacent angle) as a dependence on the interaction with guest molecules plays a key role in structural transformation so-called breathing transition. As also observed in the MIL-53 system, alteration of the metal paddle-wheel nodes as well as the organic linkers leads to a variation of breathing phenomena. The analogue structures consisting of Co-based paddlewheel node still shows the flexibility,⁴² whereas the Cu-based structure is rather rigid upon solvent adsorption process.⁴³ By expansion of the framework using the longer dicarboxylate linkers (2,6-ndc), the DUT-8 series ($M_2(2,6-ndc)_2(dabco)$, M = Cu^{2+} , Zn^{2+} , Co^{2+} and Ni^{2+}) have been synthesised.^{44,45} Here again, the degree of framework breathing transition strongly depends on the metal nodes, indicating the extremely large reversible breathing transition (> 250%) in the DUT-8(Ni) but the rigid structure in DUT-8(Cu).

The incorporation of pendant alkylether-functionalised bdc-type linkers into the layered-pillared MOFs to form $Zn_2(fu-bdc)_2(dabco)$ (fu-bdc = 2,5-alkoxy-1,4-benzenedicarboxylate) reveals a significant structural flexibility induced by polar-guest sorption⁴⁶⁻⁴⁸ and thermal excitation.⁴⁹ These materials undergo a marked breathing transition from the guest-filled large pore (**lp**) form to the activated narrow pore (**np**) form.

The degree of dynamic framework flexibility between **lp** and **np** forms can be finely tuned by the choices of pendent groups (various chain length, polarity and degree of saturation, see Figure 5.2).⁵⁰ The breathing dynamics are attributed to the interactions between the alkoxy pendent sidechains and the sidechains with the framework backbone as well as with the guest molecules.⁵⁰ Moreover, the mixed linker materials offer a way to tailor the structural dynamics and responsiveness upon guest adsorption and thermal excitation.^{50,51} These materials can be further applied in selective adsorption and separation of light hydrocarbons by means of the solvent-like sidechains of the MOFs.⁵²

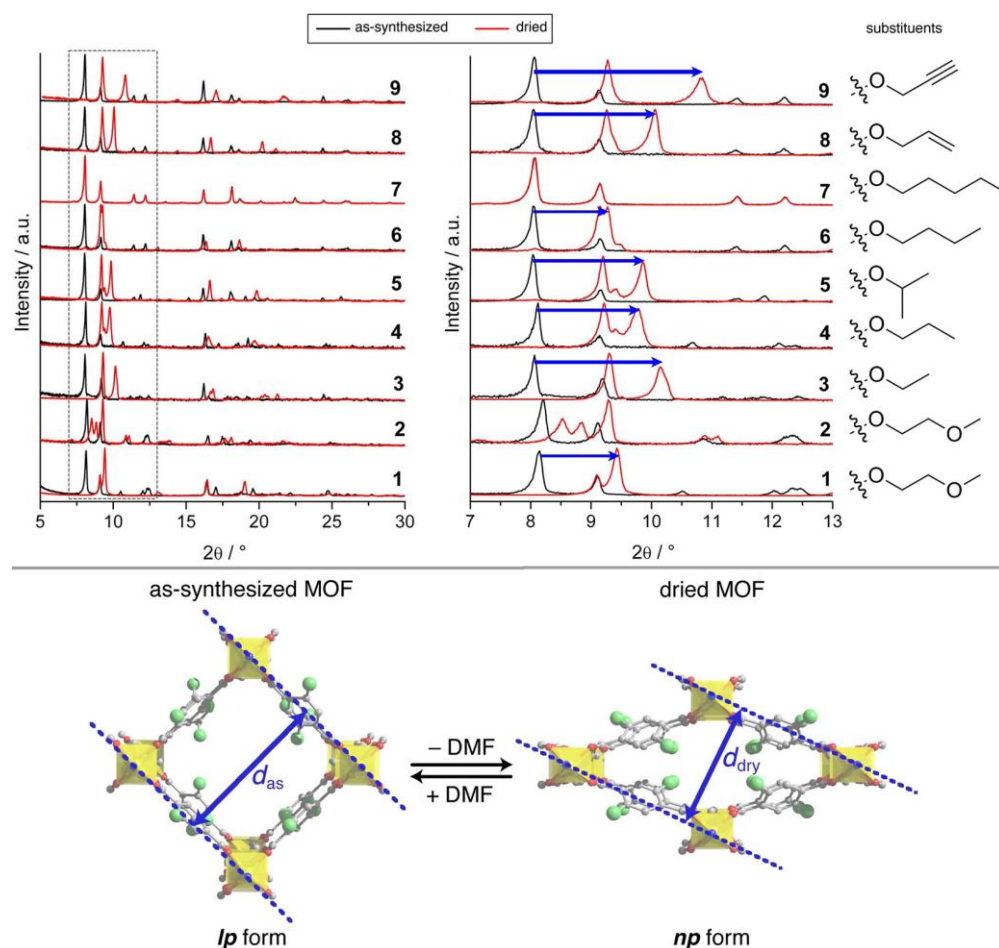


Figure 5.2 (Top) Comparison of the PXRD patterns of the as-synthesised (black) and the dried (red) phases of $Zn_2(\text{fu-bdc})_2(\text{dabco})$ compounds consisting of various alkoxy-functionalised bdc linkers (compounds **1** - **9**). Note that, the blue arrow is marked the shift of the XRD reflections belonging to equivalent lattice planes. (Bottom) Structural representation of the **lp** and **np** forms, showing the lattice planes corresponding to the shifting marked with blue arrow in the PXRD patterns. Reprint with permission. Copyright © 2012 American Chemical Society.⁵⁰

5.1.3 Nanoscale MOFs and size-dependent flexibility

In addition to tuning of MOF compositions, control of their physical form in the mesoscopic and macroscopic scales (namely, crystal size, morphology and shape of crystal aggregates) is also known to uniquely affect their properties.⁵³⁻⁵⁵ Focussing on flexible MOFs, downsizing of MOF crystallites to the nanoscale regime can alter the adsorption profiles as well as initiate the new intrinsic phenomena which only observed in this scale.⁵⁶⁻⁶⁰ For example, downsizing of the flexible MOF of a type Zn(ip)(bipy) (CID-1; CID = coordination polymer with an interdigitated structure, ip = isophthalate and bipy = 4,4'-bipyridine) to the nanosized crystal (50 nm x 320 nm, so-called NCID-1) results in a marked difference of the crystal structure and dynamic properties from the bulk material.^{56,57} Single crystal XRD data reveals the changes of cell parameters and the different 2D interlayer distances between the activated NCID-1 and the macrocrystalline CID-1 materials. Additionally, the ²H NMR measurement indicates the higher mobility of the aromatic rings of the bipy linkers within the NCID-1, which consequently leads to the increased sorption kinetics and the smooth diffusion of methanol molecules into the pores and hence the disappearance of the sorption hysteresis. These results highlight an influence of crystal downsizing to control of gas adsorption regarding to the crystal structure and the framework dynamics.^{56,57}

Sakata *et al.*⁵⁸ reported that the crystal downsizing of the two-fold interpenetrated frameworks of Cu₂(bdc)₂(bipy) modulates the framework flexibility and initiates the new intrinsic phenomena so-called a shape-memory effect in the coordination network compounds. Specifically, the micrometre-sized crystals show the elastic framework flexibility in response to guest incorporation (opened pore, **op**) and guest removal (closed pore, **cp**) by a displacement of the interpenetrated frameworks in regard to each other. By downsizing the crystal to a size below 60 nm, activation of the MOF by removal of guest molecules surprisingly maintains the empty **op** form (an unusual, metastable phase), which only can be converted back to the **cp** form by thermal treatment. This stabilisation of the empty **op** form is attributed to the suppression of the phase transition which is increased by decreasing of the crystal size. This leads to different sorption isotherm profiles of the material depending on its thermal treatment history.⁵⁸

Tailoring the characteristics of adsorption profiles and gating transition phenomena in the DUT-8(Ni) crystals has been achieved by systematic control of the crystal size by adjusting the critical synthetic parameters (such as ratio and concentration of precursors and solvent) in the bottom-up method.⁵⁹ Upon desolvation, the small DUT-8(Ni) crystals (size < 500 nm) retain in the **op** form and further show a type-I nitrogen sorption isotherm at 77 K, whereas the larger DUT-8(Ni) crystals (size > 1 μm) undergo breathing transition from the **op** to the **cp** form and further show “gate opening” in nitrogen sorption isotherm.⁵⁹ By performing the DUT-8(Ni) synthesis using the micromixer-based approach, the crystal size of DUT-8(Ni) materials can be uniformly controlled and varied within a wide range by adjusting the aging temperature and time.⁶⁰ Hence, the size-dependent flexibility can be systematically investigated. Interestingly, a significant influence of the crystal size on the gate-opening pressure and the flexible behaviour is observed. In addition to the previous work, the DUT-8(Ni) crystals with size regime between 500 nm and 1 μm shows a pore closing upon solvent removal by thermal activation, however the nitrogen gas adsorption is insufficient to reopen the frameworks back to the **op** form. This observation is possibly due to the monodomain switching without defect formation (serving as nucleation centres for reopening), and consequently leads to a high activation barrier for the guest-induced framework reopening.⁶⁰ Note that, an important implication is that the flexible MOFs exhibiting significant volume changes should be considered as materials with “*history dependent adsorption profiles*”, since changes in domain size and defect formation can occur upon undergoing framework transition, which further influences the adsorption profiles.^{59,60}

5.1.4 Transfer of flexibility into MOF-based devices

In addition to utilize MOFs as bulk materials, the implementation of MOFs as an integral part within solid-state devices (e.g. microelectronics and membranes) has received an increased attention over the last few years.^{53,61,62} Major challenges during the manufacturing process are the compatibility with the specific device configurations and the preservation (or even enhancement) of the performance profile compared to the bulk MOF materials.⁶³ Studies focusing on the transfer of flexible MOFs into a thin-film device remain scarce. The first attempt is a preparation of $\text{Fe}_3\text{O}(\text{OH})(\text{H}_2\text{O})_2(\text{bdc})_3$

(MIL-88B(Fe)) films by direct solvothermal synthesis on self-assembled monolayer (SAM) functionalized Au-coated substrate. The obtained MIL-88B(Fe) film consists of micrometre-sized crystals attached to the substrate and exhibits a framework swelling dynamic (increase of the cell volume by 40%) triggered by water vapour adsorption similar to the bulk crystals.⁶⁴

Further, an effective procedure for MOF thin-film fabrication via stepwise liquid-phase epitaxy (LPE, also known as layer-by-layer approach)⁶⁵ was employed to fabricate nanometre-size Hofmann-type MOF thin-films, which interestingly show unique structures and adsorption properties differed from the bulk phases.⁶⁶⁻⁷¹ The highly-oriented, LPE-fabricated thin-films of the 3D Fe(pz)[M(CN)₄] (pz = pyrazine, M = Ni, Pd and Pt)^{66,67} and the 3D accordion-like Fe(H₂O)₂(bipy)[Pt(CN)₄]·H₂O⁶⁸ exhibit remarkable lattice shrinkage (3 - 7 % volume shrinkage) compared with the corresponding bulk MOF materials. This observation is contributed to the increase in surface ratio (also surface energy and surface strain) as well as the increase of interface strain due to the lattice mismatch with the substrate and/or the SAM.⁶⁶⁻⁶⁸ In general, an increase of the film thickness leads to a decrease of the surface ratio and a relaxation of the interfacial strain, and consequently the same properties as the bulk materials. Moreover, chemisorption can be used to induce the dynamic structural transformation of the highly-oriented, 2D-layered Fe[Pt(CN)₄] thin-films depending on the adsorbed guest molecules.⁶⁹

Remarkably, downsizing of the rigid, non-porous interdigitated Fe(py)₂[Pt(CN)₄] (py = pyridine) bulk MOF (no guest uptake) to the nanometre-size thin-film with a well-controlled thickness (16 nm) and a preferred crystallite orientation initiates the guest-dependent, gate-opening dynamic structural transformation. Upon ethanal adsorption of the thin-film, the switching from the **cp** form to the **op** form (with approximately 1.6 % change in the unit cell parameter *b* (related to 020 diffractions) at relative vapour pressure of 0.95) is observed.⁷⁰ This phenomenon is induced by the lowering of potential energy barrier to guest diffusion within the interlayer space of the nanometre-sized thin-film. Increasing of the film thickness further leads to a suppression of the gate-opening-type structural flexibility.⁷⁰ Note that, the same properties are also observed in the Ni-based analogue films, namely Fe(py)₂[Ni(CN)₄], however with less pronounced of flexibility.⁷¹

Building up on this knowledge, we herein demonstrate the incorporation of alkylether-functionalized linkers into Cu-based layered-pillared SURMOFs fabricated by stepwise LPE on SAM-functionalized Au-coated QCM substrates. By tracking the frequency change of the QCM sensors, the growth behaviour of the SURMOFs and the adsorption isotherms of volatile organic compounds can be examined. Guest-induced structural flexibility of the obtained SURMOFs was characterized by *in-situ* synchrotron grazing incidence X-ray diffraction (GIXRD) with a custom-built, semi-quantitative vapor adsorption setup. The *in-situ* GIXRD during methanol sorption at 25 °C reveals unique structural dynamics of the alkylether-functionalized SURMOFs, which is distinct from the corresponding bulk materials. In other words, anchoring the flexible MOFs onto substrate surfaces alters the guest-induced breathing phenomena, with a marked dependence on the number of LPE deposition cycles (*i.e.* crystallite dimensions). Hereafter, the systematic control and understanding of structural flexibility when immobilizing the flexible MOFs onto the devices are discussed in great detail.

5.2 Structural flexibility of Cu-based layered-pillared bulk MOF powders upon methanol sorption

To get insight into the structural transformability upon guest-sorption of the Cu-based layered-pillared MOFs consisting of the alkylether-functionalized linkers (Figure 5.3), a dynamic guest-sorption behaviour at ambient temperature of the bulk powders is firstly investigated. Solvothermal reaction at 120 °C for 48 h of $\text{Cu}(\text{NO}_3)_2 \cdot 3\text{H}_2\text{O}$ with 2,5-diethoxy-1,4-benzenedicarboxylic acid ($\text{H}_2\text{DE-bdc}$) and dabco in dimethylformamide (DMF) affords the solvated $\text{Cu}_2(\text{DE-bdc})_2(\text{dabco})$ (**1bulk**) polycrystalline powder (as-synthesized **lp** phase). Upon drying *in vacuo* overnight at 130 °C, **1bulk** undergoes a breathing transition, during which the solvated, **lp** framework of **1bulk** transforms to the activated, **np** form due to the favourable dispersive interactions between neighbouring alkylether-functionalized pendant sidechains within the framework after solvent removal (showing a change in unit cell parameters and also the XRD patterns in Figure 5.4). Upon guest removal in **1bulk**, the square framework grids of the **lp** phase transform to the rhombic framework grids of the **np** phase, while the dabco-containing axis remains

unchanged, which is also observed for the prototypical Zn-based layered-pillared MOF consisting of the same functionalised linker.⁵⁰ Moreover, the use of the related 2,5-bis(2-methoxyethoxy)-1,4-benzene dicarboxylic acid ($H_2BME\text{-}bdc$) as a layered linker in the same solvothermal synthesis forms the analogue material $Cu_2(BME\text{-}bdc)_2(dabco)$ (**2bulk**) as a polycrystalline powder (Figure 5.4). Variation of the alkyl-functionalised sidechains within the MOF frameworks (the presence of the linkers is also confirmed by the IR spectra, Figure 5.5) leads to the different degree of framework flexibility as well as the slightly change in thermal stability (Figure 5.6).

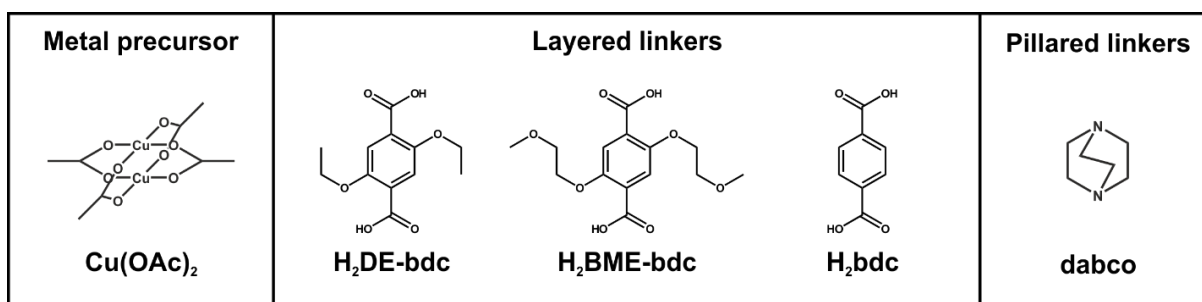


Figure 5.3 Chemical structure of organic used for preparation of layered-pillared MOFs.

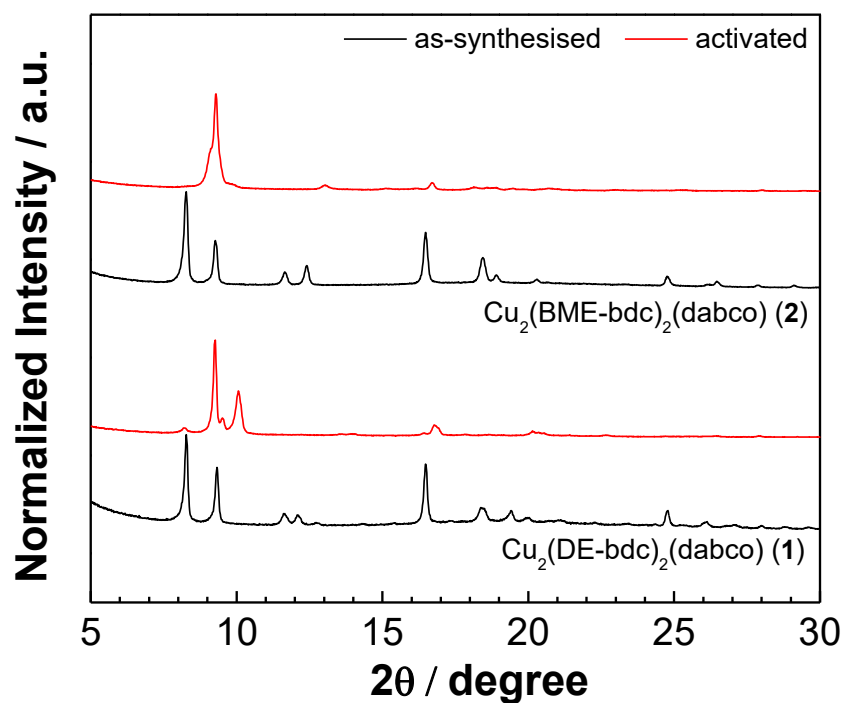


Figure 5.4 XRD patterns of as-synthesised and activated $Cu_2(DE\text{-}bdc)_2(dabco)$ (**1bulk**) and $Cu_2(BME\text{-}bdc)_2(dabco)$ (**2bulk**) powders using $Cu\ K\alpha$ radiation as an X-ray source.

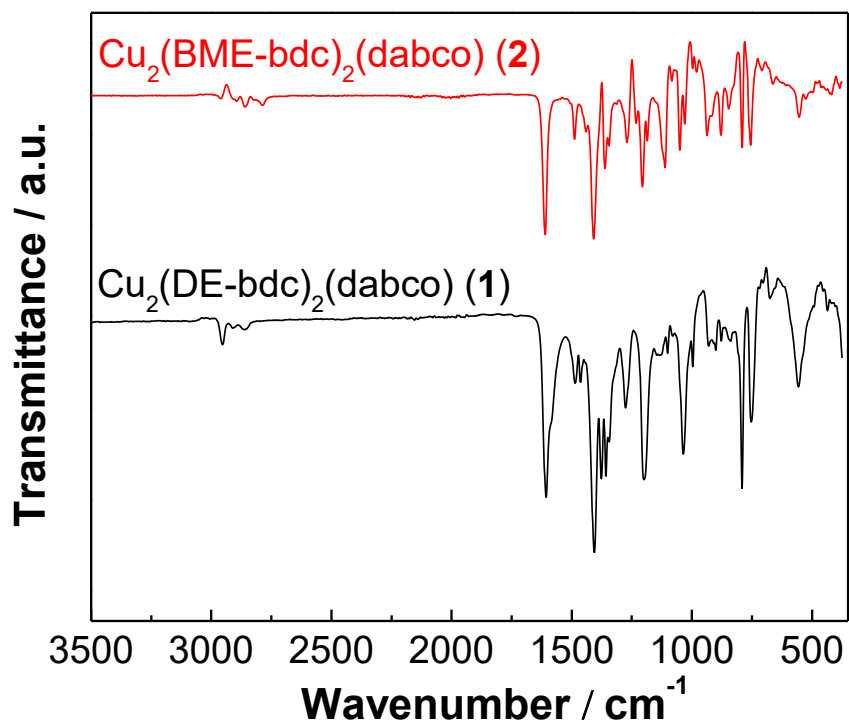


Figure 5.5 Fourier-transformed Infrared (FT-IR) spectra of the activated powders of **1bulk** and **2bulk**.

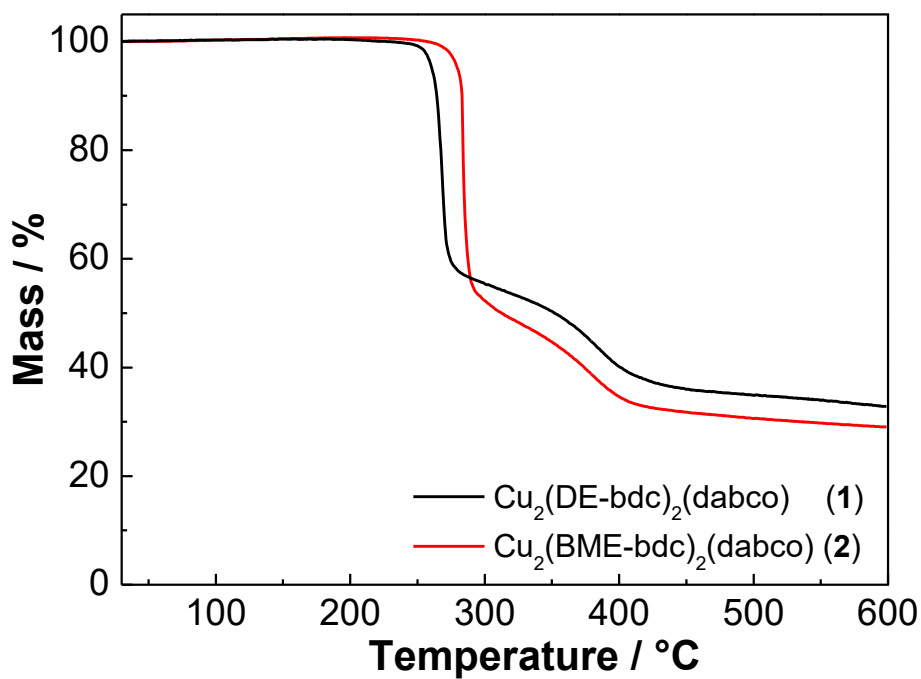


Figure 5.6 Thermal gravimetric (TG) curves of the activated powders of **1bulk** and **2bulk**.

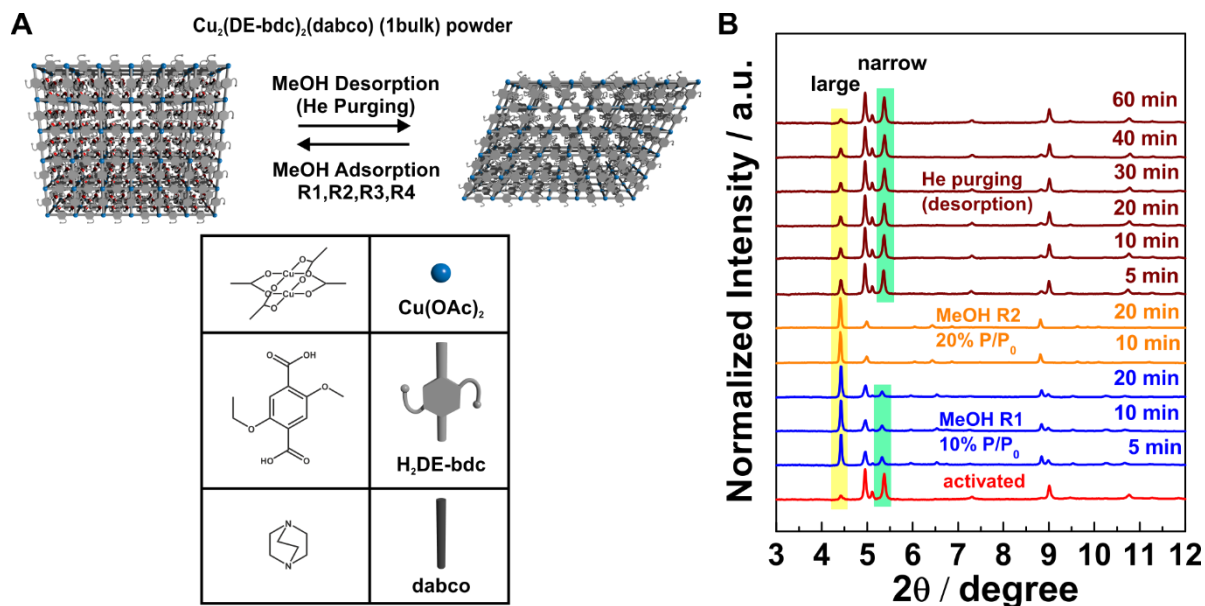


Figure 5.7 Structural responses upon methanol sorption in **1bulk**. (A) schematic representation of the framework transformation of **1bulk** upon host-guest interaction (so-called breathing transition) and its components within the **1bulk** framework; (B) GIXRD profiles (synchrotron X-ray wavelength of 0.827 Å) upon *in-situ* methanol sorption at 25 °C. Adsorption of 10% P/P_0 methanol vapour induces the framework transition (blue plots) from the **np** phase (highlighted in green) to the **lp** phase (highlighted in yellow). The transition to the **lp** phase is completed by adsorption of at least 20% P/P_0 methanol vapour (orange plots). Purging with pure He gas changes the framework back to the narrow-pore phase (wine plots). This reversible phase transition reveals the structural flexibility of **1bulk** upon methanol sorption at ambient temperature.

Building upon this characteristic feature (Figure 5.7A), we investigate the structural responses of the activated **np** powder of **1bulk** during a dynamic sorption process of polar guest molecules (herein, methanol vapour) at ambient temperature (25 °C) using synchrotron grazing incidence X-ray diffraction (GIXRD) with a self-made, semi-quantitatively controlled gas/vapour adsorption system (schematic setup is discussed in Chapter 6). According to the *in-situ* GIXRD patterns (Figure 5.7B), adsorption of methanol vapour with low relative vapour pressure (P/P_0) of 10% in a dynamic He gas stream (blue plots) into the activated **1bulk** powder initiates the framework transition from the **np** phase (highlighted in green) to the **lp** phase (highlighted in yellow). In this stage, most of **1bulk** is present in the **lp** form indicating that polar molecules within the dynamic gas stream are able to trigger the framework breathing phenomena because of interactions between

the pendant sidechains within the framework and the guest molecules. The transition towards the **lp** phase is completed by an adsorption of at least 20% P/P_0 methanol vapour (orange plots). Consequently, the **lp** phase is converted back to the **np** phase by purging with a stream of pure He gas. Prolonged exposure of the sample to the He gas leads to a higher degree of framework conversion to the **np** form (wine plots). These *in-situ* GIXRD profiles reveal the reversible structural flexibility of the **1bulk** powder upon sorption of methanol at ambient temperature. Moreover, the analogue **2bulk** exhibits a similar behaviour upon methanol sorption at 25 °C as the **1bulk** (according to the GIXRD profiles in Figure 5.8), although the degree of framework breathing phenomena (in other words, the change in unit cell parameters) is weaker than the **1bulk**. Again, adsorption of methanol vapour with 10% P/P_0 initiates the structural transformation from the activated, **np** form to the solvated, **lp** form. Note that, the reversible structural flexibility of these Cu-based bulk MOFs can be modified by altering the alkylether-functionalized sidechains of the layered dicarboxylate linker as observed in the Zn-based prototypical MOFs.⁵⁰ Substituents that are sterically less demanding and/or possess functionalities with a stronger interaction provoke a more drastic contraction of the framework during the breathing transition upon guest removal.⁵⁰

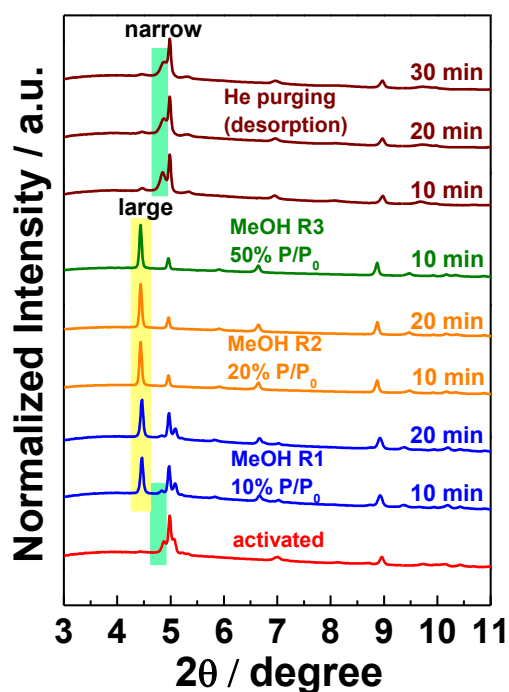


Figure 5.8 GIXRD profiles of the **2bulk** powder upon in-situ methanol sorption at 25 °C.

5.3 Structural flexibility of Cu-based layered-pillared MOF crystallites anchored at surfaces

In order to use MOFs as functional materials in real-world applications, particularly in solid-state and nanotechnology devices, the implementation of MOFs within these devices is essential. In this work, we endeavor to integrate structurally flexible MOFs (e.g. MOF **1** and **2**) into QCM sensors by surface anchoring of the MOF crystallites. The stepwise LPE process, which has been established to fabricate the parent, rigid $\text{Cu}_2(\text{bdc})_2(\text{dabco})$ (**3**) and its analogues as both homo- and heterostructured thin-films with well-defined thickness and crystallite orientation,⁶⁵ is slightly modified and used for the fabrication of **1** and **2** thin-films of varying thickness. Solutions of $\text{Cu}(\text{OAc})_2$ and the mixed organic linkers are alternately applied to the QCM substrate in a continuous flow for 40, 60, 80 or 120 cycles, in which each precursor dosing step is separated by flushing of the reactor cell with ethanol (schematic representation in Figure 5.9A). Hereafter coin the term as **1tf**_x and **2tf**_x (x = number of deposition cycles), respectively.

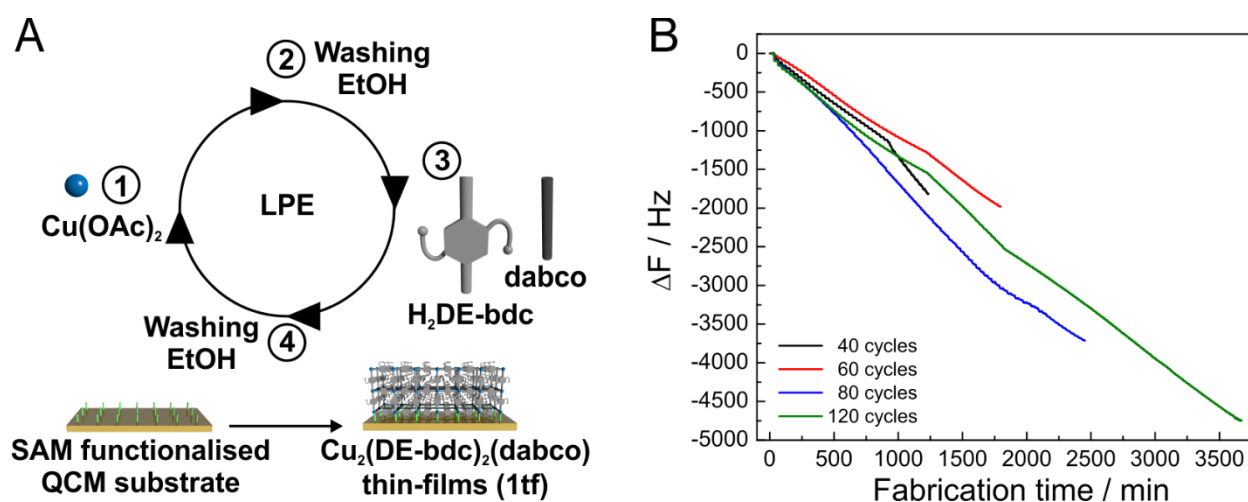


Figure 5.9 Changes in the QCM oscillator frequency (F) as a function of time during the LPE growth of **1tf**. (A) The **1tf** thin-films were fabricated via a stepwise LPE process, in which the QCM substrates were alternately exposed to the solutions of metal and organic precursors in the continuous flow mode at 40 °C followed by washing with ethanol after each precursor dosing step for a total of 40, 60, 80 and 120 cycles. (B) Generally, the **1tf** thin-films exhibit a linear growth during the LPE process. According to Sauerbrey Equation,⁷² the decrease of oscillation frequency from the fundamental frequency of the QCM sensor is proportional to the increase of the mass of the thin-films. Hence, the crystallite dimension of the thin-films corresponds to the total number of fabrication cycles.

In-situ recording of the changes in the QCM oscillator frequency (Figure 5.9B) reveals a linear growth behaviour of the 1tf_x during the whole LPE process, indicating an effective control of the deposited sample mass on the substrate by the total number of fabrication cycles. Closer inspection of the QCM frequency data (Figure 5.10), reveals a saturated deposition during each deposition step of the metal and the organic linkers illustrating a self-terminated growth of the layered-pillared MOF thin-films.

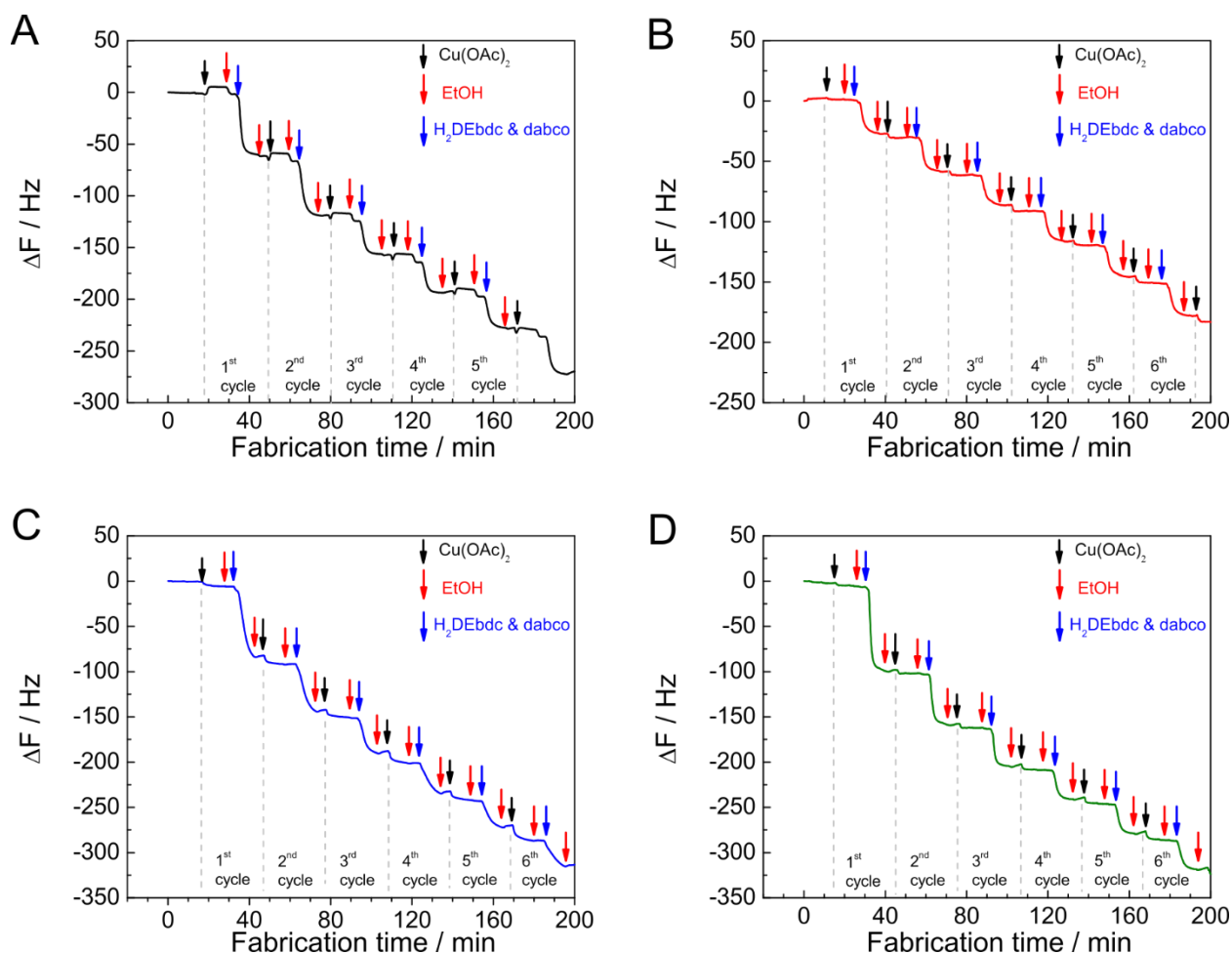


Figure 5.10 Changes in the QCM oscillator frequency (F) as a function of time at the early stage of the LPE growth of the (A) 1tf_{40} , (B) 1tf_{60} , (C) 1tf_{80} and (D) 1tf_{120} thin-films. Generally, the LPE growth of the 1tf_x show a saturated deposition in both dosing steps of the metal solution and the organic linkers solution, indicating self-terminated growth phenomena of the stepwise LPE process.

Closer inspection to the crystallinity, the as-synthesised **1tf** thin-films fabricated on the —COOH functionalised QCM substrates exhibit a high crystallinity with a preferred orientation of the (110)-related planes of the solvated, **lp** form along the film growth direction (black plots of the out-of-plane GIXRD patterns in Figure 5.11). Specifically, this means that the $\text{Cu}_2(\text{fu-bdc})_2$ grids of the **1tf** are oriented orthogonally to the substrate surface. Along this framework dimension the wine-rack-like motion of the crystal-to-crystal breathing transition occurs in the bulk material. Further, the structural responses upon guest introduction/removal in dependence of the film thickness of **1tf_x** are examined by *in-situ* GIXRD during dynamic sorption of methanol vapour. Two dimensional GIXRD patterns of the thin-films are recorded at different stages of the sorption process; namely 1) the as-synthesised or solvated stage mimicked by soaking the samples in methanol, 2) the activated, guest free stage by purging with He gas, 3) during adsorption by loading the **1tf_x** thin-films with 10%, 20%, 50% and 80% P/P₀ of methanol vapour in a dynamic He stream, and 4) during desorption by purging the material with He gas. Herein, the one-dimensional integrations of the GIXRD data in the out-of-plane and the in-plane profiles are used to indicate the crystallinity and the structural responsivity of **1tf_x** in the perpendicular and the parallel direction to the substrate surface, respectively.

Interestingly, the out-of-plane GIXRD profiles of the **1tf_x** fabricated on the —COOH functionalised QCM substrates (Figure 5.11) indicate a unique structural responsivity upon methanol sorption of the crystallites anchored perpendicular to the substrate surface (or along the film growth direction), which is significantly different from the dynamic guest-sorption behaviour observed in the **1bulk** discussed in the previous section (Figure 5.7). Remarkably, the degree of structural flexibility highly depends on the total number of LPE fabrication cycles, or in other words, the crystallite dimension. The crystallites in the **1tf₄₀** thin-film remain in the **lp** form regardless of the treatment (Figure 5.11A). This means, anchoring of the flexible MOF crystallites onto the substrate surface with relatively low crystallite dimension (low number of LPE fabrication cycles) leads to a restriction of the framework flexibility upon guest introduction and removal (Figure 5.12A). It may be explained that the LPE fabrication of MOF thin-film on the SAM-functionalised substrate leads to a strong chemical binding between the MOF crystallites and the functional groups of the SAM-functionalised surface.

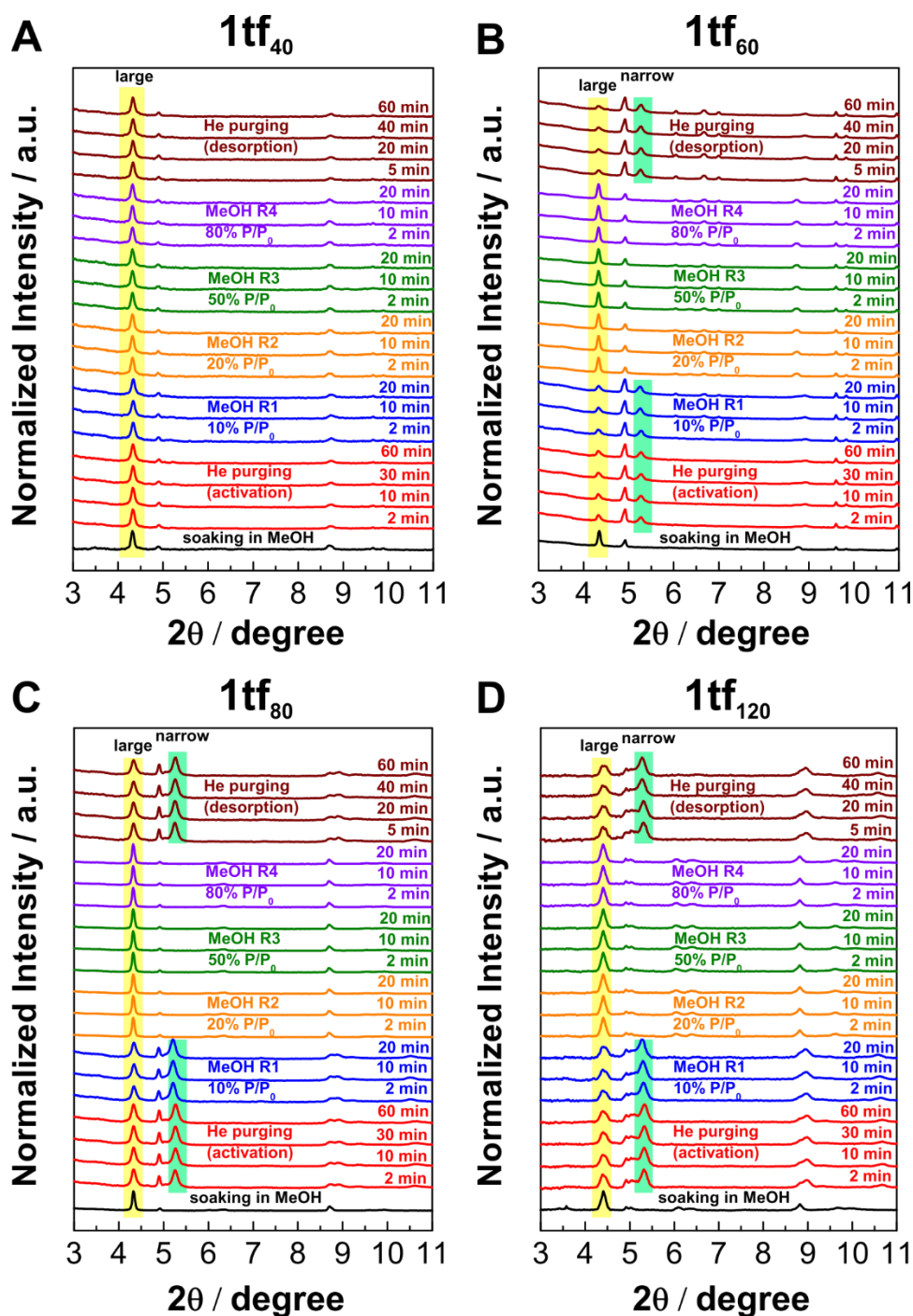


Figure 5.11 Out-of-plane GIXRD profiles of the **1tf** materials during *in-situ* methanol sorption at 25 °C. Herein, (A) **1tf**₄₀, (B) **1tf**₆₀, (C) **1tf**₈₀, and (D) **1tf**₁₂₀ thin-films were fabricated on the —COOH functionalised QCM substrates and exhibit the preferred carboxylate-related crystallite orientation along the film growth direction. The **1tf** materials anchored to the substrate surface exhibit different breathing phenomena upon methanol sorption from the **1bulk**. Note that, the degree of structural flexibility depends on the total number of fabrication cycles (see also Figure 5.12).

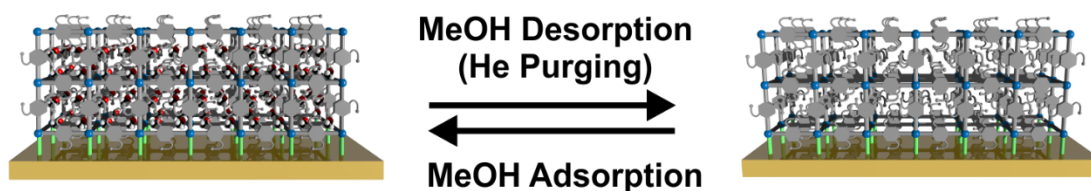
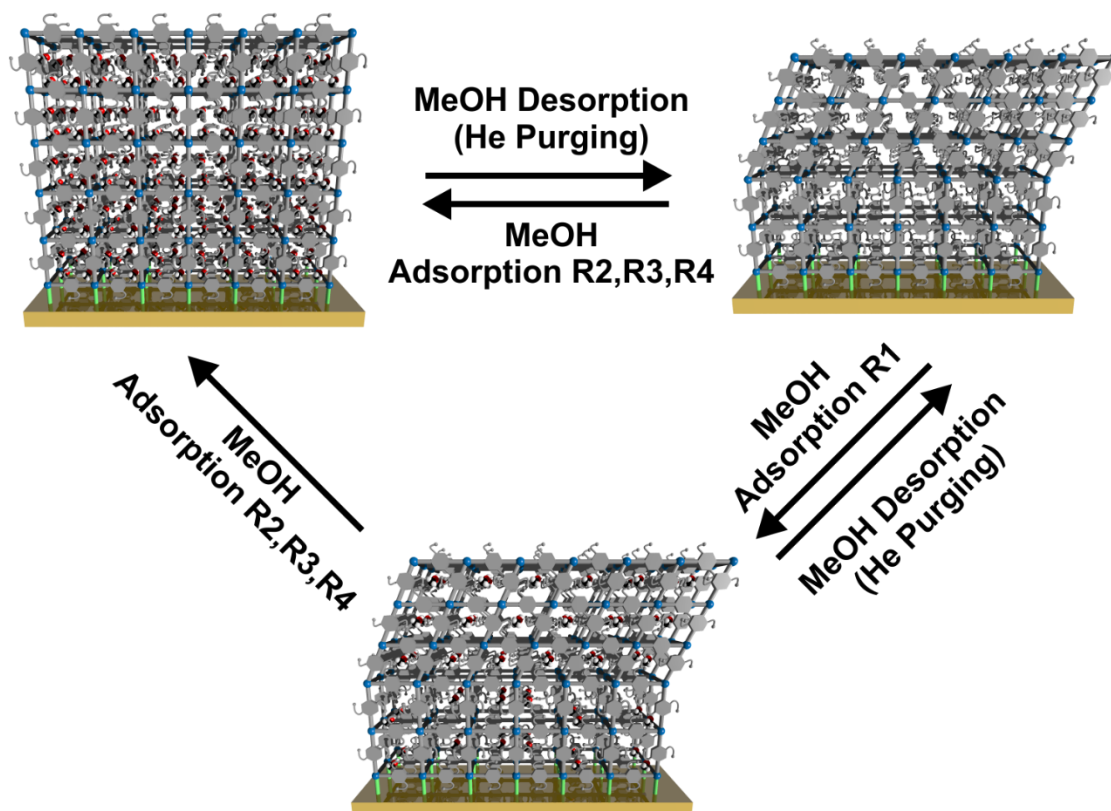
A 1tf_{40} thin-filmB 1tf_{60} , 1tf_{80} and 1tf_{120} films

Figure 5.12 Schematic representation of the structural responses upon methanol sorption for 1tf thin-films grown on carboxylate-terminated substrates. The 1tf materials exhibit unique structural flexibility depending on the number of LPE fabrication cycles (or the crystallite dimension). (A) 1tf_{40} retains the **lp** phase regardless of the methanol treatment, indicating the restriction of the framework flexibility when anchored on the surface. (B) The films with higher crystallite-dimension (1tf_{60} , 1tf_{80} and 1tf_{120}) reveal structural flexibility, which both the **lp** and the **np** phases present. Unlike **1bulk**, the structural transition is inhibited by the interaction between the MOF crystallites and the substrate surface, therefore higher P/P_0 of methanol vapour (at least 20%) is required to change from the empty **np** phase back to the loaded **lp** phase.

Upon guest removal from **1tf₄₀**, the interaction between the neighbouring alkylether-functionalised sidechains within the frameworks may not be strong enough to overcome the chemical interaction between the MOF crystallites and the functionalised surface. Moreover, the restriction of the breathing transition in the **1tf₄₀** thin-film may also be affected by the downsizing of the crystallite size and the formation of monodomain which leads to a high activation barrier for generating of the nucleation centres for structural flexibility.⁵⁸⁻⁶⁰ Combining the two perspectives, the MOF crystallites in **1tf₄₀** therefore cannot shrink to the **np** form but still remains in the **lp** form even with a total removal of the guest molecules.

The higher crystallite-dimension **1tf₆₀**, **1tf₈₀** and **1tf₁₂₀** films reveal a unique structural response upon methanol adsorption (Figure 5.11B to 5.11D). After activation by purging with He gas, these **1tf** crystallites are present in both the **lp** and the **np** forms (red plots). On the one hand, the **1tf** crystallite domains anchored closely to the surface remain in the **lp** phase due to a restriction of framework flexibility as observed in **1tf₄₀**. On the other hand, the **1tf** crystallite domains at the extended part, which have less interaction with the substrate, undergo a framework transition and are therefore present in the **np** phase after the activation process. Unlike the **1bulk**, an adsorption of methanol vapour of 10% P/P_0 (blue plots) cannot induce the transformation from the **np** back to the **lp** phase for the **1tf** with larger crystallite dimensions. Adsorption of methanol vapour with P/P_0 of at least 20% (orange, green and purple plots) are required for this structural transition, highlighting a retardation of the framework flexibility by anchoring to the substrate (Figure 5.12B). This observation emphasizes the important fact, that the presence of both the **lp** and the **np** phases in activated **1tf₆₀**, **1tf₈₀**, and **1tf₁₂₀** is not a result from a mixture between the **1tf** and the activated, **np 1bulk** powders on top of it. For **1bulk**, adsorption of 10% P/P_0 methanol vapour already leads to the **np**→**lp** transition, whereas there is no phase transition clearly observed for the same adsorption amount in the cases of the **1tf** (see Figure 5.13). This framework flexibility in the higher crystallite-dimension **1tf₆₀**, **1tf₈₀**, and **1tf₁₂₀** films is a reversible process, and the activated phase consisting of both the **lp** and the **np** forms is recovered during the desorption process by purging with pure He gas flow.

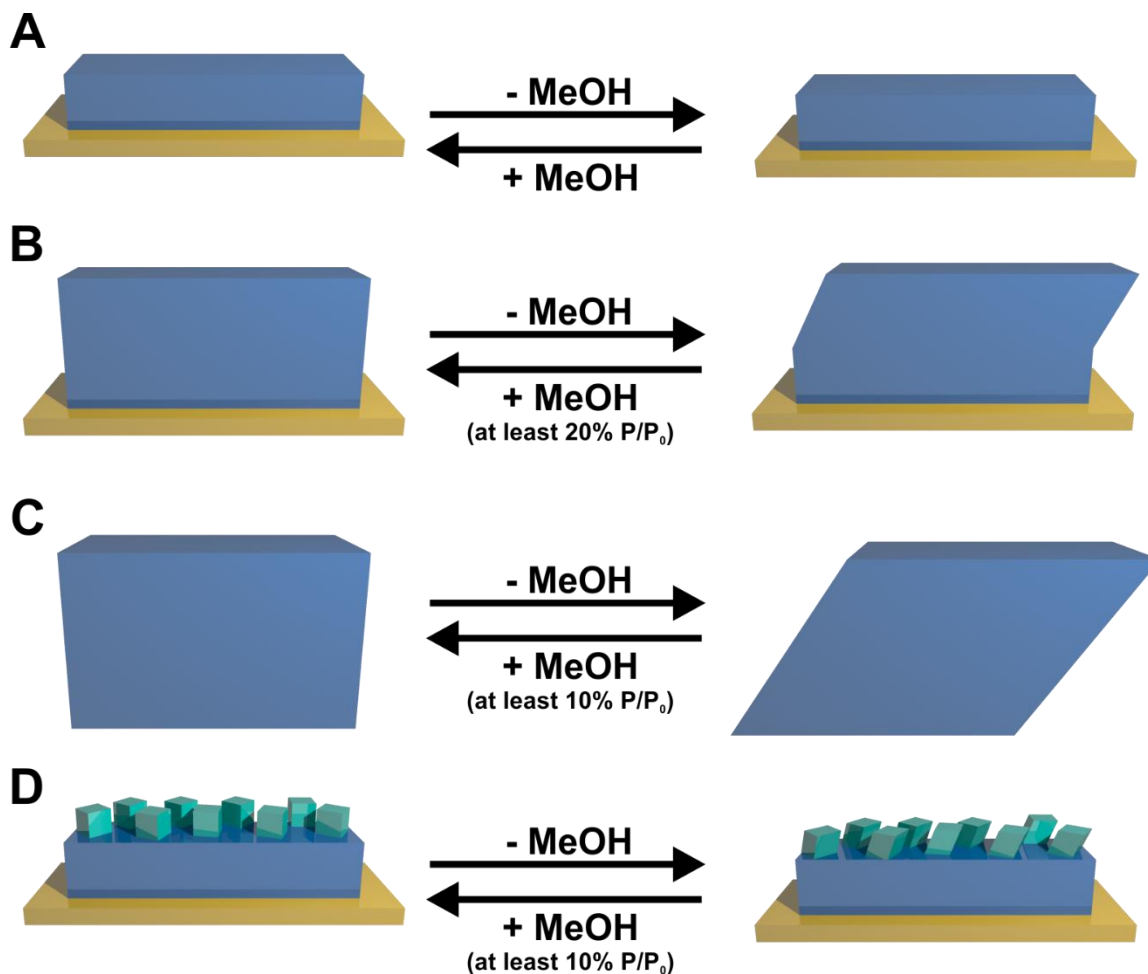


Figure 5.13 Schematic representation of the possibilities for structural responses upon methanol sorption process of the MOF **1**. A) The thin-film (**1tf₄₀**) exhibits a restriction of the framework flexibility due to the strong interaction of the MOF crystallites with the substrate surface and the formation of monodomain leading to a higher activation barrier for initiating the framework transition. Hence, only the **lp** form is observed regardless on the sorption treatments; B) The higher crystallite-dimension film (**1tf₆₀**, **1tf₈₀**, and **1tf₁₂₀**) exhibits the framework flexibility but with restriction level. Only the crystallites at the top part could undergo a breathing transition between **np** and **lp** forms during the polar guest sorption process, while the bottom part which is strongly attached to the surface still remains in the **lp** form. MeOH of at least 20% P/P₀ is required to initiate the framework transformation; C) The **1bulk** material undergoes a breathing phenomenon upon methanol sorption process even with 10% P/P₀; D) If the obtained materials consisting of the low crystallite-dimension thin-film mixed with the bulk powder on top of it, the bulk powder should undergo the breathing phenomenon by introduction of methanol of only P/P₀ of 10%. In our observation, the films obtained with higher number of fabrication cycles are fitted to the scenario B but not to the scenario D since methanol with P/P₀ of at least 20% is required for initiating the framework transition.

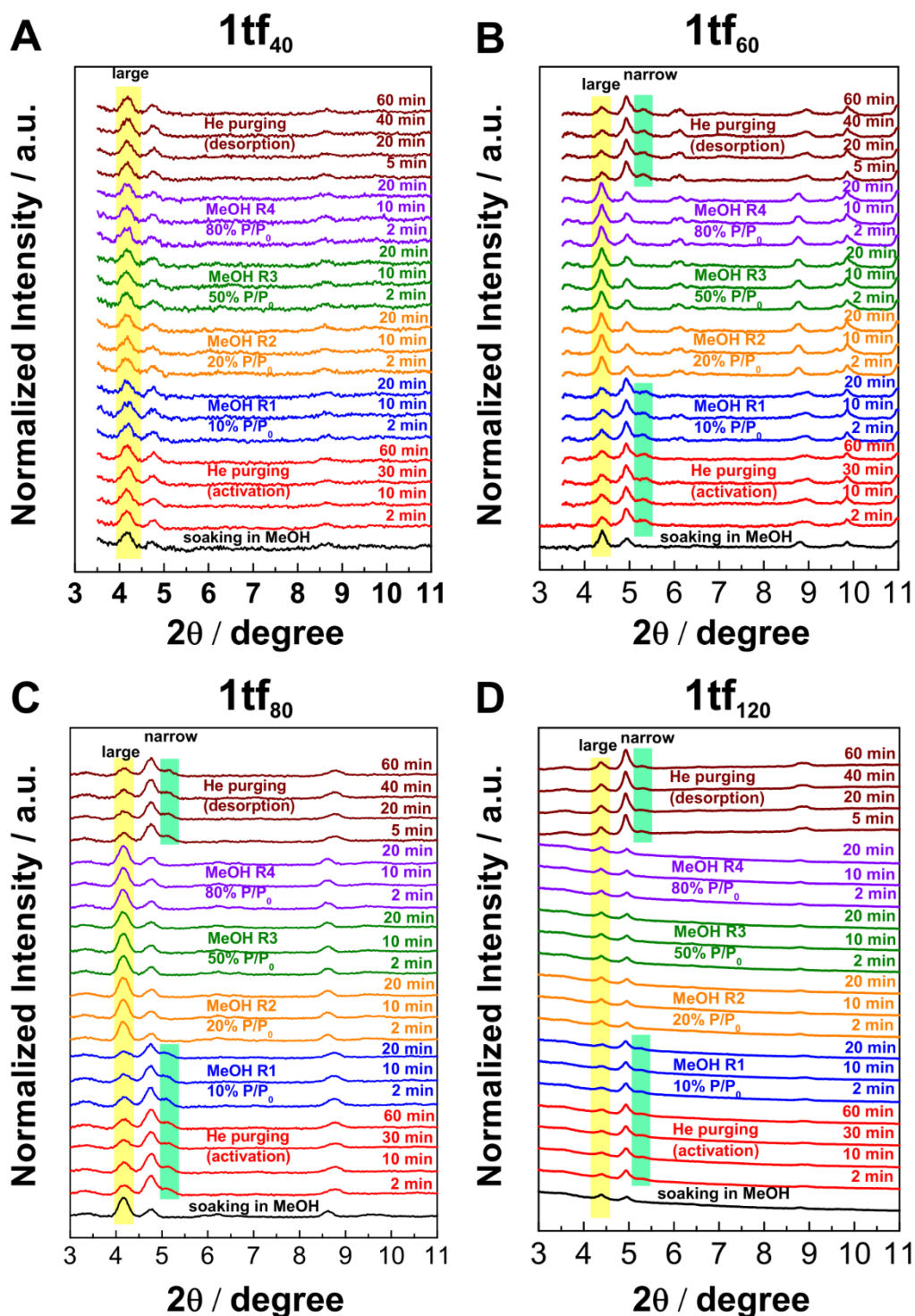


Figure 5.14 In-plane GIXRD profiles of the 1tf materials during *in-situ* methanol sorption at 25 °C. Herein, (A) 1tf_{40} , (B) 1tf_{60} , (C) 1tf_{80} , and (D) 1tf_{120} thin-films were fabricated on the $-\text{COOH}$ functionalised QCM substrates and exhibit the preferred carboxylate-related crystallite orientation along the film growth direction.

Furthermore, the in-plane GIXRD profiles of the **1tf** films (Figure 5.14) indicate the similar structural responsivity upon a dynamic methanol sorption process, although a lower ratio of the **np** phase is presented after the activation. This result indicates a more restricted form of the framework flexibility in the parallel direction to the substrate surface due to more interactions from the attachment of **1tf** to the substrate and less degree of freedom for movement comparing to perpendicular to the substrate. We reveal fine-tuning of the degree of structural flexibility in **1tf** by varying the crystallite dimension.

As complimentary results for the *in-situ* GIXRD profiles, scanning electron microscopic (SEM) images (illustrated in Figure 5.15 and 5.16) of **1tf₄₀** shows significantly smaller cubic crystallite particles (approximately 200 nm) than the thicker **1tf₆₀**, **1tf₈₀**, and **1tf₁₂₀** analogues (ranging between 400 nm to 1 μ m). Furthermore, methanol adsorption isotherms measured at 25 °C on an environmentally controlled QCM instrument indicate a different shape of the methanol adsorption curve for the different **1tf** samples (Figure 5.17 and 5.18). In details, **1tf₄₀** exhibits a single-step methanol adsorption signalling a presence of only the **lp** form due to restricted flexibility by anchoring to the substrate. In contrast, **1tf₆₀**, **1tf₈₀** and **1tf₁₂₀** show two-steps adsorption profiles. The first adsorption step (P/P_0 up to 0.15) is attributed to the combination between the adsorption into the **lp** form of the crystallite domains anchored close to the substrate surface and into the **np** form of the crystallite domains at the top of the crystallites (extended part from the substrate). A rapid change in methanol adsorption curve occurs at P/P_0 of 0.15, indicating the **np** \rightarrow **lp** framework transition of the top crystallite domains leading to the further adsorption due to the higher adsorption capacity of the **lp** form. At high P/P_0 , the total specific adsorption capacity of the different **1tf_x** analogues reaches nearly identical values (approximately 7.5 mmol of methanol per g of MOF), because all materials are solely present in the **lp** phase when P/P_0 of methanol vapour is higher than 20%. Note that, all the **1tf_x** analogues rather show a single-step desorption profile. In correspondence with the *in-situ* GIXRD results during methanol adsorption, the sorption data reveal the dependency of the structural flexibility of **1tf** on the dimension of the surface anchored crystallites.

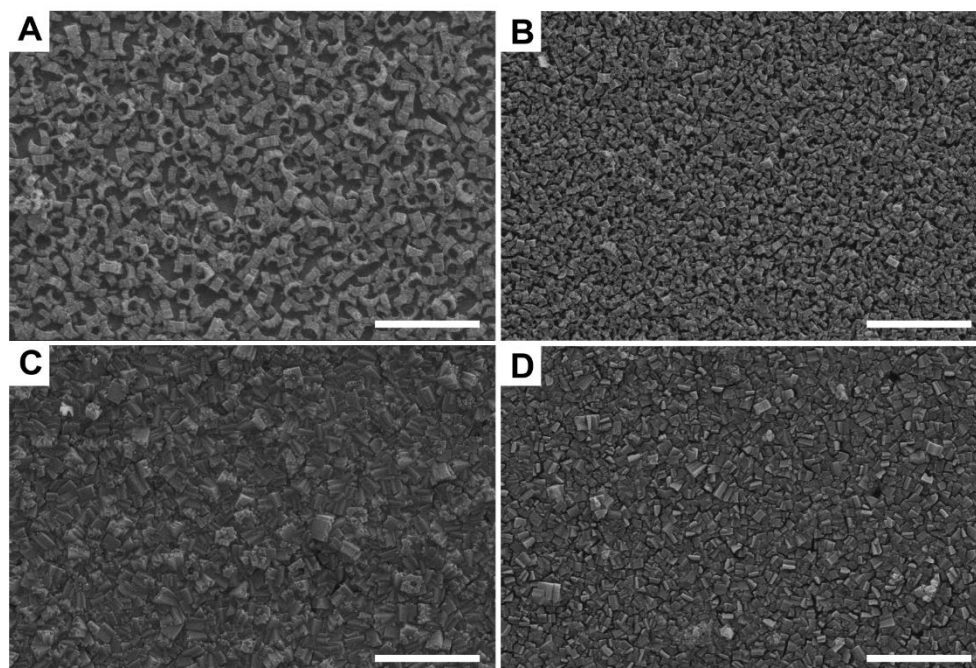


Figure 5.15 Top-view SEM images of the (A) **1tf₄₀**, (B) **1tf₆₀**, (C) **1tf₈₀**, and (D) **1tf₁₂₀** thin-films fabricated by the LPE process on the —COOH functionalised QCM substrates. Scale bar at each panel represents a length of 5 μm .

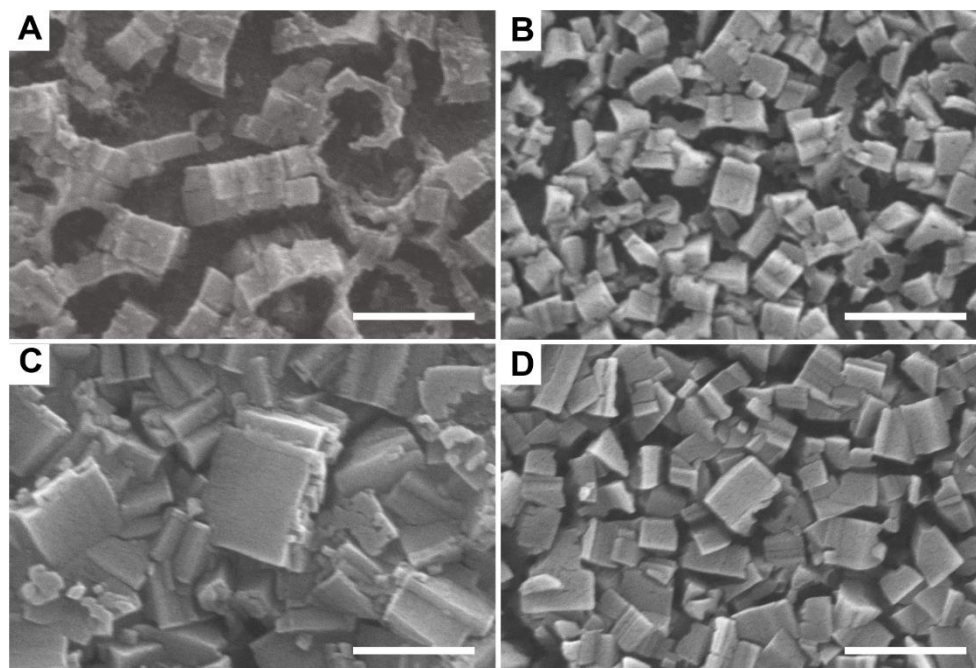


Figure 5.16 High-magnification SEM images of the (A) **1tf₄₀**, (B) **1tf₆₀**, (C) **1tf₈₀**, and (D) **1tf₁₂₀** thin-films fabricated by the LPE process on the —COOH functionalised QCM substrates. Scale bar at each panel represents a length of 1 μm .

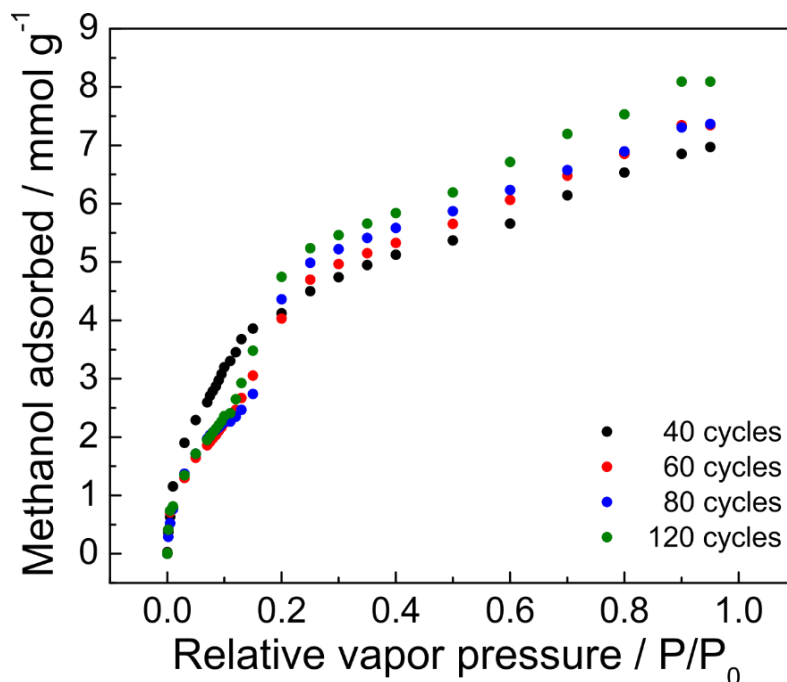


Figure 5.17 Methanol adsorption isotherms at 25 °C of **1tf** materials based on environmentally controlled QCM measurements. **1tf**₄₀ exhibits a single-step methanol adsorption, whereas **1tf**₆₀, **1tf**₈₀ and **1tf**₁₂₀ show two-steps adsorption (with a step at P/P_0 of 0.15). It reveals the dependency of the structural flexibility of **1tf** (upon the sorption of polar adsorbate at ambient temperature) on the dimension of crystallites anchored at the surface (proportional to number of LPE fabrication cycles).

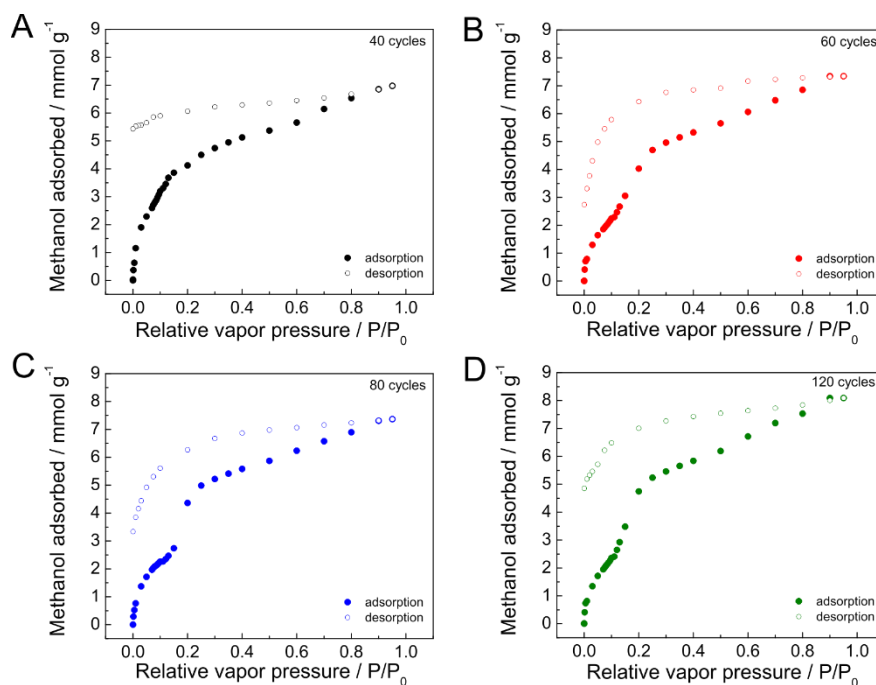


Figure 5.18 Methanol sorption isotherms at 25 °C of the (A) **1tf**₄₀, (B) **1tf**₆₀, (C) **1tf**₈₀, and (D) **1tf**₁₂₀ thin-films fabricated by LPE process on the —COOH functionalised QCMs.

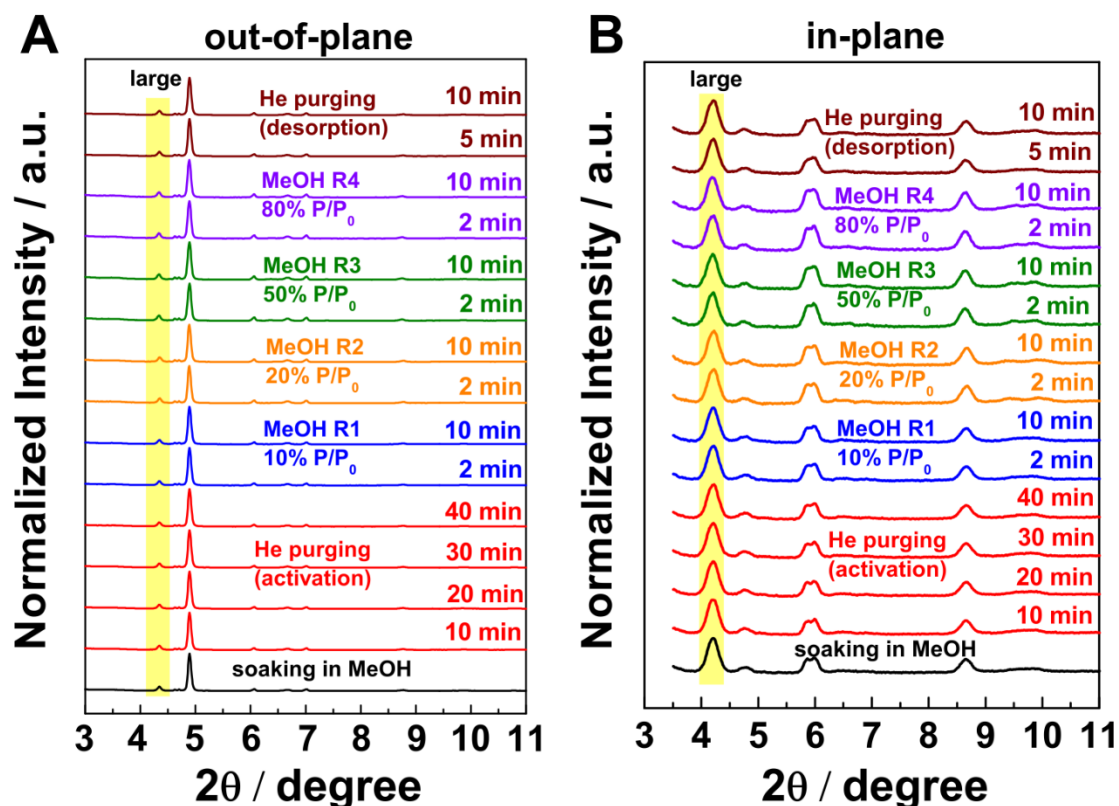


Figure 5.19 Out-of-plane and in-plane GIXRD profiles of the $1\text{tf}_{60}\text{-Py}$ thin-film fabricated by LPE process on the —pyridyl functionalised QCM substrates for 60 cycles upon in-situ methanol sorption at 25 °C. This thin-film exhibits the preferred dabco-related (001)-plane crystal-orientation along the film growth direction. Unlike the 1tf_{60} film exhibiting structural flexibility upon methanol sorption process, the $1\text{tf}_{60}\text{-Py}$ film remain in the **lp** form under all sorption treatments, indicating a more restriction of the framework breathing in this orientation.

For additional insights, 1tf is also fabricated by LPE process for 60 cycles on pyridyl-functionalised QCM substrates (coined the term as $1\text{tf}_{60}\text{-Py}$, details about functionalisation of Au substrates by SAM are explained in Chapter 6), which exhibits preferred growth along the (001)-plane, with the $\text{Cu}_2(\text{fu-bdc})_2$ sheets in parallel to the substrate surface. Interestingly, out-of-plane and in-plane GIXRD profiles (Figure 5.19) reveal a maintenance of the **lp** form under all sorption treatment conditions. Moreover, $1\text{tf}_{60}\text{-Py}$ exhibits a single-step methanol adsorption isotherm (Figure 5.20). Note that, a small deviation from the type-I isotherm curve at P/P_0 of 0.15 suggests a small degree of framework flexibility upon methanol adsorption. However, there is no phase transition

observed in the *in-situ* GIXRD profiles during methanol sorption, possibly due to the lack of a long-range ordering. The breathing of **1tf**_{60-Py} is more restricted than in the case of the **1tf**₆₀, as the Cu₂(DE-bdc)₂ grids in the **1tf**_{60-Py} would undergo their wine-rack-like motion in parallel to the stiff surface to which they are anchored via Pyridyl-terminated SAM. This observation indicates the dependency of the framework flexibility of the **1tf** films not only on the crystallite dimension but also on the crystallite orientation anchored on the substrate surface.

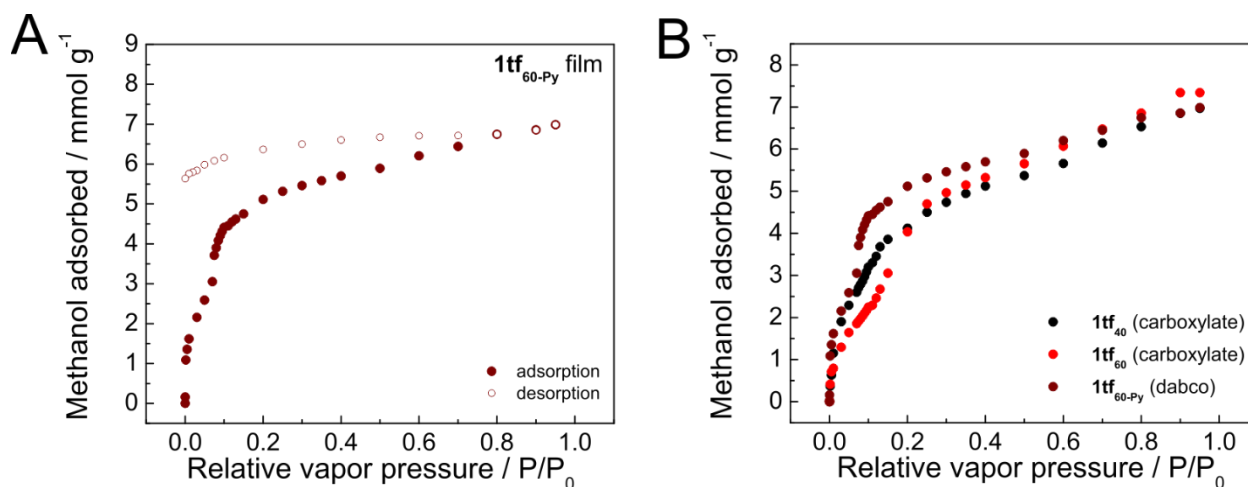


Figure 5.20 Methanol sorption isotherm at 25 °C of the **1tf**_{60-Py} thin-film fabricated by LPE process on the —pyridyl functionalised QCM substrates for 60 cycles. (A) The **1tf**_{60-Py} film with preferred (001)-plane crystallite orientation along the film growth direction exhibits a tiny step in the methanol adsorption curve at P/P₀ of 0.15, indicating a small degree of framework flexibility upon methanol adsorption process. However, there is no phase transition observed in the *in-situ* GIXRD measurement upon methanol adsorption process (Figure 5.19); (B) Methanol adsorption curve of the **1tf**_{60-Py} film compared with the ones of the **1tf**₄₀ and **1tf**₆₀ films with preferred (110)-related planes crystallite orientation along the film growth direction. The adsorption curve of the **1tf**_{60-Py} film show a closer adsorption phenomenon to the **1tf**₄₀ film than to the **1tf**₆₀ film, indicating a restriction of framework flexibility and a maintenance of **lp** phase during the whole sorption process as a result from the lower crystallite dimension and the controlled crystallite orientation. The **1tf**₆₀ film shows two-steps adsorption with a change starting at P/P₀ of 0.15 due to the **np**→**lp** framework transition of the extended-part crystallite domains. Note that, the total adsorption capacity at high P/P₀ is rather similar in all of the **1tf**₄₀, **1tf**₆₀ and **1tf**_{60-Py} films since all the MOF crystallites are in the **lp** phase at this stage, highlighting the same degree of crystallinity of the **1tf** films.

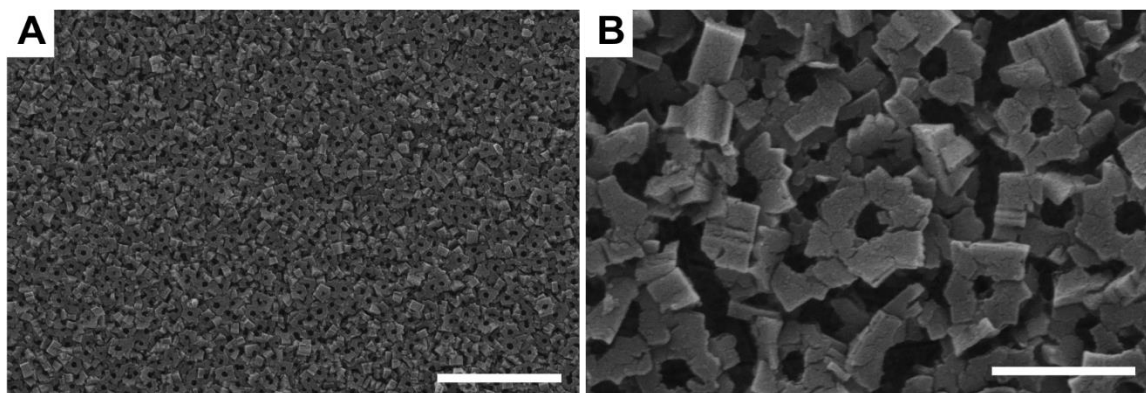


Figure 5.21 Top-view SEM images of the $1\text{tf}_{60}\text{-Py}$ thin-film fabricated by LPE process on the —pyridyl functionalised QCM substrates for 60 cycles. Scale bar at each panel represents a length of (a) $5\ \mu\text{m}$ and (b) $1\ \mu\text{m}$.

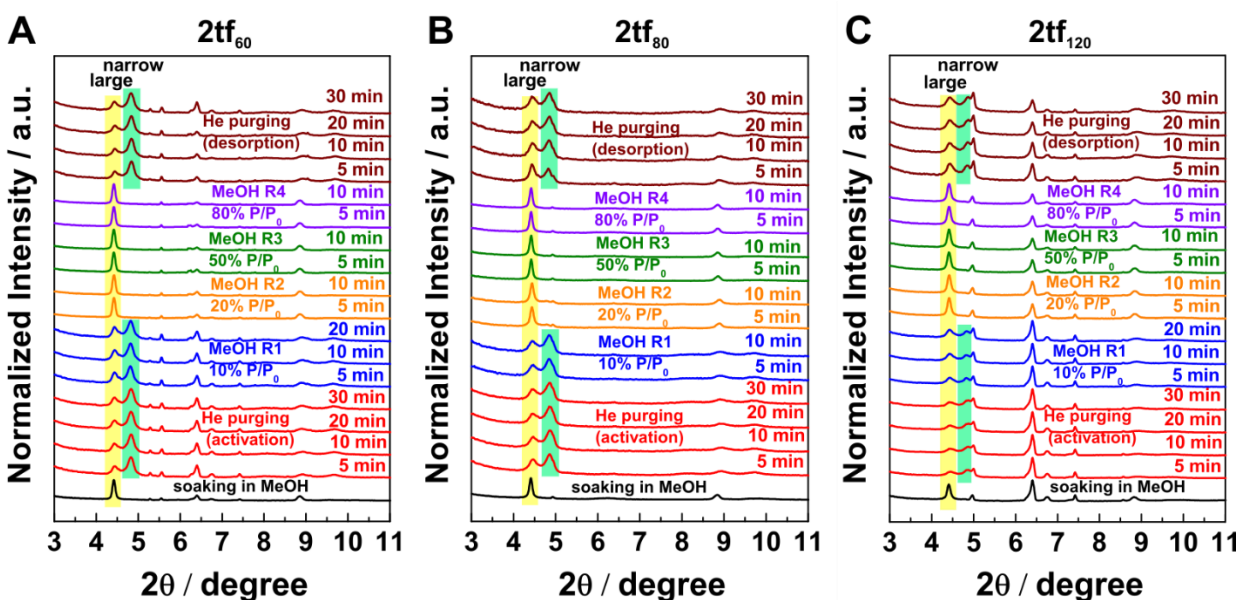


Figure 5.22 Out-of-plane GIXRD profiles upon in-situ methanol sorption at $25\ ^\circ\text{C}$ of (A) 2tf_{60} , (B) 2tf_{80} , and (C) 1tf_{120} thin-films fabricated by the LPE process on the —COOH functionalised QCM substrates and exhibiting preferred (010)-related plane orientation. The 2tf materials anchored to the substrate surface exhibit different breathing phenomena upon methanol sorption from the 2bulk . The degree of structural flexibility depends on the total number of LPE fabrication cycles like in the case of 1tf films. However, the change in unit cell parameters during the $\text{np} \rightarrow \text{lp}$ breathing transition of the 2tf is smaller than the 1tf , highlighting the fine tune of framework flexibility by the choices of alkoxy-functionalised pendent groups in the frameworks.

For a proof of concept, thin films of **2** (**2tf_x**) are prepared by LPE process for 60 (**2tf₆₀**), 80 (**2tf₈₀**) and 120 (**2tf₁₂₀**) cycles on the —COOH functionalised QCM substrates. *In-situ* GIXRD profiles (Figure 5.22) show that the **2tf_x** films exhibit such a unique structural flexibility upon methanol adsorption similar to the **1tf_x** films. A combination of both the **lp** and **np** forms after activation and a requirement of methanol vapour of at least 20% P/P₀ for initiating the framework transition indicate a restriction of the framework flexibility of the alkylether-functionalised layered-pillared MOFs when anchored to the substrate. Note that, the LPE-60-cycles **3** thin-film (**3tf₆₀**) however shows a framework rigidity upon a dynamic methanol sorption process due to a lacking of the alkylether pendant sidechains (Figure 5.23).

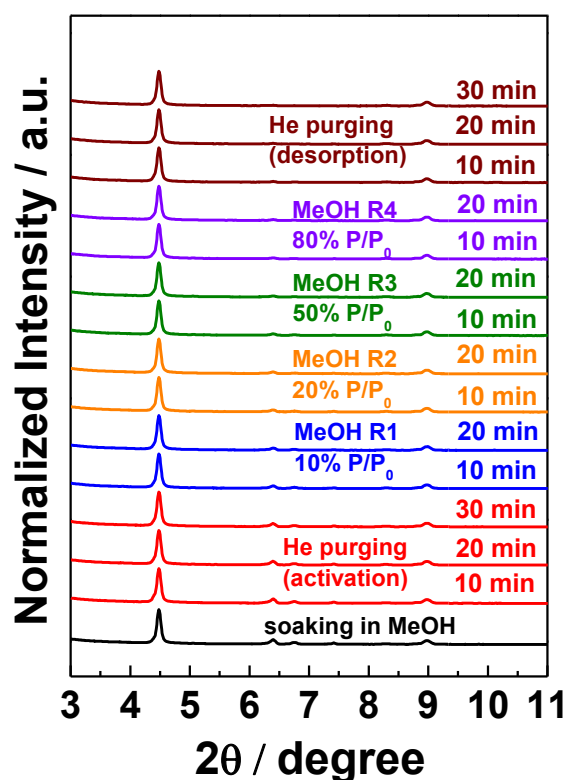


Figure 5.23 Out-of-plane GIXRD profiles upon in-situ methanol sorption at 25 °C of the **3tf₆₀** thin-film fabricated by the LPE process on the —COOH functionalised QCM substrates for 60 cycles. No framework breathing phenomena is observed during the methanol adsorption process and hence the MOF framework structure remains unchanged, indicating that the framework flexibility of the Cu-based layered-pillared MOFs is initiated by the introduction of alkoxy-functionalised pendent sidechains in the benzene-1,4-dicarboxylate linkers.

5.4 Summary

1bulk and **2bulk** undergo framework breathing transitions upon methanol vapour sorption at ambient temperature due to the favoured interaction between the polar guest molecules and the alkylether pendant sidechains within the framework. These flexible MOF crystallites are anchored on the substrates via stepwise LPE. The crystallite orientation is triggered by SAM-functionalisation of the surface and the crystallite dimension is controlled by the number of fabrication cycles. The bottom-up nucleation and growth during the LPE process induces the MOF crystallites to be chemically bound to the substrate surface. *In-situ* GIXRD profiles during methanol sorption reveal a guest-induced responsivity distinct to the bulk materials. Interestingly, the spatially-controlled anchoring of **1** and **2** MOFs to the surface (**1tf** and **2tf**) emerges a unique structural flexibility upon polar guest sorption which shows a marked dependency on the crystallite dimension (controlled by the total number of deposition cycles) and the crystallite orientation of the films. Low crystallite-dimension thin-film (e.g. **1tf₄₀**) remains in the **lp** form regardless on the sorption treatments, indicating the retardation of the framework breathing transition by the chemical restriction with the substrate and the formation of monodomain with high activation barrier for initiating the flexibility. The breathing transition is matured when fabricating as the higher crystallite-dimension films, in which the crystallites at the extended part from the substrate can undergo framework transition. However, the restriction effect from anchoring to the surface still plays a role, leading to a requirement of methanol with higher relative vapour pressure for the **np** to **lp** phase transition with respect to the transition in the bulk powder. Herein, we illustrate the understanding from the fundamental level of thin-film flexibility, which provides a systematic control of the characteristic features of the MOF-based devices to be suitable for specific applications. A further extension towards well-controlled crystallite orientation^{73,74} and a combination of various responsivities by means of heterostructured architectures would be beneficial for further development of such stimuli-responsive MOF-based devices.

5.5 References

1. R. J. C. Hilf and R. Dutzler, *Nature*, 2009, **457**, 115–118.
2. D. E. Smith, H. P. Babcock and S. Chu, *Science*, 1999, **283**, 1724–1727.
3. K. Ichimura, S.-K. Oh and M. Nakagawa, *Science*, 2000, **288**, 1624–1626.
4. J. Berna, D. A. Leigh, M. Lubomska, S. M. Mendoza, E. M. Perez, P. Rudolf, G. Teobaldi and F. Zerbetto, *Nature Mater.*, 2005, **4**, 704–710.
5. P. M. Mendes, *Chem. Soc. Rev.*, 2008, **37**, 2512–2529.
6. M. A. Cohen Stuart, W. T. S. Huck, J. Genzer, M. Müller, C. Ober, M. Stamm, G. B. Sukhorukov, I. Szleifer, V. V. Tsukruk, M. Urban, F. Winnik, S. Zauscher, I. Luzinov and S. Minko, *Nature Mater.*, 2010, **9**, 101–113.
7. S. Horike, S. Shimomura and S. Kitagawa, *Nature Chem.*, 2009, **1**, 695–704.
8. H. Li, M. Eddaoudi and O. M. Yaghi, *Nature*, 1999, **402**, 276–279.
9. O. M. Yaghi, M. O’Keeffe, N. W. Ockwig, H. K. Chae, M. Eddaoudi and J. Kim, *Nature*, 2004, **423**, 705–714.
10. S. Kitagawa, R. Kitaura and S.-i. Noro, *Angew. Chem. Int. Ed.*, 2004, **43**, 2334–2375.
11. G. Férey, *Chem. Soc. Rev.*, 2008, **37**, 191–214.
12. C. R. Murdock, B. C. Hughes, Z. Lu and D. M. Jenkins, *Coord. Chem. Rev.*, 2014, **258-259**, 119–136.
13. A. Schneemann, V. Bon, I. Schwedler, I. Senkovska, S. Kaskel and R. A. Fischer, *Chem. Soc. Rev.*, 2014, **43**, 6062–6096.
14. R. E. Morris and L. Brammer, *Chem. Soc. Rev.*, 2017, **46**, 5444–5462.
15. S. Krause, V. Bon, I. Senkovska, U. Stoeck, D. Wallacher, D. M. Töbrens, S. Zander, R. S. Pillai, G. Maurin, F.-X. Coudert and S. Kaskel, *Nature*, 2016, **532**, 348–352.
16. C. Serre, F. Millange, C. Thouvenot, M. Noguès, G. Marsolier, D. Louër and G. Férey, *J. Am. Chem. Soc.*, 2002, **124**, 13519–13526.
17. C. Mellot-Draznieks, C. Serre, S. Surblé, N. Audebrand and G. Férey, *J. Am. Chem. Soc.*, 2005, **127**, 16273–16278.

18. J. Seo, R. Matsuda, H. Sakamoto, C. Bonneau and S. Kitagawa, *J. Am. Chem. Soc.*, 2009, **131**, 12792–12800.
19. T. K. Maji, R. Matsuda and S. Kitagawa, *Nature Mater.*, 2007, **6**, 142–148.
20. R. Kitaura, K. Seki, G. Akiyama and S. Kitagawa, *Angew. Chem. Int. Ed.*, 2003, **42**, 428–431.
21. B. D. Chandler, G. D. Enright, K. A. Udachin, S. Pawsey, J. A. Ripmeester, D. T. Cramb and G. K. H. Shimizu, *Nature Mater.*, 2008, **7**, 229–235.
22. S. Yang, X. Lin, W. Lewis, M. Suyetin, E. Bichoutskaia, J. E. Parker, C. C. Tang, D. R. Allan, P. J. Rizkallah, P. Hubberstey, N. R. Champness, K. M. Thomas, A. J. Blake and M. Schröder, *Nature Mater.*, 2012, **11**, 710–716.
23. J. A. Mason, J. Oktawiec, M. K. Taylor, M. R. Hudson, J. Rodriguez, J. E. Bachman, M. I. Gonzalez, A. Cervellino, A. Guagliardi, C. M. Brown, P. L. Llewellyn, N. Masciocchi and J. R. Long, *Nature*, 2015, **527**, 357–361.
24. E. J. Carrington, C. A. McAnally, A. J. Fletcher, S. P. Thompson, M. Warren and L. Brammer, *Nature Chem.*, 2017, **9**, 882–889.
25. N. Yanai, K. Kitayama, Y. Hijikata, H. Sato, R. Matsuda, Y. Kubota, M. Takata, M. Mizuno, T. Uemura and S. Kitagawa, *Nature Mater.*, 2011, **10**, 787–793.
26. P. Horcajada, T. Chalati, C. Serre, B. Gillet, C. Sebrie, T. Baati, J. F. Eubank, D. Heurtaux, P. Clayette, C. Kreuz, J.-S. Chang, Y. K. Hwang, V. Marsaud, P.-N. Bories, L. Cynober, S. Gil, G. Férey, P. Couvreur and R. Gref, *Nature Mater.*, 2010, **9**, 172–178.
27. T. Loiseau, C. Serre, C. Huguenard, G. Fink, F. Taulelle, M. Henry, T. Bataille and G. Férey, *Chem. – Eur. J.*, 2004, **10**, 1373–1382.
28. F. Millange, N. Guillou, R. I. Walton, J.-M. Greneche, I. Margiolaki and G. Férey, *Chem. Commun.*, 2008, 4732–4734.
29. F. Millange, C. Serre and G. Férey, *Chem. Commun.*, 2002, 822–823.
30. J. P. S. Mowat, V. R. Seymour, J. M. Griffin, S. P. Thompson, A. M. Z. Slawin, D. Fairen-Jimenez, T. Dueren, S. E. Ashbrook and P. A. Wright, *Dalton Trans.*, 2012, **41**, 3937–3941.
31. C. Volkringer, T. Loiseau, N. Guillou, G. Férey, E. Elkaim and A. Vimont, *Dalton Trans.*, 2009, 2241–2249.

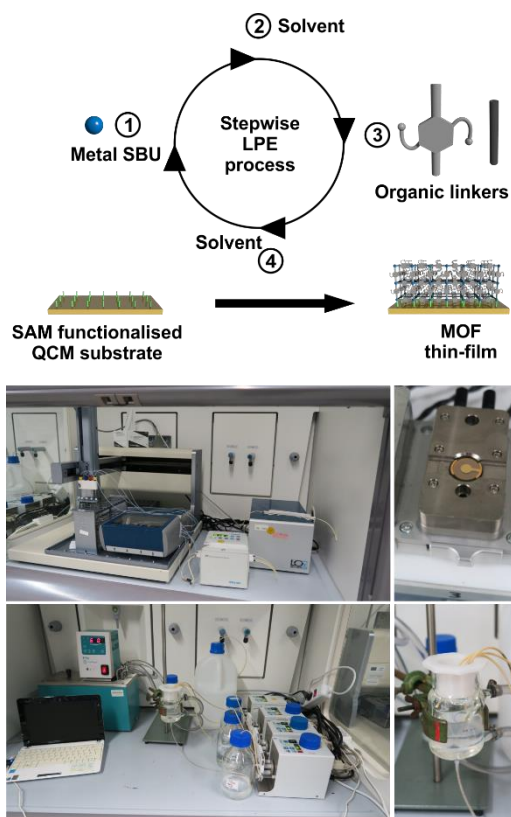
32. E. V. Anokhina, M. Vougo-Zanda, X. Wang and A. J. Jacobson, *J. Am. Chem. Soc.*, 2005, **127**, 15000–15001.
33. S. Surble, C. Serre, C. Mellot-Draznieks, F. Millange and G. Férey, *Chem. Commun.*, 2006, 284–286.
34. S. Bourrelly, P. L. Llewellyn, C. Serre, F. Millange, T. Loiseau and G. Férey, *J. Am. Chem. Soc.*, 2005, **127**, 13519–13521.
35. H. Leclerc, T. Devic, S. Devautour-Vinot, P. Bazin, N. Audebrand, G. Férey, M. Daturi, A. Vimont and G. Clet, *J. Phys. Chem. C*, 2011, **115**, 19828–19840.
36. S. Biswas, T. Ahnfeldt and N. Stock, *Inorg. Chem.*, 2011, **50**, 9518–9526.
37. T. Devic, P. Horcajada, C. Serre, F. Salles, G. Maurin, B. Moulin, D. Heurtaux, G. Clet, A. Vimont, J.-M. Greneche, B. Le Ouay, F. Moreau, E. Magnier, Y. Filinchuk, J. Marrot, J.-C. Lavalley, M. Daturi and G. Férey, *J. Am. Chem. Soc.*, 2010, **132**, 1127–1136.
38. F. Nouar, T. Devic, H. Chevreau, N. Guillou, E. Gibson, G. Clet, M. Daturi, A. Vimont, J. M. Greneche, M. I. Breeze, R. I. Walton, P. L. Llewellyn and C. Serre, *Chem. Commun.*, 2012, **48**, 10237–10239.
39. O. Kozachuk, M. Meilikhov, K. Yusenko, A. Schneemann, B. Jee, A. V. Kuttatheyil, M. Bertmer, C. Sternemann, A. Poepl and R. A. Fischer, *Eur. J. Inorg. Chem.*, 2013, 4546–4557.
40. T. Lescouet, E. Kockrick, G. Bergeret, M. Pera-Titus, S. Aguado and D. Farrusseng, *J. Mater. Chem.*, 2012, **22**, 10287–10293.
41. D. N. Dybtsev, H. Chun and K. Kim, *Angew. Chem. Int. Ed.*, 2004, **43**, 5033–5036.
42. H. Wang, J. Getzschmann, I. Senkovska and S. Kaskel, *Microporous Mesoporous Mater.*, 2008, **116**, 653–657.
43. K. Seki and W. Mori, *J. Phys. Chem. B*, 2002, **106**, 1380–1385.
44. N. Klein, H. C. Hoffmann, A. Cadiou, J. Getzschmann, M. R. Lohe, S. Paasch, T. Heydenreich, K. Adil, I. Senkovska, E. Brunner and S. Kaskel, *J. Mater. Chem.*, 2012, **22**, 10303–10312.
45. N. Klein, C. Herzog, M. Sabo, I. Senkovska, J. Getzschmann, S. Paasch, M. R. Lohe, E. Brunner and S. Kaskel, *Phys. Chem. Chem. Phys.*, 2010, **12**, 11778–11784.

46. S. Henke, R. Schmid, J.-D. Grunwaldt and R. A. Fischer, *Chem. Eur. J.*, 2010, **16**, 14296–14306.
47. S. Henke, D. C. F. Wieland, M. Meilikhov, M. Paulus, C. Sternemann, K. Yusenkov and R. A. Fischer, *CrystEngComm*, 2011, **13**, 6399–6404.
48. A. Schneemann, Y. Takahashi, R. Rudolf, S.-i. Noro and R. A. Fischer, *J. Mater. Chem. A*, 2016, **4**, 12963–12972.
49. S. Henke, A. Schneemann and R. A. Fischer, *Adv. Funct. Mater.*, 2013, **23**, 5990–5996.
50. S. Henke, A. Schneemann, A. Wütscher and R. A. Fischer, *J. Am. Chem. Soc.*, 2012, **134**, 9464–9474.
51. I. Schwedler, S. Henke, M. T. Wharmby, S. R. Bajpe, A. K. Cheetham and R. A. Fischer, *Dalton Trans.*, 2016, **45**, 4230–4241.
52. A. Schneemann, E. D. Bloch, S. Henke, P. L. Llewellyn, J. R. Long and R. A. Fischer, *Chem. Eur. J.*, 2015, **21**, 18764–18769.
53. S. Furukawa, J. Reboul, S. Diring, K. Sumida and S. Kitagawa, *Chem. Soc. Rev.*, 2014, **43**, 5700–5734.
54. H. Uehara, S. Diring, S. Furukawa, Z. Kalay, M. Tsotsalas, M. Nakahama, K. Hirai, M. Kondo, O. Sakata and S. Kitagawa, *J. Am. Chem. Soc.*, 2011, **133**, 11932–11935.
55. T. D. Bennett, S. Cao, J. C. Tan, D. A. Keen, E. G. Bithell, P. J. Beldon, T. Friscic and A. K. Cheetham, *J. Am. Chem. Soc.*, 2011, **133**, 14546–14549.
56. D. Tanaka, A. Henke, K. Albrecht, M. Moeller, K. Nakagawa, S. Kitagawa and J. Groll, *Nat. Chem.*, 2010, **2**, 410–416.
57. Y. Hijikata, S. Horike, D. Tanaka, J. Groll, M. Mizuno, J. Kim, M. Takata and S. Kitagawa, *Chem. Commun.*, 2011, **47**, 7632–7634.
58. Y. Sakata, S. Furukawa, M. Kondo, K. Hirai, N. Horike, Y. Takashima, H. Uehara, N. Louvain, M. Meilikhov, T. Tsuruoka, S. Isoda, W. Kosaka, O. Sakata and S. Kitagawa, *Science*, 2013, **339**, 193–196.
59. N. Kavoosi, V. Bon, I. Senkovska, S. Krause, C. Atzori, F. Bonino, J. Pallmann, S. Paasch, E. Brunner and S. Kaskel, *Dalton Trans.*, 2017, **46**, 4685–4695.

60. H. Miura, V. Bon, I. Senkovska, S. Ehrling, S. Watanabe, M. Ohba and S. Kaskel, *Dalton Trans.*, 2017, **46**, 14002–14011.
61. P. Falcaro, R. Ricco, C. M. Doherty, K. Liang, A. J. Hillb and M. J. Stylesb, *Chem. Soc. Rev.*, 2014, **43**, 5513–5560.
62. J. Liu and C. Wöll, *Chem. Soc. Rev.*, 2017, **46**, 5730–5770.
63. I. Stassen, N. Burtch, A. Talin, P. Falcaro, M. Allendorf and R. Ameloot, *Chem. Soc. Rev.*, 2017, **46**, 3185–3241.
64. C. Scherb, R. Koehn and T. Bein, *J. Mater. Chem.*, 2010, **20**, 3046–3051.
65. L. Heinke, M. Tu, S. Wannapaiboon, R. A. Fischer and C. Wöll, *Microporous Mesoporous Mater.*, 2015, **216**, 200–215.
66. K. Otsubo, T. Haraguchi, O. Sakata, A. Fujiwara and H. Kitagawa, *J. Am. Chem. Soc.*, 2012, **134**, 9605–9608.
67. T. Haraguchi, K. Otsubo, O. Sakata, A. Fujiwara and H. Kitagawa, *Inorg. Chem.*, 2015, **54**, 11593–11595.
68. T. Haraguchi, K. Otsubo, O. Sakata, S. Kawaguchi, A. Fujiwara and H. Kitagawa, *Chem. Commun.*, 2016, **52**, 6017–6020.
69. T. Haraguchi, K. Otsubo, O. Sakata, A. Fujiwara and H. Kitagawa, *J. Am. Chem. Soc.*, 2016, **138**, 16787–16793.
70. S. Sakaida, K. Otsubo, O. Sakata, C. Song, A. Fujiwara, M. Takata and H. Kitagawa, *Nature Chem.*, 2016, **8**, 377–383.
71. S. Sakaida, T. Haraguchi, K. Otsubo, O. Sakata, A. Fujiwara and H. Kitagawa, *Inorg. Chem.*, 2017, **56**, 7606–7609.
72. G. Sauerbrey, *Z. Phys.*, 1959, **155**, 206–222.
73. P. Falcaro, K. Okada, T. Hara⁵, K. Ikigaki⁵, Y. Tokudome, A. W. Thornton, A. J. Hill, T. Williams, C. Doonan and M. Takahashi, *Nature Mater.*, 2017, **16**, 342–348.
74. S. Wannapaiboon, K. Sumida, K. Dilchert, M. Tu, S. Kitagawa, S. Furukawa and R. A. Fischer, *J. Mater. Chem. A*, 2017, **5**, 13665–13673.

Chapter 6

Experimental



This chapter are mainly comprised in the following publications;

- “S. Wannapaiboon, M. Tu and R. A. Fischer, *Adv. Funct. Mater.*, 2014, **24**, 2696-2705” with permission from the Copyright © 2013 WILEY-VCH Verlag GmbH & Co. KGaA.
- “S. Wannapaiboon, K. Sumida, K. Dilchert, M. Tu, S. Kitagawa, S. Furukawa and R. A. Fischer, *J. Mater. Chem. A*, 2017, **5**, 13665-13673” with permission from the Copyright © The Royal Society of Chemistry 2017.
- “S. Wannapaiboon, M. Tu, K. Sumida, K. Khaletskaya, S. Furukawa, S. Kitagawa, and R. A. Fischer, *J. Mater. Chem. A*, 2015, **3**, 23385–23394.” with permission from the Copyright © The Royal Society of Chemistry 2015.

6.1 Precursor syntheses

6.1.1 Synthesis of basic zinc acetate cluster (Chapter 2-4)

Basic zinc acetate, $\text{Zn}_4\text{O}(\text{OAc})_6$, known as the metal secondary building unit (SBU) of MOF-5 analogue was synthesised by the sublimation of zinc acetate dihydrate under vacuum following the published procedure.^{1,2} Zinc acetate dihydrate (5 g) was loaded in a Schlenk fitted with a sublimation apparatus of which cold finger was cooled by tap water. First, the reactant was slowly heated to 120°C under vacuum (*ca.* 1×10^{-3} torr) in sand bath in order to remove the crystal-hydrate water. Then, it was continuously heated until 280°C for sublimation process of zinc acetate for 20 min. The product was formed as white crystals both on the cold finger and on the walls of the Schlenk. After cooling down, the product was collected and the purity of which was characterised by powder X-ray diffraction (XRD, X'Pert PanAnalytical equipment, Bragg-Brentano geometry with automatic divergent slits, Cu K_α radiation, 2θ from 5° to 50°, position sensitive detector, continuous mode, room temperature) as illustrated in Figure 6.1.

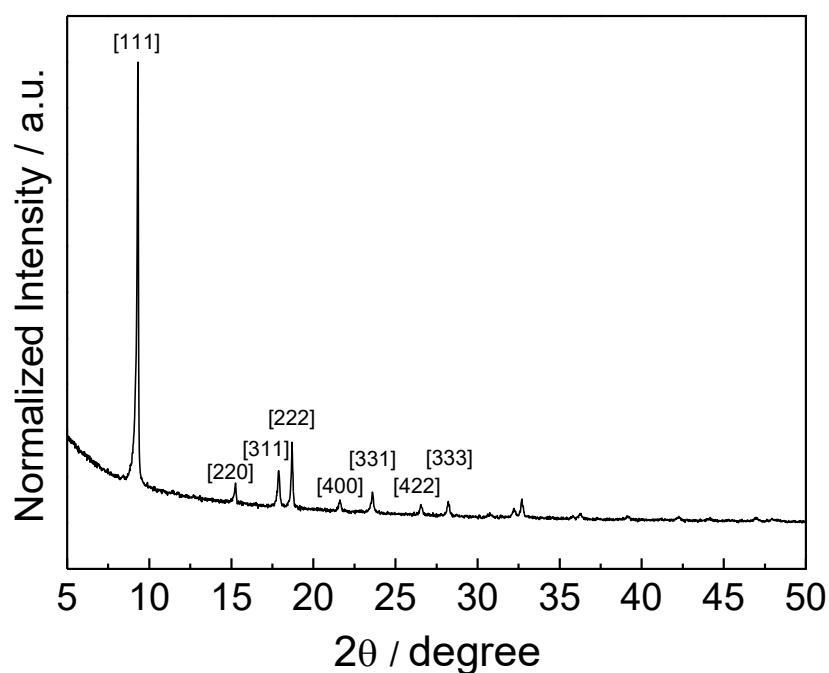


Figure 6.1 Powder XRD pattern of the $\text{Zn}_4\text{O}(\text{OAc})_6$ cluster obtained by the sublimation of zinc acetate dihydrate at 280°C under vacuum

6.1.2 Synthesis of 3-alkyl-5-alkyl-4-carboxypyrazole (H₂L) linkers (Chapter 2-4)

The syntheses of 3-alkyl-5-alkyl-4-carboxypyrazole (H₂L) functionalized linkers were sequentially performed according to the method reported by Rathke and Cowan³ as followed; the acylation of alkyl acetoacetate with alkyl acid chloride, the cyclisation of the synthetic product with hydrazine monohydrochloride and the acidification of the ester products, respectively (Figure 6.2).

To perform the acylation of alkyl acetoacetate with alkyl acid chloride, dry dichloromethane (50 mL) was used as a solvent which firstly added to the round-bottom flask (with a volume of 250 mL) under argon atmosphere. Then, dry magnesium chloride (50 mmol) and alkyl acetoacetate (50 mmol) were sequentially added (still under argon atmosphere). The flask was closed with a septum and cooled down to 0°C. After reaching the temperature of 0°C, pyridine (100 mmol) was added to the mixture via the septum inlet. The solution was stirred for 15 min before adding alkyl acid halide (50 mmol). Then, the reaction mixture was stirred at 0°C for 15 min and consequently at room temperature for 1 h. After that, the mixture was cooled again to 0°C before adding HCl (6M, 30 mL). The resulting solution was extracted with diethyl ether for 3 times. The combined organic layers were dried over MgSO₄ anhydrous and concentrated with rotary evaporator. The residue was chromatographed over silica gel using 2-4% of ethyl acetate in hexane as an eluent in order to afford the pure acylation product.

In order to synthesize ethyl esters of 3-alkyl-5-alkyl-4-carboxypyrazole, the acylation product was further performed a cyclisation with a slightly excess amount of hydrazine monohydrochloride in methanol (50 mL). The reaction mixture was then refluxed for 2 h (or up to 24 h for the more sophisticated R pendent groups). After cooling down, the solution was concentrated with rotary evaporator. Consequently, water (10 mL) and the solution of NaOH was added to the mixture until the pH reached the range of 7-9 (the yellow oil ester was formed).

To obtain the 3-alkyl-5-alkyl-4-carboxypyrazole, the acidification of the ester product was performed. The solution of NaOH (36 mmol) in ethanol (30 mL) was added and the reaction mixture was refluxed overnight. After cooling down, the methanol solvent was evaporated and then water (approximately 25 mL) was added to the residue. The

insoluble impurities were filtrated out. The clear solution was acidified with HCl (37%) until reaching pH 5. The 3-alkyl-5-alkyl-4-carboxypyrazole linker was precipitated as white solid. The structures of the linkers are schematically listed on Figure 6.3. Nuclear magnetic resonance spectroscopy (NMR, DPX 200 and DPX 250 Bruker instrument) was used to justify the purity of the organic linkers.

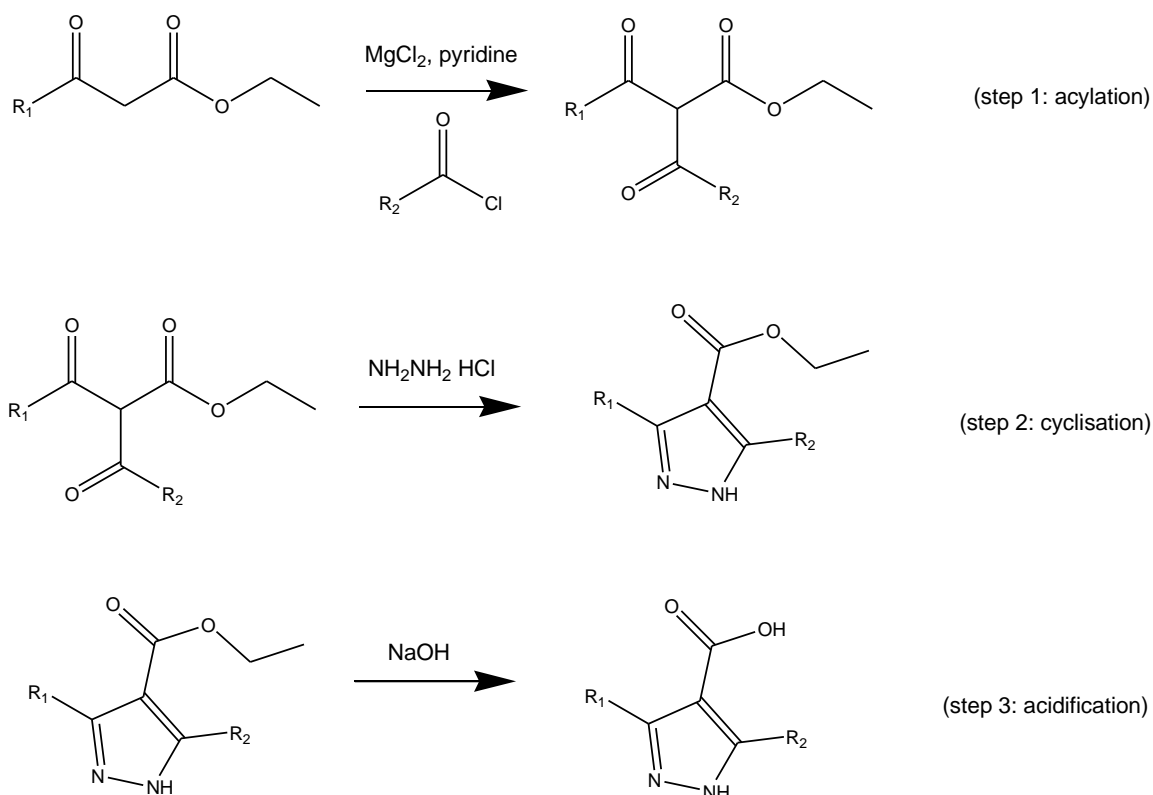


Figure 6.2 Schematic reactions for syntheses of 3-alkyl-5-alkyl-4-carboxypyrazole functionalised linkers (H₂L)

H₂DM (R₁, R₂ = methyl)

Ethyl 2-acetyl-3-oxobutanoate is commercially available and was used without further purification.

3,5-dimethyl-4-carboxypyrazole (H₂DM) was prepared from the cyclisation of ethyl 2-acetyl-3-oxobutanoate and the further acidification: ¹H NMR (250 MHz, CD₃OD) δ 2.41 (6H, s).

H₂ME (R₁ = methyl, R₂ = ethyl)

Ethyl 2-acetyl-3-oxopentanoate was prepared from the acylation of ethyl acetoacetate and propionyl chloride: ¹H NMR (200 MHz, CDCl₃) δ 4.19 (2H, q), 2.62 (2H, q), 2.25 (3H, s), 1.24 (3H, t), 1.07 (3H, t).

5-methyl-3-ethyl-4-carboxypyrazole (H₂ME): ¹H NMR (200 MHz, CD₃OD) δ 2.78 (2H, q), 2.32 (3H, s), 1.12 (3H, t).

H₂MP (R₁ = methyl, R₂ = n-propyl)

Ethyl 2-acetyl-3-oxohexanoate was prepared from the acylation of ethyl acetoacetate and butyryl chloride: ¹H NMR (200 MHz, CDCl₃) δ 4.19 (2H, q), 2.56 (2H, t), 2.25 (3H, s), 1.59 (2H, m), 1.24 (3H, t), 0.88 (3H, t).

5-methyl-3-propyl-4-carboxypyrazole (H₂MP): ¹H NMR (200 MHz, CD₃OD) δ 2.74 (2H, t), 2.32 (3H, s), 1.57 (2H, m), 0.84 (3H, t).

H₂MI (R₁ = methyl, R₂ = isopropyl)

Ethyl 2-acetyl-4-methyl-3-oxopentanoate was prepared from the acylation of ethyl acetoacetate and isobutyryl chloride: ¹H NMR (200 MHz, CDCl₃) δ 4.20 (2H, q), 3.10 (1H, sep), 2.23 (3H, s), 1.27 (3H, t), 1.08 (6H, d).

5-methyl-3-isopropyl-4-carboxypyrazole (H₂MI): ¹H NMR (200 MHz, CD₃OD) δ 3.64 (1H, sep), 2.41 (3H, s), 1.26 (6H, d).

H₂DE (R₁, R₂ = ethyl)

Ethyl 2-propionyl-3-oxopentanoate was prepared from the acylation of ethyl propionylacetate and propionyl chloride: ¹H NMR (200 MHz, CDCl₃) δ 4.27 (2H, q), 2.65 (4H, q), 1.34 (3H, t), 1.16 (6H, t).

3,5-diethyl-4-carboxypyrazole (H₂DE): ¹H NMR (200 MHz, CD₃OD) δ 2.89 (4H, q), 1.23 (6H, t).

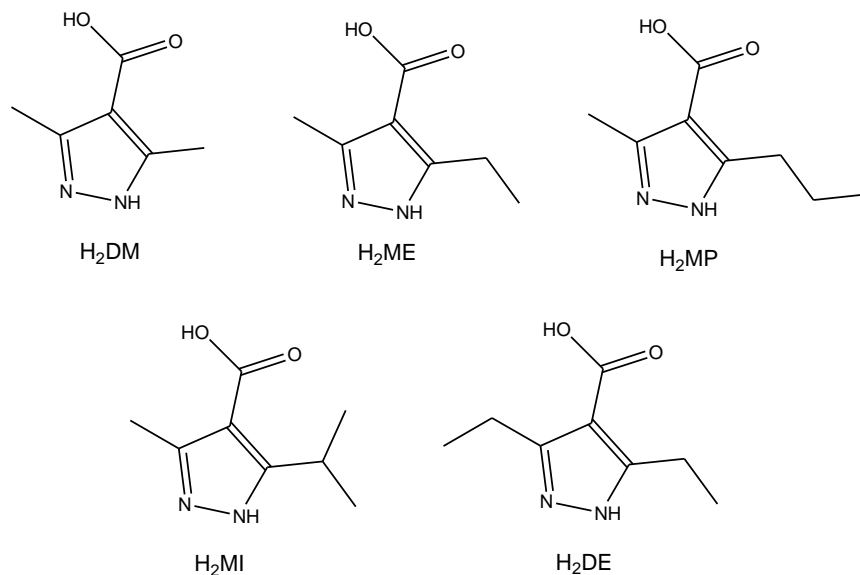


Figure 6.3 Structures of the carboxypyrazolate linkers used in this research

6.1.3 Synthesis of alkoxy-functionalised linkers (Chapter 5)

The alkoxy-functionalised linker, i.e. 2,5-diethoxy-1,4-benzenedicarboxylic acid (H₂DE-bdc) and 2,5-bis(2-methoxyethoxy)-1,4-benzenedicarboxylic acid (H₂BME-bdc), were prepared by Dr. Andreas Schneemann, Chair of Inorganic and Metal-Organic Chemistry, Technical University of Munich. These linkers were synthesised by employing the Williamson ether synthesis from dimethyl 2,5-dihydroxy-benzene-1,4-dicarboxylate according to published procedure.⁴ Schematic reactions are illustrated in Figure 6.4.

2,5-dihydroxy-benzene-1,4-dicarboxylic acid (8 g, 40.4 mmol) is used as a starting reactant. Prior to the Williamson ether synthesis, the carboxylic acid groups within the compound were converted to the methyl ester groups by refluxed with methanol (200 ml, also being a reaction solvent) in the present of BF₃·Et₂O (10 ml) overnight. After reaction, the solvent was evaporated and the remained product was washed several times with cold waters in order to remove BF₃ residues. The dimethyl 2,5-dihydroxy-benzene-1,4-dicarboxylate was obtained as yellow solid and was then dried under vacuum overnight prior to the further reaction. ¹H-NMR (250 MHz, DMSO-d₆): δ 9.81 (s, 2H), 7.27 (s, 2H) and 3.87 (s, 6H).

To synthesise H₂DE-bdc, dimethyl 2,5-dihydroxy-benzene-1,4-dicarboxylate (2 g, 8.84 mmol) and K₂CO₃ (5.56 g, 40.26 mmol) were dissolved in DMF (60 ml). Then, bromoethane (1.45 ml, 19.46 mmol) was added dropwise in to the reaction mixture and then the mixture was refluxed for 12 h. After reaction, the solvent was evaporated under reduced pressure. To convert the ester protecting groups back to the carboxylic acid, the reaction mixture was refluxed with NaOH (1.6 g) in H₂O (80 ml) for 12 h. After that, the solution was acidified with aqueous HCl 15%v/v. The precipitate (light brownish solid) was collected by filtration, washed with H₂O, and dried under vacuum overnight. ¹H-NMR (200 MHz, DMSO-d₆): δ 12.90 (s, 2H), 7.26 (s, 2H), 4.04 (d, 4H), 1.29 (t, 6H).

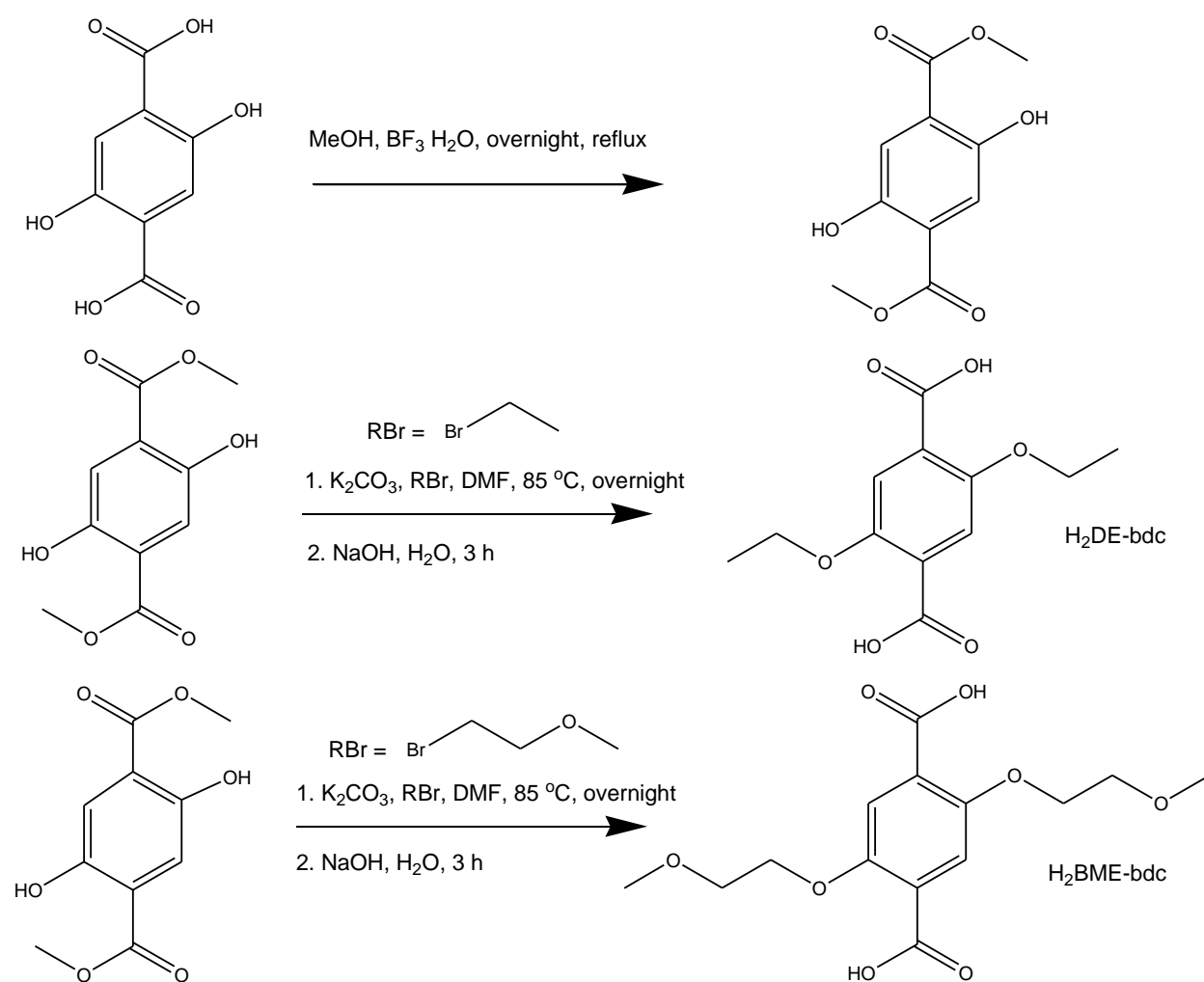


Figure 6.4 Schematic reactions for syntheses of alkoxy-functionalised linkers H₂DE-bdc and H₂BME-bdc.

To synthesise H₂BME-bdc, dimethyl 2,5-dihydroxy-benzene-1,4-dicarboxylate (2 g, 8.84 mmol) was dissolved in DMF (60 ml). Under vigorous stirring, K₂CO₃ (3.66 g, 26.66 mmol) was added. Then, 1-bromo-2-methoxyethane (3.7 g, 26.55 mmol) was added via syringe and the reaction mixture was heated to 85 °C overnight. After reaction, the DMF solvent was removed under vacuum and the remained product was further reacted with aqueous NaOH (800 mg in 150 ml) by reflux for 3 h to synthesise the desired linker. The mixture solution was filtered to remove sediments and then the filtrate was acidified to obtain the desired organic linker. The H₂BME-bdc product was filtered out and dried overnight under vacuum. ¹H NMR (250 MHz, DMSO-d₆): δ 7.30 (s, 2H), 4.12 (dd, J = 5.3, 3.9 Hz, 4H), 3.64 (dd, J = 5.3, 3.9 Hz, 4H), 3.31 (s, 6H).

6.2 Syntheses of bulk MOF powders

6.2.1 Syntheses of Zn-L MOFs by ligand replacement approach (Chapter 2)

The preliminary studies involved the syntheses of different analogues of Zn₄O(L)₃ MOFs (or Zn-L, i.e. Zn-DM, Zn-ME, Zn-MP, Zn-MI and Zn-DE) as bulk powders by direct mixing of the pre-formed metal secondary building unit (SBU) solution with the organic linker solution within a screw-capped jar, so-called a ligand replacement approach (or a controlled SBU approach). The Zn₄O(OAc)₆ solution in ethanol (1.6 mM, 8 ml) and the organic linker solution (4.8 mM, 8 ml of H₂DM, H₂ME and H₂MP in 4:1 v/v ethanol/water mixture; H₂MI and H₂DE in 5:1 v/v ethanol/water mixture) were used as precursor solutions and were prepared separately. To perform the reaction, the organic linker solution was gradually added to the metal SBU solution at ambient temperature within the screw jar (25 mL). The precipitation occurred immediately after mixing the precursor solutions. Consequently, the reaction mixtures were left in the oven at 50 °C for 24 h to allow the full crystallization under equilibrium condition. The synthesized powders were recovered by centrifugation and dried in atmosphere. The scale-up was performed by repeating the batch synthetic procedure above and collecting the whole products together. The activation process was taken in an oil bath at 120 °C for 3 days under vacuum.

6.2.2 Syntheses of Zn-L MOFs by integration of coordination modulation with the ligand replacement approach (Chapter 3)

In order to study the influences of coordination modulation, acetic acid was selected as a coordination modulator and added to the reaction conducting in the ligand replacement approach mentioned in section 6.2.1. Specifically, acetic acid was firstly mixed with the $\text{Zn}_4\text{O}(\text{OAc})_6$ solution. Subsequently, the organic linker solution was slowly added to the reaction mixture. The modulator-to-linker molar ratio (n_L) was varied from 1 to 5 for the syntheses of the three analogue MOFs and furthermore increased up to 30 in the case of **Zn-DM**. After mixing the precursor solutions at room temperature, the reaction mixtures were left in the oven at 50 °C for 24 h in order to achieve complete crystallization under this equilibrium condition. The products were collected by centrifugation and repeatedly washed with ethanol for 3 times. The activation of as-synthesized MOF powders was conducted at 120 °C under vacuum for 3 days prior to the adsorption measurements.

6.2.3 Syntheses of $\text{Cu}_2(\text{fu-bdc})_2(\text{dabco})$ MOFs (Chapter 5)

Syntheses of bulk MOF powders of the type $\text{Cu}_2(\text{fu-bdc})_2(\text{dabco})$ (fu-bdc = 2,5-alkoxy-functionalised-benzene-1,4-dicarboxylate) was conducted by Dr. Andreas Schneemann, Chair of Inorganic and Metal-Organic Chemistry, Technical University of Munich.

$\text{Cu}_2(\text{DE-bdc})_2(\text{dabco})$ powder was prepared under solvothermal reaction condition, which was slightly modified from the previous-reported procedure.⁴ $\text{Cu}(\text{NO}_3)_2 \cdot 3\text{H}_2\text{O}$ (241.6 mg, 1 mmol), $\text{H}_2\text{DE-bdc}$ (254.2 mg, 1mmol) and dabco (56 mg, 0.5 mmol) were suspended in DMF (15 ml) and sonicated until the precursors were fully dissolved. The solution was left at room temperature for 20 min and the precipitate was formed. This precipitate was removed by filtration prior to transferring the filtrate into a screw jar (25 ml), which was sealed and subsequently heated at 120 °C for 48 h. After cooling down to room temperature, the mother liquor was firstly decanted and then exchanged by fresh DMF, and the mixture was stirred for 30 min and left to settle for 24 h. After that, the DMF was exchanged by CHCl_3 , the mixture was again stirred for 30 min and left to settle for 24 h. The solvent exchange procedure with CHCl_3 was repeated for 2 times prior to collecting

the compound $\text{Cu}_2(\text{DE-bdc})_2(\text{dabco})$ by filtration with a frit. The collected product was further washed with CHCl_3 for 3 times and dried at ambient condition. After that, the $\text{Cu}_2(\text{DE-bdc})_2(\text{dabco})$ powder was activated (dried) *in vacuo* at 130 °C overnight. $\text{Cu}_2(\text{BME-bdc})_2(\text{dabco})$ was prepared with the same synthetic procedure for preparing $\text{Cu}_2(\text{DE-bdc})_2(\text{dabco})$ unless the $\text{H}_2\text{BME-bdc}$ (314.3 mg, 1 mmol) was used instead.

6.3 Characterisations of MOF powders

Crystalline phase and purity of the obtained **Zn-L** powders were characterized by powder X-ray diffraction (XRD) patterns collected on an X'Pert PanAnalytical instrument (Bragg-Bentano geometry with automatic divergent slits, $\text{Cu K}\alpha$ radiation, 2θ range from 5° to 35°, scan step size 0.02°, position sensitive detector, operated at ambient atmosphere). Crystalline phase formation of the $\text{Cu}_2(\text{DE-bdc})_2(\text{dabco})$ and $\text{Cu}_2(\text{BME-bdc})_2(\text{dabco})$ bulk powders was identified by XRD (D8 Bruker-AXS advance instrument, flat mode, Debye-Scherrer geometry, slit width of 0.05°, $\text{Cu K}\alpha$ radiation, 2θ from 5° to 50°, position sensitive detector, Ni filter and step size of 0.0141°).

Infrared (IR) spectra were recorded on a Bruker Alpha-P FT-IR (ATR-Mode, 48 scans) situated in a glovebox. Thermogravimetric analysis (TGs) were recorded on a Netzsch STA 409 PC TG-DSC apparatus (in a stream of N_2 gas 99.9999% with constant flow rate of 20 ml/min, temperature range 30 – 700 °C and heating rate of 5 °C /min). The samples were placed in a pre-weighted, clean aluminium oxide crucible. The TG curves were background-corrected by subtracting with a measurement conducted with an empty crucible under the same conditions.

Morphology of the synthesized MOFs was determined by scanning electron microscopic (SEM) images collected on a JEOL JSM-7500F electron microscope using an emission voltage of 15 kV. The samples were activated to remove the residue solvent molecules, then attached to the sample holder using double-side carbon tape, and were coated with osmium nanoparticles to increase the conductivity before loading into the SEM instrument.

To investigate the adsorption properties of the MOF powders, nitrogen sorption measurements at 77 K were performed on a BELSORP-max adsorption analyser (BEL Japan, Inc.). Before the measurements, all MOF samples were activated under dynamic vacuum at 150 °C for 2 h. The specific surface area was calculated using the Brunauer-Emmett-Teller (BET) model.

6.4 Fabrication of MOF thin-films

6.4.1 Preparation of functionalised QCM substrates

Au-coated quartz crystal microbalance sensors (QCM, Q-Sense, AT cut type, Au electrode, diameter 14 mm, thickness 0.3 mm and fundamental frequency ca. 4.95 MHz) were used as substrates. Prior to the fabrication of MOF thin-films, the substrates were immersed in 20 μM solution of 16-mercaptohexadecanoic acid (MHDA) in ethanol and 5% v/v acetic acid for 24 h in order to functionalize the substrate surface. The self-assembled monolayer (SAM) formed by thiol bonding of MHDA molecules on the Au surface provides the—COOH terminated functionality at the substrate surface. These substrates were consequently used for the fabrication of MOF films. In order to generate the pyridyl-terminated surface, the 20 μM solution of 4-(4-pyridyl)phenylmethylthiol (PBMT) was used instead of MHDA during the SAM functionalisation procedure.

6.4.2 Fabrication of Zn-L thin-films by stepwise LPE process (Chapter 2)

For each experiment,⁵ the precursor solutions were freshly prepared as follow: $\text{Zn}_4\text{O}(\text{OAc})_6$ solution (0.5 mM) in ethanol; H_2DM , H_2ME and H_2MP solution (0.5 mM) in 4:1 v/v ethanol/water mixture; H_2MI and H_2DE in 5:1 v/v ethanol/water mixture. Typical stepwise LPE depositions of the **Zn-L** thin-films were carried out on the automated QCM instrument (Q-Sense E4 Auto) at 40 °C in a continuous flow fashion with a flow rate of 100 $\mu\text{L min}^{-1}$. Every individual cycle, the functionalized QCM substrate surface was successively exposed to the solution of $\text{Zn}_4\text{O}(\text{OAc})_6$ (10 min), ethanol solvent (5 min), the H_2L linker (10 min) and finally ethanol solvent (5 min). Herein, the homostructured **Zn-L** thin-films were fabricated for total 40 cycles. The change of QCM frequency was recorded in-situ during the MOF film fabrication to study the MOF film growth.

6.4.3 Fabrication of Zn-L thin-films by integration of coordination modulation with stepwise LPE process (Chapter 3)

In addition to the standard stepwise LPE procedure mentioned in section 6.4.2, herein, acetic acid (used as the coordination modulator) was mixed in the $\text{Zn}_4\text{O}(\text{OAc})_6$ solution.⁶ In order to investigate the influences of the modulator, the modulator-to-metal cluster molar ratio (r_M) were varied ranging from 1 to 5. Three different **Zn-L** films (**Zn-DM**, **Zn-ME** and **Zn-DE**) were selected to fabricate by integrating coordination modulation with the LPE process for total 45 repeated cycles at controlled temperature of 40 °C using the automated QCM instrument (Q-Sense E4 Auto) operated in the continuous flow mode with a flow rate of 100 $\mu\text{L min}^{-1}$. In each deposition cycle, the functionalized QCM substrate was alternatingly exposed to the precursor solutions as follow: $\text{Zn}_4\text{O}(\text{OAc})_6$ mixed with acetic acid 10 min, ethanol (as a solvent) 5 min, organic linker 10 min and finally ethanol 5 min.

To probe the role of coordination modulation in optimising LPE fabrication, three main sets of experiments were performed: (A) **Zn-L** films grown for total 45 cycles without self-seeding layer (in other words, the $\text{Zn}_4\text{O}(\text{OAc})_6$ solution mixed with acetic acid was used from the first deposition cycle), (B) **Zn-L** films grown for 40 cycles on top of the 5-cycles pre-deposited MOF films of the same type grown by typical LPE method without using the modulator as a self-seeding layer (here, the $\text{Zn}_4\text{O}(\text{OAc})_6$ solution mixed with acetic acid was used from the sixth deposition cycle), and (C) **Zn-L** films grown for total 45 cycles without self-seeding layer, however mixing acetic acid with the linker solution instead of the $\text{Zn}_4\text{O}(\text{OAc})_6$ solution.⁶ Moreover, the MOF films grown by typical stepwise LPE method were grown as a control experiment. The change of QCM frequency was recorded in-situ during the MOF film fabrication to study the MOF film growth.

6.4.4 Fabrication of heterostructured, core-shell Zn-L thin-films by stepwise LPE process (Chapter 4)

The standard stepwise LPE procedure mentioned in section 6.4.2 was used. Herein, **Zn-DM** or **Zn-ME** consisting of the larger pore size and pore opening were firstly fabricated as a core layer. Further, **Zn-MI** or **Zn-DE** consisting of the smaller pore size and pore opening were fabricated as a shell layer deposited on the pre-formed core layer.

Herein, three different types of the shell-on-core heterostructured films were produced: **Zn-MI-on-Zn-DM**, **Zn-DE-on-Zn-DM** and **Zn-MI-on-Zn-ME**. The heterostructured films were continuously grown between the core and the shell components by a pre-programmed set-up at the specific dosing step to switch the precursors (used for the growth of the first MOF component to the second one). Consequently, control of the number of deposition cycles of each individual MOF component was straightforward. A variation of the number of deposition cycles (from 10, 15, 20 and 30 cycles) of the core and/or the shell MOF component leads to an optimisation of the synergistic properties emerging in the heterostructured films by mean of the hierarchical structuring architecture.⁷ Again, during the film growth, the change of QCM frequency was recorded to investigate the growth mechanism and examine the quality of the deposited films.

6.4.5 Fabrication of alkoxy-functionalised layered-pillared MOF films by stepwise LPE process (Chapter 5)

Thin-films of $\text{Cu}_2(\text{DE-bdc})_2(\text{dabco})$ and $\text{Cu}_2(\text{BME-bdc})_2(\text{dabco})$ were fabricated by stepwise LPE growth at controlled temperature (40 °C) using an automated QCM instrument (Q-Sense E4 Auto) operated in the continuous flow mode with a constant flow rate of $100 \mu\text{L min}^{-1}$ for a total of 40, 60, 80 and 120 deposition cycles (Figure 6.5). During each deposition cycle, the functionalized QCM substrate was alternately exposed to the precursor solutions as follows: $\text{Cu}(\text{OAc})_2 \cdot \text{H}_2\text{O}$ (0.5 mM in ethanol) 10 min, ethanol (as a solvent) 5 min, the mixed organic linkers ($\text{H}_2\text{DE-bdc} + \text{dabco}$ for $\text{Cu}_2(\text{DE-bdc})_2(\text{dabco})$ and $\text{H}_2\text{BME-bdc} + \text{dabco}$ for $\text{Cu}_2(\text{BME-bdc})_2(\text{dabco})$, 0.2 mM in ethanol) 10 min and finally ethanol 5 min. Note that, the QCM frequency change was monitored *in-situ* during the fabrication process.

For additional insights into the control parameters of structural flexibility in thin-films, $\text{Cu}_2(\text{DE-bdc})_2(\text{dabco})$ film was also fabricated by LPE process for 60 cycles on the pyridyl-functionalised QCM substrates, which led to the preferred growth along the (001)-plane, with the $\text{Cu}_2(\text{DE-bdc})_2$ sheets in parallel to the substrate surface. Moreover, the parent layered-pillared $\text{Cu}_2(\text{bdc})_2(\text{dabco})$ was also prepared as thin-film by the similar LPE procedure (for total 60 cycles). In this case, the commercially available 1,4-benzenedicarboxylic acid (H_2bdc) was used as the layered linker.

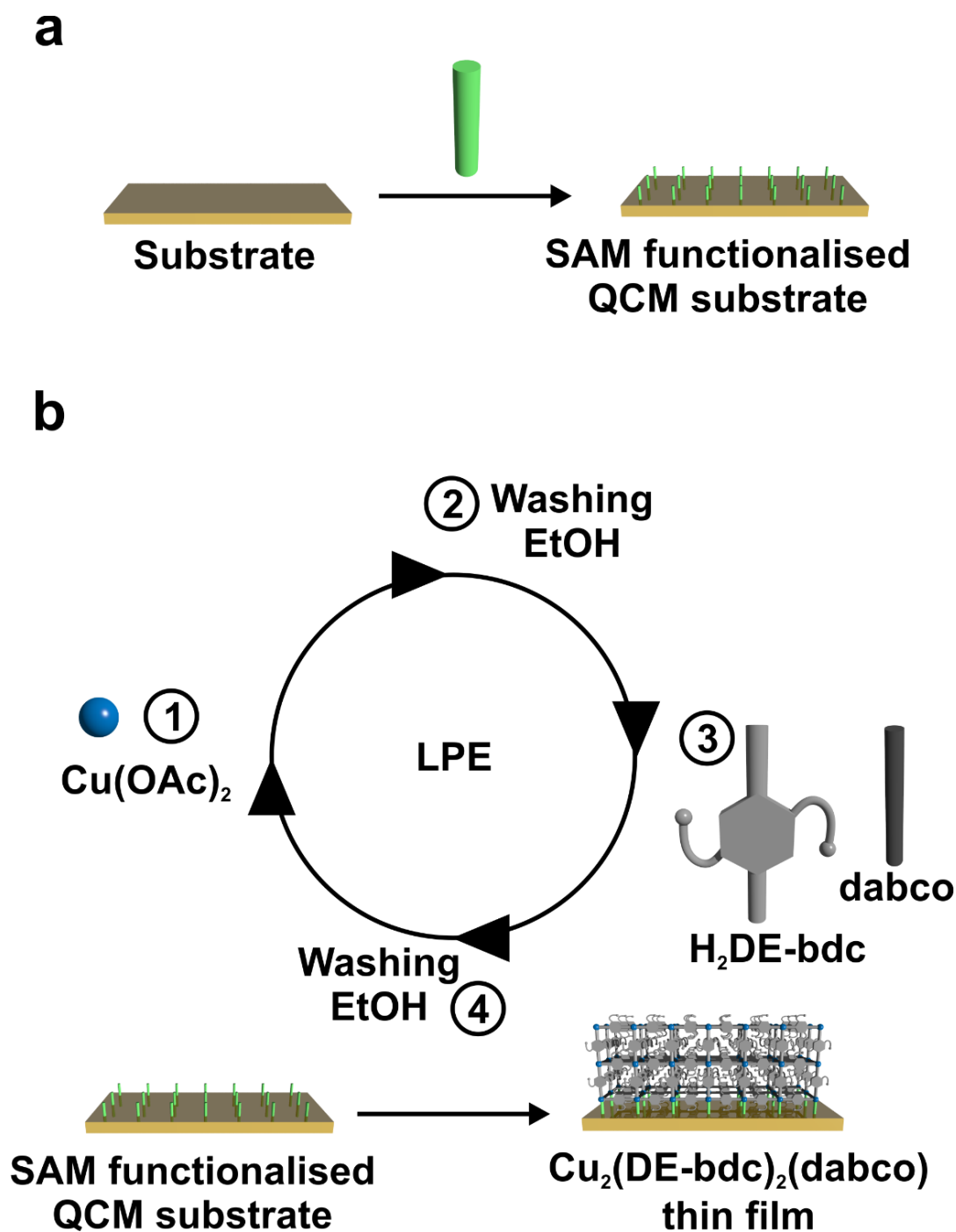


Figure 6.5 Stepwise liquid-phase epitaxial growth of layered-pillared $\text{Cu}_2(\text{DE-bdc})_2(\text{dabco})$ thin-film. (a) The Au-coated QCM substrate was firstly functionalised by SAM of MHDA providing the $-\text{COOH}$ terminated functionality at the substrate surface. (b) In each LPE deposition cycle, the functionalized QCM substrate was alternately exposed to the precursor solutions as follow: $\text{Cu}(\text{OAc})_2$ (10 min), ethanol (5 min), $\text{H}_2\text{DE-bdc}$ and dabco mixture (10 min), and ethanol (5 min) operated in the continuous flow mode and controlled temperature of 40 °C.

6.5 Characterisations of MOF thin-films

The fabricated MOF films were identified the crystalline phase by powder XRD using an X'Pert PanAnalytical instrument (Bragg-Bentano geometry, Cu K_{α} radiation, 2θ range from 5° to 20° with scan step size of 0.01). Two-dimensional grazing incidence X-ray diffraction (2D-GIXRD) were performed at Beamline 9, DELTA Synchrotron facility, Germany⁸ (using X-ray wavelength of 1.0013 Å, incidence angle of 0.6° and refined sample-to-detector distance of 440.0 mm) to characterize the crystal orientation of the fabricated MOF films. Moreover, the crystalline phases of the MOF thin-films perpendicular and parallel to the substrate surface could be also determined by the out-of-plane and the in-plane cuts of the 2D-GIXRD patterns, respectively.

Top-view and cross-sectional SEM images were taken by a field emission scanning electron microscope (FESEM, LEO Zeiss 1530 Gemini and ZEISS Gemini Sigma 300 VP) as well as an environmental scanning electron microscope (ESEM, FEI ESEM Dual Beam™ Quanta 3D FEG) in order to investigate surface morphology and surface coverage of the MOF films. Here, the samples were sputtered with carbon (or gold) in order to increase the conductivity (or avoid charging effect) before loading to the SEM instrument. Infrared reflection adsorption spectra of the activated MOF films were measured inside a glovebox by a Bruker Alpha-P FTIR instrument operated with the external reflection module. The bare SAM-functionalised gold-coated QCM substrate was used for the measurement of background signal.

6.6 Organic vapour sorption measurements

6.6.1 Single-component sorption isotherms measured by QCM (Chapter 2-5)

Sorption properties of the MOF films fabricated on QCM substrates were carried out on an environmental-controlled QCM (BEL-QCM-4 instrument, MicrotracBEL Corp.), of which the schematic setup is illustrated in Figure 6.6. All sorption experiments were measured at controlled temperature of 25°C . Alcohols (such as methanol, ethanol, and isopropanol) and water were used as probe molecules. Prior to the sorption measurements, the films were activated *in-situ* within the BEL-QCM instrument by heating

at 80 °C together with a dry He gas purging with a flow rate of 100 sccm for total 2 h until the change of QCM frequency was stable within the range of ± 5 Hz in 20 min. After activation, the QCM cell was cooled down to 25 °C and the QCM frequency was automatically recorded when the frequency was stable within the range of ± 5 Hz in 20 min.

The masses of the MOF films (as a conversion according to Sauerbrey's equation⁹ of the difference between the QCM frequency at the final activation and the fundamental frequency of the SAM-functionalised QCM substrates) were recorded. After that, organic vapour sorption isotherms were collected by varying the relative vapour pressure (P/P_0) of saturated probe vapour in the He gas flow at 25 °C from 0.0 to 95.0%. The adsorption amounts were calculated according to the Sauerbrey's equation:

$$\Delta F = -\frac{2F_0^2}{A\sqrt{\mu \cdot \rho}} \cdot \Delta M \quad (1)$$

F_0 : fundamental frequency, A : surface area of electrode, μ : shear stress of quartz ($2.947 \times 10^{10} \text{ kg}\cdot\text{m}^{-1}\cdot\text{s}^{-2}$) and ρ : density of quartz ($2648 \text{ kg}\cdot\text{m}^{-3}$).

The adsorption amount at each P/P_0 (ΔM) on the MOF thin-films (M_0) was derived as:

$$\text{Adsorption amount (g/g): } \frac{\Delta M}{M_0} = \frac{F - F_s}{F_s - F_0} \quad (2)$$

M_0 : initial weight of the MOF film sample, F : measuring frequency at each relative vapour pressure and F_s : frequency after final activation of the MOF film sample.

6.6.2 Multiple-component sorption isotherms measured by QCM (Chapter 4)

The sorption properties of the heterostructured MOF thin films were studied by an environmental-controlled QCM instrument (BEL-QCM-4 equipment, MicrotracBEL Corp.) equipped with two vaporisers for different volatile organic compounds (VOCs) with their own set of mass flow controllers. Herein, two alcohols with different kinetic diameter size (methanol (3.6 Å) and isopropanol (4.7 Å)) as well as water (2.6 Å) were selected as probe volatile compounds. Schematic representation of experimental setup for sorption

experiments on MOF-deposited QCM substrates are shown in Figure 6.7. All sorption experiments were carried out at 25 °C. The samples were activated prior to the sorption experiments by immersion in dichloromethane for 24 h (exchanging molecules within the pores) followed by drying under an argon stream. Then, the samples were heated in the BEL-QCM instrument at 70 °C under a dry helium gas flow (100 sccm) for 2 h until the QCM frequency was stable (± 5 Hz over 20 min). For multiple-components adsorption, the experiments were performed using two different probe compounds. Here, the P/P_0 of one probe compound was kept constant at a certain amount (maximum 45% P/P_0), while the other was varied between 0–45% P/P_0 . The total gas flow through the system was fixed at 100 sccm, with mixing of the two components in the manifold prior to exposure to the QCM cell (see Figure 6.7).

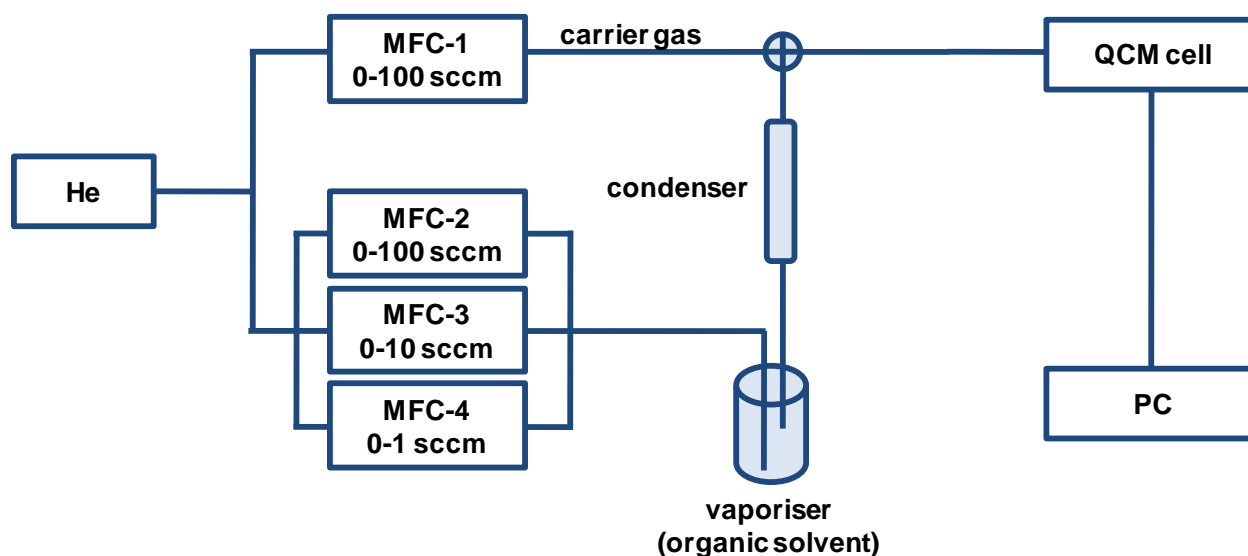


Figure 6.6 Schematic experimental setup of an environmental-controlled QCM instrument used for single-component organic vapour adsorption of MOF thin-films.

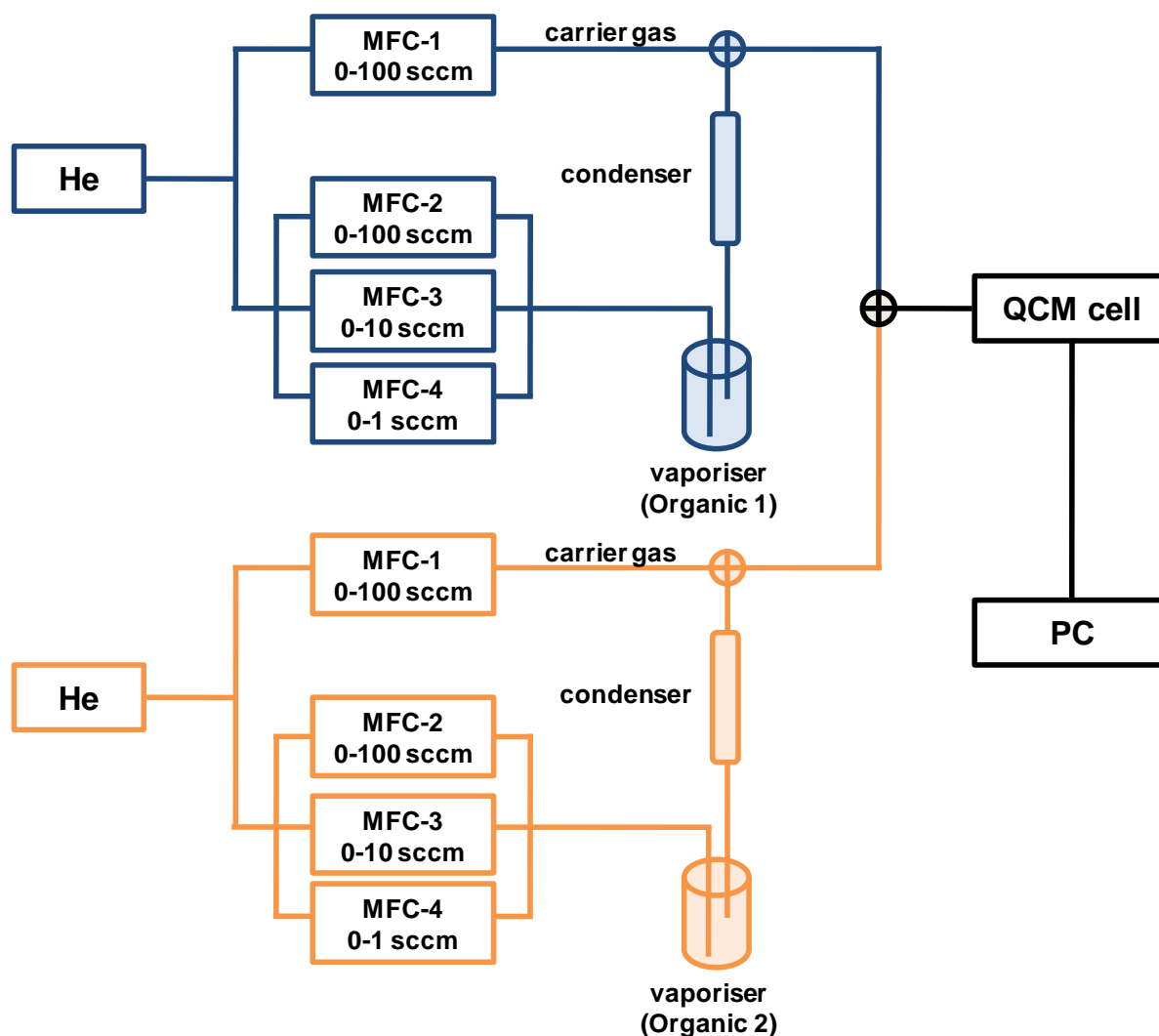


Figure 6.7 Schematic experimental setup of an environmental-controlled QCM instrument used for multiple-component organic vapour adsorption of MOF thin-films. The total gas flow to the QCM cell was kept constantly to be 100 sccm.

6.6.3 In-situ synchrotron X-ray diffraction during methanol adsorption. (Chapter 5)

Crystalline phase and structural flexibility during methanol adsorption of the bulk powders and thin-films of $\text{Cu}_2(\text{DE-bdc})_2(\text{dabco})$ and $\text{Cu}_2(\text{BME-bdc})_2(\text{dabco})$ were identified by 2D-GIXRD (Beamline BL 9 DELTA Synchrotron Germany⁸, X-Ray energy 15.0 keV, wavelength 0.827 Å, incidence angle of 0.6° and refined sample-to-detector distance of 599.2 mm). In order to investigate the structural flexibility of the MOFs upon

adsorption and desorption of polar guest molecules (i.e. methanol) at ambient temperature (25 °C), the synchrotron sample stage was mounted with a temperature-controlled dome-type attachment (DHS 1100, Anton Paar) connected with a self-made He gas flow system in order to semi-quantitatively control the feeding amount of methanol vapour to the chamber (the schematic setup is illustrated in Figure 6.8).

The MOF sample was placed in the sample chamber and covered with the graphite dome. Temperature of the sample chamber was controlled to be 25 °C within the whole experiment. *In-situ* GIXRD patterns were recorded in different stages of adsorption and desorption process: 1) soaking in methanol (mimicking the as-synthesised stage), 2) purging with pure He gas (activation), 3) loading with methanol vapour with 4 different relative vapour pressures (P/P_0 of 10%, 20%, 50% and 80%), and 4) purging with pure He gas (methanol desorption). Note that, the P/P_0 was semi-quantitatively controlled by adjusting the pressure controller at the pure He gas line and the one that passed through the methanol vaporiser to change the mixing ratio, while the total pressure was kept constant behind the sample chamber.

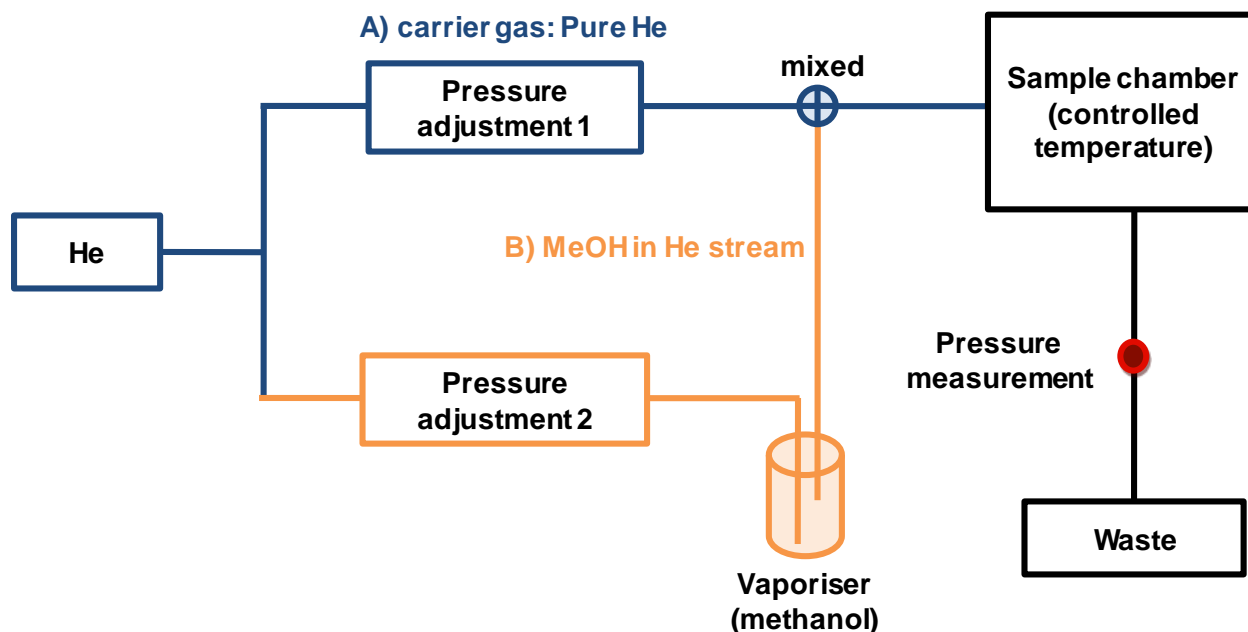


Figure 6.8 Schematic experimental setup of the in-situ GIXRD measurements during variable methanol vapour sorptions.

6.7 References

1. S. Hausdorf, F. Baitalow, T. Böhle, D. Rafaja and F. O. R. L. Mertens, *J. Am. Chem. Soc.*, 2010, **132**, 10978–10981.
2. A. Betard, S. Wannapaiboon and R. A. Fischer, *Chem. Commun.*, 2012, **48**, 10493–10495.
3. M. W. Rathke and P. J. Cowan, *J. Org. Chem.*, 1985, **50**, 2622–2624.
4. S. Henke, A. Schneemann, A. Wütscher and R. A. Fischer, *J. Am. Chem. Soc.*, 2012, **134**, 9464–9474.
5. S. Wannapaiboon, M. Tu and R. A. Fischer, *Adv. Funct. Mater.*, 2014, **24**, 2696–2705.
6. S. Wannapaiboon, K. Sumida, K. Dilchert, M. Tu, S. Kitagawa, S. Furukawa and R. A. Fischer, *J. Mater. Chem. A*, 2017, **5**, 13665-13673.
7. S. Wannapaiboon, M. Tu, K. Sumida, K. Khaletskaya, S. Furukawa, S. Kitagawa, and R. A. Fischer, *J. Mater. Chem. A*, 2015, **3**, 23385–23394.
8. C. Krywka, C. Sternemann, M. Paulus, N. Javid, R. Winter, A. Al-Sawalmih, S. Yi, D. Raabe, M. Tolan, *J. Synchrotron Rad.*, 2007, **14**, 244–251.
9. G. Sauerbrey, *Z. Phys.*, 1959, **155**, 206–222.

Chapter 7

Conclusions and outlook

Primary challenges facing in real-world technologies are the discovery of novel materials with specific functions as well as the development of enhanced and optimized fabrication processes. These novel materials need to be compatibly structuralized on the specific device configurations, while maintaining or even improving the performance profile of the materials in the bulk stage. Metal-organic frameworks (MOFs) are a novel class of microporous solids assembled from metal-based nodes and organic bridging linkers to form infinite, microporous crystalline networks. The tremendous diversity of components that can be used to construct these materials provides opportunities for precise, bottom-up design of both the framework structures and the chemical properties of the pore surfaces. This versatility has led to the investigation in a variety of potential applications, including gas storage, molecular separations, heterogeneous catalysis, sensing, optics, electronics and biomedicines.

Several techniques have been developed to integrate MOFs into the devices known as MOF thin-films or surface-anchored MOFs (SURMOFs). In our research, we have comprehensively studied and developed the fabrication process so-called the stepwise liquid-phase quasi epitaxial growth (LPE), which offers, in principle, a very high control of crystal orientation and microstructure. However, the application of LPE for SURMOFs is limited to few cases and mainly on MOFs featuring dinuclear paddlewheel-based nodes of substitutional-labile metal ions. Herein, we aim for the fundamental understanding the MOF thin-film fabrication and further exploiting this knowledge to design and modify the properties of MOF thin-films in order to serve the use in practical applications.

Firstly, structural designs of the MOF precursors (i.e. metal nodes and organic linkers) used for the LPE process allow us to control the formation of MOF thin-films from the molecular assembly level, providing MOF-based devices with desired functions. The series of $Zn_4O(3\text{-alkyl-5-alkyl-4-carboxypyrazole})_3$ (**Zn-L**) thin-films integrated on functionalized gold-coated quartz crystal microbalance (QCM) sensors shows a high potential for adsorption selectivity with a high tolerance against moisture atmosphere. Moreover, the LPE fabrication process has been modified by employing coordination modulation in order to enhance the characteristics of MOF-based devices. Coordination

modulation is a technique that is often employed for controlling nucleation and growth of MOF bulk crystals. This technique is additionally integrated into the typical LPE process and the **Zn-L** type MOF thin-films are selected to be the studied model cases. Fabrication of **Zn-L** films on QCM substrates allows both the film growth and the molecular adsorption to be precisely probed *in-situ*. Addition of a monofunctional carboxylate as modulator in optimized molar fraction during a specifically-selective growth cycle greatly enhances the properties of the resulting thin-films, boosting their crystallinity, orientation uniformity, and adsorptive capacity. Closer inspection of the QCM data reflects a change in growth kinetics, which influences the quantity of MOF deposition per growth cycle and the overall growth rate controlled by the modulator. The results clearly demonstrate proof-of-principle of this integrated procedure for higher quality SURMOFs. It is likely to overcome current limitation of a more general applicability of LPE to various MOFs, a development of which is crucial for precision applications including electronics, microfluidics, sensing, and optics. The current challenge lies in fully understanding the molecular interactions that dictate the final properties of the film. Furthermore, studies that address the use of broader scope of modulator types in the fabrication of a greater variety of MOFs are noteworthy for the further development of MOF-based devices.

In addition to modification and tuning of the MOF compositions and the fabrication procedure at the molecular assembly level, structuring and control of the MOF physical form in the mesoscopic and macroscopic scales are recognized to affect the MOF functions. Hierarchical engineering of two analogous MOFs with different pore sizes and pore opening windows as heterostructured MOF-on-MOF thin-films consisting of such specific spatial-controlled ordering provides a way to tune the selective adsorption properties of the MOF-based devices. Specifically, size-selective adsorption of alcohols as well as molecular recognition of methanol over water have been extensively investigated. For widespread industrial use, the greater control over the uniformity of the MOF thin-film on larger substrates (as well as spatial localisation of the MOF film to small working units within specific devices), as well as investigations directed toward understanding the mechanical stability will provide an additional perspective toward developing these materials within next-generation devices.

Apart from the well-known structural-rigid MOFs, another fascinating subclasses of MOFs are soft porous crystals, which possess an inherent structural flexibility and can undergo a framework transition when exposed to an external stimulus, such as guest sorption, heat, light or pressure. Based on our knowledge, investigation of structural flexibilities of such flexible MOFs anchored at the substrate surface has been barely reported. In this work, Cu-based pillared-layered $\text{Cu}_2(\text{fu-bdc})_2(\text{dabco})$ (fu-bdc = 2,5-dialkoxy-1,4-benzenedicarboxylate) MOFs are selected to fabricate as thin-films on the QCM substrate by LPE process. The in-situ grazing incidence X-ray diffraction (GID) during the organic vapour sorption could be a promising characterisation to get insight into the flexibility phenomena. Unusual structural flexibility phenomena of the surface-anchored MOF crystallites are emerged which show various degrees of restriction of the framework wine-rack-like breathing transition differing from the bulk materials and markedly depending on the crystallite dimension and the crystallite orientation on the substrate. A systematic control of the flexibility is achieved by controlling the fabrication process for anchoring the MOFs on the substrate. A further extension towards well-controlled crystallite orientation and a combination of various responsivities by means of heterostructured architectures would be beneficial for further development of such stimuli-responsive MOF-based devices.

Appendix



List of scientific publications

A) Publications relevant and partly reproduced in this dissertation

1. **S. Wannapaiboon**, M. Tu and R. A. Fischer, “Liquid phase heteroepitaxial growth of moisture-tolerant MOF-5 isotype thin films and assessment of the sorption properties by quartz crystal microbalance”, *Adv. Funct. Mater.*, 2014, **24**, 2696–2705.
2. **S. Wannapaiboon**, M. Tu, K. Sumida, K. Khaletskaya, S. Furukawa, S. Kitagawa and R. A. Fischer, “Hierarchical structuring of metal–organic framework thin-films on quartz crystal microbalance (QCM) substrates for selective adsorption applications”, *J. Mater. Chem. A*, 2015, **3**, 23385–23394.
3. L. Heinke, M. Tu, **S. Wannapaiboon**, R. A. Fischer and C. Wöll, “Surface-mounted metal–organic frameworks for applications in sensing and separation”, *Microporous Mesoporous Mater.*, 2015, **216**, 200–215.
4. **S. Wannapaiboon**, K. Sumida, K. Dilchert, M. Tu, S. Kitagawa, S. Furukawa and R. A. Fischer, “Enhanced properties of metal–organic framework thin films fabricated via a coordination modulation-controlled layer-by-layer process”, *J. Mater. Chem. A*, 2017, **5**, 13665–13673.
5. **S. Wannapaiboon**, A. Schneemann, I. Hante, M. Tu, K. Epp, C. Sternemann, M. Paulus, G. Kieslich and R. A. Fischer, “Systematic control of structural flexibility of MOF crystallites anchored at surfaces”, 2017, *manuscript in preparation*.

B) Contribution in other research projects

1. **S. Wannapaiboon** and A. Rujiwatra, “Ammonothermal preparation of barium zirconate fine powders”, *Adv. Mater. Res.*, 2008, **55-57**, 85–88.
2. A. Bétard, **S. Wannapaiboon** and R. A. Fischer, “Assessing the adsorption selectivity of linker functionalized, moisture-stable metal-organic framework thin films by means of an environment-controlled quartz crystal microbalance”, *Chem. Commun.*, 2012, **48**, 10493–10495.
3. M. Tu, **S. Wannapaiboon** and R. A. Fischer, “Programmed functionalization of SURMOFs via liquid phase heteroepitaxial growth and post-synthetic modification”, *Dalton Trans.*, 2013, **42**, 16029–16035.

4. M. Tu, **S. Wannapaiboon** and R. A. Fischer, “Liquid phase stepwise growth of surface mounted metal–organic frameworks for exploratory research and development of applications”, *Inorg. Chem. Front.*, 2014, **1**, 442–463.
5. K. Khaletskaya, S. Turner, M. Tu, **S. Wannapaiboon**, A. Schneemann, R. Meyer, A. Ludwig, G. Van Tendeloo and R. A. Fischer, “Self-directed localization of ZIF-8 thin film formation by conversion of ZnO nanolayers”, *Adv. Funct. Mater.*, 2014, **24**, 4804–4811.
6. M. Tu, **S. Wannapaiboon**, K. Khaletskaya and R. A. Fischer, “Engineering zeolitic-imidazolate framework (ZIF) thin film devices for selective detection of volatile organic compounds”, *Adv. Funct. Mater.*, 2015, **25**, 4470–4479.
7. W. Zhang, K. Freitag, **S. Wannapaiboon**, C. Schneider, K. Epp, G. Kieslich and R. A. Fischer, “Elaboration of a highly porous Ru^{II} analogue of HKUST-1”, *Inorg. Chem.*, 2016, **55**, 12492–12495.
8. W. Wattanathana, C. Veranitisagul, **S. Wannapaiboon**, W. Klysubun, N. Koonsaeng, A. Laobuthee, “Samarium doped ceria (SDC) synthesized by a metal triethanolamine complex decomposition method: Characterization and an ionic conductivity study”, *Ceram. Int.*, 2017, **43**, 9823–9830.
9. W. Wattanathana, **S. Wannapaiboon**, C. Veranitisagul, N. Laosiripojana, N. Koonsaeng and A. Laobuthee, “Preparation of palladium-impregnated ceria by metal complex decomposition for methane steam reforming catalysis”, *Adv. Mater. Sci. Eng.*, 2017, **2017**, Article ID 5828067.
10. W. Wattanathana, W. Nantharak, **S. Wannapaiboon**, P. Jantaratana, C. Veranitisagul, N. Koonsaeng and A. Laobuthee, “Barium ferrite prepared by modified Pechini method: effects of chloride and nitrate counter ions on microstructures and magnetic properties”, *J. Mater. Sci.: Mater. Electron.*, 2017, DOI: 10.1007/s10854-017-8064-2.

List of scientific presentations

A) Selected oral presentations

1. *“Liquid phase heteroepitaxial growth of moisture-tolerant MOF-5 isotype thin films and assessment of the sorption properties by quartz crystal microbalance”* The 4th Asian Conference on Coordination Chemistry (ACCC4), Jeju, Korea (November 4 - 7, 2013)
2. *“Continuous liquid phase epitaxial growth of moisture-tolerant metal-organic framework thin films: crystallinity enhancing and assessment of selective sorption properties”* Pure and Applied Chemistry International Conference (PACCON) 2015, Bangkok, Thailand (January 21 - 23, 2015)
3. *“Structural designs and modification of surface-anchored metal-organic frameworks from fundamental study towards applications”* Thai Student Academic Conference 2016 (TSAC2016), Alghero, Italy (May 12, 2016), and lecture at Vidyasirimedhi Institute of Science and Technology (VISTEC), Rayong, Thailand (January 26, 2017)
4. *“Systematic control of structural flexibility of layered-pillared metal-organic Framework Crystallites Anchored at Surfaces”* Thai Student Academic Conference 2017 (TSAC2017), Geneva, Switzerland (September 2, 2017)

B) Selected poster presentations

1. *“Crystallinity and adsorption capacity enhancing of stepwise liquid phase epitaxial moisture-tolerant MOF thin film growths by coordination modulation method”* The 4th International Conference on Metal-Organic Frameworks & Open Framework Compounds (MOF2014), Kobe, Japan (September 28 - October 1, 2014)
2. *“Systematic control of structural flexibility of layered-pillared MOF crystallites anchored at surfaces”* The 5th International Conference on Metal-Organic Frameworks & Open Framework Compounds (MOF2016), Long Beach, California, USA (September 11 - 15, 2016)
3. *“Metal-organic framework thin-films fabricated by coordination modulation assisted stepwise liquid phase epitaxial growth”* The 3rd European Crystallography School, Bol, Croatia (September 25 - October 2, 2016)

Curriculum Vitae

A) Personal information

Name	Suttipong Wannapaiboon
Gender	Male
Date of birth	March 20, 1987
Place of birth	Lampang, Thailand
Nationality	Thai
E-mail	suttipong.wannapaiboon@gmail.com

B) Educational background

2016-2017	Ph.D. candidate at Technical University of Munich, Munich, Germany (transfer from Ruhr University of Bochum)
2013-2016	Ph.D. student (Inorganic Chemistry) at the Ruhr University Bochum, Bochum, Germany
2011-2013	Master of Science (Chemistry), Ruhr University Bochum, Bochum, Germany (GPA 1.0, ECTS grade: excellent)
2005-2008	Bachelor of Science (Chemistry), Chiang Mai University, Chiang Mai, Thailand (GPA 4.00, First Class Honours with the first ranking of the Faculty of Science, Chiang Mai University)
2002-2004	Upper Secondary School Certification (G.10-12), Bunyawat Wittayalai School, Lampang, Thailand (GPA 3.92 with the second ranking among the graduated students)

C) Scholarships

2010-2017	<u>Graduated scholarship</u> : The Royal Thai Government Scholarship under the Office of the Civil Service Commission (OCSC), Thailand
2005-2008	<u>Undergraduate scholarship</u> : Development and Promotion of Science and Technology Talent Project (DPST) of the Institute for the Promotion of Teaching Science and Technology (IPST), Ministry of Science and Technology, Thailand

D) Research grants

- 2014-2017 International Realization Budget (IRB), Research School Plus, Ruhr University Bochum, Germany
- 2009 Thai student representatives participating in “DESY Summer Student Program 2009”, Deutsches Elektronen Synchrotron (DESY), Germany
- 2005-2008 Junior Science Talent Project (JSTP) of the National Science and Technology Development Agency (NSTDA), Thailand

E) Academic awards

- 2014 Nominated by the Faculty of Chemistry and Biochemistry for the RUB award, Ruhr-University Bochum, 2014
- 2005-2008 Excellent Academic Awards for school year 2005, 2006, 2007 and 2008 from the Faculty of Science, Chiang Mai University, Thailand
- 2006 Excellent Academic of Science Students from the Professor Dr. Tab Nilanithi Foundation (August 28, 2006)
- 2006 2nd award of “The Young Thai Science Ambassadors 2006” (April 24-28, 2006) National Science Museum, Pathum Thani, Thailand

F) Research presentation awards

- 2016 First Prize, Outstanding Poster Award 2016 entitled “*Systematic control of structural flexibility of layered-pillared MOF crystallites anchored at surfaces*” The 5th International Conference on Metal-Organic Frameworks & Open Framework Compounds (MOF2016)
- 2015 Outstanding Oral Presentation Award in title “*Continuous liquid phase epitaxial growth of moisture-tolerant metal-organic framework thin films: crystallinity enhancing and assessment of selective sorption properties*” Pure and Applied Chemistry International Conference (PACCON) 2015

- 2009 Outstanding Oral Presentation Award in title "*Influences of ultrasonic wave on phase formation and characteristics of barium zirconate powders synthesized under ammonothermal conditions*" Pure and Applied Chemistry International Conference (PACCON) 2009
- 2008 Outstanding Poster Presentation Award in title "*Ammonothermal preparation of barium zirconate fine powders*" CGI Award for Young Scientists 2008
- 2008 1st Prize in the conference poster competition in title "*Ammonothermal synthesis of barium zirconate powder*" SMARTMAT-'08 & IWOFM-2, Chiang Mai, Thailand (April 22-25, 2008)

G) Selected extracurricular activities and achievements

- 2014-2015 Advisory committee of Thai Student Association in Germany
- 2013-2014 Vice president of Thai Student Association in Germany
- 2012-2013 Executive committee of Thai Student Association in Germany
- 2008 Certificate of Excellent Student Activities among students in the Faculty of Science, Chiang Mai University, Thailand
- 2007 Certificate of members of "Science Student Union of Chiang Mai University"
- 2005-2008 Chairman of the "Representatives of Science Students"
- 2004 Chairman of the Bunyawat Wittayalai Student Council

Suttipong Wannapaiboon

(Mr. Suttipong Wannapaiboon)

Date of record: 27.10.2017

Munich, Germany